DISS. ETH NO. 17050

Detailed Studies of the CMS Potential to Measure the Standard Model Higgs Boson in the $gg \rightarrow H \rightarrow WW \rightarrow \ell\nu\ell\nu$ Channel at LHC

A dissertation submitted to the

Swiss Federal Institute of Technology Zurich

for the degree of

Doctor of Sciences

presented by

Giovanna Madlaina Davatz

Dipl. Phys., ETH Zurich

born 23.07.1977

Citizen of Fanas, Switzerland

accepted on recommendation of

Prof. Dr. Felicitas Pauss (examiner)

Prof. Dr. Zoltan Kunszt (co-examiner)

Dr. Michael Dittmar (co-examiner)

- 2007 -

Abstract

Questa lavur da doctorat preschenta ina studia detagliada dal canal Higgs pp $\rightarrow$ H $\rightarrow$ WW $\rightarrow$ $\ell\nu\ell\nu$ per ina quantitad da 150 e 180 GeV. Il signal e la sistematica dal fundus èn vegnids observads en detagl. La studia cuntegna la implementaziun da las correcturas QCD sin aut nivel per signal e fundus. Per lemprima giada ha ins fatg in'entira simulaziun detectoriala en quest chanal. Il fundus è vegnì valità cun ina analisa che sa basa sin ina banca da datas. Ins po chattar cun ina luminositad integrada da main che 1 fb^{-1} en quest chanal in model da standard Higgs boson, sch'i ha ina quantitad da radund 165 GeV. Per ina quantitad tranter 150 e 180 GeV po ins scuvrir in signal da 5σ cun ina luminositad da radund 10 fb^{-1}. Cun la supposiziun che l'acceleratur da hadrons LHC chatta era in signal cumparegliabel sco il Higgs en quest chanal, ha ins analisà diversas observablas experimentalas per vesair co e quant exact ins po mesirar la quantitad Higgs. Schins combinescha il tagl traversal ipotetic cun il momentum spectral dals leptons e calculescha cun ina intschertezza dal fundus stimada sin 10-15%, po ins quintar cun ina exactadad da 2-2.5 GeV per in signal da standard Higgs en la regiun da 150 a 180 GeV. En cas ch'i na vess betg da procurar per in meglierament en la sistematica, mussa noss'analisa che la determinaziun da la quantitad vegn dominada da l'intschertezza da la sistematica schina luminositad da radund 10 fin 20 fb^{-1} stat a disposiziun.

Abstract

A study of the Higgs channel pp $\rightarrow$ H $\rightarrow$ WW $\rightarrow \ell\nu\ell\nu$ for a mass between 150 and 180 GeV is presented. Signal and background systematics are investigated in detail, including the implementation of most up-to-date higher order QCD corrections for signal and background. For the first time full detector simulations are performed in this channel. A data driven approach to determine the size of the backgrounds is used. A Standard Model Higgs boson can be discovered in the H $\rightarrow$ WW $\rightarrow \ell\nu\ell\nu$ channel with an integrated luminosity of less than 1 fb^{-1} if its mass is around 165 GeV. If it has a mass between 150 and 180 GeV, a 5σ signal can be seen with a luminosity of about 10 fb^{-1}. Assuming that the LHC experiments will discover a Higgs-like signal in this channel, different experimental observables have been analysed in order to establish how and how well the Higgs mass can be measured in this mass range. Combining the hypothetical cross section measurement with the lepton p_{T} spectra and the estimated systematic uncertainties of 10 to 15%, associated with this signature, we find that the mass of a Standard-Model-Higgs-like signal in the mass range between 150 and 180 GeV can be measured with an accuracy of 2 to 2.5 GeV. In case that no further improvements in the systematics for this channel can be achieved, our analysis shows also that such a mass measurement will be dominated by systematic uncertainties once integrated luminosities of about 10-20 fb^{-1} can be analysed.

Contents

Chapter 1

Introduction

The idea to describe the immense complexity of the world around us by fundamental laws, and to describe matter as being made of some few basic constituents, is very attractive. This approach is not new. Already the ancient Greeks came up with the idea that matter consists of fundamental unbreakable entities called atoms. For a long time atoms were thought to be the elementary building blocks of matter. In the beginning of the 20th century, E. Rutherford deduced the existence of a compact atomic nucleus consisting of smaller particles from scattering experiments. During the last century, the development of particle colliders allowed the exploration of matter at smaller and smaller scales. The atoms were found to be composed of clouds of very light particles called electrons surrounding a dense nucleus consisting of more massive particles, the protons and neutrons. In the 1960's it became clear that also the protons and neutrons consist of smaller particles, the so-called quarks and gluons.

The discovered particles and the forces interacting between them are described in the so-called Standard Model of Particle Physics (SM). The SM describes phenomena for energies which are accessible at today's accelerators at very high precision. The forces represented within the SM are the weak, strong and the electromagnetic interaction. The electromagnetic and weak interaction are combined in the so-called electroweak interaction. The ansatz to describe interactions in a common form has its roots in the beginning of the last century, when J.C. Maxwell constructed equations which link together electricity and magnetism. He also suggested the wave-like character of electromagnetism, and that electromagnetic energy could be transmitted in this way. This was confirmed years later by H. Hertz. The picture of electromagnetic waves changed with the advent of quantum theory - leading to the idea of wave/particle dualism: the photons were determined to be the particles communicating electromagnetism. This lead to the theory of quantum electrodynamics (QED).

Following the success of QED in the 1950s, attempts were undertaken to formulate a similar theory for the weak nuclear force. This culminated around 1968 in a unified theory of electromagnetism and weak interactions by S. Glashow, S. Weinberg, and A. Salam [1]. Their electroweak theory postulated the carrier of the weak force: the $W^{\pm}$ bosons. The fact that the W and Z bosons have mass while photons are massless was a major obstacle in developing the electroweak theory. These particles are accurately described by $SU(2)$ gauge theory, but

the bosons in a gauge theory have to be massless.
The way to obtain masses for gauge bosons, while preserving a local gauge symmetry, leads to the concept of spontaneous symmetry breaking. It assumes the existence of a scalar field, the so-called Higgs field, giving masses to particles [2]. This is called the Higgs mechanism. The scalar fields interact with each other in such a way that the degenerate ground state acquires a non-zero field strength, and by choosing one state, the electroweak symmetry is broken spontaneously. It is therefore also called 'the hidden symmmetry'. The interaction energies of electroweak gauge bosons, leptons and quarks with this field manifest themselves as non-zero masses of these particles. The SM Higgs mechanism leads to an additional particle: the Higgs boson. The Higgs boson is something like the holy grail in the Standard Model, as it is not discovered yet. Finding this particle and studying its fundamental properties is one of the main goals of today's and future high energy particle colliders.

Since the 1980s, an impressive amount of theoretical knowledge was obtained on the Higgs boson properties, its principal production and decay modes. Advances in computer technology allowed to perform very complicated calculations for loop-diagrams and multi-particle processes, for the signal as well as for different background processes. In order to compare data with theoretical predictions, Monte Carlo event generators for various processes were developped. Many parton-level analyses and Monte Carlo simulations have been performed to assess to what extend the Higgs particle can be observed and its properties studied in given processes at various accelerators.

Since many years, the search for the Higgs bosons has been one of the main analysis topics at different accelerators worldwide. The Higgs was searched for at the LEP accelerator at CERN in Geneva [3], at HERA in Hamburg (e.g. [4, 5]), and in the two detectors D0 and CDF at the proton-antiproton accelerator Tevatron at Fermilab in Chicago [6]. A new collider is about to be completed at CERN: the LHC, which is scheduled to start operation in May 2008, will collide protons at a center-of-mass energy of 14 TeV. Two detectors, ATLAS and CMS, which are placed in the LHC tunnel, should be able to detect a Higgs boson with a mass between 100 GeV and 1 TeV. Direct searches at LEP and indirect constraints from LEP and Tevatron predict a Higgs mass between 114.4 GeV and 186 GeV (at 95 % CL) [3, 6]. Out of the large interaction rate at LHC, CMS and ATLAS will collect a huge amount of data. The production rate of Higgs bosons is relatively small and thus represents only a small fraction of the collected data. Therefore, characteristic observables have to be chosen carefully, and signatures with very good selection criteria are required to reduce the huge number of background events. This is a challenging task from both the experimental and theoretical point of view. It requires not only excellent detectors but also outstanding analysis methods. In the last decade, we could witness impressive progress in both the analytic and numerical methods on how to calculate processes up to higher order accuracy in perturbation theory. As the higher order corrections can be large, these calculations have to be taken into account in the analyses performed for the LHC.

The work presented in this thesis shows how a Standard Model Higgs boson with a mass in the region between 150 and 180 GeV can be detected and its mass be measured. The following

chapters will describe the systematics which have to be taken into account, from theoretical as well as from experimental aspects. First, an introduction to the Standard Model is given in Chapter 2, and the LHC accelerator and the CMS experiment are presented (Chapter 3). The SM Higgs production and decay processes are discussed in Chapter 4. The way particle interactions are simulated in high energy physics is explained in Chapter 5 and the systematics due to different Monte Carlo predictions for the Higgs p_{T} spectrum, as well as for the jet veto efficiency, shown (Chapter 6). The matrix element calculations of the Higgs production through gluon fusion, which is the main production process at hadron colliders, is presented in Chapter 7. A way how those higher order QCD corrections can be included in parton shower Monte Carlo programs is presented in Chapter 8 and applied to the $\mathrm{gg} \to \mathrm{H} \to \mathrm{WW} \to \ell\nu\ell\nu$ channel in Chapter 9. The background from $\mathrm{t\bar{t}}$ and Wtb is discussed in Chapter 10, with emphasis put on how to include higher order corrections in the simulations of these backgrounds in the most accurate way. It is shown that the predictions from different Monte Carlo generators vary quite a lot. Hence, it is important to find a way how to determine the background from data. In addition, even though higher order corrections were performed for most of the backgrounds, they are not under the same theoretical control as the signal, and thus, a data driven method to obtain the background systematics is needed, which is described in Chapter 11. Results including full detector simulation and background systematics are presented. Summing up, Chapter 12 introduces a method how and how well the Higgs mass can be determined in this channel.

Chapter 2

The Standard Model of Particle Physics

2.1 Particle Content of the Standard Model

The Standard Model of particle physics (SM) is the theory which describes best the experimental observations accessible at today's energies. The Standard Model is a relativistic quantum field theory based on the groups of symmetries $SU(3)_C \times SU(2)_L \times U(1)_Y$. These three local symmetry groups dictate the three interactions between the particles in the SM. The theory is perturbative at sufficiently high energies [7] and renormalizable [8]. The $SU(3)_C$ group is related to the strong interaction between quarks, governed by Quantum Chromodynamics (QCD), and implies the existence of eight coloured gluons. The $SU(2)_L \times U(1)_Y$ groups are associated to the electroweak interaction. The electroweak interaction is the unified description of electromagnetism and the weak interaction. Although these two forces appear very different at low energy, the theory models them as two different aspects of the same force. Above the electroweak unification energy, which is of the order of 100 GeV, they merge into a single force. The constituents of matter are fermions, i.e. particles of spin 1/2.

	1st family		2nd family		3rd family	
leptons	$\begin{pmatrix} \nu_e \\ e \end{pmatrix}$	$< 3\,\text{eV}$ $0.511\,\text{MeV}$	$\begin{pmatrix} \nu_\mu \\ \mu \end{pmatrix}$	$< 0.19\,\text{MeV}$ $106\,\text{MeV}$	$\begin{pmatrix} \nu_\tau \\ \tau \end{pmatrix}$	$< 18.2\,\text{MeV}$ $1.777\,\text{GeV}$
quarks	$\begin{pmatrix} u \\ d \end{pmatrix}$	$\sim 7\,\text{MeV}$ $\sim 3\,\text{MeV}$	$\begin{pmatrix} c \\ s \end{pmatrix}$	$\sim 1.2\,\text{GeV}$ $\sim 115\,\text{MeV}$	$\begin{pmatrix} t \\ b \end{pmatrix}$	$175\,\text{GeV}$ $\sim 4.25\,\text{GeV}$

Table 2.1: The building blocks of the Standard Model [9].

The fermions are divided into groups of leptons and quarks which are found within three families of identical structure and very different masses (Table 2.1). To each fermion, there

exists a corresponding anti-particle, a so-called anti-fermion with exactly the same couplings as the fermions[1]. The reason for arranging them in families is that the fermions in each family behave almost exactly like their counterparts in the other families. This property, with respect to weak interaction, is also referred to as universality. As an example, the electron and the muon both have half-integer spin, unit electric charge and do not participate in the strong interaction, but the muon is about 200 times heavier than the electron and its lifetime is 2.2 μs.

Up to now quarks have only been observed in $q\bar{q}$ states, so-called "mesons" (e.g. the pi-meson) or $qqq/\bar{q}\bar{q}\bar{q}$ states, so-called "baryons" (e.g. protons, neutrons). The two members of every family differ by one unit of electric charge: the leptons (quarks) in the top row of Table 2.1 carry charge 0 (2/3), the ones in the bottom row carry charge -1 (-1/3). Besides electric charge, the quarks also possess the called colour charge. This is relevant for their strong interaction, which binds them together inside mesons and baryons (hadrons). Every quark appears in three different colour states, belonging to a $SU(3)_C$ triplet, while the leptons are colourless $SU(3)_C$ singlets.

The interactions between the particles[2] are described by an exchange of so called gauge bosons, i.e. spin 1 particles, which are interpreted as excitations of the gauge fields describing the associated interaction. The exchange bosons of the electromagnetic, weak and strong interactions are the photon (γ), the $W^{\pm}$ and Z^0 boson, and the gluon, respectively. They are listed in Table 2.2.

The $SU(2)_L \times U(1)$ gauge theory is the simplest unification of the parity violating weak force and the parity conserving electromagnetic force. The $SU(2)_L$ gauge bosons couple only to the left-handed components Ψ_L of the fermion fields leading to the observed parity violation. The $U(1)$ gauge boson couples to both the left-handed and the right-handed components Ψ_L and Ψ_R. The left-handed projections of ther fermion fields form $SU(2)_L$ doublets

$$\Psi_L = \begin{pmatrix} \nu_e \\ e^- \end{pmatrix}_L, \begin{pmatrix} \nu_\mu \\ \mu^- \end{pmatrix}_L, \begin{pmatrix} \nu_\tau \\ \tau^- \end{pmatrix}_L, \begin{pmatrix} u \\ d \end{pmatrix}_L, \begin{pmatrix} c \\ s \end{pmatrix}_L, \begin{pmatrix} t \\ b \end{pmatrix}_L \tag{2.1}$$

while the right-handed components are $SU(2)_L$ singlets

$$\Psi_R = e_R^-, \mu_R^-, ... \tag{2.2}$$

$SU(2) \times U(1)$ is a non-Abelian group which is generated by the isospin operators I_1, I_2, I_3 and the hypercharge Y (the elements of the corresponding Lie-Algebra). Each of these generalized charges is associated with a vector field: a triplet of vector fields $W_\mu^{1,2,3}$ with $I_{1,2,3}$ and a singlet field B_μ with Y. The isotriplet W_μ^a, a=1,2,3, and the isosinglet B_μ lead to the field strength tensors, as will be shown later. Since the γ is massless, the range of

[1]Note that all atoms are made of fermions from the first family. The other particles are short-lived and can be produced in cosmic rays or at accelerators.

[2]Except the gravitation, which is not included in the SM.

Interaction	Electromagnetic	Weak	Strong
Current Theory	QED	Electroweak Theory (GWS theory)	QCD
Carrier	γ	$W^{\pm}$, Z^0	8 gluons
Mass	0	80, 91 [GeV]	0

Table 2.2: Gauge bosons of the Standard Model.

electromagnetic interactions is infinite. The W^+ and W^- bosons and the neutral Z boson are massive ($\backsim$ 100 GeV), the weak interaction is therefore short ranged. The gluons, which are the quanta of the strong interaction field, acting between colour-charged quarks, have zero mass and carry colour-charge. They can interact among each other which leads to a phenomena called confinement, restricting the strong force to nuclear distances. The electroweak theory postulated the W bosons to explain the beta decay. The existence of W and Z bosons mediating the electroweak theory was experimentally established in two stages: the first step being the discovery of neutral currents in neutrino scattering by the Gargamelle collaboration in 1973 [10]. This was interpreted as a neutrino interacting with the electron by the exchange of a virtual Z boson. In 1983 by the UA1 and the UA2 collaborations discovered the W and Z gauge bosons in proton-antiproton collisions at the Super Proton Sychrotron SPS at CERN [11].

2.1.1 Global and Local Gauge Invariance

The description of interactions relies on the work of Yang and Mills, who generalized the gauge structure of electromagnetism. The SM is a relativistic quantum field theory, and the particle content can be described by the Dirac and Klein-Gordon equations in the case of free fermions and bosons, respectively[3]. For fermions, the equation of motions is derived from the Lagrangian

$$\mathcal{L} = \bar{\Psi} i\gamma_\mu \partial^\mu \Psi - m\bar{\Psi}\Psi \tag{2.3}$$

where Ψ is a 4-component complex field (Dirac spinor) representing a free fermion field with mass m. The properties of bosons are determined by a Klein-Gordon Lagrangian

$$\mathcal{L} = \partial_\mu \Phi^\star \partial^\mu \Phi - m\Phi^\dagger \Phi \tag{2.4}$$

with Φ being a complex scalar field with mass m.
We will see in the following how the particle interactions are dictated by so-called local gauge symmetries. As an example, we will discuss the case of an electron, described by a complex field $\Psi(x)$, and then generalize. The equation of motion of the electron are derived from the Dirac Lagrangian 2.3, which is invariant under the phase transformation

[3] "Free" means here in the absence of a gauge field.

$$\Psi(x) \rightarrow e^{i\alpha}\Psi(x) \tag{2.5}$$

where α is a real constant.

The family of phase space transformation $U(\alpha) = e^{i\alpha}$ forms a unitary Abelian group known as the $U(1)$ group[4]. The fact that the Lagrangian remains invariant under phase transformation means that the Lagrangian possesses global $U(1)$ gauge symmetry, as α is constant in space and time; α has no physical meaning and is not measurable. Following the Noether theorem one can expect that the $U(1)$ -invariance imposes the conservation of a quantity, and indeed, the electric charge is the conserved quantity of the $U(1)$ invariance.

Now, if the Lagrangian is also invariant under the phase transformation

$$\Psi(x) \rightarrow e^{i\alpha(x)}\Psi(x) \tag{2.6}$$

where α is an arbitrarily function of the space-time vector x, $\alpha = \alpha(x)$, it possess local gauge invariance. However, the Lagrangian is not invariant under such a transformation, since the derivative of Ψ transforms into

$$\partial_\mu\Psi \rightarrow e^{i\alpha(x)}\partial_\mu\Psi + ie^{i\alpha(x)}\Psi\partial_\mu\alpha(x). \tag{2.7}$$

and thus breaks the invariance. In order to make the Lagrangian invariant under local gauge transformations, one can replace the derivative ∂_μ by a so-called "covariant derivative" D_μ, which is defined as

$$D_\mu \equiv \partial_\mu - ieA_\mu, \tag{2.8}$$

where e is an arbitrary constant and the vector field A_μ transforms as

$$A_\mu \rightarrow A_\mu + \frac{1}{e}\partial_\mu\alpha(x). \tag{2.9}$$

D_μ transforms like Ψ itself:

$$D_\mu\Psi \rightarrow e^{i\alpha(x)}D_\mu\Psi. \tag{2.10}$$

The gauge field A_μ is an arbitrary function of space and time, which compensates the local gauge transformation of the phase in order that the Lagrangian becomes gauge invariant:

[4]An Abelian group is commutative such that a * b = b * a for all a and b in the group.

$$\mathcal{L} = \bar{\Psi} i\gamma^\mu D_\mu \Psi - m\bar{\Psi}\Psi = \bar{\Psi}(i\gamma^\mu \partial_\mu - m)\Psi + e\bar{\Psi}\gamma^\mu \Psi A_\mu$$
$$= \mathcal{L}_{free} + e\bar{\Psi}\gamma^\mu \Psi A_\mu \tag{2.11}$$

The first part is the equation of the free lepton, while in the second part, the coupling of the lepton to a vector field A_μ (called the gauge field) is described. This corresponds exactly to the situation where a photon field couples to an electron with charge -e. Therefore, by requiring local phase invariance of the free fermion Lagrangian, the interacting field theory emerges. In order to give dynamics to the photon field A_μ, an additional term $-\frac{1}{4}F_{\mu\nu}F^{\mu\nu}$, representing the kinematic energy of the photon field, can be inserted, where $F_{\mu\nu} = \partial_\mu A_\nu - \partial_\nu A_\mu$ represents the electromagnetic field strength tensor. Adding this term, the local gauge invariance is still preserved.

This procedure can not only be applied to the electromagnetic interaction (quantum electrodynamics or QED) which results from the $U(1)$ gauge symmetry, but also to the weak and the strong interaction. The weak interactions can be derived from a $SU(2)$ symmetry group, the strong interactions from a $SU(3)$ group.
In general, the theoretical picture is the following: A symmetry G becomes local, if a covariant derivative D_μ is introduced; D_μ has to generalize the usual derivative ∂_μ, for the Lagrangian to remain invariant under the gauged symmetry. This can be done by introducing a set of real vector fields A^a_μ such that $D_\mu = \partial_\mu - igA^a_\mu T^a$, where g is the gauge coupling, and T^a are the generators of group G.
In order to give a dynamic to these gauge fields, a gauge tensor $F_{\mu\nu}$ has to be introduced, which must be antisymmetric in its two spatial indices, so it is natural to define $igF_{\mu\nu} = [D_\mu, D_\nu]$. In the case above, the dynamics of the field was introduced by $F_{\mu\nu} = \partial_\mu A_\nu - \partial_\nu A_\mu$. In the case of the electroweak interaction, the covariant derivative

$$D_\mu \equiv (\partial_\mu - ig\overrightarrow{T}\overrightarrow{W}_\mu - ig'\frac{Y}{2}B_\mu), \tag{2.12}$$

is introduced, where g and g' are the coupling constants related to $SU(2)_L$ and $U(1)_Y$, respectively. The electroweak Lagrangian includes kinematic terms for the gauge fields like

$$-\frac{1}{4}W^i_{\mu\nu}W^{\mu\nu}_i - \frac{1}{4}B_{\mu\nu}B^{\mu\nu}. \tag{2.13}$$

where the field strength tensors are

$$W^i_{\mu\nu} = \partial_\mu W^i_\nu - \partial_\nu W^i_\mu - g\epsilon^{ijk}W_{\mu j}W_{\nu k}, \tag{2.14}$$

with ϵ^{ijk} as the total asymmetric tensor, and $B_{\mu\nu}$= $\partial_\mu B_\nu - \partial_\nu B_\mu$. As the $SU(2)_L$ group is non-Abelian, the Lagrangian contains self-interaction terms among the three W^i_μ gauge bosons. These gauge fields can then be rewritten as a linear combination of the electroweak interaction eigenstates

$$W_\mu^\pm = W^\pm = \frac{1}{\sqrt{2}}(W_\mu^1 \mp iW_\mu^2), \tag{2.15}$$

$$Z_\mu = -\sin\theta_W B_\mu + \cos\theta_W W_\mu^3, \tag{2.16}$$

$$A_\mu = \cos\theta_W B_\mu + \sin\theta_W W_\mu^3 \tag{2.17}$$

where $W_\mu^\pm$, Z_μ , and A_μ represent the physical gauge bosons. θ_W is the weak mixing angle, which defines the rotation in the neutral sector. $SU(2)_L$ and $U(1)_Y$ cannot be considered separately, since the two components of the doublets have distinct electric charges, which also means that $U(1)_Y$ is distinct from the electromagnetic interaction $U(1)_{EM}$. This translates into the Gell-Mann-Nishijima relation:

$$Q = T_3 + \frac{Y}{2} \tag{2.18}$$

where T_3 is the z-projection of the weak isospin, Y is the weak hypercharge, and Q is the electric charge operator. The elementary charge e is then linked via the weak mixing angle and the coupling constants of the weak isospin and hypercharge by

$$e = g\sin\theta_W = g'\cos\theta_W \tag{2.19}$$

Experimentally, the weak mixing angle is measured to $\sin^2\theta_W(Q^2 = m_Z^2) = 0.23122 \pm 0.00015$ [9].
The problem is, however, that the field equations require the gauge bosons to be massless particles. This can be seen from Eq. 2.11, where adding a mass term $\frac{1}{2}m^2 A_\mu A^\mu$ for the gauge boson would break the gauge invariance, as

$$\frac{1}{2}m^2 A_\mu A^\mu \to \frac{1}{2}m^2(A_\mu - \frac{1}{e}\delta_\mu\alpha)(A^\mu - \frac{1}{e}\delta^\mu\alpha) \neq \frac{1}{2}m^2 A_\mu A^\mu. \tag{2.20}$$

Thus, terms like $m_W^2 W_\mu W^\mu$ and $\frac{1}{2}m_Z^2 Z_\mu Z^\mu$ cannot be added explicitely to the Lagrangian, as they would violate the $SU(2)_L \times U(1)_Y$ gauge invariance. The conflict between this fact and the experimental evidence that the Z and W are heavy particles requires further theoretical insight. The gauge boson masses must thus be generated in a gauge invariant way.

2.1.2 Chirality and the Elektroweak Theory

In addition, also mass terms to fermions have to be added in a gauge invariant way. To make the problem clear, we can rewrite the Dirac Lagrangian 2.3 in a different way by choosing a particular representation of the Dirac matrices

$$\gamma^\mu = \begin{pmatrix} 0 & \sigma^\mu \\ \bar{\sigma}^\mu & 0 \end{pmatrix}. \tag{2.21}$$

The elements of the matrix are 2 x 2 matrices with $\sigma^\mu = (1, \overrightarrow{\sigma})$, $\bar{\sigma}^\mu = (1, -\overrightarrow{\sigma})$, and $\overrightarrow{\sigma}$ are the Pauli matrices. The Dirac spinor Ψ (e.g. an electron) can now be written as

$$\Psi = \begin{pmatrix} \Psi_L \\ \Psi_R \end{pmatrix} \tag{2.22}$$

Ψ_L and Ψ_R are called left-handed and right-handed Weyl spinors. The left-and right-handed components can be derived from the Dirac spinor using the projection operators

$$P_{L,R} \equiv \frac{1}{2}(1 \mp \gamma_5) \tag{2.23}$$

with the representation

$$\gamma^5 = \begin{pmatrix} -1 & 0 \\ 0 & 1 \end{pmatrix}, \tag{2.24}$$

The left-or right-handedness of spinors is called their chirality. Antifermions can be represented by adjoint spinors

$$\bar{\Psi} \equiv \Psi^\dagger \gamma^0 = (\bar{\Psi}_R, \bar{\Psi}_L) \tag{2.25}$$

where the γ^0 factor has interchanged the left- and right-handed components $\Psi_{L,R}$. The Lagrangian 2.3, can now be written as

$$L = \Psi_L^\dagger i\bar{\sigma^\mu}\partial_\mu \Psi_L + \Psi_R^\dagger i\sigma^\mu \partial_\mu \Psi_R - m(\Psi_L^\dagger \Psi_R + \Psi_R^\dagger \Psi_L) \tag{2.26}$$

In the first part, where the derivative is involved, the left- and right-handed spinors are seperate, whereas the mass term in the second part of the Lagrangian mixes them. Fields of distinct chirality can be handled separately as long as the fermion is massless. Any mass term will nevertheless mix the two components, since the mass term obtained above is proportional to $(\bar{\Psi_L}\Psi_R + \bar{\Psi_R}\Psi_L)$. This means that adding explicit mass terms for the fermions violates global gauge invariance.

In order to allow massive particles for the fermions and W and Z bosons, one has to dynamically break the $SU(2)_L \times U(1)_Y$ symmetry in such a way that the photon remains massless. The exact mechanism by which the masses of the vector bosons and fermions of the SM are generated remains unverified. However, it is widely believed that the Higgs mechanism is the key to explaining this mass generation. The Higgs mechanism is the application of spontaneous symmetry breaking to a local gauge group [2, 13]. It also predicts the existence of a massive scalar particle known as the Higgs boson. The best experimental verification of the existence of the Higgs mechanism would be the discovery of the Higgs boson.

2.2 Electroweak Symmetry Breaking

To get massive particles, the electroweak symmetry must be broken in such a way that all symmetry predictions are still preserved. In addition, the $W^{\pm}$ and Z bosons must acquire large masses while the photon must remain massless. This can be achieved through a mechanism called spontaneous symmetry breaking. In spontaneously broken theories, the Lagrangian describing the dynamics of the theory is still invariant under the gauge transformations, but the ground state (vacuum) no longer possesses the gauge symmetry. In the SM, one needs an external field to break the electroweak gauge symmetry in this way. This field is called the Higgs field. In order to generate masses for the three gauge bosons $W^{\pm}$ and Z, without generating a photon mass, at least three degrees of freedom are needed. The simplest realization of the Higgs mechanism is then to add a complex SU(2) doublet of scalar fields ϕ:

$$\Phi = \begin{pmatrix} \phi^+ \\ \phi^0 \end{pmatrix} = \begin{pmatrix} \phi_1 + i\phi_2 \\ \phi_3 + i\phi_4 \end{pmatrix} \tag{2.27}$$

Thus, the Standard Model Higgs field consists of two charged and two neutral component fields, ϕ^+ and ϕ^0. It has no colour charge and will therefore not affect the $SU(3)_C$ sector. The Lagrangian L and scalar potential V of the Higgs field is given by

$$\mathcal{L} = (D_\mu \Phi)^\dagger (D^\mu \Phi) - V(\Phi) = (D_\mu \Phi)^\dagger (D^\mu \Phi) - \mu^2 \Phi^\dagger \Phi - \lambda (\Phi^\dagger \Phi)^2 \tag{2.28}$$

where D_μ denotes the covariant derivative, μ is a mass parameter and λ is the strength of the Higgs self-interaction ($\lambda > 0$). For $\mu^2 > 0$ the scalar potential V has a global minimum at $\Phi = 0$, which would not break electroweak gauge symmetry. In the case $\mu^2 < 0$, the potential has a circle of non-zero degenerate minima at

$$|\,\Phi_0\,|^2 = -\frac{\mu^2}{\lambda} \equiv \frac{v^2}{2} \qquad\qquad \Phi_0 \equiv < \Phi > \frac{1}{\sqrt{2}} v e^{i\zeta}. \tag{2.29}$$

In Figure 2.1, a 2-d slice of the potential V(Φ) for both solutions to the spontaneous symmetry breaking condition is shown. Thus, the degenerate ground state acquires a non-zero field strength, and by choosing one state, the electroweak symmetry is broken spontaneously.
Φ can be expanded around its vacuum expectation value (VEV) v

$$\Phi(x) = \frac{1}{\sqrt{2}} (\rho(x) + v) e^{i(g + \frac{\xi(x)}{v})} \tag{2.30}$$

with $\rho(x)$ and $\xi(x)$ being real fields. In this expansion, the introduction of $\rho(x)$ takes into account oscillations around the Mexican Hat minimum at $x = \frac{v}{\sqrt{2}}$ while $\xi(x)$ parametrises motion around the minimum (in a flat circle). The Lagrangian is then given by

$$L = \frac{1}{2} \delta_\mu \rho \delta^\mu \rho + \frac{1}{2} \frac{(\rho + v)^2}{v^2} \delta_\mu \xi \delta^m u \xi + \mu^2 \rho^2 - \Lambda v \rho^3 - \frac{\Lambda}{4} \rho^4 - \frac{\mu^2 v^2}{4} \tag{2.31}$$

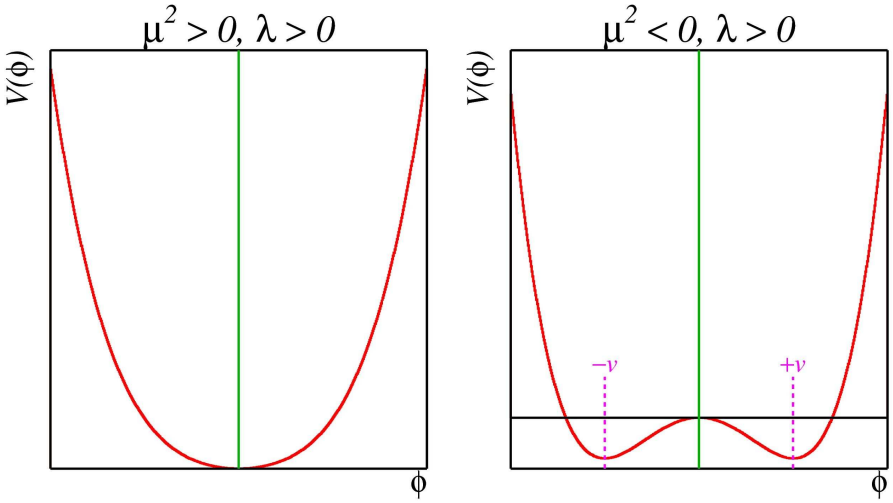

Figure 2.1: Higgs scalar potential V(Φ) with global minimum at $\Phi = 0$ (left), and degenerated non-zero minima for $\mu^2 < 0$ (right).

which is the Lagrangian for two real scalar fields, one of which ($\rho(x)$) has a positive mass while the other ($\xi(x)$) is massless. This Lagrangian does not explicitely exhibit the original invariance under phase rotations (due to the expansion of Φ around its VEV), yet, by its very construction, the Lagrangian still possesses the underlying internal symmetry of the gauge group. Because of this, the symmetry has been spontaneously broken, resulting in the appearance of a massless field (Nambu Goldstone boson), which is free to move along the minima of the Mexican Hat potential.

This is explained by the Goldstone's theorem [12], which states that whenever a continuous symmetry is spontaneously broken, new massless scalar particles appear in the spectrum of possible excitation. There is one scalar particle - called a Goldstone boson - for each generator of the symmetry that is broken, i.e., that does not preserve the ground state. Now in our case, the problem is that we need to create massive gauge bosons, while massless scalar particles are predicted. There is no potential energy cost to move around the bottom of the circular valley, so the energy of such a particle is pure kinetic energy, which in quantum field theory implies that its mass is zero. However, no massless scalar particles were detected. It was Higgs' insight that when a gauge theory is combined with a spontaneous symmetry-breaking model, the two problems solved themselves rather elegantly. Higgs had found a loophole in the Goldstone theorem: when the scalars are coupled to the gauge theory, the Goldstone bosons are "eaten" by the gauge bosons. The latter become massive and their new, longitudinal polarization is provided by the Goldstone boson.

2.2.1 The Higgs Mechanism

We again consider the complex scalar field Φ, but this time we require it to be invariant under local gauge transformation. The Lagrangian 2.28 now becomes

$$L = -\frac{1}{4}F_{\mu\nu}F^{\mu\nu} + (D_\mu\Phi)^\dagger D^\mu\Phi - \mu^2|\Phi|^2 - \Lambda|\Phi|^4 \tag{2.32}$$

where $F_{\mu\nu}$ is the field strength and the covariant derivative D_μ is given by

$$D_\mu\Phi_i(x) = (\delta_\mu + igQ_iA_\mu(x))\Phi_i(x) \tag{2.33}$$

As before, we can expand Φ around its VEV in order to recover the physical scalar fields, but the expansion is a little more complicated due to the local nature of the required gauge invariance. In this case, the second term of the Lagrangian presented in 2.32 becomes

$$\begin{aligned}(D_\mu\Phi)^\dagger D^\mu\Phi = \frac{1}{2}\delta_\mu\rho\delta^\mu\rho + \frac{1}{2}\frac{(\rho+v)^2}{v^2}(\delta_\mu\xi)^\dagger\delta^m u\xi \\ -g\frac{(\rho+v)^2}{v}A^\mu\delta_\mu\xi + \frac{1}{2}g^2(\rho+v)^2A^\mu A_\mu\end{aligned} \tag{2.34}$$

Again the field redefinition generates mass, but this time for a vector gauge field. An additional term is also generated which does not correspond to a standard interaction. However, this can be remedied by means of a redefinition of the gauge field, allowing the introduction of a massive field $B_\mu(x)$ defined by

$$B_\mu(x) = A_\mu(x) + \frac{1}{gv}\delta_\mu\xi(x) \tag{2.35}$$

which restores the Lagrangian to the form:

$$\begin{aligned}L = -\frac{1}{4}B_{\mu\nu}B^{\mu\nu} + \frac{1}{2}m_B^2B^\mu B_\mu + \frac{\lambda^2}{2}(\rho^2+2\rho v)B^\mu B_\mu \\ +\frac{1}{2}\delta_\mu\rho\delta^m u\rho - \frac{1}{2}m_\rho^2\rho^2 - \frac{\Lambda}{4}\rho^4 - \Lambda v\rho^3\end{aligned} \tag{2.36}$$

One of the physical fields introduced in the symmetry breaking process ($\xi(x)$) has disappeared. Once all trace of the Nambu Goldstonde boson field $\xi(x)$ has been removed, instead of a massless gauge field the theory contains a massive vector gauge field $B_\mu(x)$ of mass $m_B = gv$, as well as a massive scalar, $\rho(x)$ of mass $m_\rho = \sqrt{-2\mu^2}$. What happened is that the spontaneous symmetry breaking has caused the original massless gauge field to absorb the Nambu Goldstone boson $\xi(x)$. The massless vector boson has "eaten" the scalar field $\xi(x)$, and in doing so has become the massive vector gauge field. The same mechanism allows the calculation of the W and Z vector boson masses, given by the following formulae:

$$m_W^2 = \frac{g^2 v^2}{4}, m_Z^2 = (g^2 + g'^2)\frac{v^2}{4} = \frac{m_W^2}{cos^2\theta_W} \tag{2.37}$$

where g and g' are coupling constants and θ_W the Weinberg angle. Thus after the electroweak gauge symmetry is spontaneously broken, the Goldstone bosons do not appear as physical particles, but give mass to the gauge vector bosons $W^{\pm}$ and Z. If the W and Z bosons were massless they would be just like the photon and have 2 polarization states (both transverse to the propagation direction). The W and Z thus acquire longitudinal polarization (third degree of freedom) by absorbing 3 Goldstone Higgs bosons. Since the $U(1)_Q$ symmetry is still unbroken, its generator, the photon, remains massless as it should be.

The values of v, of g and g' can be derived from measured quantities such as the Fermi weak coupling constant G_F, $sin^2\Theta_W$ (with Θ_W the Weinberg angle), and the electric charge e. The vacuum expectation value v is estimated to be ~ 246 GeV.
The obtained value for the ratio of the W to the Z mass, m_W/m_Z, is very close (within the one-loop uncertainty) to the measured ratio m_W/m_Z[5]. The Higgs mechanism therefore provides a remarkably simple and successful solution to the electroweak symmetry breaking problem.
Like the gauge boson masses within the SM, also the fermion obtain masses from the interaction with the Higgs field. However, they have to be introduced arbitrarily using so-called Yukawa coupling constants, which are free parameters of the theory. They do not result from the introduction of the covariant derivative, as in the case of the boson masses. The masses obtained for e.g. electron, up-and down-quark are

$$m_e = \frac{\lambda_e\, v}{\sqrt{2}} \;\;,\;\; m_u = \frac{\lambda_u\, v}{\sqrt{2}} \;\;,\;\; m_d = \frac{\lambda_d\, v}{\sqrt{2}}. \tag{2.38}$$

The mass of the Higgs boson, obtained after spontaneous symmetry breaking, is given by

$$m_H = \sqrt{2\lambda v} \tag{2.39}$$

where λ is still a free parameter. The Higgs mass can therefore not be predicted by theory. The Higgs mechanism was proposed in 1964 by Higgs, Brout, Englert, Guralnik, Hagen and Kibble [2].
With this generating mechanism, the SM predicts the existence of a Higgs boson (the physical manifestation of the Higgs mechanism) but does not predict its mass, because very little of the SM we have observed depends directly on this mass. However, by imposing certain requirements of internal consistency on the theory, the range of possibilities may be narrowed.

[5]The connection to the Weinberg mixing angle θ_W is given by $\sin^2\theta_W = 1 - m_W^2/m_Z^2$.

2.3 Constraints on the Higgs Boson Mass

Even though the Higgs mass can not be predicted, upper and lower bounds can be set. One of them is the constraint that in a theory without a Higgs boson, the amplitude of the process $W_L W_L \rightarrow W_L W_L$ would be proportional to the center-of-mass energy s, and thus violate unitarity at high energy, which is at $\sqrt{s} \approx 1.2$ TeV. To avoid this violation, an upper limit on the Higgs mass is imposed [13]:

$$m_H < (\frac{4\pi\sqrt{2}}{3G_F})^{\frac{1}{2}} \approx 700\text{GeV} \tag{2.40}$$

Quite restrictive bounds on the Higgs mass depend on the energy scale Λ up to which the SM is valid, i.e. the scale up to which no new interactions and no new particles should appear. Such bounds are derived from the evolution of the quartic Higgs self-coupling λ at the energy E. The one-loop RGE for the quartic coupling, including the fermion and gauge boson contributions, becomes [14]:

$$\frac{d\lambda}{dt} = \frac{1}{16\pi^2}(12\lambda^2 + 12\lambda g_t^2 - 12g_t^4 - \frac{3}{2}\lambda(3g^2 + g'^2) + \frac{3}{16}\lambda(2g^4 + (g^2 + g'^2)^2)) \tag{2.41}$$

with t= $\log(E^2/v^2), g_t$ the energy dependent top-Higgs Yukawa coupling, g and $g^{'}$ the electroweak gauge couplings.

2.3.1 The Trivitality bound

For moderate top masses, the first term in 2.41 coming from Higgs loops dominates

$$\frac{d\lambda}{dt} \approx \frac{3}{4\pi^2}\lambda^2, \tag{2.42}$$

leading to

$$\lambda(E^2) = \frac{\lambda(v^2)}{1 - \frac{3\lambda(v^2)}{4\pi^2} log\frac{E^2}{v^2}} \tag{2.43}$$

Thus, $\lambda(E)$ varies logarithmically with the squared energy E^2. If the energy is much smaller than v, $E^2 \ll v^2$, λ becomes extremely small and eventually vanishes. The theory becomes trivial, i.e. non interacting, since the coupling is zero [15]. On the other hand, λ grows to infinity as the energy E increases. One can establish the energy domain in which the SM is valid, i.e. the energy cut-off Λ_C below which the self-coupling λ remains finite,

$$\frac{1}{\lambda(\Lambda_C)} > 0, \text{i.e. } 0 < \lambda(\Lambda_\text{C}) < \infty \tag{2.44}$$

which, when inserting $m_H = \sqrt{2\lambda}v$, leads to an upper bound on the Higgs mass,

$$m_H^2 < \frac{8\pi^2 v^2}{3log(\Lambda_C^2/v^2)} \tag{2.45}$$

If Λ_C is large, the Higgs mass should be small. On the other hand, if the cut-off Λ_C is small, the Higgs boson mass can be rather large.
For example, assuming that the electroweak theory is valid up to the Planck scale $m_{Pl} = 10^{19}$ GeV[6], this bounds the Higgs mass to be smaller than 180 GeV. Lowering the scale of new physics Λ_C, the coupling constant enters a non-perturbative region and the above equations are no longer sufficient.

2.3.2 Vacuum Stability

A lower bound on the Higgs mass is obtained by requiring that λ remains positive at all scales Λ_C. Otherwise the potential $V(\Phi)$ has no lower bound and the vacuum becomes unstable [16–18]. For small λ we have the effect of the top loops

$$\frac{d\lambda}{dt} \approx \frac{1}{16\pi^2}(-12g_t^4 + \frac{3}{16}\lambda(2g^4 + (g^2 + g'^2)^2)) \tag{2.46}$$

which drives λ to negative values for large g_t. By requiring $\lambda(\Lambda_C) > 0$ we obtain

$$m_H^2 > \frac{v^2}{8\pi^2}(-12g_t^4 + \frac{3}{16}\lambda(2g^4 + (g^2 + g'^2)^2))log\frac{\Lambda^2}{v^2}. \tag{2.47}$$

This puts a strong constraint on the Higgs boson mass from below, which depends on the value of the cut-off Λ_C. For example, if $\Lambda_C \sim 10^4$ GeV, $m_H \geq 70$ GeV, if $\Lambda_C \sim 10^{16}$ GeV, $m_H \geq 130$ GeV[7]. The theoretical Higgs mass constraints are summarized in Figure 2.2. From the above discussion, the SM with one Higgs doublet might describe the whole particle physics up to the GUT scale, provided $130 < m_H < 180$ GeV [19]. The observation of a Higgs mass above or below these values would indicate new physics at a scale Λ_C.
The direct searches for the Higgs boson at the LEP2 collider in the Higgs-strahlung process $e^+e^- \rightarrow HZ$ and the vector-boson fusion processes $e^+e^- \rightarrow H\nu\bar{\nu}$ and He^+e^- resulted in a lower limit of 114.4 FeV at 95%CL [3].
The precision electroweak data from LEP, SLC and Tevatron strongly support the SM with a weakly coupling Higgs boson and lead to an upper bound for the Higgs mass of 186 GeV (at 95 % CL) [3, 6].

[6]The so-called Planck mass is a fundamental scale in nature, at which quantum gravitational effects become important. It is defined as $m_{Pl} = \sqrt{\frac{hc}{G}} \approx 10^{19} GeV$, with c the speed of light, h the Planck constant and G the Newtons constant.

[7]The lower mass limit on the Higgs boson can be loosened somewhat if the vacuum is meta-stable, and if the chosen top mass is different to 175 GeV.

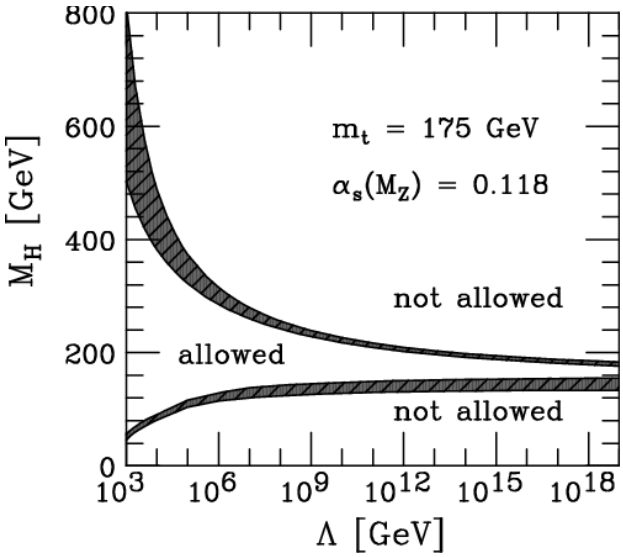

Figure 2.2: The upper and the lower Higgs mass bounds as a function of the energy scale Λ_C, at which the SM breaks down, assuming $m_t = 175$ GeV and $\alpha_s(m_Z) = 0.118$. The shaded areas reflect the theoretical uncertaintes in the calculations of the Higgs mass bounds [20].

2.4 Shortcomings of the SM

The predictions of the SM have been tested and verified to unprecedented precision by experiments at LEP, SLAC, Tevatron and many other experiments. However, apart from the missing Higgs particle, there are several open questions in the SM, such as:

- **Neutrino oscillations:** Neutrinos had been thought to be the only fermions which do not have mass. In light of the discovery of neutrino-oscillations, that long-standing belief has to be revised. It is interesting to note here that the right-handed neutrino interacts only via a symmetry breaking sector, such as the Higgs field.

- **Dark matter candidate:** What is the invisible dark matter that accounts for the missing mass of the universe according to gravitational astronomy? Since neutrinos are not massive enough to explain the observations, a new candidate (or a new force?) for this cold dark matter is needed [21–23].

- **Three families:** Why are there three families of quarks and leptons?

- **Gravitation:** Is there a way to include the gravitational force in the model?

- **The hierarchy problem:** From measurements of the properties of the weak interactions it is known that the squared Higgs mass is of the order $m_H^2 \sim (100\ \text{GeV})^2$. Now, m_H^2 is affected by enormous corrections from the virtual effects of every particle which couples, directly or indirectly, to the Higgs field. For example, the correction to m_H^2

from a loop containing a Dirac fermion f with mass m_f is given by

$$\delta m_H^2 = \frac{|\lambda_f|^2}{16\pi^2}(-2\Lambda_{UV}^2 + 6m_f^2 ln(\Lambda_{UV}/m_f) + ...) \tag{2.48}$$

where Λ_{UV} is an ultraviolet momentum cut-off used to regulate the loop integral [8]. The largest corrections come from the top quark with $\lambda \approx 1$. If Λ_{UV} is of the order of m_{Pl}, this quantum correction to m_H^2 is 30 orders of magnitude larger than the aimed-for value of $m_H^2 \sim (100\ \text{GeV})^2$. If no new physic enters between the electroweak and the Planck scale, then $\Lambda \approx m_{Pl}$ and the quantum correction becomes very large with negative sign. Thus, in order to get a Higgs mass of the order of 100 GeV, the bare Higgs mass would also need to be of the order of the Planck scale. If the loop corrections would be bigger than the bare Higgs mass, electroweak symmetry would not be broken, because this would lead to a scalar potential with $\mu > 0$, opposite to the needed term $\mu < 0$ in order to get a global non-zero minimum for the Higgs potential. If the SM is valid up to such a large scale, there should be very exact cancellations that remove the divergences in the Higgs mass which are caused by radiative corrections. This is the so called naturalness or hierarchy problem: fine-tuning is needed up to the highest mass scales to keep the Higgs boson mass small.

- **Unification of gauge couplings:** The SM combines the colour forces and the unified electroweak force which is often notated by $SU(3)_C \times SU(2)_L \times U(1)_Y$. The $SU(3)_C$ of QCD, however, is not included in a unified form. The success of the electroweak symmetry as a common description of the electromagnetic and the weak interactions lead to the hope that also the electroweak and strong interactions can be understood as the result of a single simple symmetry group. This implies that their coupling strengths should unify at some energy scale. In the SM, however, no unification at a single point is possible.

These incomplete aspects of the model imply that the SM is only an effective theory. That is, the SM is a low energy approximation to an underlying theory. In the last years, a lot of effort has gone in the development of new theories, extending the SM and finding answers to such questions. Experimental evidence for such a new theory has so far not be found- the LHC and future colliders will be able to tell us more.
The impressive success of the SM sets strong limits on models for new physics: in general, models that preserve the SM structure and introduce soft improvements are clearly preferred. A possibility to extend the Standard Model might be achieved through Grand Unified Theories (GUTs), which unify the different interaction couplings at high energies by embedding the Standard Model gauge group $SU(3) \times SU(2) \times U(1)$ into a higher group, like $SO(10)$. However, such groups have to fulfill rather strict requirements, as they have to fit into todays measurements, $SU(5)$, for example, is already excluded due to its proton decay limit.

The most popular theory extending the SM is SUSY, introducing a symmetry between bosons and fermions [24–27]. Each particle should have a SUSY partner, a sparticle, with a spin differing by 1/2. The two-Higgs-doublet model (2HDM) is the most straightforward extension

[8] It should be interpreted as the energy scale at which new physics enters to alter the high-energy behavior of the theory.

of the EWSB mechanism of the SM. The theory proposes a pair of scalar SU(2) doublets, both with hypercharge Y=1. Depending on the version of the 2HDM, these scalars may couple in various ways to the quarks and leptons. After the electroweak symmetry is broken, the spectrum of the Higgs sector consists of five physical Higgs bosons: two neutral CP-even scalars (h^0 and H^0), a neutral CP-odd scalar (A^0) and a pair of charged scalars ($H^{\pm}$). These particles could be detected via direct production at colliders, but their effects may also be visible indirectly, through their contributions as intermediate states in decay processes. SUSY can solve some of the problems addressed above, e.g. it provides an elegant mechanism for the hierarchy problem and a dark matter candidate. On the other hand, as none of the superpartners have been found yet, SUSY must be a broken theory and more then 100 new parameters arise from SUSY breaking. The number of free parameters can be reduced depending on the model, but one might debate that including so many new parameters might be a bit artificial.

This thesis will be mainly concerned about the search for the Higgs boson. However, there are also other mechanism for the EWSB, which should be mentioned here. In extra dimensional scenarios, the electroweak symmetry can be broken by fundamental Higgs, by boundary conditions or by some dynamical mechanism. Generically all three possibilities could be present altogether. In the SM the conventional Higgs doublet plays several roles, in particular, ensuring perturbative unitarity in e.g. $W_L^+W_L^-$ scattering and generating fermion as well as the W/Z masses with $\rho = 1$[9]. As the nature of electroweak symmetry breaking is not clear, there are also many other attempts to describe EWSB, e.g. with Higgsless models [28]. Signatures of Higgsless models are light Kaluza Klein states, which might be found at LHC. In order to identify such a resonance found at LHC as a Kaluza Klein state arising from Higgsless models, a linear collider will be neccessary.
As mentioned before, all of theses extensions of the SM are so far theories without experimental evidence, as none of the proposed new particles have been found yet. The next years will show which theory is best suited to describe experimental signatures or, in the other case, if totally new theories have to be build to explain signatures observed (or not observed) at future colliders.
The goal of this thesis is to show how a SM Higgs particle can be found in the region between 150 and 180 GeV.

[9]The relation between the gauge boson masses and the weak mixing angle is conveniently parametrized by Veltman's rho parameter, i.e. $\rho = m_W^2/m_Z^2 c_W^2$, which is equal to one at tree level ($\rho_0 = 1$). The presence of at least a triplet of Higgs fields gives rise to $\rho_0 \neq 1$.

Chapter 3

LHC and CMS

3.1 Collider Physics

The development of accelerators and storage rings has allowed to collide particles at higher and higher energies. In accordance with Einsteins famous equation, $E = mc^2$, several hundreds of short-lived particles could be found at the various accelerators, in addition to the few stable particles (like protons and electrons) of which the universe is built. The particles that can be accelerated are usually electrons, positrons, protons, antiprotons, and ions. There are different motivations why to choose to collide protons or leptons in an experiment. As leptons are point-like, the energy of the interacting particles is known. The event kinematics is thus completely constrained. Leptons are therefore chosen, if i.e. the mass of the particle to discover is already predicted rather precisely by theory. In a hadron beam the hadron energy is shared between its constituent partons, the quarks and gluons; these are the interacting particles at high energies, and the energy of the two colliding partons is therefore not fixed. The event kinematics is thus only partially known and only part of the beam energy is used. In order to discover a particle which mass is not known, it is more convenient to use protons, as automaticlly a larger mass range is addressed. On the other hand, leptons have the advantage that the signatures are produced in a clean environment, while in a proton collider there are a lot of minimum bias events.

When speaking about accelerators, one has to distinguish between colliding-beam experiments and fixed target experiments. In a colliding-beam experiment two beams of high-energetic particles cross. For colliding particles with energy E, the available energy to create new particles is thus $E_{cm} = 2 \times E$[1]. On the other hand, the energy to create new particles of a high-energetic particle with energy E colliding with a fixed target particle of mass m is given by $E_{cm} = \sqrt{2 \times E \times mc^2}$. Thus, to obtain a center-of-mass energy E_{cm} of 100 GeV, two particles with an energy of 50 GeV each are required in a collider experiment ($E_{cm} = 2 \times 50$ GeV), while in a fixed target experiment a particle with 5000 GeV is required (assuming mc^2 of the fixed target to be 1 GeV) to get the same center-of-mass energy, according to $E_{cm} = \sqrt{2 \times 5000\text{GeV} \times 1\text{GeV}}$.

[1] E_{cm} being the energy in the center-of-mass frame.

A disadvantage of colliding beams is, however, that the luminosity is much lower than with a fixed target, as the target is much smaller.
Besides the type of the particle collisions, one can also distinguish between linear and circular accelerators. In a linear accelerator (so-called Linac's), particles are accelerated in a straight line. In a circular accelerator, particles move in a circle until they reach the desired energy. The advantage of circular accelerators over linear accelerators is that the ring topology allows continous acceleration, as the same particles pass through the same accelerating elements many times. Dipole magnets keep particles in a circular orbit while quadrupole magnets focus the beam. However, circular accelerators have the disadvantage that the particles emit synchrotron radiation. Synchrotron radiation occurs when any charged particle is accelerated; it emits electromagnetic radiation and secondary emissions. As a particle travelling in a circle is always accelerating towards the center of the circle, it continuously radiates towards the tangent of the circle. The energy loss due to synchrotron radiation for highly relativistic particles is described as:

$$\Delta E = \frac{4\pi\alpha}{2R}\beta^3\gamma^4, \text{with } \gamma = \frac{\mathrm{E}}{\mathrm{mc}^2} \text{ and } \beta = \frac{\mathrm{v}}{\mathrm{c}} \approx 1 \tag{3.1}$$

with R the radius of the accelerator, E the energy of the particle and m its mass. To reduce the energy loss due to synchrotron radiation, there are two possibilities: either to increase the radius of the collider or to increase the mass of the accelerated particles. Cyclic leptonic machines suffer such large synchrotron losses that they cannot be realistically constructed much larger than the LEP[2] - at a LEP center-of-mass-energy of about 200 GeV, all the energy that was added to the beam in the radio frequency cavities was radiated off again by synchrotron radiation.

It is not easy to accelerate particles in a Linac to high luminosities over realistic distances. The TESLA Test Facility [3] [29] demonstrated good performances, and one expects to have a linear collider in the future using this technology. However, this will not occur in the next years.

The other possibility to avoid synchrotron radiation is to collide heavy particles, and thus to build proton colliders. Since protons are about 2000 times heavier than electrons, the energy loss is $(2000)^4 \approx 10^{13}$ times smaller than for electrons in the same tunnel. Thus by using proton colliders, synchrotron radiation can be eliminated as a limiting factor for (not too high energy) colliders.

Another idea to get to high energies is to collide muons with antimuons in a large circular collider. Muons have a mass about 200 times larger than the electron but their lifetime in a rest frame is only 2.2 μs. When accelerated, this laboratory lifetime increases. It is, however, unrealistic at present to produce, accelerate and collide muons at high energy and high luminosity. Developments are ongoing [30], but will very likely not lead to actual machines

[2]The Large Electron Positron (LEP) Collider at CERN operated from 1989 until Nov. 2000 at a center-of-mass-energy between 90 and 209 GeV.

[3]The TeV Energy Superconducting Linear Accelerator (TESLA) is a linear collider for collision energies between 500 GeV and 800 GeV.

before decades.

While proton colliders can reach very high energies, the design introduces some extra challenges. Colliders that use antiparticles must find ways of producing them in large numbers and then storing them while the beam is brought up to full energy. Unless the beams are very tightly focused there will only be a few collisions per revolution so the antimatter may have to be stored for hours. In addition, to bend high-energetic protons in the ring, very strong beam magnets are needed. LHC will therefore use superconducting magnets [31].

3.2 The Large Hadron Collider

The Large Hadron Collider (LHC) was approved by the CERN council in December 1994. It is scheduled to start operation in May 2008. The LHC is a circular proton collider. The nominal energy of 14 TeV in the center-of-mass frame should be reached end of 2008. The LHC is built in the former LEP tunnel, and has a circumference of 26,7 km. Four experiments will be

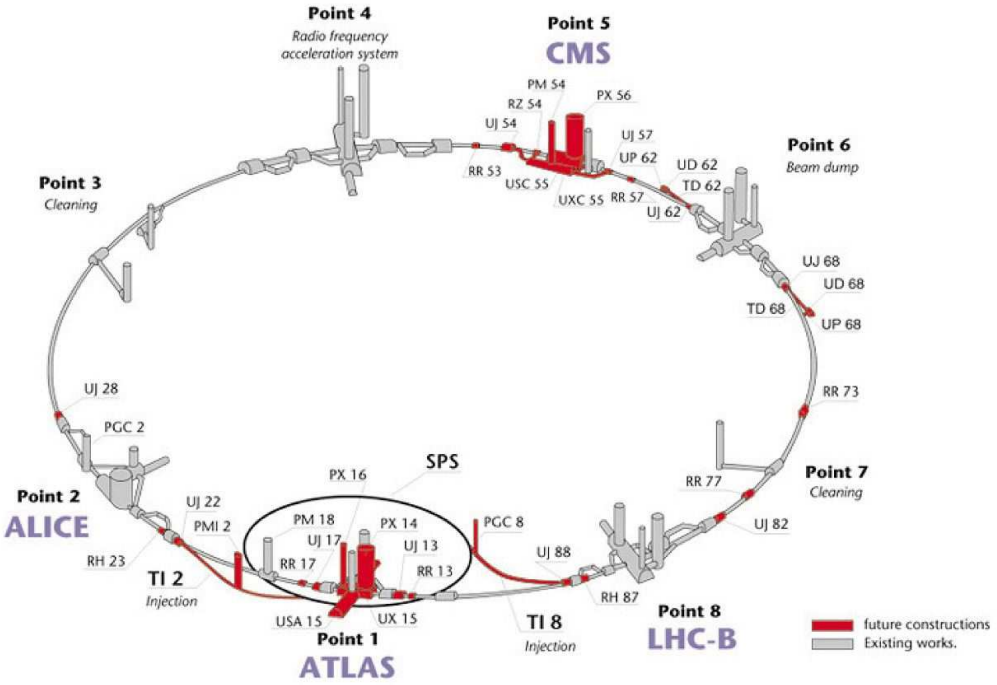

Figure 3.1: The Large Hadron Collider at CERN.

located in the LHC tunnel: ATLAS (A Toroidal LHC ApparatuS) [32], CMS(Compact Muon Solenoid) [33], LHCb [34], and ALICE (A Large Ion Collider Experiment) [35] (Figure 3.1). ATLAS and CMS are general multipurpose detectors. The three main topics of the physics program of CMS and ATLAS are to investigate electroweak symmetry breaking through the detection of one or more Higgs bosons (or, in case they do not exist, to study alternative

electroweak symmetry breaking mechanisms); to search for phenomena beyond the Standard Model, such as supersymmetric particles; and to study the high-Q^2 region in more detail. LHCb is dedicated to B-physics and CP-violation studies, while ALICE investigates heavy ion physics. The aim of such high energy heavy ion collisions is to study the properties of a quark-gluon plasma. The protons are initially accelerated by a Linac, transferred to the

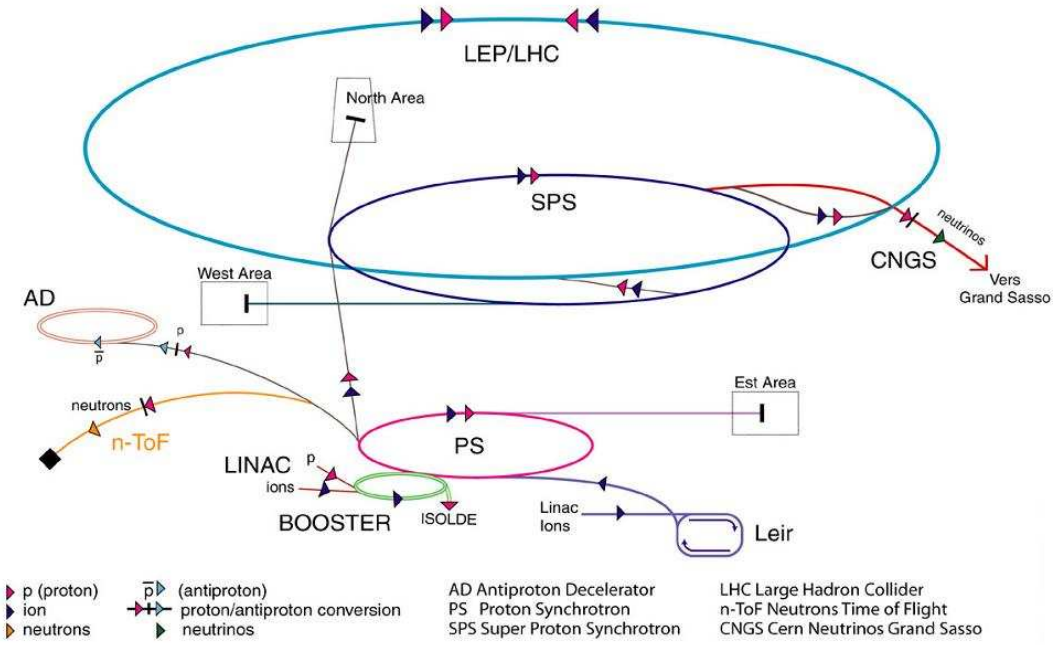

Figure 3.2: The LHC accelerator chain.

Booster and then injected into the Proton Synchrotron (PS). After these three accelerator steps, the protons gained an energy of 26 GeV. Then, they are fed into the SPS, which delivers them further to the LHC at an energy of 450 GeV, in bunches of $1.1\text{x}10^{11}$ protons. 2808 bunches, separated by a distance of 7 m are then accelerated in the LHC to achieve an energy of 7 TeV each. A summary of LHC paramters is given in Table 3.1. The chain of accelerators is shown in Figure 3.2. In addition to the proton-proton collision, heavy ions will be accelerated and brought to collisions in the LHC. In $Pb-Pb$ collisions, the center-of -mass energy reaches 1140 TeV, which is almost 30 times the center-of-mass energy of today's most energetic heavy ion collider RHIC in Brookhaven [36].

If particles with same mass and electric charge are accelerated in opposite directions, it is no longer possible to convey particles in a unique vacuum tube (as was the case at LEP). The

Circumference	26 659 m
Dipole operating temperature	1.9 K (-271.3 C)
Number of dipoles	1232
Number of RF cavities	8 per beam
Nominal energy, protons	7 TeV
Energy at injection	450 GeV
Nominal energy, ions (energy per nucleon)	2.76 TeV/u
Peak magnetic dipole field (at 7 TeV)	8.33 T
Minimum distance between bunches	$\sim$ 7 m
Design luminosity	10^{34} cm$^{-2}s^{-1}$
Collision rate	45 MHz
Number of bunches per proton beam	2808
Number of protons per bunch (at start)	$1.1x10^{11}$

Table 3.1: Some of the LHC parameters [31].

LHC is therefore a two ring superconducting accelerator and collider. An approximatively 130 m long common pipe is shared by the two beams near the interaction regions. For the dipole magnets, LHC chose an elegant solution and uses twin bore magnets, which consist of two sets of coils and beam channels sharing the same mechanical structure.

The maximal energy a proton beam can obtain is determined by the maximal magnetic dipole field which can be achieved to compensate the centrifugal force of the particles, given by E[TeV] $\approx 0.84B$[Tesla]. To achieve high magnetic fields, new types of superconducting magnets had to be developed, which operate at liquid helium temperatures. By lowering the temperature down to 1.9 K, an extra 1.5 T can be gained over standard superconducting elements. This represents a 20% gain in beam energy. Such a high magnetic field induces huge mechanical constraints on the surrounding material. In order to counter these forces, non-magnetic austenitic steel collars are used to maintain the conductors in place. The dipole magnets reach a nominal field of 8.33 T, which allows to bend protons with energies up to 7 TeV. There will be 1232 dipole magnets each 14.3 meter long, placed in the LHC ring. In addition, about 400 quadrupoles will be placed along the ring to keep the particles trajectories close to each other and guide them along the beam pipe.
The luminosity $\mathcal{L}$ of an accelerator which collides bunches containing n_1 and n_2 particles at a frequency f is given by

$$\mathcal{L} = f\frac{n_1 n_2}{4\pi\sigma_x\sigma_y} \tag{3.2}$$

where σ_x and σ_y characterize the Gaussian transverse beam profiles. To achieve a high luminosity, a small transverse beam profile, high bunch collision frequency and a large number of particles per bunch are required. The total expected cross section for a center-of-mass energy of 14 TeV is 110 mb [37].
The nominal number of protons per bunch at injection is about 10^{11} for a nominal luminosity of 10^{34}cm^{-2}s^{-1}, which is the LHC design luminosity.

Because of this large number, the average number of inelastic pp collisions (minimum bias events) per bunch crossing is high, up to 25 for the design luminosity. This imposes difficult experimental conditions, since the rare interesting events that may occur in a bunch crossing are superimposed (piled-up) on top of many minimum bias events. A way to minimize the number of pile-up events while keeping the luminosity constant is to operate at a high collision frequency. The LHC bunch crossing rate will be 40 MHz, which means that a bunch crossing will occur every 25 ns. Such a high frequency, however, imposes stringent requirements on the response times of the LHC detectors.
The LHC luminosity is not constant over a physics run, but decays exponentially $\mathcal{L} = \mathcal{L}_0 e^{-i\tau_\mathcal{L}}$ due to the degeneration of the circulating beams. As the total cross section is large, the collisions themselves limit significantly the beam life-time. The decay time of the bunch intensity due to this effect is written as

$$\tau_{col} = \frac{N_{tot,0}}{\mathcal{L}\sigma_{tot}k}, \tag{3.3}$$

where $N_{tot,0}$ is the initial number of particles in the beam, $\mathcal{L}$ the luminosity, σ_{tot} the total cross section (σ_{tot} =110 mb at 14 TeV), and k the number of interaction points. For nominal LHC conditions, the resulting decay time is 44.9 h. The time required to reach $1/e$ of the luminosity is written $\tau_{col,1/e}$. In addition, other sources of luminosity loss have to be taken into account, which are intra-beam scattering (IBS)[4] and beam-gas interactions. Since all these effects induce an exponential luminosity drop, the net luminosity lifetime can be approximated as

$$\frac{1}{\tau_\mathcal{L}} = \frac{1}{\tau_{col,1/e}} + \frac{1}{\tau_{IBS}} + \frac{1}{\tau_{gas}}, \tag{3.4}$$

which gives $\tau_\mathcal{L} = 15$ h.
To get the integrated luminosity per year, an estimate of the number of luminosity fills per year is needed. From PS and SPS experience, the time before physical data can be taken, τ_{fill}, which is time to fill the LHC, to ramp magnets etc., can be estimated to be around 70 minutes. From HERA[5] it is known that this time could also be six times larger – thus in the following the upper limit of 7 hours and lower limit of 70 minutes are considered and the resulting luminosities compared. With an estimated run time of X days per year, the total luminosity per year is

$$\mathcal{L}_{tot} = \frac{X \times 24}{T_{run}[h] + T_{fill}[h]} \mathcal{L}_0 \tau_L (1 - e^{-T_{run}/\tau_\mathcal{L}}), \tag{3.5}$$

with T_{run} the total length of the luminosity run which can be used for physics, and $\mathcal{L}_0$ the initial luminosity. For a design luminosity of 10^{34} cm^{-2}s^{-1} and an estimated run time of

[4]Intra-beam scattering is the multiple Coulomb scattering between charged particles in a bunched or unbunched beam.

[5]HERA (German for "Hadron Elektron Ring Anlage") is DESY's largest synchrotron and storage ring. The DESY (German for "Deutsches Elektronen Synchrotron") is the biggest German research center for particle physics, with sites in Hamburg and Zeuthen.

X =200 days, this leads to a total luminosity between 80 fb^{-1} and 120 fb^{-1} per year (for the lower and upper limit of τ_{fill}, respectively), which meets the original objectives of the machine. If one assumes that only 40 days per year can be used for physics [38], this results in luminosities between 16 fb^{-1} and 24 fb^{-1} per year for a peak luminosity of 10^{34} cm$^{-2}s^{-1}$.

3.3 The CMS Detector

The Compact Muon Solenoid (CMS) is one of the two general purpose experiments at LHC. End of 2006, approximately 2300 people from 159 scientific institutes worked in the CMS collaboration. CMS will be located 100 m below surface at Cessy in France.
CMS has a cylindrical structure, covering almost 4π, in order to detect a large fraction of high p_{T} particles produced in a collision. It has an overall length of 21.6 m and a diameter of 15 m. The detector is divided into barrel and endcaps, and weights in total 12500 tons. It contains subsystems which are designed to measure the energy and momentum of photons, electrons, muons, and hadrons. In addition, the aim is to be as hermetic as possible, in order to measure the missing energy of an event. A trajectory of particles through the CMS detector is shown in Figure 3.3, starting from the beam pipe. The tracker allows precise momentum measurement and the impact parameter of charged particles. It is surrounded by a scintillating crystal electromagnetic calorimeter, which is surrounded by a sampling calorimeter for hadrons (Figure 3.4). Outside the solenoid lies the return yoke of the magnet, interleaved by four layers of muon chambers. The barrel covers a pseudorapidity range $|\eta| < 1.5$, while endcaps cover the range $1.5 < |\eta| < 3$ [6]. The relative error on the particle p_{T} measurement by a tracker goes like

$$\frac{\Delta p_T}{p_T^2} \sim \frac{1}{BR^2}, \tag{3.6}$$

where B is the magnetic field in a direction orthogonal to the particle momentum, and R is the tracker radius.
The magnetic field of the solenoid is about 4 T with a diameter of roughly 6m and a length of 13 m. To create such a high magnetic field a very high current (20 kA) has to be generated, circulating in superconducting strands. To allow superconductivity, the magnet will be cooled down to 4.2 ° K with liquid helium. At the nominal current of 20 kA, the coil will store 2.7 GJ in the magnetic field. Ramping to this current will take five hours, while discharge will last up to 18 hours. In case of emergency, this energy has to be evacuated quickly or both the coil and the detectors could be damaged. Therefore, a fast discharge in 50 mΩ resistors is used – the decay time is then 280 s. In August 2006, the maximum field

[6] The rapidity is defined as:

$$y \equiv \frac{1}{2} \cdot \ln \frac{E + p_z}{E - p_z}$$

where E is the particle energy and p_z the momentum in the beam direction. For p much bigger than the mass of the particle and $\theta \gg 1/\gamma^7$, the rapidity can be approximated by the so called pseudorapidity η :

$$\eta \equiv -\ln(\tan(\theta/2)),$$

where $\theta = \arccos(p_z/p)$ is the scattering angle with respect to the beam axis [9].

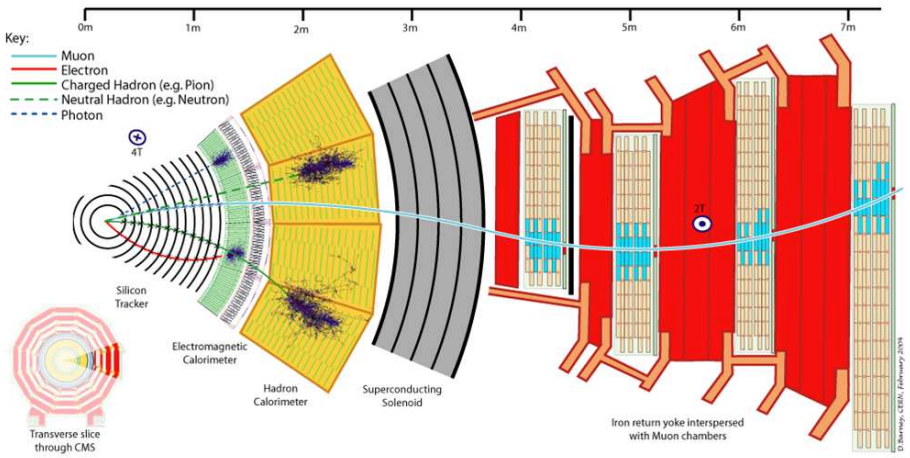

Figure 3.3: A slice of the CMS detector. The traces of particles to be detected are shown.

of 4 T could be successfully obtained in the magnet test.

The magnetic flux is returned through a saturated iron yoke, which is split into five barrel rings and two endcap discs housing the muon chambers. Muons are particles with minimal ionizing power, which make them particularly easy to separate from the other particle types. In the following paragraphs, a brief description of each subdetector is given. More details about the CMS detector can be found in [33].

3.3.1 The Tracking System

The tracker has to fulfill the condition to be radiation hard as well as to offer high granularity. The tracker will occupy a cylindrical volume with the length of about 5.4 m and a diameter of 2.4 m. The large volume of the tracker together with the 4 T magnetic field allows a significant bending of the track and therefore an accurate momentum measurement of high energetic charged particles. Placed around the interaction point, the CMS Tracker consists of silicon pixel detectors and silicon micro-strip detectors. Three pixel layers and ten silicon strip layers will be installed in the barrel, and two pixel layers, three inner and nine outer forward discs of silicon detectors will be placed in each endcap.
Closest to the beam pipe are the three barrel layers of the pixel detectors. Perpendicular to them, two pixel discs will be positioned at each side (see Figure 3.5). A compromise between cost and accuracy lead to a square pixel shape of 150 x 150 μm^2. About 16000 readout chips are bump-bonded to the detector modules, adding up to about 44 million readout channels. The pixel detectors will allow a precise vertex reconstruction and provide the first step in the track reconstruction. The expected pixel hit resolution is $\sigma_{r\phi} \sim 10\ \mu m$ and $\sigma_{rz} \sim 17\ \mu m$. The efficiency to find three pixel hits on a track (in the three-layer geometry) is above 90 % for $|\eta| < 2.2$.

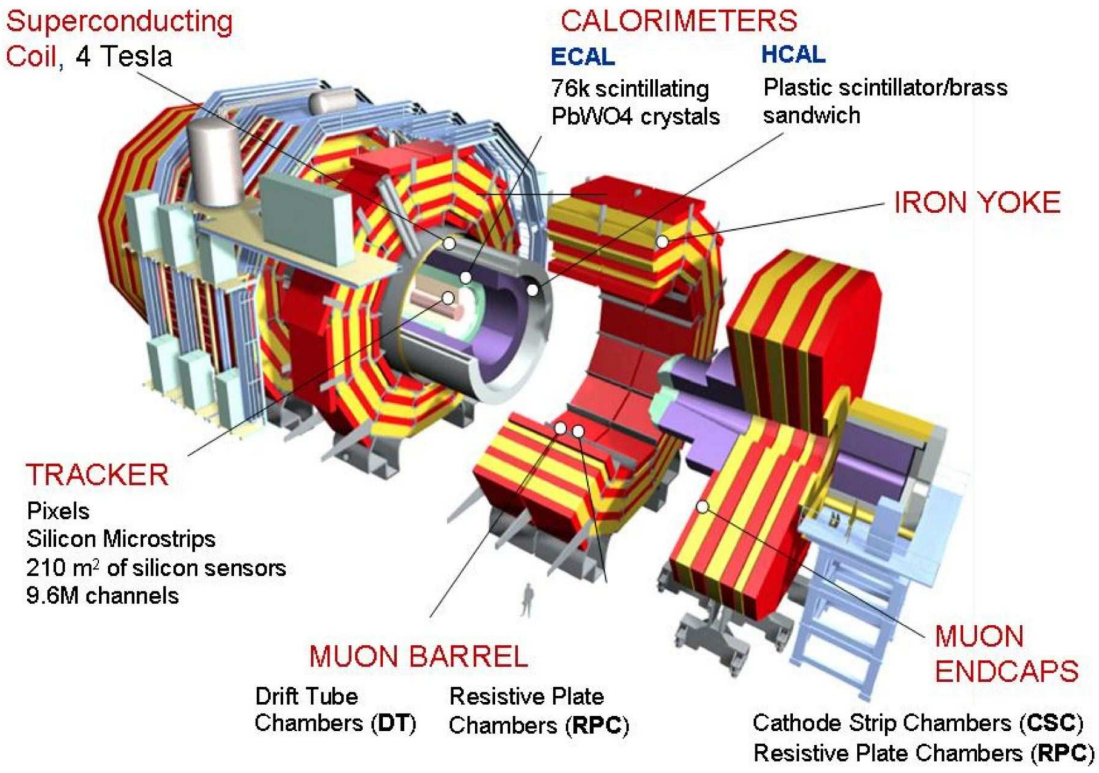

Figure 3.4: Schematic view of the CMS detector.

The silicon strip detector consists of four tracker inner barrel (TIB) layers, six tracker outer barrel (TOB) layers and in each endcap nine tracker endcap (TEC) layers. On each side of the TIB, there are three tracker inner discs (TID) installed. The expected hit resolution for the silicon strip is $\sigma_{r\phi}$ = 10-60 μm and σ_{rz} = 500 μm. Combining these numbers, the expected CMS tracking resolution ranges from $\Delta p_T/p_T^2 = 0.015\%$ for $|\eta| < 1.6$ up to $\Delta p_T/p_T^2 = 0.06\%$ for $|\eta| = 2.5$. Thus, a muon with a p_{T} of 100 GeV can be reconstructed with an accuracy of $\pm$1.5 GeV for $|\eta| < 1.6$. To protect the silicon detectors from aging due to the high radiation flux, which causes an increase in leakage current, the full silicon tracker will be operated at $-10°$C. A thermal shield placed outside of the tracker volume provides insulation while a cooling system extracts 60 kW of heat dissipated by the front end electronics.

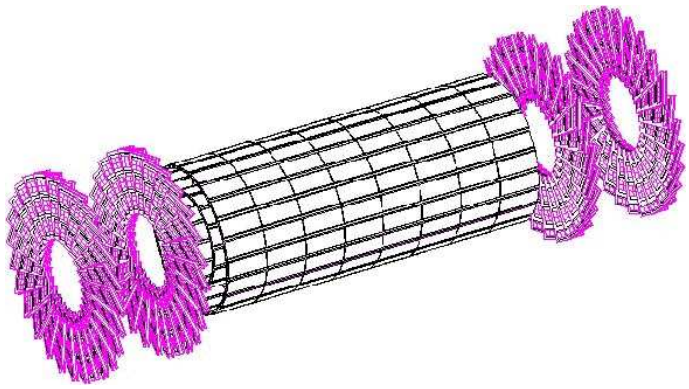

Figure 3.5: The CMS pixel detector (Three barrel layers and two endcaps layers at each side).

3.3.2 The Electromagnetic Calorimeter

The electromagnetic calorimeter (ECAL) is placed around the tracker. The design of the ECAL is driven by the requirement to provide an excellent di-photon mass resolution for the $H \rightarrow \gamma\gamma$ decay mode. A crystal-based scintillating calorimeter (as opposed to sampling calorimeters) offers the best performance for energy resolution from electrons and photons, since most of the energy is deposited inside the active volume. The choice of lead tungstate ($PbWO_4$) was motivated by its fast light decay time, its small Molière Radius, its high density of 8.28 g/cm^3 (allowing a compact design) and its good radiation resistance, as the crystals have to endure very high radiation doses. After 15 ns, already 60% of the light should be emitted by the crystals (compared to 300 ns for BGO crystals, which were used e.g. in L3), and 100 ns should be enough to collect the emitted light. The small Molière Radius of 2.19 cm allows for lateral shower containment inside a few crystals. Furthermore, $PbWO_4$ is a fast scintillator compatible with the high event rate at LHC. The crystal dimension is roughly 2.2 cm x 2.2 cm x 23 cm for the barrel crystals and 2.5 cm x 2.5 cm x 22 cm in the endcaps. This corresponds to a granularity of $\Delta\phi$ x $\Delta\eta$ of 0.0175 x 0.0175 in the barrel. The

size of the crystals corresponds to about 26 radiation lengths. For 35 GeV electrons, about 94% of the electron energy is contained a 3 x 3 crystal array, and 97% in a 5 x 5 crystal array. A drawback of the lead tungstate is its relatively low light yield, which is about 14 times smaller than the one from BGO crystals. This requires strong amplification within the photodetector at the end of the crystal. The photodiodes have to operate in a rather hostile environment. Photomultipliers can not be used in such a strong magnetic field, and thus avalanche photodiodes, which can operate in strong transverse magnetic fields, will be used in the barrel part of the calorimeter, while vacuum phototriodes will be used in the endcaps, in order to cope with the higher levels of radiation. The ECAL is built out of $\sim$ 76000

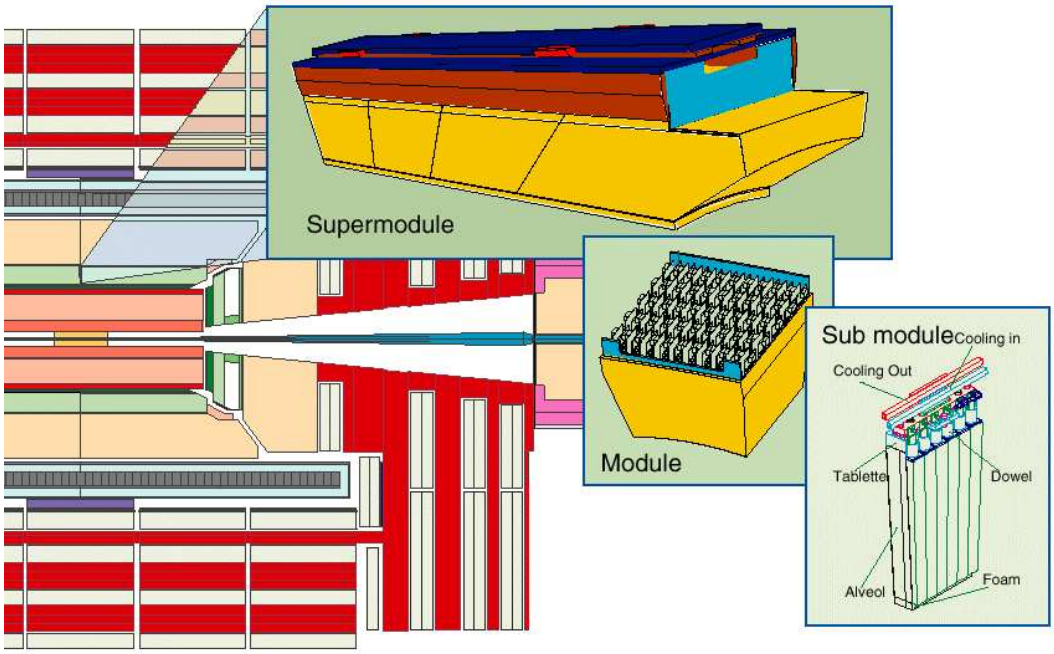

Figure 3.6: The Supermodules, Modules and Submodules of the ECAL detector.

individual crystals. The crystals are mechanically organized into modules and supermodules. In the barrel, the crystals are tilted in the transverse plane by 3 degrees, in order to minimize the probability that particles pass through the inactive area between crystals. The barrel crystals are assembled into 36 supermodules, each consisting of 4 modules with 50 submodules in the first module and 40 in the remaining three modules. This is shown in Figure 3.6. Those submodules are composed of 2 x 5 crystals assembled into a fiberglass alveolar structure. In total, the barrel contains 61200 crystals. The supermodules have a wedge shape and subtend an angle of 20 degrees.
The design guarantees a maximum distance between crystal faces of 0.4 mm within a supermodule and 0.6 mm across two submodules. A crack of about 6 mm is expected between two supermodules in ϕ and 6.8 and 7.8 mm between two modules at different η. The endcap

ECAL is built up of identical 5 x 5 crystals, To ensure a hermetic design, the crystals will be oriented toward a point located 1.3 cm away from the interaction point. Thus the crystals are off-pointing to a similar extend as the barrel crystals.

A preshower built in front of the endcap calorimeter ($|\eta| > 1.653$) should allow to reject high p_T π^0's by measuring the transverse profile of the electromagnetic shower after roughly three interaction lengths. The preshower is built like a sampling calorimeter with lead as absorber and a layer of silicon strip sensors for the measurement of the charged particles created in the shower. Strips from one plane are orthogonal to these of the second plane, which gives a two-dimensional position measurement with a precision of 300 μm for a 50 GeV π^0.

The energy resolution can be parametrized as a function of the energy as

$$(\frac{\Delta E}{E})^2 = (a/\sqrt{E})^2 + (b/E)^2 + c^2 \tag{3.7}$$

The first term is the stochastic term, the second the noise, and c^2 is the constant term. The stochastic term includes contributions from photostatistics and fluctuations in the shower containment. The noise term incorporates contributions from the electronics readout and pile-up, and therefore depends on the luminosity. The design goal is to reach a stochastic

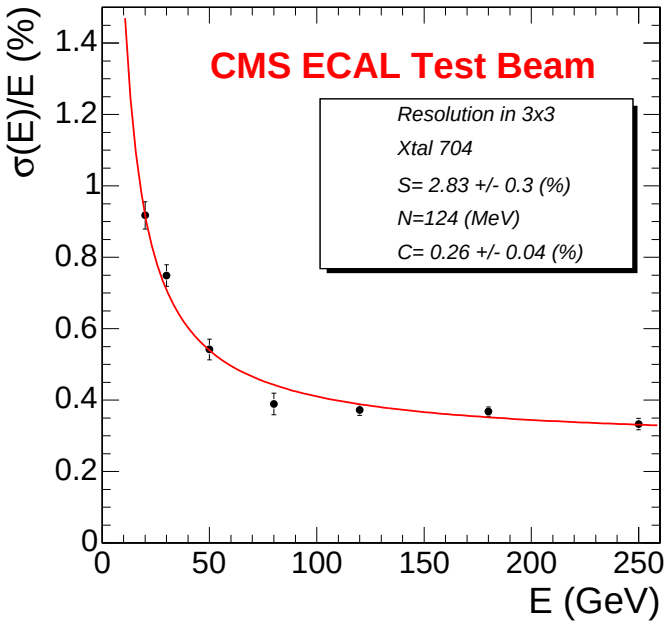

Figure 3.7: Energy resolution as a function of the reconstructed energy in a 3 x 3 crystal matrix, Testbeam 2004 data [39].

term of $a = 2.7$ % in the barrel and $a = 5.6\%$ in the endcap, a constant term of $c = 0.55\%$

and a noise term of $b = 210$ MeV in the barrel and 245 in the endcap (at high luminosities). The intrinsic ECAL energy resolution measured in the testbeam 2004 (by summing up the deposited energy in the 3 x 3 array of crystals around the crystal in the beam) resulted in a stochastic term $a = 2.83\% \pm 0.3\%$, a constant term $c = 0.26\% \pm 0.04\%$ and a noise term $b = 124$ MeV, which matches the desing resolution for a perfectly calibrated detector. Miscalibration will directly affect the constant term c, degrading the overall ECAL performance. The energy resolution of the testbeam crystal 704 is shown in Figure 3.7. The data was taken at series of beam momenta corresponding to the energies of 20, 30, 50, 80, 120, 180 and 250 GeV.

3.3.3 The Hadronic Calorimeter

The hadronic calorimeter (HCAL) consists of a barrel and two endcaps. The barrel is 9m long and covers a pseudorapidity region $|\eta| < 1.48$. The endcaps are 1.8 m thick, and cover the pseudorapidity range $1.48 < |\eta| < 3$. The thickness corresponds to at least ten nuclear interaction lengths, enough to contain a large fraction of the hadronic showers. A set of (very) forward calorimeters completes the acceptance of the detector.

The HCAL is placed between ECAL and solenoid. The hadron calorimeter is a sampling calorimeter with copper absorber plates interlaced with 4 mm thick plastic scintillators. Copper was chosen for its relatively low Z, which minimizes multiple scattering for muons. It is also a non-magnetic metal, which is important since the calorimeter is placed within the 4 T solenoid. The produced blue scintillation light is captured and shifted toward green in wavelength shifting fibers and then transported to photodiodes. The calorimeter granularity of $\Delta\eta$ x $\Delta\phi$ was chosen with the goal that highly boosted dijets from W and Z decays can still be distinguished. In order to get a good measurement of the missing transverse energy, jets are expected to be reconstructed up to a rapidity of 5. The hadronic calorimeter (HCAL) is designed to measure the direction and energy of hadrons produced either as remnants of the proton, during the hadronization of quarks and gluons from the hard process, or from tau decays. By combining all calorimetric activity, a missing transverse energy is determined. The missing transverse energy is the only variables sensitive to neutrinos and other weakly interacting particles that could be a sign for new physics. Since the longitudinal momentum is not measured in hadron collisions (as it is parallel to the beam axis) only transverse quantities (e.g. transverse momentum or transverse mass) are generally considered.

3.3.4 The Muon System

The muon system consists of four muon stations interleaved with the return yoke plates and is divided in a barrel part and two endcaps. The total thickness of the return yoke before the last muon station is reached represents 16 interaction lengths. This allows a good muon identification. As muons, unlike the electrons, emit almost no Bremsstrahlung, they are expected to give very clear signatures. In addition, the muon system has to measure precisely the position of pass-through muons and must deliver a quick response that can be used by the hardware trigger. Also, the muon chambers must sustain the 2 T magnetic field in the

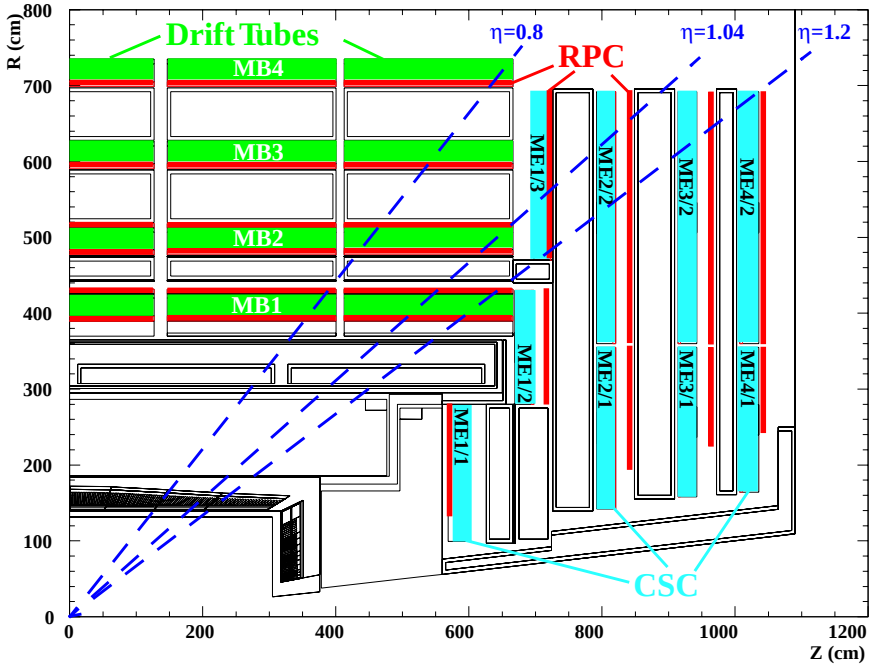

Figure 3.8: Longitudinal view of one quarter of the muon system with DTs, CSCs and RPCs.

return yoke. These constraints led to a redundant design that combines three technologies: drift tubes (DT) in the barrel region, cathode stripe chambers (CSC) in the endcap region and resistive plate chambers (RPC) in both the barrel and endcap, see Figure 3.8.

DTs are suited to the barrel as the magnetic field is mainly contained by the return yoke. DTs are assembled in drift chambers containing 12 layers of tubes, which are organized in three independent subunits made up of four planes with parallel wires. Two subunits measure the coordinate in the bending plane, the third measures the track coordinate along the beam. Measurements in a chamber are combined to form an oriented segment used later on for track reconstruction. The forward environment is very different from the central one, as the high particle flux requires a finer granularity and a faster response. CSCs can sustain the highly varying magnetic field present in this transition region between the solenoid and the return yoke. CSC are multiwire proportional chambers where the cathode is subdivided into strips perpendicular to the anode wires.

The resistive plate chambers, which are used in both the barrel and the endcaps, provides a lower spatial resolution than the CSCs and DTs, but provide a faster timing signal with a time resolution of $\sim$ 2-3 ns. A RPC consists of two parallel resin plates, with a high bulk resistivity, separated by a gas-filled gap of a few millimeters. On the outside, electrodes are coated made of a conductive graphite paint. Avalanches in the gas induce a fast charge on the cathodes, that can be exploited without costly electronics. RPCs complement drift tubes and CSCs, acting as additional sensitive planes in higher trigger levels and offline reconstruction.

The efficiency of the reconstruction of muon tracks is above 90% for 100 GeV muons in the pseudorapidity range covered by the muon chambers. The momentum resolution of tracks measured in the muon system depends strongly on the pseudorapidity since for $|\eta| > 1.5$ the tracks exit the solenoid and become therefore less bent. Together with the information from the tracking chambers, a resolution of about 1%-1.5% for 10 GeV muons For 10 GeV muons is expected, depending on the pseudorapidity. For 1 TeV muons it ranges from 6 to 17%.

3.3.5 The Trigger System

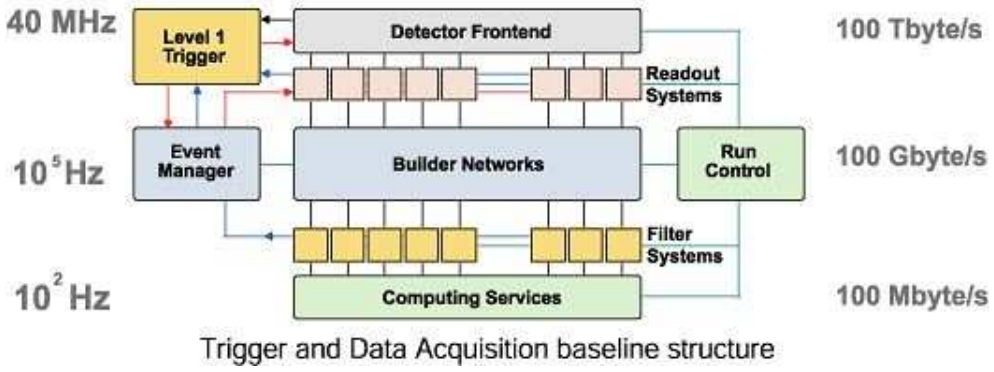

Figure 3.9: The CMS Trigger system.

At LHC, on average 20 interactions per bunch crossing are expected every 25 ns for a design luminosity of 10^{34} cm^{-2}s^{-1}. This makes almost one billion interactions per second. Moreover, CMS possesses almost one hundred million detector channels. This corresponds to about 1MB of zero-suppressed data per event, resulting in 100 TeraByte of data per second. This is far too much to be handled and stored with present technology. Since most of the events are background events, it is the challenging task of the trigger system to preselect only the interesting events. The challenge for the trigger system is therefore to reduce 45 MHz down to 100 Hz and a data rate of $\sim$ 100 MB/s, which is the maximum rate that can be achieved for off-line analysis by the DAQ system. The trigger system is shown in 3.9. The Level-1 trigger (L1) is purely hardware based. It is fast and allows for the first rough estimation of relevant quantities. Rough information from the pattern recognition of the muon chambers combined with coarse energy measurements from the calorimeters are used for the first trigger decision. The four most energetic objects for each of the following candidates are investigated: muons, isolated electrons/photons, non-isolated electrons/photons, central jets, forward jets and specific τ-jets. Threshold cuts are applied for example on the transverse momentum and the isolation, to achieve an output L1 trigger rate of 50 kHz at startup of the LHC, and, once all the electronics is ready, 100 kHz. After 3.2 μs, it is decided whether the event passes the Level-1 trigger or is rejected. This time includes the information transfer back and forth from the front-end electronics and the L1 processing elements. While waiting for the decision, the complete detector information for each event

is stored in a pipeline. If required, this information is read out and passed on to the next level.

The events are then pulled to the filter farm, where the High-Level trigger (HLT) selection is performed. The HLT can be divided into two levels, Level 2 and 3: From Level 2 on, the trigger decisions are made by a processor farm with standard CPU's. This makes a more elaborate trigger decision possible. On average, the L2 obtains an event every 10 μs and thus enables a fast physics selection algorithm to combine more accurate position knowledge with a more precise energy measurement. In addition, primary tracking information from the pixel detectors is taken into account (Level-2.5). A rate reduction factor of 10 is accomplished that way. The final step of the trigger decision uses full event reconstruction. The entire information of the full tracker is available, thus enables to acquire the fully reconstructed physics event. The output rate of L3 is decreased compared to the input rate by a factor of 100. Finally the output rate of 100 Hz is obtained. The current schemes show that the foreseen selections do not reduce the physics program of CMS.

Chapter 4

SM Higgs Production and Decay Processes at LHC

4.1 Higgs Production Processes

The Large Hadron Collider (LHC) will be the highest-energy particle collider in the world, producing proton-proton collisions at a center of mass enery of 14 TeV. One of the major goals at LHC is to investigate the physics of electroweak symmetry breaking, and thus to find or exclude the SM Higgs boson. The Higgs couplings to fermions and electroweak gauge bosons are proportional to the corresponding masses (and squared masses, respectively) :

$$g^{SM}_{f\bar{f}H} \propto \frac{m_f}{v} = (\sqrt{2}G_F)^{\frac{1}{2}} m_f,\ g^{SM}_{VVH} \propto \frac{m_V^2}{v^2} = (\sqrt{2}G_F)^{\frac{1}{2}} m_V^2, \tag{4.1}$$

with (V = W, Z), v the vacuum expectation value $v = 2m_W/g \approx$246 GeV, and G_F the Fermi constant [13]. Thus, the Higgs boson couples preferentially to heavy particles, that is the top quark, the W and Z vector bosons, and, to a smaller extent, the bottom quark. Note that the coupling ggH is induced by a one-loop graph in which the Higgs boson couples to a virtual $Q\bar{Q}$ pair.

The four major SM Higgs production channels at the LHC are therefore the following [41]:

- Gluon fusion (gg $\rightarrow$ H)
- Vector boson fusion (VBF) ($qq \rightarrow qq$H)
- Associated production with vector bosons ($qq \rightarrow$ WH, $qq \rightarrow$ ZH)
- Associated production of the Higgs boson with heavy quark pair (mostly t$\bar{\text{t}}$) (pp $\rightarrow Q\bar{Q}$H)

Their corresponding Feynman diagrams are shown in Figure 4.1. Gluon fusion is the dominant production channel for Higgs bosons at proton colliders. In gluon fusion, the coupling of the Higgs boson to gluons is mediated by a heavy quark loop, mainly the top quark.

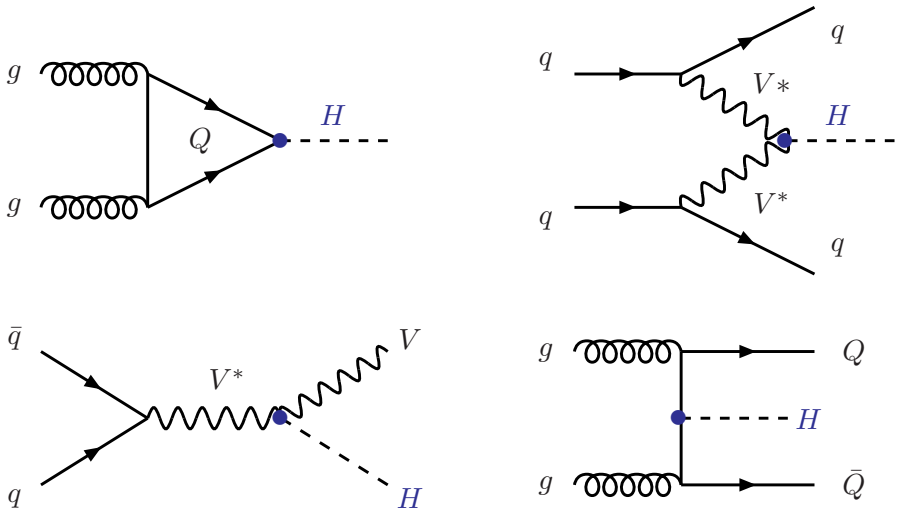

Figure 4.1: The dominant SM Higgs boson production mechanisms in hadronic collisions. From left to right: gluon fusion, vector boson fusion (VBF), associated production with weak bosons and associated production with heavy quarks [45].

The leading order of the process is described by a one-loop diagram. The second dominant Higgs production mechanism is vector boson fusion. Higgs production through gluon fusion is about ten times higher then vector boson fusion (VBF) at masses up to 600 GeV at the LHC. It becomes comparable at around 1 TeV (Figure 4.2). The VBF channel, even though numerically smaller than the gluon fusion channel, is interesting because it provides additional information about the Higgs boson couplings. For $m_H \approx 100$ GeV, the associated Higgs production channels $q_i\bar{q}_j \rightarrow WH$, $q_i\bar{q}_j \rightarrow$ ZH and gg,$q_iq_j \rightarrow$ t$\bar{\text{t}}$H have cross sections comparable to the VBF cross section, while they become very small at higher masses [44]. Applying appropriate analysis cuts, also production processes with smaller cross sections can be identified, like for example the production channel $qq \rightarrow qq$H, where the signature includes two energetic forward jets originating from the incoming quarks; due to the lack of colour flow between the initial state quarks of the signal, a central jet veto can be applied. Production channels involving several Higgs bosons, e.g. Higgs pair production (pp $\rightarrow$ HHX), are suppressed.

4.2 Higgs Decays and Detection

The main SM Higgs decay channels and their branching ratios are shown in Figure 4.3. A summary is given e.g. in [45]. To study the different Higgs signatures, the total cross sections (Figure 4.2) have to be multiplied with these branching ratios (BR's), as illustrated in Figure 4.4. To search for and discover the SM Higgs at LHC, lepton and photon final states are favoured to hadronic final states, because of the large QCD background at hadron colliders. In addition, the energy resolution of leptons and photons is better than the energy resolution

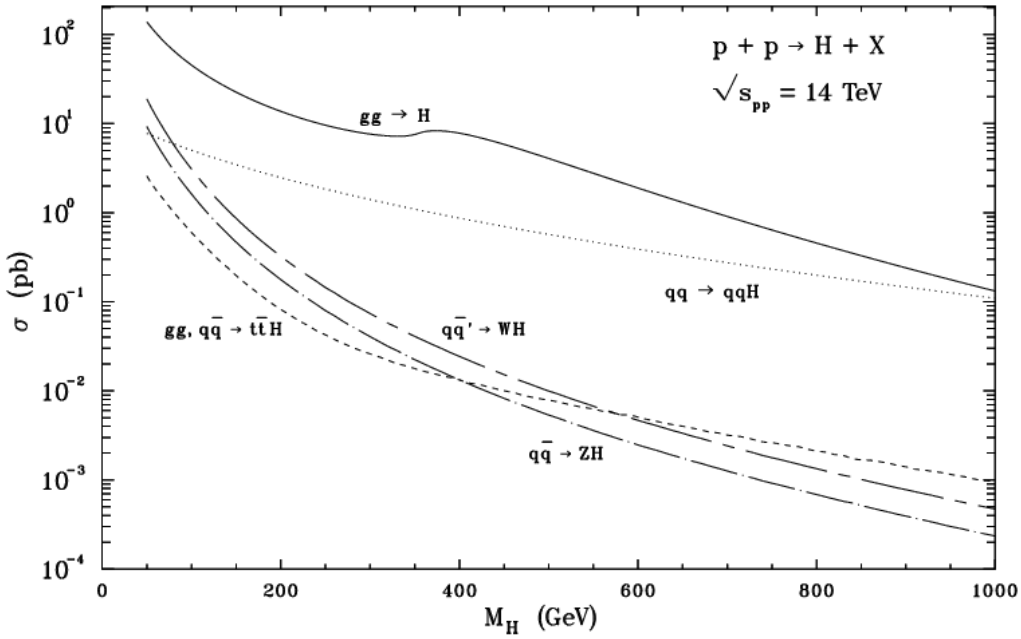

Figure 4.2: Higgs production cross section in NLO as a function of the Higgs mass at LHC [42].

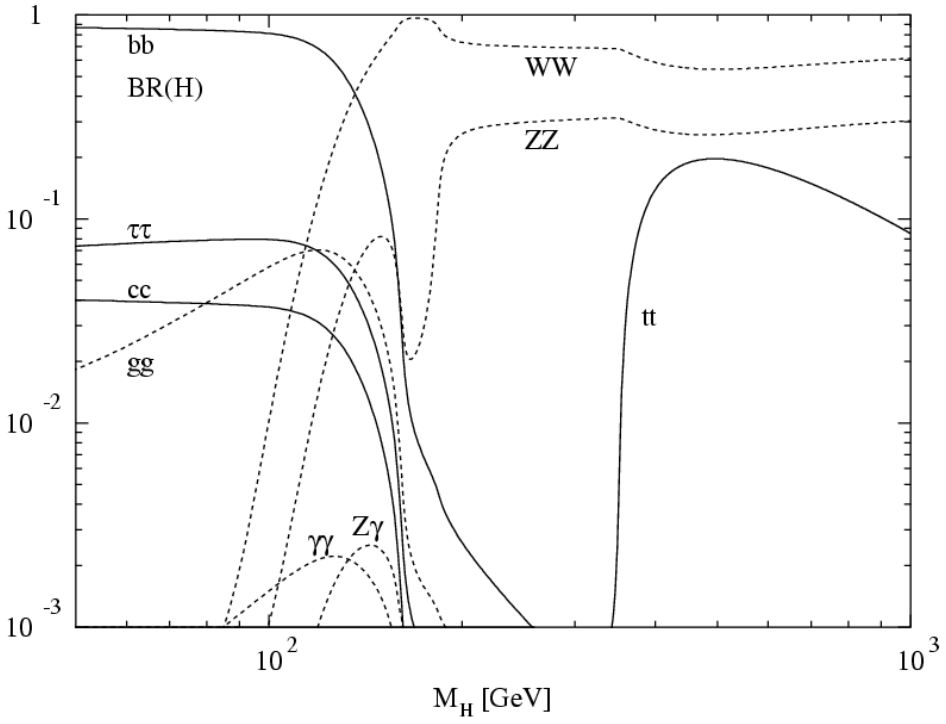

Figure 4.3: The decay branching ratios of the Higgs versus its mass [43].

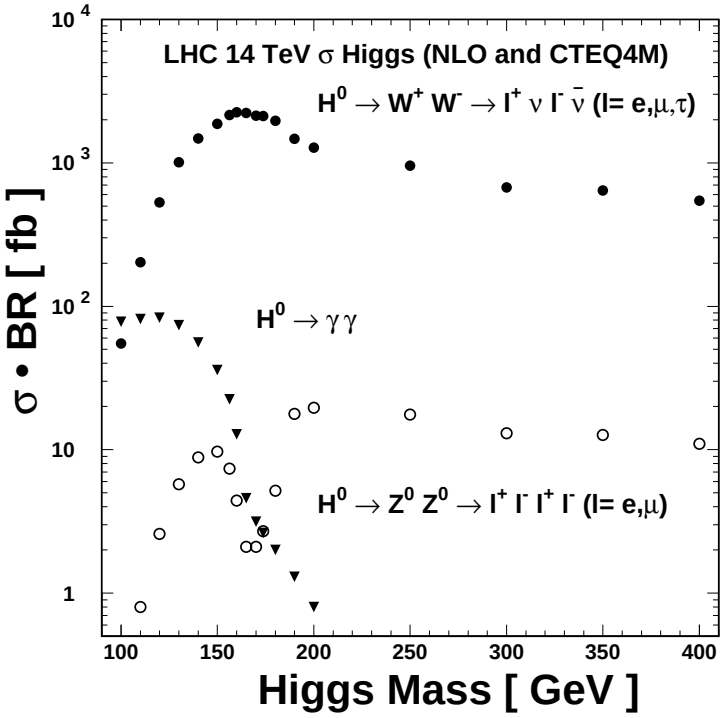

Figure 4.4: Cross sections multiplied by the decay branching ratios of the Higgs as a function of its mass [40]. The assumed Higgs cross section (NLO) are taken from [42] while the branching ratios are taken from [43].

of jets and thus clearer signatures can be found. Figure 4.4 shows the estimated $\sigma\times$ BR for the Higgs search modes H $\rightarrow \gamma\gamma$, H $\rightarrow$ ZZ $\rightarrow 4\ell$ and H $\rightarrow$ WW $\rightarrow \ell\nu\ell\nu$ at NLO.
As the dominant decay H $\rightarrow$ b$\bar{\text{b}}$ is overwhelmed by large QCD backgrounds, H $\rightarrow \gamma\gamma$ is expected to be the discovery signature for a Higgs mass between 100 and 130 GeV. Between 130 and 150 GeV, the main discovery channel is H $\rightarrow$ ZZ* $\rightarrow 4\ell$.
For m_H between 150 and 180 GeV, gg $\rightarrow$ H $\rightarrow$ WW $\rightarrow \ell\nu\ell\nu$ is the discovery signature, as the branching ratio of H $\rightarrow$ ZZ* in this region is very low.
Above W-pair and below Z-pair threshold (between 160 and 180 GeV), the decay H $\rightarrow$ WW is essentially the only relevant mode with a branching ratio of almost 1.
For Higgs masses above the Z-pair threshold, the most likely process to discover the Higgs will be the H $\rightarrow$ ZZ $\rightarrow 4\ell$ signature. In addition to this signature, two additional channels H $\rightarrow$ ZZ $\rightarrow \ell\ell\nu\nu$ and $qq \rightarrow qq$H $\rightarrow$ WW $\rightarrow \ell\nu$jj [46] dominate the region above 300 GeV.
It is interesting to understand the experimental challenges to discover the Higgs in those channels. These are summarized in the following for the major Higgs discovery channels at LHC. The gg $\rightarrow$ H$\rightarrow$ WW$\rightarrow$ $\ell\nu\ell\nu$ channel will be discussed in detail in the following chapters.

- The decay H $\rightarrow \gamma\gamma$ can be observed if a very good photon resolution is obtained to isolate the $\gamma\gamma$ signal peak from the large continuum $\gamma\gamma$ background. The QCD background from jets faking photons is huge, but simulation studies have shown that this background might be reduced to the level of the irreducible backgrounds, which are the direct $q\bar{q} \rightarrow \gamma\gamma + X$ production and the loop induced channel gg $\rightarrow \gamma\gamma + X$.
  These backgrounds can, in principle, be determined by measuring the two-photon in-

variant mass distribution in the sidebands of the resonance peak. For an evaluation of the detection significance and measurements of the Higgs properties, the background needs to be precisely modelled [47]. Since the Higgs boson width is small (a few MeV for Higgs masses between 110 and 140 GeV), the measured mass peak is entirely dominated by the experimental resolution. An additional task is to efficiently reduce the very large number of π^0's with high transverse momentum, decaying into two photons. Since the decay $H \to \gamma\gamma$ is rare, a large amount of luminosity is required for a discovery. Therefore, at low luminosities, all $H \to \gamma\gamma$ production channels have to be combined, which means Higgs production through gluon fusion, associated Higgs production HW, where an additional lepton comes from the decay of a W boson, or in $t\bar{t}H$ production with $t \to bW \to b\ell\nu$.

- In order to get a good signature for the decay $H \to WW$, at least one of the W bosons has to be observed in its leptonic decays. The BR($W \to \ell\nu$) is around 30% with $\ell = \mu, e, \tau$. A good detection of isolated high transverse momentum muons and electrons and an accurate calorimetry with hermetic coverage to measure the transverse energy of the missing neutrinos is needed. The dominant irreducible backgrounds are nonresonant WW production, $t\bar{t} \to WbWb$ and Wtb. Other potential backgrounds are Drell-Yan[1], WZ and ZZ, which can be removed relatively easily. $H \to WW \to \ell\nu\ell\nu$ turned out to be the most promising detection modes of a Higgs boson in the mass range from 150 GeV up to $m_H \sim 2m_Z$ [48,49]. Since the Higgs mass cannot be reconstructed as a narrow mass peak in this process, the signal should be observed from a clear excess of events above backgrounds which need therefore to be known as accurately as possible.
  At high Higgs masses, the decay channel $H \to WW \to \ell\nu jj$, combined with $H \to ZZ \to \ell\ell jj$ and the $H \to ZZ \to \ell\ell\nu\nu$ channel, extend the discovery reach to masses up to 1 TeV at high luminosities, after reducing the large $t\bar{t}$ and W+jets backgrounds [50].

- In the high mass region, $m_H > 2m_Z$, The decay $H \to ZZ \to 4\ell$ provides a very clear signature, as a a narrow mass peak can be reconstructed with the four leptons. The decay into electrons and muons is considered as the "gold-plated" channel. This channel should allow for Higgs detection up to masses of $\mathcal{O}(1\,\text{TeV})$ [32, 51, 52]. The Higgs is expected to be observed as a clear mass peak [53–56]. The main background is continuum $ZZ \to 4\ell$ production, which is known rather precisely [57, 58] and can be measured directly from the side bands of the resonance peak and interpolated to the signal region. This allows for direct information about deviations from the estimated background which are higher than the normal background fluctuations.
  As the BR($H \to ZZ \to 4\ell$) $\sim 0.1\%$ is small and the total Higgs width becomes large. Therefore, high luminosities are required. To increase the statistics, in addition the $H \to ZZ \to \ell\ell\nu\nu$ decays [59] can be used. In the region below 150 GeV and above 130 GeV, the $H \to ZZ^* \to 4\ell$ decays [60] is considered to be the discovery channel, with a very sharp peak in the 4ℓ invariant mass distribution. In this region, additional backgrounds from $t\bar{t}$ [61] and $Zb\bar{b}$ [62] production contribute in addition to $ZZ^*, Z\gamma^*$ events.

[1] $q\bar{q} \to Z^*/\gamma^* \to \ell\ell$, with ℓ being an electron, muon or tau.

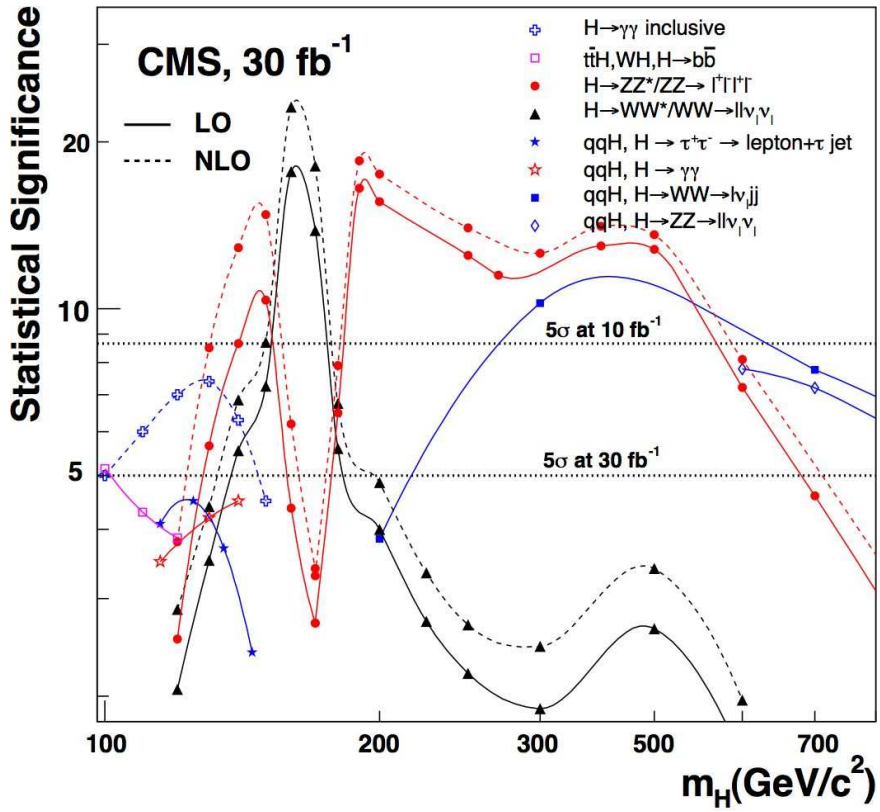

Figure 4.5: The significance for the SM Higgs boson discovery in various channels in CMS as a function of m_H and for 30 fb^{-1}.

As the branching ratios to some final states are small, a combination of different Higgs decay channels have to be used in order improve the sensitivity to discover the Higgs boson.

4.3 Discovery Expectations at the LHC

The significance of the signals in the various Higgs production and decay channels at the LHC is shown as a function of m_H in Figure 4.5, where an integrated luminosity of 30 fb^{-1} is assumed. The detection relies mostly on the $gg \rightarrow H$ production mechanism with the decays H $\rightarrow \gamma\gamma$, WW$^{(*)}$ and ZZ$^{(*)}$ (where one of the vector boson is allowed to decay hadronically in the high Higgs mass range), supplemented by the processes pp $\rightarrow$ t$\bar{\text{t}}$H, b$\bar{\text{b}}$, and pp $\rightarrow$ WH with H decaying into two photons. In the region where H $\rightarrow$ VV* decays are not yet dominant ($m_H \lesssim 130$ GeV), the significance of the signal is relatively small. Note that the cross section in CMS are given to NLO. NNLO corrections would slightly increase the significance in most channels.
Figure 4.6 shows the integrated luminosity that is needed to achieve a 5σ discovery in the various detection channels in CMS. The cross sections are shown at NLO. Thus, with the first year of LHC luminosity (a few fb^{-1}), only the gg $\rightarrow$ H $\rightarrow$ WW $\rightarrow \ell\nu\ell\nu$ channel is accessible while for other mass regions some hints are possible.
Summarizing the above, one can expect that the SM Higgs boson will be found at the LHC provided that a luminosity of around $\int \mathcal{L} = 30$ fb^{-1} is collected and the detectors perform as expected. For higher luminosities, more channels can be used, thus strengthening the signal and providing answers to the question if indeed a scalar Higgs boson has been observed.

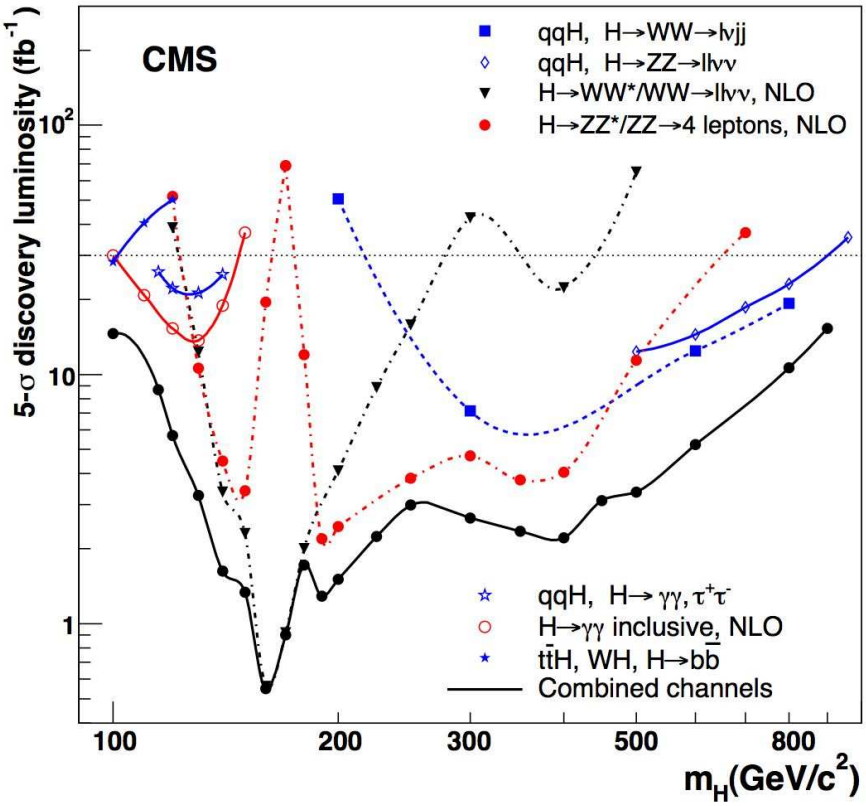

Figure 4.6: The required integrated luminosity that is needed to achieve a 5σ discovery signal in CMS using various detection channels as a function of m_H [63].

At low luminosities, and in particular in the low Higgs mass range $m_H \lesssim 135$ GeV, several channels must be combined in order to establish a clear evidence for the Higgs particle.
As the K-factors can increase the LO cross section by a large amount, e.g. 200 % for gluon fusion at NNLO, those corrections need to be included in the experimental analyses. They allow not only more accurate predictions of the discovery potential but can also lead to a better cut optimization, as will be discussed in the following chapters.

For comparison, also the discovery channels at Tevatron are mentioned. Also here, gluon fusion is the main production process. The second dominant Higgs production mechanism is, contrary to the production channels at LHC, quark-antiquark annihilation. This can be explained by the fact that in antiproton-proton colliders, antiquarks are available already as valence quarks, carrying a large fraction of the total proton energy, while at proton-proton colliders, antiquarks come from the sea and therefore carry less energy then the quarks. As the cross section depends directly on the center of mass energy ($\sqrt{s}$) of the interacting system, antiquarks contribute more in antiproton collisions and quarks in proton collisions.
The signatures which are sensitive to detect or exclude Higgs bosons at Tevatron are: the W+Higgs and Z+Higgs channels (where the Higgs decays to $b\bar{b}$ and the W and Z decay leptonically) for a Higgs mass below 140 GeV and the Higgs boson decays to WW (where one W may be virtual) above 140 GeV.
Up to December 2006, an integrated luminoisty of 1.8 fb^{-1} was achieved by each of the two experiments, and the goal is to reach a luminosity of 8 fb^{-1} by the end of the run (August 2009). This might be enough for a 3σ evidence for $m_H \lesssim 125$ GeV and, in the absence of any signal, to set a 95% CL exclusion limit for Higgs masses up to 180 GeV [6].

Chapter 5

Simulations of Particle Interactions at the LHC

The event rate and the production of various final states of colliding particles in an accelerator is given by the cross section, which characterize the probability that a particular reaction will take place.
The number of signal events S observed is defined as

$$S = N - B = \sigma \times \mathcal{L} \times \epsilon, \tag{5.1}$$

where N is the total number of observed events, B the number of background events, σ the cross section, $\mathcal{L}$ the luminosity, and ϵ the detection efficiency. In order to interpret any measurements, the observed number of events are compared to the theoretical predictions. The theoretical cross section and the experimental determination should therefore be performed as accurate as possible.

In a hadron collider, the cross section pp $\rightarrow X$ has to be calculated by convoluting the hard-scattering partonic cross section with the parton distribution functions (PDFs) of the colliding hadrons[1]. PDFs provide the link between the colliding protons and their interacting constituents, parametrizing the quark and gluon structure of the proton. The cross section for a given process pp $\rightarrow X$ for two hadrons a and b with momenta P_a, P_b can be written as

$$\begin{aligned} &\sigma_{pp\rightarrow X}(P_a, P_b) = \\ &\sum_{a,b} \int_0^1 dx_a dx_b f_a(x_a, \mu_f) f_b(x_b, \mu_f) \times \sigma_{ab\rightarrow X}(p_a, p_b, \alpha_S(\mu_R^2), Q^2/\mu_R^2, Q^2/\mu_f^2) \end{aligned} \tag{5.2}$$

where the sum runs over the involved partons a and b, x_a and x_b are the parton momentum fractions ($x_i = p_{\text{parton i}}/P_{\text{hadron i}}$), integrated over the whole kinematic range, f_a and f_b are the corresponding PDFs, and $\sigma_{ab\rightarrow X}$ is the partonic cross section, which depends on the strong coupling constant α_S at a given renormalization scale μ_R. In addition, the PDFs depend on a factorization scale μ_f and the partonic cross sections depend also on the energy

[1] More information about the PDFs can be found in Section 7.3.

scale Q^2 at given renormalization and factorization scales μ_R and μ_f. The PDFs describe the probability to find a parton (such as valence and sea quarks and gluons) with a given momentum fraction x in a hadron. The cross section $\sigma_{\mathrm{pp}\to\mathrm{X}}$ is thus factorized into the PDFs and the partonic cross section $\sigma_{ab\to X}$.

In leading order (LO), the matrix element of a process $ab \to X$ (a $2 \to X$ process), where X can be one single particle like the Higgs, or a system of particles like the WW system, is defined at tree level. This means that X gets no transverse momentum.
The matrix elements can be calculated at higher orders, which include real additional parton emissions and virtual loops. Most higher order matrix element programs calculate only total cross sections and no differential distributions, e.g. the transverse momentum of an emitted particle.

Recently, a program called FEHIP was developed that describes the next-to-next-to leading order (NNLO) cross section and fully differential distributions for gluon fusion Higgs boson production and Drell-Yan at NNLO. The $\mathrm{H} \to \gamma\gamma$ decay is implemented and the decay $\mathrm{H} \to \mathrm{WW} \to \ell\nu\ell\nu$ is expected to be implemented in the near future [64, 65]. Cuts can be imposed on partonic jets and on the decay products of the Higgs boson. As a pure fixed-order program, regions of phase-space close to kinematic boundaries can not be described, which manifests itself in large perturbative corrections at special kinematic regions, such as the low Higgs p_{T} region, where the bulk of events lies. To overcome the problems encountered in the low p_{T} region in fixed order perturbative calculations, the resummation of soft gluon effects to all orders in perturbation theory is performed. This resummation can be obtained using analytical techniques [66, 67]. The transverse momentum distribution of some processes, e.g. the gluon fusion Higgs production, can be obtained using the program HqT [68], which avoids the fixed order problems in the low p_{T} region by resummation up to next-to-next-to leading logarithmic terms (NNLL). This is currently the most up-to-date transverse momentum spectrum for a Higgs boson produced in proton collisions.
A similar technique as the resummation technique described above is applied in parton shower Monte Carlo event generaters, where the low p_{T} emissions of additional partons are described by a parton shower. In this case, X can obtain transverse momentum through the emission of partons in the initial state. These emissions occur at low Q^2, where $\alpha_S \approx 1$. As α_S is large for soft emissions, these emissions can not be calculated perturbatively. Note that X obtaines thus a transverse momentum in a LO parton shower Monte Carlo, while the p_{T} of X is zero in fixed LO matrix element calculations. LO parton shower Monte Carlos can obtain high p_{T} jets by applying higher order matrix element corrections. These, however, are only approximations.
As exact matrix element calculations do not predict final hadronic states, and parton shower Monte Carlo event generators can not include higher order corrections accurately, it is desirable to find a way in which the virtues of both methods are combined.

Novel approaches, described in Refs. [69–73], merge cross sections computed in fixed order perturbation theory with LO event generators, such as PYTHIA [74] and HERWIG [75]. Significant progress has been achieved, and the pioneering Monte Carlo event generator

MC@NLO [69] combines consistently NLO perturbative calculations with HERWIG for a number of processes at hadron colliders. However, no method exists which merges parton shower algorithms with NNLO partonic cross sections consistently. Especially in the gg $\rightarrow$ H production channel, NNLO corrections are important, contributing a factor of more than 30% to the total cross section. In addition, many processes are not described yet in MC@NLO, or only partly, as for example the H $\rightarrow$ WW $\rightarrow \ell\nu\ell\nu$ channel, where the spin correlations are so far not accurately included. As the cut based on spin correlations is crucial to reduce the main WW background in this channel, MC@NLO can presently not be used for a full analyis of this process.

In Ref. [76] we presented a method how most up-to-date higher order QCD corrections can be merged into parton shower Monte Carlos, such as PYTHIA and HERWIG.
So far, NNLO corrections were applied to parton shower Monte Carlos by simply scaling the results obtained using the MC with an inclusive K-factor, so that the total cross sections computed perturbatively and the scaled Monte-Carlo simulation cross section agree. If the cuts applied depend not too much on jet activity and the event kinematics, this approach is believed to provide a reasonable simulation environment, which allows to study the acceptance for many signatures. In the context of Higgs searches, an example is the decay of Higgs bosons into four leptons, H $\rightarrow$ ZZ $\rightarrow 4\ell$. This signature is not very sensitive to additional jet activities, and it is usually assumed that the search sensitivity depends mainly on signal and background cross sections, the particular detector model and the applied selection criteria. Consequently, a simple scaling of signal and background with the inclusive K-factor, according to the most accurate theoretical prediction, should give reliable results. This assumption has been confirmed in a quantitative study [77].

However, it is not correct to multiply the events with an inclusive K-factor when, in addition to some particle identification, a jet veto has to be applied to separate the signal from backgrounds. This is the case in the H $\rightarrow$ WW $\rightarrow \ell\nu\ell\nu$ channel, which requires a jet veto in order to remove $t\bar{t}$ events. Consequently, we cannot expect that the inclusive K-factors can be used directly and a more careful investigation is needed.
A better approach is thus described in the following Chapters 8,9, where the Monte Carlo output and the perturbative calculation are matched at the differential level [76, 119]. A realistic set of observables has to be chosen, and verified if the reweighted simulation gives a reliable prediction for other observables.

The effects of a jet veto on the K-factor in gg $\rightarrow$H production have been studied in QCD perturbation theory up to NNLO in Ref. [78], where the results were compared with an exact evaluation of the Born cross section. This study showed that the impact of higher-order QCD corrections is reduced by about 40% if a jet veto is applied. However, this comparison did not include jets expected from the parton shower. We found that the impact of higher order QCD corrections is reduced by only 10-15%, instead of 40%, when applied to a parton shower Monte Carlo such as PYTHIA (Chapter 9).

Large higher order corrections are also observed in the nonresonant WW production $qq \rightarrow$

WW. If no cuts are applied, the NLO cross section is up to 70% larger than the LO cross section. It was shown in 1999 that if a jet veto is applied, the cross section impact of higher order QCD corrections is reduced by 40 - 50% [79]. We performed this study with full parton shower simulation, and found that if all cuts are applied in the gg $\rightarrow$ H $\rightarrow$ WW $\rightarrow \ell\nu\ell\nu$ channel (including a jet veto), the total NLO K-factor was only about 15-20 % smaller than the inclusive one (Chapter 9).
The LO calculations of the nonresonant WW production through gluon fusion gg$\rightarrow$WW$\rightarrow$ $\ell\nu\ell\nu$ were recently performed for the first time [80,81]. It was demonstrated that, while the process provides only 5% to the inclusive W-pair production at LHC, it becomes sizeable after a jet veto is applied, and enhances the theoretical WW background estimate for Higgs searches in gg $\rightarrow$ H $\rightarrow$ WW $\rightarrow \ell\nu\ell\nu$ by about 30%. This conclusion resulted from a parton level study. We added parton showering to the parton level program provided by N.Kauer [81], and included it in our analysis (Chapter 11, [82]).
In addition, it was not clear for a long time how the top background should be treated, as the $t\bar{t}$ process contributes to the NLO diagrams of single top production Wtb. Together with J. Campbell, F. Maltoni and S. Willenbrock we came to the conclusion that the two processes can be separated, if a jet veto is applied [83]. Thus, we could include the top background at NLO. This is discussed in Chapter 10.
Chapter 6 describes how different LO Monte Carlo programs treat the production process gg $\rightarrow$ H. The Higgs p_{T} spectrum obtained with different Monte Carlo generators is discussed as well as the efficiency uncertainty resulting from a jet veto. The matrix element calculations of the gg$\rightarrow$H cross section up to NNLO are presented in Chapter 7, and the relevance of the higher order QCD corrections is shown.
The method to include higher order QCD corrections into parton shower Monte Carlos is presented in Chapter 8. The kinematics of the Higgs is basically described by its p_{T} and rapidity η. As we select in the gg $\rightarrow$ H $\rightarrow$ WW $\rightarrow \ell\nu\ell\nu$ analysis mostly central events, where the rapidity distribution is relatively flat, we consider the p_{T} distribution of the Higgs as the most important distribution to describe its kinematics and the kinematics of its decay products. By reweighting each event obtained in a parton shower Monte Carlo with a weight corresponding to the ratio of the higher order p_{T} distribution over the p_{T} distribution obtained with the parton shower MC, the Monte Carlo output is forced to agree with certain observables computed in perturbative QCD. Thus the virtues of both parton shower MCs and exact matrix element calculations are combined in an elegant way. This method was used to estimate effective K-factors and is described in the following chapters. The reweighting method is applied to the gg $\rightarrow$ H $\rightarrow$ WW $\rightarrow \ell\nu\ell\nu$ analysis, and the effective "experimental" K-factor is obtained, in combination with a detailed simulation of cuts for both signal and the nonresonant WW background (Chapter 9).
The effect of taking into account also the rapidity of the Higgs in the reweighting procedure is discussed in Chapter 9. In addition, uncertainties in the predictions of the Higgs p_{T} spectrum can be reduced when reweighting to the most accurate p_{T} spectrum is performed. The remaining uncertainty of the jet veto efficiency due to the use of different Monte Carlo generators can be reduced by a data driven approach, discussed in Chapter 11, where a full detector study of signal and backgrounds is performed.

Chapter 6

Higgs Transverse Momentum Spectrum

6.1 $H \to WW \to \ell\nu\ell\nu$ in Monte Carlo Parton Shower Event Generators

The parton shower Monte Carlo process can be divided into a few Elementary steps: first the calculation of the Matrix Element of the hard scattering, then the application of initial parton showers via the corresponding evolution equations and finally, after the parton shower is applied to the final state, the hadronization. The generated events can thus be treated like data, and cuts can be applied on hadronic final states. In a LO parton shower Monte Carlo model, only LO Matrix Elements are calculated correctly and additional partons emitted in the soft and collinear limit are added. Soft and collinear means that no high p_T particle is produced by the parton showering step. Parton shower Monte Carlos can therefore generate several parton emissions, resulting in one or more soft jets. Parton shower approaches can be tuned with data such that they accurately describe low p_T emission. If a hard emission is required, Matrix Element corrections have to be included in the parton shower generator. Examples for parton shower Monte Carlos are PYTHIA and HERWIG. Depending on the process, both use Matrix Element corrections to describe the high p_T region more accurately.

Let us now consider the $gg \to H \to WW \to \ell\nu\ell\nu$ channel, where gluon fusion $gg \to H$ is the dominant production process. Due to the pure leptonic structure of the final state particles, only initial state gluon radiation occurs in this process (as leptons do not emit additional gluons or quarks), leading to a transverse momentum of the Higgs boson. The decay process can be separated from the production process - and added at the end by simply multiplying the production cross section with the branching ratios of the decaying particles in order to get the total cross section of the process. Thus, in the following, only the $gg \to H$ production process in the parton shower approach is considered; the calculation of the Matrix Elements in gluon fusion $gg \to H$ up to NNLO is discussed in Chapter 7.
A leading order parton shower MC simulation of $gg \to H$ without ME corrections applied looks like this: the hard scattering process consists of the Matrix Element $2 \to 1$ ($gg \to H$). In the hard process at LO, the p_T of the Higgs is zero and the additional energy of the

process goes into the longitudinal momentum of the Higgs. Parton showers are applied now: a gluon can emit another gluon (or a quark), such that g → gg. The total energy of the initial gluon g_1 is split in the energy fraction z, carried by the emitted gluon g_2, and the fraction $(1-z)$, carried away by the remaining gluon g_3. Each of the emissions of an additional parton is characterized by a splitting kernel $P_{1\to 23}(z)$. The branching rate is proportional to the integral $\int P_{1\to 23}(z)dz$. Once formed, the daughters g_2 and g_3 may in turn branch, and so on. The probability for a parton to branch is given by the DGLAP evolution equations [84, 85] in the case of PYTHIA and HERWIG.
Parton showers take only the emitted partons in the soft and collinear limit into account, which means, when $\theta \to 0$ and $p_{\mathrm{T}} \to 0$. Therefore, a parton added in a showering process is soft/collinear and thus the p_{T} of the Higgs boson, which is balanced by the emitted partons, is smaller than m_H.
In the Matrix Element approach, a finite cross section is only obtained because the large positive real and large negative virtual contributions cancel. The LO parton shower approach does not include any full higher-order Matrix Elements with loop corrections and thus the cross sections for the processes would diverge when $p_{\mathrm{T}} \to 0$. A finite result can be obtained by introducing cut-offs, e.g. on z and the angle θ, and subsequent resummation into so-called Sudakov form factors, which are described below.
The relative cross section of the emission of an additional soft/collinear parton from a parton n factorizes as

$$d\sigma_{n+1} = d\sigma_n \alpha_s/2\pi P_{ab}(z)dz\frac{d\cos\theta}{1-\cos\theta}$$

where θ is the angle between the two partons after splitting. The splitting function $P_{ab}(z)$ is the term which is softly divergent when $z \to 0$, while the term including $\cos\theta$ is collinear divergent when $\theta \to 0$.
In the soft and collinear approximation, which means when both $z \to 0$ and $\theta \to 0$, $\cos\theta \sim 1 \pm \frac{\theta^2}{2}$ and $\frac{d\cos\theta}{1-\cos\theta} \approx \frac{d\theta^2}{\theta^2}$, and the term inlcuding z becomes proportional to $\frac{dz}{z}$. Cut-off values for z and θ can then be introduced to avoid singularities and the cross section can thus be written as

$$\sigma \sim \alpha_s/2\pi \; C \int_{z_{min}}^{z_{max}} \frac{dz}{z} \int_{\theta_{min}}^{\theta_{max}} \frac{d\theta^2}{\theta^2}, \tag{6.1}$$

with C being a constant term that does not depend on z or θ. The relative cross section is then proportional to two large logarthimic terms L, $\sigma \sim \alpha_s L^2$. This is also called the leading log term, "LL". In parton showers, many gluons are emitted. Thus, LL means all terms proportional to $\alpha_s^n L^{2n}$.
In the soft or collinear case,

$$\sigma \sim \alpha_s/2\pi \; K_z \int_{\theta_{min}}^{\theta_{max}} \tag{6.2}$$

or

$$\sigma \sim \alpha_s/2\pi \int_{z_{min}}^{z_{max}} \frac{dz}{z} \; K_\theta. \tag{6.3}$$

The term is then proportional to $\alpha_s L$, which is called next-to-leading log NLL. NLL is proportional to $\alpha_S^n L^{2n-1}$, NNLL proportional to $\alpha_s L^{2n-2}$ etc. PYTHIA and HERWIG include all LL terms and some NLL terms.
Now, if cut-offs are included to avoid singularities, what happens with the contributions of the terms below these cut-offs and the virtual terms? The terms with branchings below the cut-off (i.e. with very small z or θ) are called unresolvable, as the emitted parton is too soft to be detected. Both the virtual and unresolvable real contributions are divergent and need thus to be considered.
Unitarity requires that the parts which are not taken into account and the resolved parts add up to unity. Using this approach, the real emission part above the cut-off values can be used to get the remaining contributions from the unresolved and virtual terms:

$$\text{Remaining Terms} = 1 - \text{Resolved Terms}$$

$$= 1 - \alpha_s \int_{q^2}^{Q^2} \frac{dk^2}{k^2} \int_{Q_0^2/q^2}^{1-Q_0^2/q^2} dz \frac{1}{2\pi} P_{ab}(z) \tag{6.4}$$

$$= exp(-\alpha_s \int_{q^2}^{Q^2} \frac{dk^2}{k^2} \int_{Q_0^2/q^2}^{1-Q_0^2/q^2} dz \frac{1}{2\pi} P_{ab}(z)).$$

where Q is the virtuality of the parton and q the scale of the next branching. This exponential factor is called the Sudakov form factor. The system can undergo an arbitrary number of emissions (branchings) with probability controlled by this Sudakov form factor. At fixed z, this probability factor tends to 1 when α_s goes to 0, that is, no emission is possible in the zero coupling limit. On the other hand, when $\alpha_s \to \infty$, the Sudakov form factor goes to 0, which means that it is impossible for the system not to emit a parton. The Sudakov form factor can thus be interpreted as the probability of evolving between two scales without any resolvable radiation. The No-branching probability is the sum of virtual and unresolvable real contributions, both are divergent, but their sum is finite, and thus a finite result is obtained. The total cross section in LO parton shower MC programs such as PYTHIA and HERWIG is the LO cross sections.
The key difference between the different MC simulations lies in the choice of the evolution variable. For the evolution scale, either the virtuality, Q^2, the transverse momentum p_{T}, or the angle θ is usually chosen. All are the same in the collinear limit.
HERWIG and PYTHIA model the parton shower in different ways. In HERWIG the shower is strictly angular ordered, where the angle between emitted partons is smaller at each branching. PYTHIA applies the collinear algorithm with a cascade ordered according to the virtuality Q^2. A veto on the angle of the parton is then applied to reproduce the effect of the angular ordered shower. The evolution variable Q^2 of the PYTHIA cascade has traditionally been associated with the m^2 of the branching parton. The choice is not unique, and from PYTHIA version 6.3 onwards, a p_{T}-ordered showering with $Q^2 = p_T^2 = z(1-z)m^2$ is available instead of the mass-ordered one. As in the p_{T}-ordered showering model highest p_{T} emissions are chosen first, this model favors high p_{T} jets.
The high p_{T} region, which is not covered by this approximation is taken into account by

applying (NLO) Matrix Element corrections. In addition to the LO $2 \to 1$ ($gg \to H$) Matrix Element, also some Matrix Elements with real emissions $2 \to 2$ (e.g. when one extra gluon or quark is emitted in the initial state) are then taken into account. Examples are $gg \to Hg$, $qg \to Hq$ and $gq \to Hg$. Note that the extra gluon can now be emitted with high p_T and at large angle. Still, in a LO parton shower MC the cross section is the LO Matrix Element cross section.
The hadronization step is simulated by the string (also called Lund-) model in PYTHIA and the cluster model in HERWIG.
In MC@NLO, the hard scattering part is always given at NLO. Thus, there is in addition to the Born level ($2 \to 1$ process), real gluon radiation ($2 \to 2$) and virtual radiation (loops). When real gluons are emitted, the p_T of the additional gluon can be large, balancing the p_T Higgs. MC@NLO is matched to HERWIG for the parton showering and hadronization. The total cross section is normalized to NLO predictions. So far, the $gg \to H \to WW \to \ell\nu\ell\nu$ channel is not correctly included in MC@NLO, as the spin correlations are not described consistently.

6.2 Comparison of Monte Carlo Event Generators

In this section the Higgs p_T spectra in different Monte Carlo predictions are compared. The way parton showers are implemented affects the emission of soft gluons in the gluon fusion production $gg \to H$, and therefore both the transverse momentum of the produced Higgs, as well as the p_T of the balancing jets.
The jet veto is crucial to reduce the top background in the $H \to WW \to \ell\nu\ell\nu$ channel. The jet veto efficiency is therefore studied in the different Monte Carlo generators. In detail the following MCs using parton shower models are discussed by comparing PYTHIA 6.319[1] and HERWIG 6.507, and the comparison with MC@NLO (version 2.31) leads to an estimate of the higher-order effect uncertainty. In addition, CASCADE 2.009 [86] is also studied where we compare the DGLAP approach to the CCFM formalism [87, 88].
CASCADE is a full hadron level Monte Carlo event generator for $e-p$, $\gamma-p$, $p-p$ and $p-\bar{p}$ processes, which uses the CCFM evolution equation for the initial state cascade in a backward evolution approach supplemented with off-shell Matrix Elements for the hard scattering. CASCADE was used for the low-x F_2 data and forward jet data from HERA, and became recently available for pp scattering processes. Until now, CASCADE only includes gluon chains in the initial state cascade. Different sets of unintegrated gluon densities are available, which all describe HERA data equally well [86]. This comparison is the first one where different MCs are compared to CASCADE for Higgs production at the LHC. One has to keep in mind that this Monte Carlo is dedicated to low-x physics. It is still questionable if the unintegrated gluon densities are applicable for Higgs production.
In the parton cascade as implemented in e.g. PYTHIA, the parton emissions are calculated using the DGLAP approach, with the partons ordered in virtuality. DGLAP accurately describes high-energy collisions of particles at moderate values of the Bjorken-x by resummation of the leading log terms of transverse momenta. In the CCFM formalism there is no strict ordering along the parton ladder in transverse energy, contrary to the DGLAP

[1] The number is the Monte Carlo version used for the analysis.

formalism. CCFM is expected to provide a better description of the gluon evolution at very low values of x compared to DGLAP, as it also takes leading-logs of longitudinal momenta $((\alpha_s \ln x)^n)$ into account.
PYTHIA, HERWIG and MC@NLO treat the high p_{T} region in different ways: PYTHIA includes Matrix Element corrections in the $m_{top} \to \infty$ limit, whereas HERWIG has so far no hard Matrix Element corrections included in gg $\to$ H. MC@NLO includes the NLO Matrix Elements in an exact way.
For PYTHIA, two different samples were generated for the comparison: One with the default Q^2-ordered showering model and one with the new p_{T}-ordered showering model. Comparisons are made with the default Q^2-ordered showering and then also the new p_{T}- ordered showering model is considered. If not stated differently, the Q^2-ordered shower is meant. In the following, the LO PDF set CTEQ5L is used in HERWIG and PYTHIA, and the corresponding NLO set CTEQ5M in MC@NLO.
For this study, jets are reconstructed using an Iterative Cone Algorithm with Cone Size 0.5. The leading particle (seed) of the jet has to have a p_{T} higher than 1 GeV. The $|\eta|$ of the jet should be smaller than 4.5 (approximating the expected CMS/ATLAS detector acceptance [32, 33]). An event is rejected if it contains a jet with a p_{T} higher than 30 GeV. The Higgs mass for this study is set to 165 GeV. The top mass is set to 175 GeV. First, all events are studied without considering the underlying event. PYTHIA is also studied including different underlying event schemes. Different predictions of these programs for the high part of the transverse momentum spectrum of the Higgs will also be described and compared. More details about this study can be found in [89] and [82].

6.3 Higgs Transverse Momentum Spectrum Comparison

At leading order, the transverse momentum of the Higgs boson, $p_{\mathrm{T}}^{\mathrm{H}}$, is zero. However, parton shower Monte Carlos emit soft gluons which balance the Higgs and introduce a transverse momentum in LO parton shower Monte Carlos. As the Higgs is balanced by jets, the transverse momentum is very sensitive to the jet p_{T} and in turn also the efficiency of a jet veto dependends strongly on $p_{\mathrm{T}}^{\mathrm{H}}$. In Figure 6.1, the normalized $p_{\mathrm{T}}^{\mathrm{H}}$ spectra are shown for PYTHIA, HERWIG and MC@NLO. HERWIG and MC@NLO are similar at low p_{T}, as can be seen in Figure 6.1(left) with linear scale. This can be expected as the soft and collinear emissions (describing the low p_{T} region) of MC@NLO are treated by HERWIG. PYTHIA has a softer p_{T} Higgs spectrum than HERWIG, because of the way jets are generated in the different MCs. HERWIG implements angular ordering exactly and thus correctly sums the LL (Leading Log) and part of the $\mathrm{N^kLL}$ contributions.
In Figure 6.1(right), the high p_{T} region is shown. MC@NLO correctly treats the hard radiation up to NLO, combining the high p_{T} spectrum with the soft radiation of HERWIG. As PYTHIA includes hard Matrix Element corrections, PYTHIA looks similar to MC@NLO at high p_{T}. On the other hand one can see that the spectrum predicted by HERWIG drops rather quickly. This is because the current version of HERWIG does not treat hard radiation corrections and thus underestimates the high p_{T} region. In Figure 6.2, the efficiency of the jet veto is shown for the three different Monte Carlos as a function of $p_{\mathrm{T}}^{\mathrm{H}}$. One observes a strong dependence of $p_{\mathrm{T}}^{\mathrm{H}}$ on the jet veto. Once a jet veto is defined, the efficiency starts

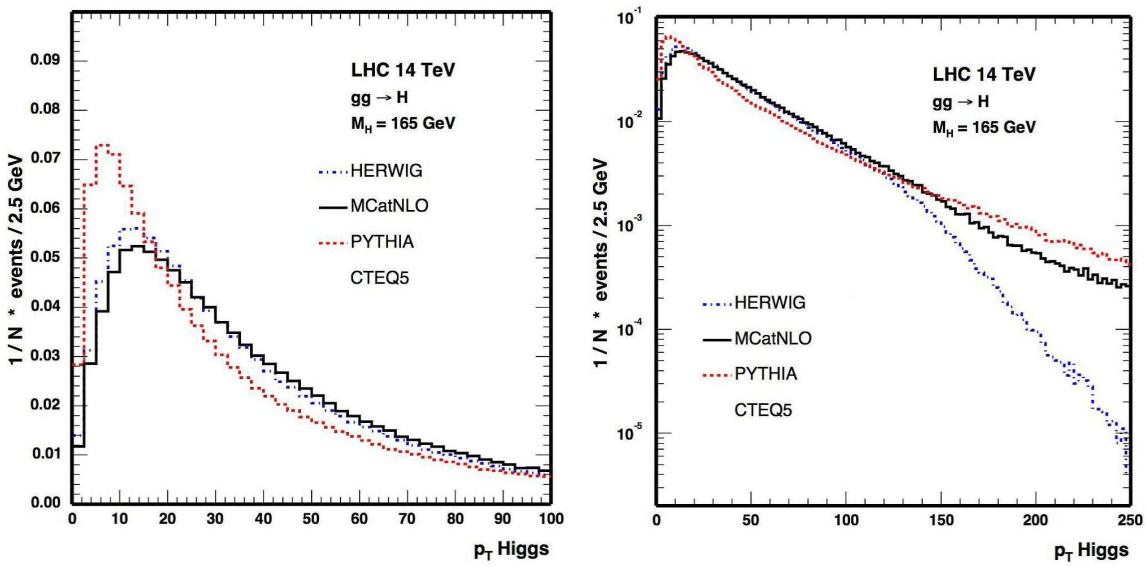

Figure 6.1: $p_{\mathrm{T}}^{\mathrm{H}}$ spectra for PYTHIA, HERWIG and MC@NLO in linear and logarithmic scale.

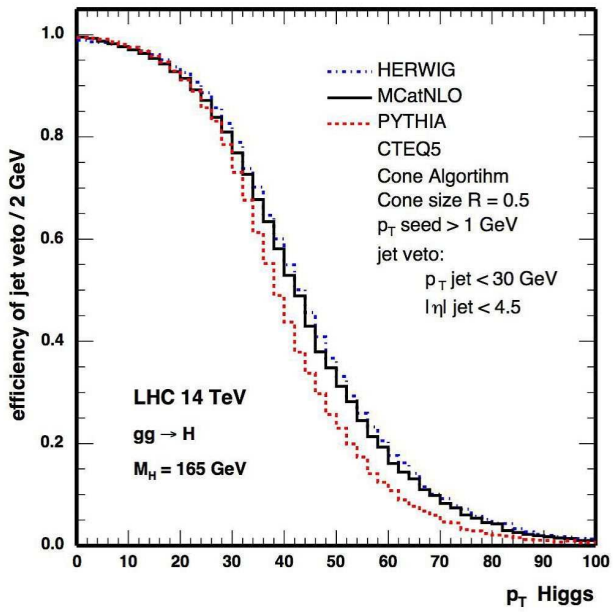

Figure 6.2: Efficiency of the jet veto of 30 GeV as a function of p_{T} Higgs. The other selection cuts favour also the low p_{T} Higgs region.

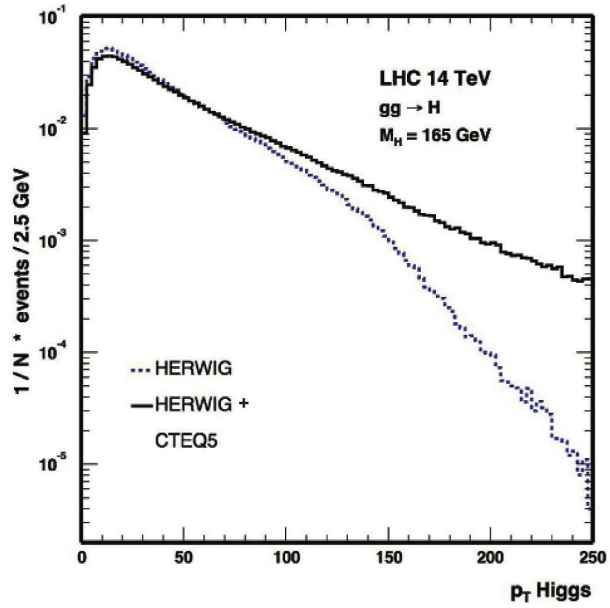

Figure 6.3: HERWIG with and without hard Matrix Element corrections, logarithmic scale, "+" means "with Matrix Element corrections".

to drop quickly as soon as $p_{\mathrm{T}}^{\mathrm{H}}$ is close to the p_{T} used to define a jet veto. However, as the transverse momentum of the Higgs can be balanced by more than one jet, the efficiency is not zero above this value. At low p_{T} Higgs, the efficiencies of the jet veto are remarkably identical.

G. Corcella provided a preliminary version of HERWIG including hard Matrix Element corrections for gg → H [90]. The high p_{T} Higgs spectrum looks now similar in PYTHIA and HERWIG. The Matrix Element corrections lead to harder jets, as illustrated in Figure 6.3. When applying a jet veto, more events are rejected and the jet veto is therefore more effective than in the version without ME corrections.

Table 6.1 shows the efficiencies of the jet veto of 30 GeV for MC@NLO, PYTHIA and HERWIG with and without Matrix Element corrections, and CASCADE, which will be discussed in 6.3.5. In the second column, the number of the efficiency for $p_{\mathrm{T}}^{\mathrm{H}}$ between 0 and 80 GeV is shown. The third column shows the inclusive efficiency for all events. The efficiency is thus defined as the ratio $\epsilon = \frac{\mathrm{N_{jv}}}{\mathrm{N}}$ in the exclusive case and $\epsilon = \frac{\mathrm{N_{jv}(0< p_T^H <80\ GeV)}}{\mathrm{N(0< p_T^H <80\ GeV)}}$ in the region with a p_{T} Higgs between 0 and 80 GeV. $\mathrm{N_{jv}}$ is the number of remaining events after the jet veto is applied. One has to keep in mind that after all selection cuts are applied, only Higgs events in the low p_{T} region are important [76].

	Efficiency for events with a $p_{\mathrm{T}}^{\mathrm{H}}$ between 0 and 80 GeV	Efficiency for all events (no restriction on $p_{\mathrm{T}}^{\mathrm{H}}$)
MC@NLO	0.69	0.58
PYTHIA, Q^2-ordered	0.73	0.62
PYTHIA, p_{T}-ordered	0.68	0.53
HERWIG	0.70	0.63
HERWIG + ME Corr.	0.68	0.54
CASCADE	0.65	0.55

Table 6.1: Efficiency of the jet veto for MC@NLO, PYTHIA with Q^2- and p_{T}-ordered shower models, HERWIG with and without ME corrections, and CASCADE.

6.3.1 Including Jet Energy Resolution

In order to estimate the effect from the detector resolution on the jet veto, the E_T of the jet is smeared with the jet resolution of CMS, as given by [91]:

$$\Delta E_T/E_T = 120\%/\sqrt{E_T} + 5\%. \tag{6.5}$$

When the jet resolution is taken into account, normally more low p_{T} jets are shifted to higher p_{T} than vice versa, as the p_{T} distribution of the jets decreases when going to higher p_{T}. Thus, one can expect that now more events are rejected. Note that there is also a minimum cut-off at a p_{T} of 20 GeV, below which the particles are not considered as a jet. On this boarder, including the resolution will also move low p_{T} particles to higher ones (and vice versa). However, as the lower cut is at 20 GeV and the jet veto applied at 30 GeV, it should not have an effect on the jet veto efficiency. The resulting effect on the jet veto efficiency with or without jet resolution is smaller than 1 % .

6.3.2 Effect of the Underlying Event

	Efficiency for events with a $p_{\mathrm{T}}^{\mathrm{H}}$ between 0 and 80 GeV	Efficiency for all events (no restriction on $p_{\mathrm{T}}^{\mathrm{H}}$)
PYTHIA no UE	0.73	0.62
PYTHIA default	0.72	0.61
ATLAS tune	0.71	0.60
CDF tune	0.71	0.60

Table 6.2: Efficiency numbers for different underlying event tunings in PYTHIA.

So far all events were generated without considering the underlying event. However, to study a jet veto, it is important to consider also this effect. Therefore, we study PYTHIA with

different underlying event tuning schemes, which are the ATLAS Tune [92], CDF Tune A [93] and PYTHIA default (MSTP(81)=1, MSTP(82)=3 [74]). The different tunings lead to approximately the same efficiency. The difference in the efficiency with and without underlying event is smaller than 1% (Table 6.2).

6.3.3 Comparing Q^2- and p_T-ordered showering in PYTHIA

We consider the recently developed p_T-ordered showering model in PYTHIA. Note that the underlying event is not taken into account here. In Figure 6.4(left), the p_T Higgs distribution for the two different models is shown and in Figure 6.4(right) the same distribution for the p_T-ordered showering in PYTHIA, MC@NLO and HERWIG with ME corrections, in logarithmic scale. In Figure 6.5(left) this p_T Higgs distribution is shown in linear scale and

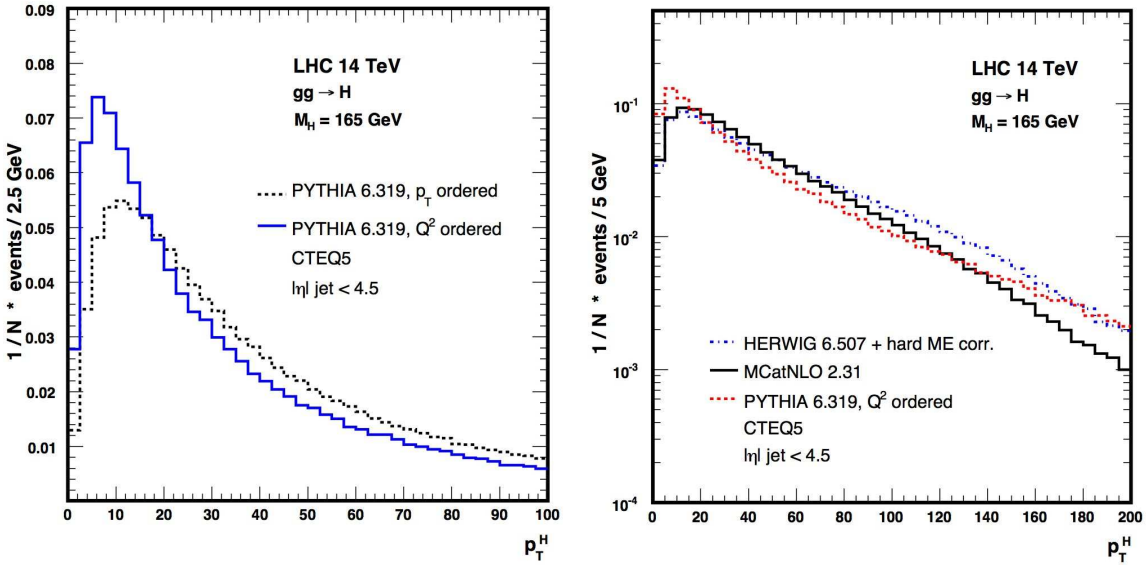

Figure 6.4: (left) The p_T Higgs spectrum for the default Q^2-ordered and the new p_T-ordered showering models is shown. (right) The p_T Higgs spectrum for HERWIG with Matrix Element corrections in comparison with PYTHIA (Q^2 ordered showering) and MC@NLO.

in Figure 6.5(right) the jet veto efficiency is plotted. As the p_T-ordered showering model favors high p_T jets (compared to the Q^2-ordered showering model), PYTHIA and HERWIG look now similar also in the low p_T region and the efficiency uncertainty of the jet veto is reduced. The efficiencies when applying a jet veto of 30 GeV are listed in Table 6.1. One can see that in the region important for the Higgs search in the WW channel (second row), the difference between the new p_T-ordered PYTHIA version, HERWIG with Matrix Element corrections, and MC@NLO has decreased to about 1%. The overall uncertainty between all these different simulations (HERWIG with and without hard Matrix Element corrections, PYTHIA with different showering models, and MC@NLO) is thus about 10%.

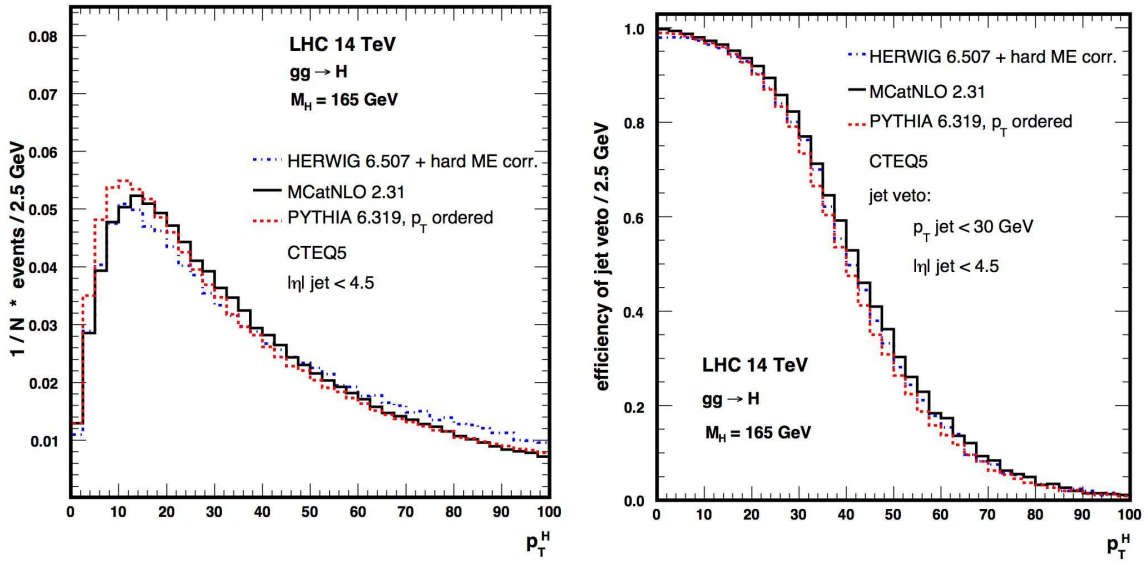

Figure 6.5: p_{T} Higgs distribution and efficiency after a jet veto is applied for HERWIG with Matrix Element corrections, PYTHIA with new p_{T} -ordered shower model and MC@NLO.

6.3.4 MC@NLO: Effect of Varying the Factorization and Renormalization Scale

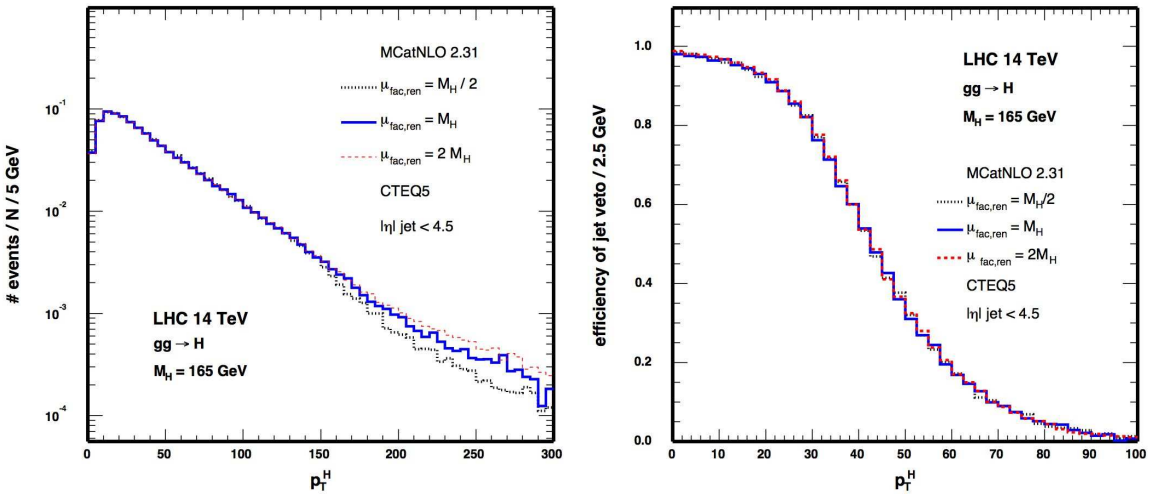

Figure 6.6: Number of events and efficiency after a jet veto 30 GeV is applied for MC@NLO with different scale choices.

To get an estimate of the uncertainty due to different factorization and renormalization

	Efficiency for events with a p_T^H between 0 and 80 GeV	Efficiency for all events (no restriction on p_T^H)
$\mu_{fac,rec} = m_H/2$	0.69	0.59
$\mu_{fac,rec} = m_H$	0.69	0.58
$\mu_{fac,rec} = 2m_H$	0.69	0.58

Table 6.3: Efficiency of the jet veto for MC@NLO with different scale choices.

scales, three MC@NLO samples were produced with scales $\mu_{fac,rec}$ between $m_H/2$ and $2m_H$[2]. In Figure 6.6(left), the p_T Higgs spectrum and in Figure 6.6(right) the efficiency of a jet veto at 30 GeV are shown for these three samples. The only difference is at very high p_T, whereas the bulk of the events is at low p_T. Therefore, as can be seen also in Table 6.3, the effect of different scales on the jet veto efficiency is negligible in MC@NLO.

6.3.5 DGLAP versus CCFM

Now we compare PYTHIA, HERWIG and MC@NLO with CASCADE. In Figure 6.7, the p_T^H spectra for PYTHIA, HERWIG+ME corrections, MC@NLO and CASCADE are shown. The prediction from CASCADE lies within the ones from PYTHIA and HERWIG. When looking at different p_T regions, one generally observes that CASCADE produces more jets compared to the other Monte Carlos, and that the jets are harder. The main difference

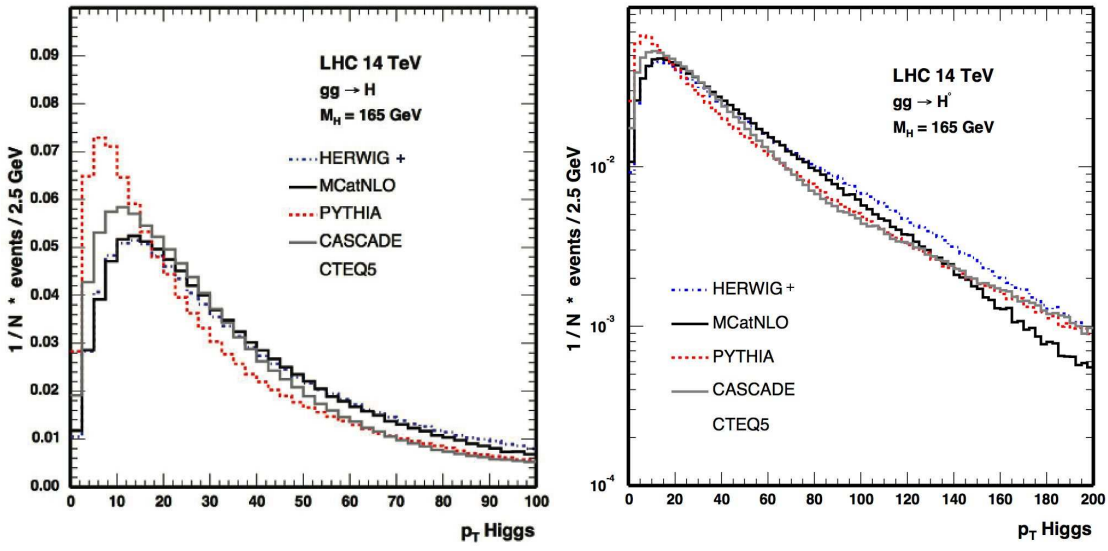

Figure 6.7: p_T Higgs of PYTHIA, HERWIG + ME corrections, MC@NLO and CASCADE, linear and logarithmic scale.

[2]This method is described in more detail in Section 7.4.

between the three MCs and CASCADE in the jet veto efficiency lies in the low p_{T} range. The efficiency of the jet veto in CASCADE is slightly lower than the others (which are equal) in the low p_{T} region. A reason for this is that in the low p_{T} Higgs region, the Higgs boson is balanced by more than one jet, with at least one of the jets with a p_{T} higher than 30 GeV and thus vetoed. For the same reason, the efficiency in general is lower than for the other Monte Carlo programs at low $p_{\mathrm{T}}^{\mathrm{H}}$.
As can be seen in Table 6.1 , the overall uncertainty of the jet veto efficiency between those parton shower Monte Carlos is thus about 10%. The question is now if this 10% uncertainty can be reduced. It will be shown in chapter 11, that this can be done by estimating the jet energy scale in a data driven approach. The uncertainty in the p_{T} Higgs spectrum due to the different MC predictions is reduced in an elegant way when reweighting is performed, as all spectrums are matched to the most accurate one calculated in higher order QCD.

Chapter 7

Higgs Production in the Gluon Fusion Channel: Matrix Element Calculations

The theoretical understanding of Higgs couplings and decays has been established during the last decades. Motivated by the need to include higher order QCD corrections, e.g. demonstrated in the Drell-Yan process, higher order QCD corrections were calculated in the Higgs sector and found to be especially large in the Higgs production channel through gluon fusion. Theoretical NNLO calculations for gluon fusion are now well under theoretical control and exhibit nicely converging perturbative series and small dependence on the renormalization and factorization scale. A recent study has shown that N^{3}LO[1] calculations change the NNLO result by less than 5% [94]. These computations made it clear that accurate calculations of the Higgs boson cross section and its backgrounds need to be completed. Therefore it is also necessary to account for such higher order corrections in a realistic analysis. However, the calculations for the backgrounds are far less advanced than for the signal and data driven methods will be needed to get an estimate on the background systematics. In the following, the higher order QCD corrections for the gg $\rightarrow$ H signal are discussed. Chapter 8 then describes how those higher order corrections can be included in Monte Carlo Event Generator studies, and Chapter 11 describes how the backgrounds can be estimated from data.

7.1 Higgs Production through Gluon Fusion

Gluon fusion is the dominant production channel for Higgs bosons at the LHC. The coupling of the gluons to the Higgs boson is mediated by a heavy quark triangle, dominated by top quarks, such that the Feynman diagram to lowest order is given by the left diagram in Figure 7.1. The Higgs boson interaction with gluons is a loop-induced process and therefore sensitive to all coloured particles. In most of the calculations only the heavy top quark mass is taken into account [2]. In the beginning of the 1990's, the NLO corrections to gluon fusion

[1] N^{3}LO means next-to-next-to-next-to leading order.

[2] Note that in non-SM scenarios, the Higgs coupling to the bottom quark may be enhanced and thus bottom-quark fusion can then become the largest source of Higgs production.

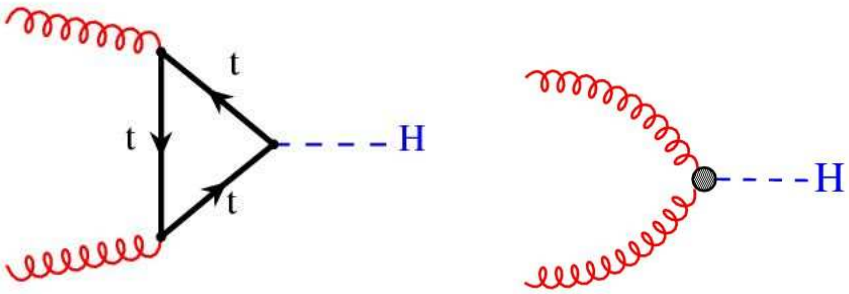

Figure 7.1: Lowest order contribution to gg → H in full QCD (left) and in the effective theory (right) [97].

were calculated by A. Djouadi et al. [95] and by S. Dawson [96]. These NLO corrections turned out to be very large, namely about 70-100%, depending on the Higgs boson mass. The magnitude of the next to leading order terms was one of the main motivations to evaluate the second order corrections. In this process, some problems were faced, the first of them being the large amount of matrix elements which have to be calculated, as well as some technical and mathematical problems in the process, e.g. the treatment of infinite terms. As higher order calculations are difficult to carry out, good approximations are needed to facilitate the calculations. NNLO calculations were only finished in the last years. We summarize in the following how higher order corrections in the gluon fusion channel were obtained.
Although the Born cross section is known as a function of the top mass m_t and the Higgs mass m_H, it is hard to obtain the exact analytic dependence of the cross section on the mass of the top quark in higher orders of perturbative theory. In order to simplify the calculations in a reasonable way, this coupling is usually approximated by an effective Lagrangian corresponding to the limit $m_t \to \infty$, which is valid for a large Higgs mass range, including the currently favoured region between 100 and 200 GeV. Using this large-m_t approach, the contribution of the heavy quark loop is embodied by an effective vertex, thus reducing by one the number of loop integrals to be explicitely carried out.
Using this effective interaction, the lowest order contribution is a tree level diagram, shown on the right hand side of Figure 7.1. The cross section can then be computed via the following effective Lagrangian

$$L^{eff}_{ggH} = -\frac{1}{4v} C(\alpha_s) G^a_{\mu\nu} G^{\mu\nu}_a H, \tag{7.1}$$

with $v \approx 246$ GeV the vacuum expectation value of the Higgs field, $G^a_{\mu\nu}$ the field strength of the SU(3) color gluon field and H the Higgs boson field. In the large-m_t limit, the interactions inside the top loop happen in a short time scale $\propto \frac{1}{2m_t}$ and can be computed into the Wilson Coefficients $C(\alpha_s)$. The interactions between the gluons and the Higgs, which happen at a slower timescale $\propto \frac{1}{m_H}$, are accounted for in the second part of the term, $G^a_{\mu\nu} G^{\mu\nu}_a$ H, representing the interactions of the gluons and the Higgs field. Thus the effective Lagrangian can be used as an approximation as long as $m_H \ll 2m_t$.

The validity of the heavy top mass approximation was checked by comparing LO and NLO results for the effective and exact Lagrangian. Provided the exact dependence on m_H/m_t is included in the LO term, the effective Lagrangian does agree at NLO within 5% with the full calculation below the top threshold, and was found to agree within 10% for Higgs masses as large as 1 TeV [95]. This is shown in Figure 7.2, where the two approaches at NLO are compared. The K-factor given in this Figure is the ratio of the NLO cross section over the LO cross section. It is assumed that the heavy top mass limit continues to be a good approximation at NNLO. In order to improve the heavy top approximation, the cross section can be normalized to the exact Born cross section with the full m_t dependence.

At NLO, there are two classes of correction: real contributions (all Feynman diagrams with

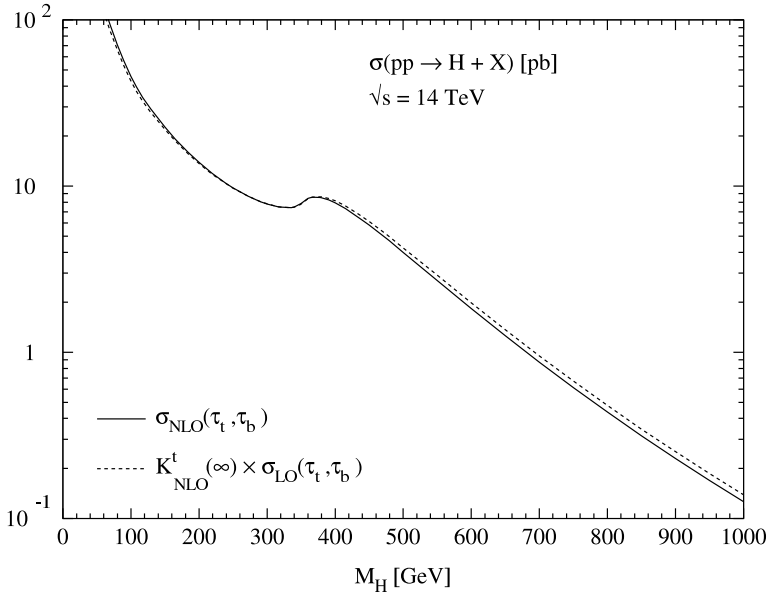

Figure 7.2: Comparison of the exact and approximate NLO cross section for gluon fusion at LHC. The solid line shows the exact cross section including full t, b quark mass dependence, the dashed line corresponds to the analytic expression in the heavy quark limit, represented here as the exact LO cross section multiplied by the K-factor which was calculated in the heavy top limit [95].

an additional (wrt Born) parton in the final state) and virtual contributions (all one-loop feynman diagrams that can be obtained from Born diagrams). The real and virtual corrections do not interfere, as the diagrams have different numbers of legs. The real contributions lead to an infinite term, as the matrix elements are divergent, due to the soft and collinear gluon emissions. Collinear means that the p_{T} of the additional emitted parton goes to zero, while in the soft limit, x, defined by $\hat{s} = x_1 x_2 s \equiv m_H^2/x$, goes to 1 and thus the partonic center-of-mass energy $\hat{s}$ gets close to the Higgs mass.

The virtual corrections lead to a divergent result (minus infinity) in perturbative theory. By

regularizing and summing up virtual and real contributions term by term one gets to a finite result. This was generalized in the Kinoshita-Lee-Nauenberg (KLN) theorem [**?**], which states that in the computation of inclusive quantities, infrared divergences cancel and the result is finite. At NNLO, however, no general algorithm was found to cancel divergences as in the NLO case. NNLO calculations were performed for Higgs and Drell-Yan processes, but are generally difficult to extend to arbitrary large multiplicities.

At NNLO, three kinds of matrix element corrections have to be taken into account in addition to the Born matrix element: virtual, single and double real emissions. Examples of single and double real emission diagrams are shown in Figure 7.3.
The first step towards the full calculation was the evaluation of the virtual two-loop corrections, first calculated by Harlander and Kilgore [97]; a sample is shown in Figure 7.4.
The main obstacle in performing the full NNLO calculation turned out to be the phase

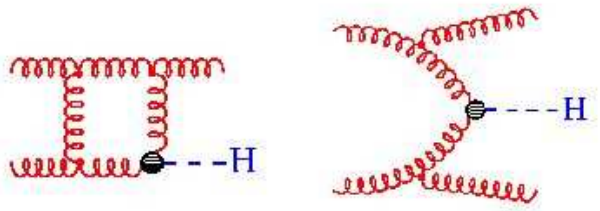

Figure 7.3: Examples of diagrams for single (left) and double (right) real emissions in the gluon fusion process [97].

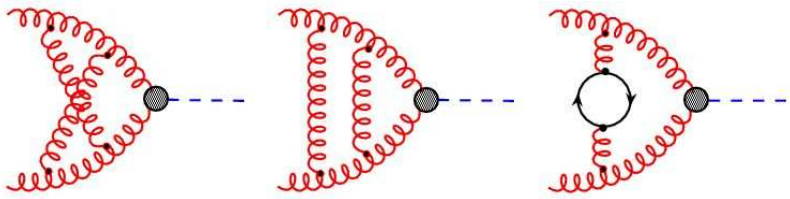

Figure 7.4: Examples of two-loop diagrams contributing to the gluon fusion process [97].

space integration of the double real emission contribution. A similar calculation had been performed only once up to now, namely the NNLO Drell-Yan calculation by R. Hamberg et al. [98]. However, the integrals simplify drastically if one expands the double real emission integrals as power series around the soft limit, which is the limit at which the partonic center of mass enery $\sqrt{\hat{s}}$ gets equal to the mass of the Higgs ($m_H^2 \approx \hat{s}$).
In combination with the virtual contributions, this leads then to an infrared finite result. This calculation has been performed by two groups: R.Harlander and W. Kilgore [99], and S. Catani, D. de Florian, and M. Grazzini [100], based on the principle to extract contributions to the partonic cross section that are singular in the soft limit.

Subsequently, Harlander and Kilgore [101] performed an expansion around the soft limit which reached very high accuracy. C. Anastasiou and K. Melnikov [102] calculated then the full analytic result for the NNLO corrections to the Higgs boson production. In their approach, no expansion around a special kinematic point was needed and therefore, expressions are valid for an arbitrary ratio $m_H^2/\hat{s}$. These results confirmed the calculations of [101].

The contributions from expansions around the soft limit are the dominant ones when calculating the total cross section. Thus, it is instructive to look at this expansion in more detail (Refs. [99–101]). In the soft limit and heavy top mass approximation, the partonic cross section can be described in a form where the virtual corrections, single real emission and the effects of mass factorization are computed in closed analytic form and the double real emission in the form of power series. The closed analytic form can also be expressed as power series, such that the full partonic cross section can be described as an expansion in (1-x) and ln(1-x):

$$\hat{\sigma}_{ij} = \sum_{n\geq 0} (\frac{\alpha_s}{\pi})^n \hat{\sigma_{ij}}^{(n)}, \tag{7.2}$$

$$\hat{\sigma}_{ij}^{(n)} = a^{(n)}\delta(1-x) + \sum_{k=0}^{2n-1} b_k^{(n)} \left[\frac{ln^k(1-x)}{1-x}\right]_+ + \sum_{l=0}^{\infty}\sum_{k=0}^{2n-1} c_{lk}^{(n)}(1-x)^l ln^k(1-x)$$

where the second term including b_k are so-called "+ distributions" [3]. If all coefficients are computed, this is an exact expression for the partonic cross section. In practice, only a finite number of terms can be computed. In this approximation, the major contribution to the partonic cross section originates from the soft and virtual terms. Hard contributions, which are present in all partonic channels, lead to finite corrections in the limit $x \to 1$. The terms proportional to the distributions $[(ln^i(1-x))/1-x]_+$ and $\delta(1-x)$ define the so-called soft-virtual (SV) approximation. These are the most singular terms when $x \to 1$. It was stated by M.Kramer, E.Laenen, and M.Spira in 1998 [103] that the $a^{(2)}$ and $b_k^{(2)}$ terms are not sufficient to arrive at a reliable prediction for the total cross section. They showed that the subleading terms c_{03}, which are proportional to $ln^3(1-x)$, are numerically important. The coefficient $c_{03}^{(2)}$ at NNLO was then evaluated, using resummation techniques [103]. The unknown sub-leading terms $c_{0i}^{(2)}$ with $i \leqslant 2$ were treated in different ways in [100] and [101], leading to significant deviations in the numerical results. Harlander and Kilgore [99] and Catani, de Florian and Grazzini [100] showed, that the NLO-SV approximation tends to underestimate the exact result by about 15 %, while the NLO-SVC approximation, which in addition includes collinear terms c_{0k} with k up to 3, only slightly overestimates it, showing the importance of the term $ln(1-x)$, added in the SVC approximation. In Figure 7.5 the K-factors for these approaches are shown, defined as the ratio of the higher order cross section over the LO cross section. On the left there are the K-factors obtained with the SV and SVC results in NLO. One can see that all the NLO results agree within the theoretical bands, which confirms the validity of the soft approximation to estimate higher order corrections. The right-hand side of Figure 7.5 shows the SV and SVC results at NNLO. As in the NLO

[3] A "+ distribution" is defined like this: $\int_0^1 dx\ [\frac{f(x)}{1-x}]_+\ h(x) = \int_0^1 dx\ f(x)[\frac{h(x)-h(1)}{1-x}]$.

case, the SVC band sits higher than the SV one. Indeed, the true NNLO correction is even a bit smaller than predicted by the SVC approximation. Nonetheless it verifies that the SVC is a good approximation of the total cross section. The ratio of the corresponding cross sections SVC over SV is almost the same as the one at NLO, as shown in the inset plots [104].

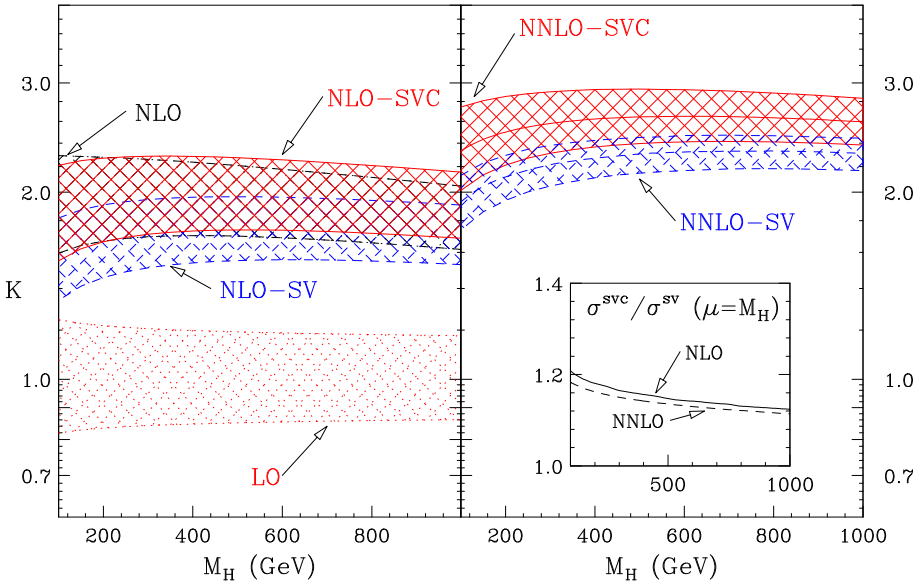

Figure 7.5: K-factors of the exact NLO result, NLO-SV and NLO-SVC approximations on the left and of the NNLO-SV and NNLO-SVC approximations on the right [104].

In the next step, Harlander and Kilgore reported on the analytical evaluation of the coefficients $c_{lk}^{(2)}$, k=0,..,3 and l $\geqslant$ 0 as an expansion around the soft limit. They computed all coefficients $c_{lk}^{(2)}$ through l=16. In Figure 7.6 the rapid convergence of the power series expansion in (1-x) is shown. One can see that the purely soft contributions underestimate the cross section by $\backsim$ 10% − 15%, while the next term, which is proportional to $(1-x)^0$, overestimates it by about 5%. By the time the third term in the series, proportional to $(1-x)^1$ is included, one is within 1 % of the result obtained by computing the first 18 terms (through $(1-x)^{16}$) [101]. With this calculation, the ambiguities of Ref. [100] and [101] were resolved and a realistic prediction for the Higgs production cross section for pp (and p$\bar{\text{p}}$) collisions found. This method was succesfully tested by applying it to the Drell-Yan process at NNLO, where the full x-dependence is known in analytical form [98].
The cross sections $\sigma(pp \to \text{H} \to X)$ at LO, NLO and NNLO, are shown in Figure 7.7 at the LHC as a function of the Higgs mass, using the MRST parton distributions at the given order. The factorization and renormalization scales are set to $\mu_R = \mu_F = \frac{1}{2}m_H$ (upper curves) and $\mu_R = \mu_F = 2m_H$ (lower curves). To improve the heavy quark approximation, the LO cross section contains the full top mass dependence, with m_t = 175 GeV. Considering first the relative magnitude of the cross sections at the different orders of perturbation theory, one can see that while from LO to NLO, the cross section increases at the LHC by 70%

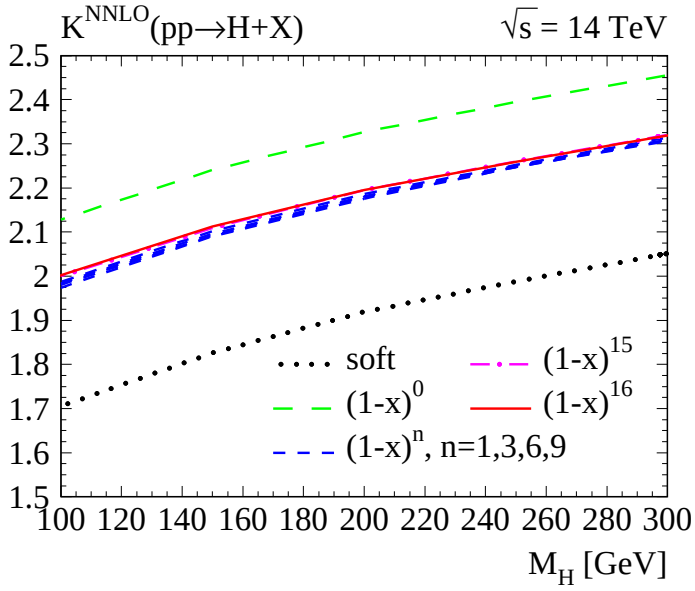

Figure 7.6: K-factor for Higgs production at the LHC. Each line corresponds to a different order in the expansion in (1-x). The renormalization and factorization scales are set to m_H.

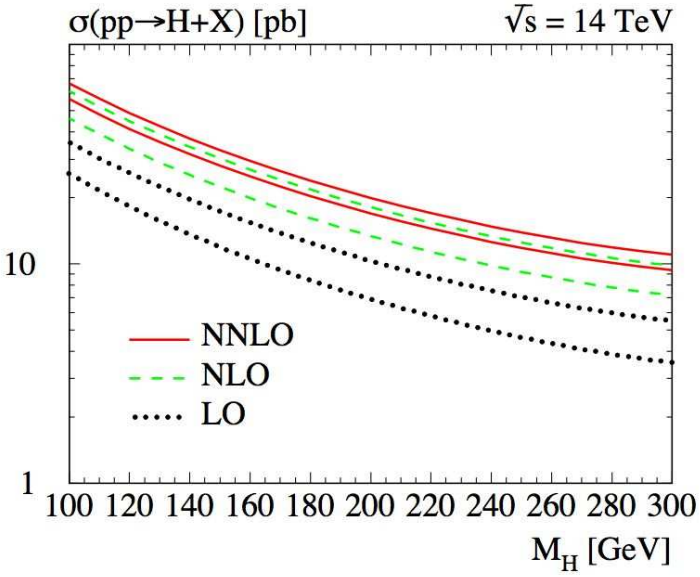

Figure 7.7: The cross sections for Higgs production in the gg $\rightarrow$ H+X fusion mechanism at the LHC at LO (dotted), NLO (dashed) and NNLO (solid) for two factorization and renormalization scales: $\mu_R = \mu_F = \frac{1}{2}m_H$ (upper curves) and $\mu_R = \mu_F = 2m_H$ (lower curves). The MRST PDFs are used; from Ref. [105].

for moderate Higgs boson masses, the increase from NLO to NNLO of about 30%, is more modest. This explicitly shows that the perturbative series converge.

7.2 The Soft-Gluon Resummation up to NNLL

If one wants to calculate the p_{T} spectrum of the Higgs in fixed higher order calculations, a problem is encountered. as in pure fixed order calculation the p_{T} Higgs distribution diverges if $p_{\mathrm{T}} \to 0$. When studying the p_{T} distribution of the Higgs boson in QCD perturbative theory, it is thus convenient to start by considering separately large and small p_{T} regions. In case the transverse momentum of the Higgs boson is large ($p_{\mathrm{T}}^{\mathrm{H}} \approx m_H$), the perturbative series is controlled by a small expansion parameter, $\alpha_S(m_H^2)$, and the fixed-order prediction is reliable. In the small p_{T} region, $p_{\mathrm{T}} \ll m_H$, where the bulk of events is produced, the convergence of the fixed order expansion is spoiled, since the coefficients of the perturbation series in $\alpha_s(m_H^2)$ are enhanced by powers of large log terms, $ln^k(m_H^2/p_T^2)$, due to an incomplete cancellation of soft and virtual contributions. To obtain reliable perturbative predictions, these terms have to be systematically resummed to all orders in α_s. In the case of the Higgs boson, the resummation of the logarithmic contributions has been explicitely performed up to next-to-next-to-leading logarithmic accuracy (NNLL) and is consistently matched to the fixed-order (NNLO) result valid at large $p_{\mathrm{T}}^{\mathrm{H}}$, in order to avoid double counting. The effect of resummation, relevant below $p_{\mathrm{T}} \sim 100$ GeV, leads to a physically well defined distribution at $p_{\mathrm{T}} \to 0$ at NNLO [68].

7.3 The Parton Distribution Functions

PDFs play a central role at hadron colliders to predict the production cross sections of the various signal and background processes. A precise knowledge of the PDFs over the energy Q^2, at which the process takes place, and a wide range of the proton momentum fraction x, carried by the parton, is mandatory. While partonic cross sections can be expanded in perturbative theories, PDFs can not. PDFs give thus the necessary non-perturbative inputs and have to be extracted from data. The measurable part of the PDFs should be independent of the factorization scale μ. Requiring this and setting $\mu^2 = Q^2$ one obtains the DGLAP (also called Altarelli-Parisi) equations [84, 85]:

$$\frac{\partial q_i(x,Q^2)}{\partial log(Q^2)} = \frac{\alpha_S}{2\pi}\int_x^1 \frac{dy}{y} P_{q_i q_j}(y,\alpha_S) q_j(\frac{x}{y},Q^2) + P_{q_i g}(y,\alpha_S) g(\frac{x}{y},Q^2)$$

$$\frac{\partial g(x,Q^2)}{\partial log(Q^2)} = \frac{\alpha_S}{2\pi}\int_x^1 \frac{dy}{y} P_{g q_j}(y,\alpha_S) q_j(\frac{x}{y},Q^2) + P_{gg}(y,\alpha_S) g(\frac{x}{y},Q^2) \tag{7.3}$$

with $P_{q_i q_j}$ the so-called splitting functions giving the probability that a parton of type q_i is evolving in a parton of type q_j. The DGLAP evolution equation is an accurate description of high-energy collisions of particles at moderate values of x.
The theoretical uncertainties are dominated by uncertainties coming from a global fit to the available data from deep-inelastic scattering, Drell-Yan and hadronic data, or from the

DGLAP evolution to the higher Q^2 relevant to the scattering processes, as well as from effects of unknown perturbative higher order corrections.
For the Higgs production channel through gluon fusion in the Higgs mass range between 150 and 200 GeV, the difference in the cross section using the PDFs is found to be smaller than 5%; this can be seen in Figure 4 in Ref. [106], where uncertainty bands for the NLO cross sections are given for CTEQ, MRST and ALEKHIN. These errors can be expected to decrease when going to NNLO PDFs [107].

7.4 The Scale Dependence

In order to evalutate the residual theoretical uncertainties in the production cross sections or in distributions which evolve due to the not yet calculated higher order corrections, the cross section dependence on the renormalization scale μ_R and on the factorization scale μ_F are explored. The standard is to vary the two scales, either together or independently (which means for example, keeping one scale fixed at the reference value), starting from a reference scale μ_0 which is considered as the "natural scale" of the process and is expected to absorb the large logarithmic corrections. The scales are normally varied within

$$\mu_0/2 \leq \mu_F, \mu_R \leq 2\mu_0 \tag{7.4}$$

By varying the scales, one obtains an uncertainty band in a given distribution: the narrower the band is, the smaller the higher–order corrections are expected to be. In most cases, the scale uncertainty is reduced when higher-order corrections are included.
A smaller value of the factorization scale than the conventional choice $\mu = m_H$ brings the advantage that the NNLO corrections decrease, indicating better convergence of the perturbative series [102]. As an example, at $\mu_R = \mu_F = \frac{1}{2}m_H$, the NLO correction increases while the NNLO correction decreases, with a total cross section which increases compared to the choice $\mu_R = \mu_F = m_H$. Therefore, since the difference between the NLO and NNLO contributions is small, the convergence of the perturbative series is improved for $\mu_R = \mu_F = \frac{1}{2}m_H$. Moreover, the fixed order results are in better agreement with recent estimates of the cross section based on threshold resummation when choosing a smaller scale factor [108].

Chapter 8

The Reweighting Technique

It was shown in Chapter 7 that corrections beyond LO are particularly significant for Higgs boson production in the channel gg → H. The Higgs boson cross section can be estimated only after many orders in perturbation theory are considered. It is therefore necessary to account for higher order corrections in a realistic analysis of the Higgs boson signal. As discussed before, parton showering and hadronization are only included in parton shower Monte Carlo event generators, a method has thus to be found how to merge higher order QCD matrix calculation to parton shower Monte Carlos. We present in the following a method how most-up-to-date higher order QCD corrections can be included in parton shower MCs. The method is called the reweighting technique [76, 119]. It is a good approximation for most processes. If high p_{T} jets are involved in a specific process, the validity of the approach has to be studied in detail, as LO parton shower Monte Carlos cannot describe high p_{T} jets accurately.

8.1 Including Higher Order QCD Correction: K-factors and the Reweighting Technique

The cross sections computed with a generator $G = \{\text{e.g. PYTHIA, MC@NLO}\}$ for the process pp → H+X are given as

$$\sigma^G = \sum_m \int d\Pi_m f_m^G\left(\{p_i\}\right) \mathcal{O}_m\left(\{p_i\}\right), \tag{8.1}$$

where the sum goes over all final-state multiplicities m, and the events f_m^G are integrated over the phase-space variables $d\Pi_m$ of all $i \leq m$ particles in the final state. The function $\mathcal{O}_m$ selects the kinematic configurations to be accepted in the measured cross section. The events depend implicitly on the renormalization and various factorization scales. The simplest observable is the total cross section σ^G_{incl}, corresponding to $\mathcal{O}_m\left(\{p_i\}\right) = 1$.
The integrand in Eq.(8.1) can be multiplied with a function K^G,

$$\sigma^{R(G)} = \sum_m \int d\Pi_m f_m^G\left(\{p_i\}\right) K^G\left(\{p_i\}\right) \mathcal{O}_m\left(\{p_i\}\right), \tag{8.2}$$

in order to reweight the events f_m^G,

$$f_m^G \to f_m^{R(G)} = f_m^G K^G. \tag{8.3}$$

The reweighting factors K^G model the effect of higher order corrections through a certain order in perturbation theory. The factors K^G are determined by requiring that Eq.(8.2) reproduces the fixed-order perturbative results for selected distributions,

$$\sigma^{R(G)}\left(\mathcal{O}_{\text{special}}\right) = \sigma_{\text{T}}^{p}\left(\mathcal{O}_{\text{special}}\right). \tag{8.4}$$

It is important to note that Eq.(8.2) is an approximate ansatz to describe effects of higher order corrections in the absence of a rigorous treatment. Strictly speaking, higher order corrections do depend on parton multiplicities. For example, pp $\to$ H +0 jets is renormalized differently compared to, pp $\to$ H +1 jet. This feature is ignored in Eq.(8.2), where the reweighting factors K_G do not depend on the multiplicities m. A more detailed version of reweighting would not be universal, because matrix elements with fixed multiplicities of partons are divergent in perturbation theory. Independent renormalization of events with different multiplicities has to depend on a globally-defined set of cuts, e.g. the jet finding algorithm, which invalidates the unweightedness of events, the single most important feature of parton shower Monte Carlo event generators. We discuss the possible errors in the reweighting procedure caused by neglecting the dependence on parton multiplicities later in Chapter 9, when PYTHIA reweighted to fixed NLO is compared to MC@NLO.
Having pointed out the approximate nature of the reweighting procedure, we discuss a choice of a suitable distribution for which the agreement of a Monte Carlo generator and the perturbative calculation can be imposed. Since, as we discussed in the previous paragraph, the reweighting ansatz is unsuitable for resolving the structure of QCD radiation, we use the kinematic variables which describe the Higgs boson. Up to an angle in a plane transverse to the collision axis, the Higgs boson kinematics is determined by its transverse momentum p_{T} and rapidity Y (note that the rapidity Y is chosen instead of the pseudorapidity η to be more general); we can thus normalize the events f_m^G to the magnitudes and shapes of the NNLO bin-integrated double differential distributions in Y and p_{T}, if both distributions are available. We expect that such a normalization renders the events more realistic in predicting other observables of the process. Without a technique for combining NNLO results with parton showering in the spirit of MC@NLO, this is the best way we have of combining these calculations with event generators. It has to be noted that we are not changing the properties of the radiation produced by the Monte Carlo generators. We are only changing the normalization of these events to reproduce certain distributions. The reweighted generators therefore do not better describe events with multiple hard radiations. We choose

$$\mathcal{O}_{\text{special}} = \left\{ \begin{array}{l} 1, \text{ if } p_{\text{T}} \in \left[p_T^j, p_T^{j+1}\right] \text{ and } Y \in \left[Y^i, Y^{i+1}\right] \\ 0, \text{ otherwise,} \end{array} \right\} \tag{8.5}$$

and define the K-factors as

$$K_{ij}^G := K^G(\{p_f\}) = \frac{\Delta\sigma_{ij}^{p_{\text{T}}}}{\Delta\sigma_{ij}^G} \quad \text{if } p_{\text{T}} \in \left[p_T^j, p_T^{j+1}\right] \text{ and } Y \in \left[Y^i, Y^{i+1}\right], \tag{8.6}$$

where $\Delta\sigma_{ij}^{p_{\mathrm{T}},G}$ are the accepted cross section computed at fixed order perturbation theory and with the generator G, respectively. The values of the bin boundaries $p_{\mathrm{T}}^{\mathrm{Jet}}$ and Y^i are chosen in such a way that they capture the shape of the Higgs p_{T} and rapidity distributions and span the allowed kinematic range for Y and p_{T}.

In the following, the PYTHIA $p_{\mathrm{T}}^{\mathrm{H}}$ spectrum is reweighted to the most up-to-date NNLO+NNLL spectrum by Grazzini et al, calculated with the HqT program. As the rapidity spectrum is not predicted by this program, we can only reweight to the p_{T} spectrum. However, as the Higgs produced in gluon fusion is rather flat in the central region, which is the region where $\mathrm{gg} \to \mathrm{H} \to \mathrm{WW} \to \ell\nu\ell\nu$ events are selected, it was assumed that the influence of the rapidity spectrum is not as big as the influence of the p_{T} Higgs spectrum. This is shown in [119] and section 9.3, where this ansatz is compared with a different reweighting procedure to fixed order NNLO in p_{T} and Y. The reweighting procedure to NNLO+NNLL is also described in [76, 109].

8.2 Reweighting PYTHIA to the Resummed NNLO + NNLL p_{T} Higgs Distribution

The expected Higgs $p_{\mathrm{T}}^{\mathrm{H}}$ spectra for $m_{\mathrm{H}} = 165$ GeV in PYTHIA and the resummed calculation are shown in Figure 8.1. It can be seen that PYTHIA provides a softer $p_{\mathrm{T}}^{\mathrm{H}}$ spectrum and differs from the perturbative calculation over the whole range of $p_{\mathrm{T}}^{\mathrm{H}}$. The formalism used in the program HqT implements a unitarity constraint, such that the integral of the distribution is the total NNLO cross section. The $p_{\mathrm{T}}^{\mathrm{H}}$ spectrum is obtained using the MRST2002 NNLO [107] parton distributions and α_{S} computed in the three-loop approximation. The corresponding MRST PDF at LO is chosen in PYTHIA. The renormalization and factorization scales are set to $\mu_R = \mu_F = m_H$. The $p_{\mathrm{T}}^{\mathrm{H}}$-dependent K-factor, which is the ratio between the two predictions, rises from approximately 1 at small $p_{\mathrm{T}}^{\mathrm{H}}$, to 3 at a $p_{\mathrm{T}}^{\mathrm{H}}$ around 50 GeV, and then decreases again to about 2.2 at a $p_{\mathrm{T}}^{\mathrm{H}}$ of 200 GeV, as shown in Figure 8.2. Note that at relatively large transverse momenta, the PYTHIA event generator is supplemented with hard matrix element corrections [110], thus explaining the approximately flat K-factor at large $p_{\mathrm{T}}^{\mathrm{H}}$. The $p_{\mathrm{T}}^{\mathrm{H}}$-dependent K-factor can be used to apply a weight to events generated with PYTHIA. The idea of the reweighting procedure is based on the assumption that the kinematics of Higgs events for a particular $p_{\mathrm{T}}^{\mathrm{H}}$ is reasonably well described by PYTHIA and that the efficiency of the cuts is computed correctly. Since the p_{T} spectrum is generated by multiple radiation from the incoming partons, the rapid variation of the K-factor for $p_{\mathrm{T}}^{\mathrm{H}} < 40$ GeV in Figure 8.2 could suggest an improper treatment of the effect of a jet veto in PYTHIA. In order to check the reliability of our reweighting procedure we have compared the efficiency of a jet veto with the one obtained with HERWIG, which is known to provide a better description of the $p_{\mathrm{T}}^{\mathrm{H}}$ spectrum in the small-$p_{\mathrm{T}}^{\mathrm{H}}$ region [111]. When $p_{\mathrm{T}}^{\mathrm{H}} < 40$ GeV, the efficiencies differ by less than 5%, thus confirming the validity of our approach.
Consequently, it is possible to obtain an approximation for the (N)NLO distributions of the kinematic observables used to select the final state by simply reweighting each PYTHIA event in such a way that the new $p_{\mathrm{T}}^{\mathrm{H}}$ spectrum matches the one from the QCD calculation.

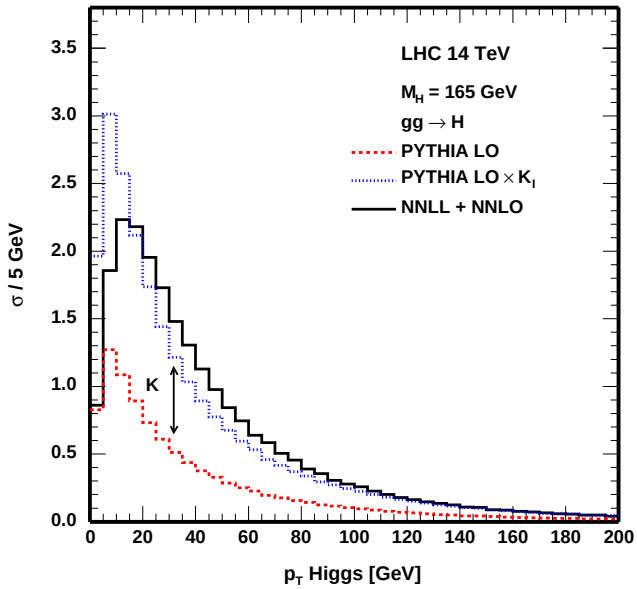

Figure 8.1: The Higgs production cross section for gg $\rightarrow$ H, as a function of the Higgs transverse momentum $p_{\mathrm{T}}^{\mathrm{H}}$, for a Higgs mass of 165 GeV, obtained with PYTHIA and with the NNLL+NNLO calculation. The spectrum from PYTHIA rescaled with the inclusive K-factor is also shown for comparison.

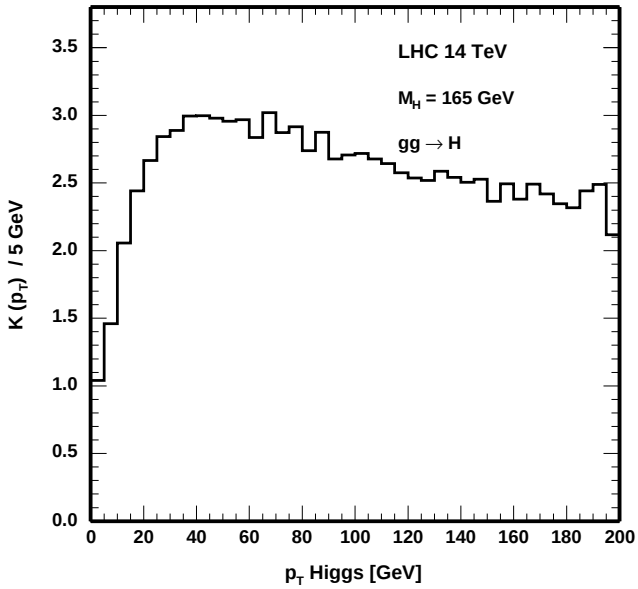

Figure 8.2: The $p_{\mathrm{T}}^{\mathrm{H}}$ dependence of the K-factor.

8.3 Reweighting PYTHIA to the Resummed NLO + NLL p_{T} WW Distribution

The program HqT also calculates the resummed nonresonant WW background. Thus, a similar procedure as for the Higgs p_{T} spectrum can be applied for the continuum production of WW pairs, which is a main background for the $\mathrm{gg} \to \mathrm{H} \to \mathrm{WW} \to \ell\nu\ell\nu$ channel. Here transverse momentum spectra obtained with PYTHIA are reweighted according to QCD predictions at next-to-leading-logarithmic (NLL) accuracy, which are matched to the perturbative NLO result [79, 112], valid at large transverse momenta $p_{\mathrm{T}}^{\mathrm{WW}}$ of the WW pair. For this calculation[1] MRST2002 NLO densities and a running α_{S} in the two-loop approximation are used, so that the integral of the spectrum is fixed to the total NLO cross section [113]. In order to compare the p_{T}-dependent WW spectrum from PYTHIA with the one from the higher-order calculation, the dependence on the mass of the WW system has to be taken into account. This is done for three different mass intervals, 170 ± 5 GeV, 200 ± 5 GeV and 250 ± 5 GeV, which cover the mass range where the WW events are a potential background for a Higgs signal with $m_H \approx 165$ GeV. The expected $p_{\mathrm{T}}^{\mathrm{WW}}$ spectra from the two calculations in the WW mass range of 170 ± 5 GeV are shown in Figure 8.3. The K-factors, as a function of $p_{\mathrm{T}}^{\mathrm{WW}}$ for the three different WW mass intervals, are shown in Figure 8.4.
The difference between the $p_{\mathrm{T}}^{\mathrm{WW}}$ spectrum in PYTHIA and the one calculated in NLL+NLO

[1]The NLL resummed WW cross section is computed according to the formalism of Refs. [**?**, **?**]. The NLO result used for the matching is obtained with the MCFM package [112].

QCD are particularly large for large transverse momenta. This is because, contrary to the Higgs signal, for WW production no hard matrix-element corrections are applied in PYTHIA , and thus the corresponding spectrum falls rather quickly as $p_{\mathrm{T}}^{\mathrm{WW}}$ increases.

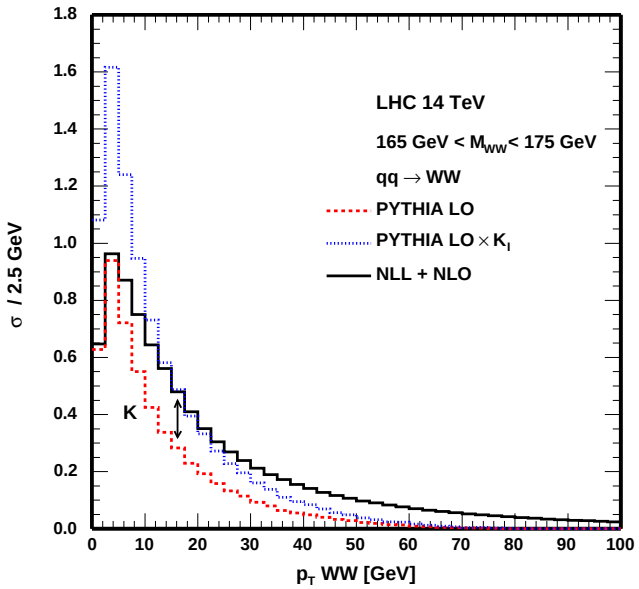

Figure 8.3: The p_{T} spectrum of the non-resonant WW system with a mass of 170 ± 5 GeV, obtained from PYTHIA and from the NLL+NLO calculation. The spectrum from PYTHIA rescaled with the inclusive K-factor is also shown for comparison.

The region in which K-factors are most important depends always on the analysis under consideration. In the $\mathrm{H} \rightarrow \mathrm{WW} \rightarrow \ell\nu\ell\nu$ analysis, only events with relatively small p_{T} are relevant. The corresponding event weights in this low p_{T} region for the non-resonant WW production are found to increase from about 1 at small transverse momentum to almost 4 at a transverse momentum of 50 GeV, slightly depending on the mass of the WW system. However, since most of the relevant continuum WW background comes from events with an invariant mass around threshold and relatively low transverse momentum, we take as an approximate weighting factor for the WW events the one obtained for the mass range 170 ± 5 GeV. As can be seen from Figure 8.4, this will slightly overestimate the rate of the WW production.
Once all cuts are applied in an analysis, an effective K-factor can be obtained, which is the ratio of accepted events at (N)NLO and at LO. This effective K-factor is in general smaller than the inclusive K-factor. In the following, the reweighting procedure is applied to the $\mathrm{gg} \rightarrow \mathrm{H} \rightarrow \mathrm{WW} \rightarrow \ell\nu\ell\nu$ channel to give an example how the reweighting is applied. The $\mathrm{gg} \rightarrow \mathrm{H} \rightarrow \mathrm{WW} \rightarrow \ell\nu\ell\nu$ is discussed in more detail in the next chapter.

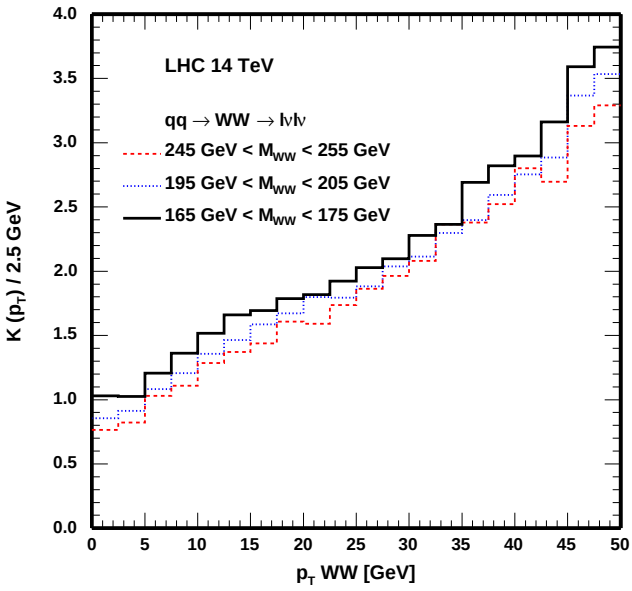

Figure 8.4: The p_{T} dependence of the K-factor for the non-resonant WW system and three different WW mass intervals.

Chapter 9

The H $\rightarrow$ WW $\rightarrow \ell\nu\ell\nu$ Channel

9.1 Higgs Signal Selection in H $\rightarrow$ WW $\rightarrow \ell\nu\ell\nu$

Let us recall the motivation for this channel. In the mass region below 155 GeV and above 180 GeV, Higgs detection with large significance is possible by the observation of narrow mass peaks in the decays $H \rightarrow \gamma\gamma$ and $H \rightarrow ZZ \rightarrow 4\ell$. The region between 155 and 180 GeV was for a long time regarded as difficult for Higgs discovery, as the Higgs decays almost exclusively into a pair of on-shell W's, which subsequently decay either in jets or lepton-neutrino pairs. The decays that provide a narrow mass peak, e.g. $H \rightarrow ZZ \rightarrow 4\ell$, are therefore suppressed. In addition, the ZZ decay into 4 charged leptons has a branching ratio of less than 0.45 %. Multiplied with the corresponding branching ratios $H \rightarrow ZZ \rightarrow 4\ell$, one obtains a $\sigma\times$ BR of about 10-20 fb. Due to this low statistics, an integrated luminosity of at least 100 fb^{-1} would be needed for a Higgs discovery in the ZZ decay in this mass range.

The W decays either in jets or lepton-neutrino pairs. The decays of W's into jets is difficult to distinguish from the abundant jet background at the LHC, even if one of the gauge bosons decays leptonically [56]. Therefore, only the leptonic final states are considered, which provide clean and detectable events signatures. However, no narrow mass peak can be reconstructed in this decay due to the neutrino final states. The LO cross section in the mass range between 155 and 180 GeV is around 1 pb, which is very large compared to the second largest $H \rightarrow ZZ \rightarrow 4\ell$ cross section in this region; as will be discussed below, this large statistics compensates for the absence of a narrow mass peak.

The main backgrounds for the $gg \rightarrow H \rightarrow WW \rightarrow \ell\nu\ell\nu$ channel are nonresonant WW production $q\bar{q} \rightarrow WW \rightarrow \ell\nu\ell\nu$, and the background from top quark production, $t\bar{t} \rightarrow WbWb \rightarrow \ell\nu\ell\nu bb$ and $Wtb \rightarrow WWb \rightarrow \ell\nu\ell\nu b$. In NLO, the cross section of the top background is about 45 times larger than the signal, while the nonresonant WW background is about 6 times larger than the signal, if no cuts are applied. Therefore, very good selection criteria are needed to reduce this large background. The absence of suitable cuts was for a long time the main reason why this mass region was considered to be difficult.

The decay $H \rightarrow WW \rightarrow \ell\nu\ell\nu$ with $\ell = e, \mu, \tau(\rightarrow \ell\nu\bar{\nu})$ was first studied by Glover at al [114]

for the LHC. They did explicitely not consider the background from $t\bar{t}$ production and focused on the WW background, for which they did not find any discriminating cuts. Subsequently, Barger et al. [115] performed a more detailed parton level analysis of this signature for the LHC. They also included the significant $t\bar{t}$ background for different top masses, as the top mass was not yet known. Again, they did not find cuts to significantly reduce the WW background. Such a cut was found in 1997 by Dittmar and Dreiner, who studied the effects of spin correlations and the mass of the resonant and non-resonant WW system. This resulted in a small opening angle between the leptons in the plane transverse to the beam and a somewhat mass-dependent characteristic p_{T} spectrum of the charged leptons. The angle between the leptons in the transverse plane is thus a measure to distinguish between the signal and WW background, and the WW background could then be reduced significantly [116]. The angle ϕ between the two charged leptons, originating from the WW decays of the signal and the nonresonant $qq \rightarrow$ WW background, is shown in Figure 9.1. In addition, the authors applied a jet veto against the $t\bar{t}$ background and found that the signal events are more central than the background. After these cuts were found, the region between 155 and 180 GeV

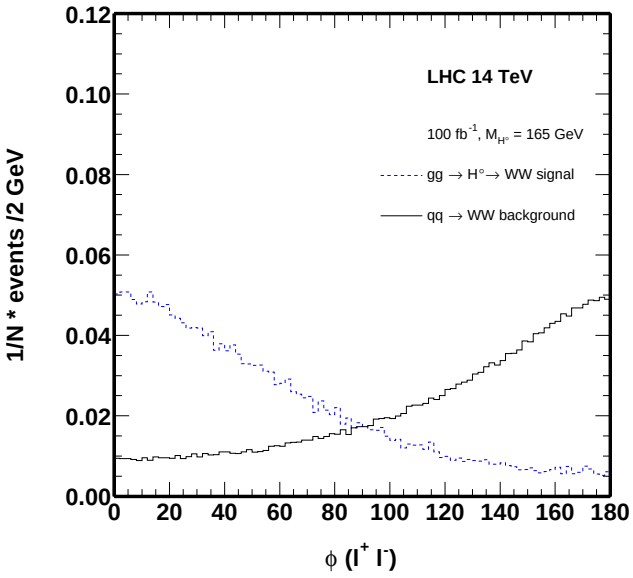

Figure 9.1: The angle ϕ between the two charged leptons originating from the WW decays of the signal and the continuous $qq \rightarrow$ WW background. Due to the spin correlations, a small opening angle between the leptons results for the Higgs. The only cut applied is the one that there must be two charged leptons in the event.

was no longer a critical region and despite of the absence of a narrow mass peak, the decay H → WW → $\ell\nu\ell\nu$ with $\ell = e, \mu, \tau(\rightarrow \ell\nu\nu)$ provided a straightforward discovery channel.

In the following, the criteria based on cuts described in [76,109,117,118] are described. First, events that contain exactly two isolated and oppositely charged high-p_{T} leptons (electrons or muons) are selected. These leptons originate mainly from the decays of W bosons. They

should not be back-to-back in the plane transverse to the beam and their invariant mass should be considerably smaller than the Z mass. Furthermore, a significant missing transverse momentum is required. Essentially, these criteria select only events that contain a pair of W's, these being either signal events or backgrounds from non-resonant WW production $q\bar{q} \to WW \to \ell\nu\ell\nu$, from $t\bar{t} \to WbWb \to \ell\nu\ell\nu bb$ and $Wtb \to WWb \to \ell\nu\ell\nu b$.
After this preselection, the cuts for the second step are based on the following criteria:
(i) WW pairs originating from the production and decay of top quark pairs are usually accompanied by jets and can be strongly reduced by a properly adjusted jet veto.
(ii) The WW pair, originating from the Higgs decay, is produced dominantly in the gluon fusion process while the continuum WW events are produced mainly from $q\bar{q}$ scattering. As a result, the signal events have a shorter rapidity plateau then the continuum WW background events.
(iii) The effects of spin correlations mentioned before, which result in a small opening angle for the Higgs in the plane transverse to the beam.
(iv) The observable lepton transverse momentum spectra show a Jacobian peak-like structure allowing to further optimize the signal over background ratio.

The criteria are quantified in the following. First, criteria 1-5 selects events which contain two isolated high p_T leptons which come largely from resonant or non resonant events of the type WWX. In the second group of cuts, criteria 6-8, the resonant H → WW signal events are separated from continuum WWX events.
In detail, the following cuts are applied:

1. The event should contain two leptons, electrons or muons, with opposite charge, each with a minimal p_T of 10 GeV and a pseudorapidity $|\eta|$ smaller than 2.

2. In order to have isolated leptons, it is required that the transverse energy sum from detectable particles, defined as "stable" charged or neutral particles with a p_T larger than 1 GeV, found inside a cone of $\Delta R = \sqrt{\Delta\eta^2 + \Delta\phi^2)} < 0.5$ around the lepton direction, should be smaller than 10% of the lepton energy and the invariant mass of all detectable particles within the cone should be smaller than 2 GeV. Furthermore, at most one additional detectable particle inside a cone of $\Delta R < 0.15$ is allowed.

3. The dilepton mass, $m_{\ell\ell}$, has to be smaller than 80 GeV.

4. The missing p_T of the event, required to balance the p_T vector sum of the two leptons, should be larger than 20 GeV.

5. The two leptons should not be back-to-back in the plane transverse to the beam direction. The opening angle between the two leptons in this plane is required to be smaller than 135°.

Dilepton events, originating from the decays of W and Z bosons, are selected with the criteria 1 and 2. Lepton pairs which originate from the inclusive production of Z → $\ell\ell(\gamma)$, including Z decays to τ leptons, are mostly removed with criteria 3–5.

Starting with this initial set of requirements, the following criteria exploit the differences between Higgs events and the so-called "irreducible" background from continuum production of pp → WW events [1].

6. The opening angle ϕ between the two charged leptons in the plane transverse to the beam should be smaller than 45° and the invariant mass of the lepton pair should be smaller than 35 GeV[2].

7. Jets are formed with a cone algorithm, requiring a minimum jet transverse momentum in order to be considered as a jet. For this analysis, events which contain a jet, with $p_{\mathrm{T}}^{\mathrm{Jet}} > 30$ GeV and with a pseudorapidity $|\eta^{\mathrm{Jet}}| < 4.5$, are removed.

8. Finally, the p_{T} spectrum of the two charged leptons is exploited. For this, the two leptons are classified according to their p_{T} (p_{Tmin}^{ℓ} and p_{Tmax}^{ℓ}). It is found that the p_{Tmax}^{ℓ} and p_{Tmin}^{ℓ} show a Jacobian peak-like structure for the signal, which depends on the simulated Higgs mass. In case of a Higgs mass close to 165 GeV, p_{Tmax}^{ℓ} should be between 35 and 50 GeV, whereas the p_{Tmin}^{ℓ} should be larger than 25 GeV.

In the following, the signal and the main backgrounds, $qq \rightarrow$ WW, $\mathrm{t\bar{t}}$ and Wtb, are generated with PYTHIA and higher order QCD corrections are included by applying the reweighting procedure to the gg → H → WW → $\ell\nu\ell\nu$ signal and the WW background.

9.2 Including Higher Order QCD Corrections to the gg → H → WW → $\ell\nu\ell\nu$ Channel

The p_{T} spectrum of the Higgs is reweighted to the resummed p_{T} spectrum at NNLO+NNLL, as shown in the previous chapter, and the WW background $qq \rightarrow$ WW is reweighted to the resummed WW spectrum at NLO+NLL. The background from top production is not as sensitive to additional jet production as the signal and the nonresonant WW background, because the leading order matrix element already contains two high energetic jets. Therefore a constant K-factor is applied in this approximation. For this analysis a K-factorof 1.5 has been chosen, which was generally assumed to be a good approach at the time this study was performed. In Chapter 11, the K-factors for the top background are discussed in more detail, resulting in a smaller cross section of the top backgrounds and therefore smaller contributions than used here. Thus, an even better signal over background ratio is obtained when more up-to-date treatment of the top background is included. After the reweighting is performed, the selection criteria are applied to signal and background.
The gg → H → WW → $\ell\nu\ell\nu$ analysis mainly selects signal events with low p_{T} Higgs. The efficiency to detect a Higgs boson with the selection criteria mentioned above, defined as the ratio of all accepted over all generated events, can be studied as a function of the generated transverse momentum of the Higgs. The results for different jet veto cuts ($p_{\mathrm{Tmin}}^{\mathrm{jet}} = 20$, 30 and

[1] In a recent paper the importance of the heavy flavour background has been investigated [120]. As our selection criteria are much stronger than the ones discussed in this paper, no relevant contribution from this background is expected.

[2] A minimal angle of 10° (or minimal mass of 10 GeV) might be needed in order to reject badly measured $\Upsilon \rightarrow \mathrm{e^+e^-}(\mu^+\mu^-)$ decays. Such a cut would not change the signal efficiency in any significant way.

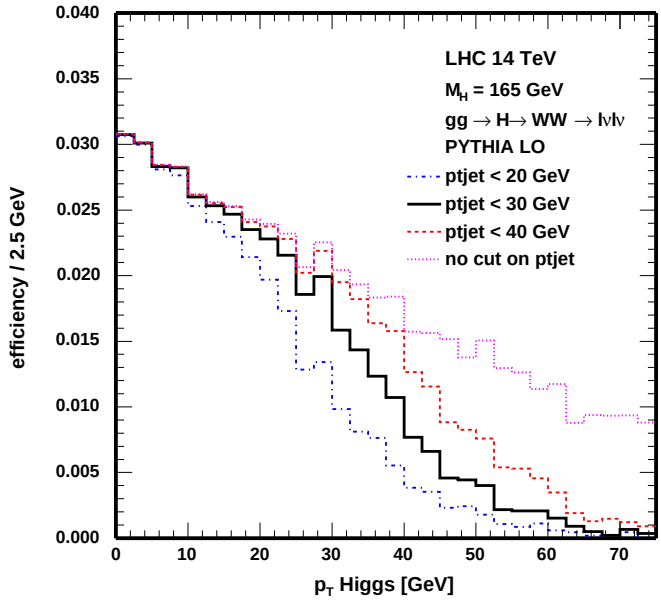

Figure 9.2: Signal selection efficiency as a function of the Higgs transverse momentum, for a Higgs mass of 165 GeV and three different jet veto cuts. For completeness, the efficiency curve for all cuts, excluding the jet veto, is also shown.

40 GeV) are shown in Figure 9.2. As expected, Higgs events with large $p_{\mathrm{T}}^{\mathrm{H}}$ are almost always rejected with the proposed criteria, and the efficiency drops rather quickly as $p_{\mathrm{T}}^{\mathrm{H}}$ reaches the value of the jet veto $p_{\mathrm{Tmin}}^{\mathrm{jet}}$.

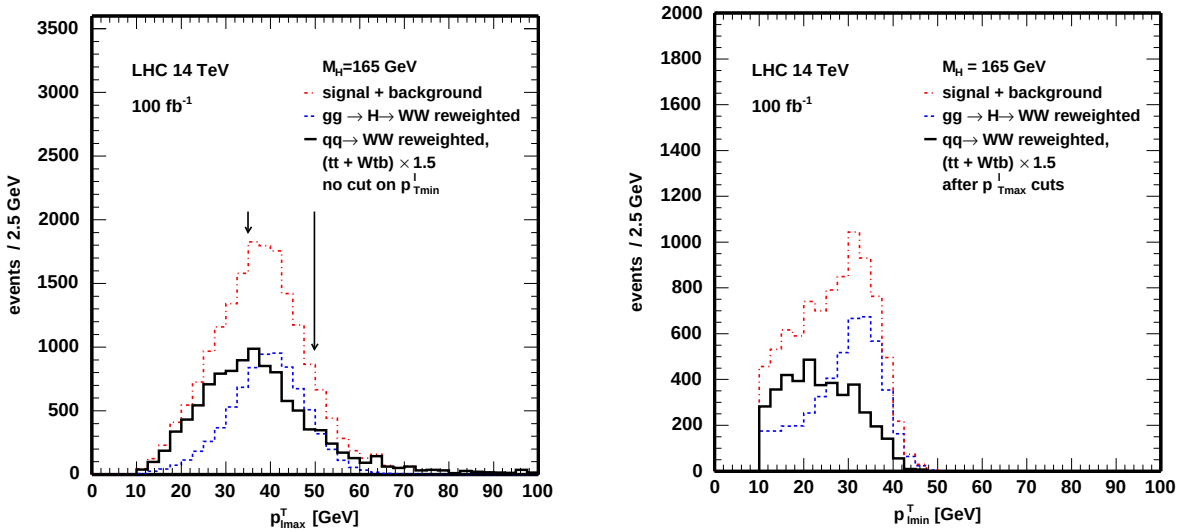

Figure 9.3: Transverse momentum spectra of the leading lepton (left) and the lepton with the smaller p_{T} (right) from gg → H → WW → $\ell\nu\ell\nu$ and the considered backgrounds, as obtained from PYTHIA with event reweighting. The expected background from non-resonant W-pair production is reweighted using the p_{T}-dependent weighting factor, while the ones from $\mathrm{t\bar{t}}$ and Wtb are simply scaled by a factor of 1.5. In the left plot, all cuts are applied except the cuts on p_{T} of the leptons, while in the right plot all cuts are applied except the cut on p_{Tmin}^{ℓ} .

The effective experimental K-factor can be computed from the sum of the accepted cross section over all the p_{T} bins. The signal efficiency vanishes for $p_{\mathrm{T}}^{\mathrm{H}}$ above 65 GeV. Therefore, high K-factors which occur at $p_{\mathrm{T}}^{\mathrm{H}}$ above 65 GeV will not contribute when computing the effective experimental K-factor K_{eff}. From the integration over all $p_{\mathrm{T}}^{\mathrm{H}}$ bins, the inclusive K-factor with respect to PYTHIA , without any selection cuts, is found to be $K_{\mathrm{I}} = 2.37$ for a Higgs with a mass 165 GeV. This is roughly 15% larger than $K_{\mathrm{eff}} = 2.04$, which is obtained after all cuts are applied, including the jet veto at 30 GeV. This means that the number of accepted reweighted events is a factor of 2.04 larger than in the unweighted case. Similar numbers are obtained for Higgs masses of 140 and 180 GeV. The estimated effective K-factor for the WW background, integrating over the entire WW mass spectrum and using the p_{T}-dependent weighting factor determined for the WW mass interval of 165–175 GeV, is found to be 1.36. More numbers obtained in this study can be found in [76].
The transverse momentum spectra of the two leptons, p_{Tmax}^{ℓ} and p_{Tmin}^{ℓ} , after the reweighting and with all cuts applied, are shown in Figure 9.3 for $m_{\mathrm{H}} = 165$ GeV. The $\mathrm{t\bar{t}}$ and Wtb backgrounds are included using an inclusive K-factor of 1.5.

So far, the reweighting was only performed to the p_{T} Higgs spectrum at NNLO+NNLL, as the rapidity spectrum is not available in the HqT program. It was assumed that the influence of the rapidity of the Higgs boson does not change much the kinematics, as the rapidity in the central region, which is the region of the Higgs signal selection in the $\mathrm{gg} \to \mathrm{H} \to \mathrm{WW} \to \ell\nu\ell\nu$ channel, is flat. As Anastasiou et al. [64] found a method to calculate fully differential distributions in p_{T} and the rapidity η of the Higgs boson production at NNLO, we could check the influence of the rapidity to the reweighting. This will be presented in the following.

9.3 Reweighting to the NNLO p_{T} and Rapidity Distribution of the Higgs Boson

In this study, PYTHIA and MC@NLO are matched to a double differential distribution in the Higgs boson transverse momentum and rapidity. The renormalization and factorization scale is equal to $m_H/2$.

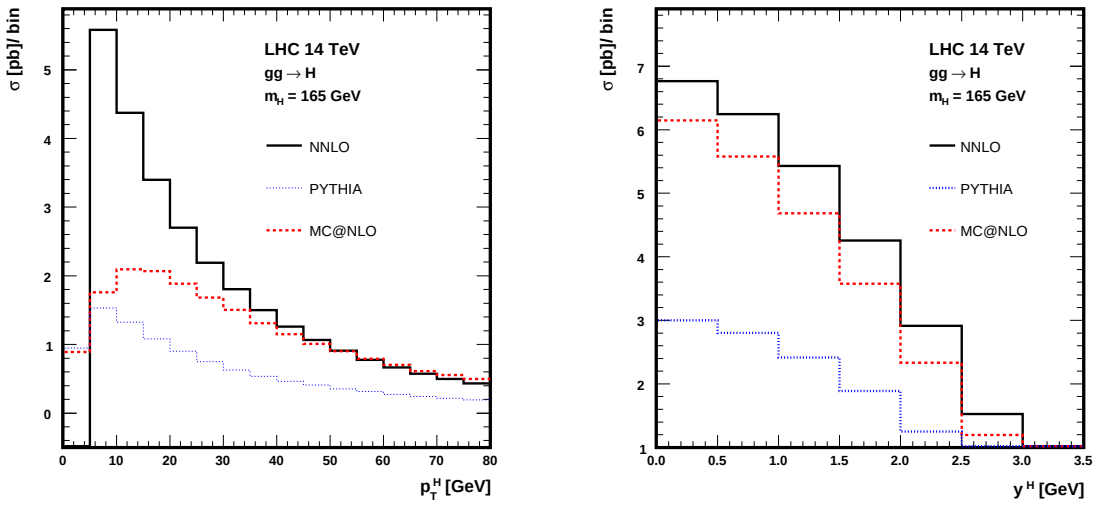

Figure 9.4: Distributions of the Higgs transverse momentum (left) and rapidity (right).

The choice of the bin boundaries in the p_{T} distribution of the Higgs boson is a subtle issue when reweighting to fixed order calculations, as the Higgs p_{T} distribution in the low p_{T} region is not correctly described in fixed-order calculations. Logarithms of the form $\log p_T/m_H$ become large and require a resummation. Nevertheless, fixed order calculations for cross-sections integrated over p_{T} of the Higgs boson are still viable, provided that the integration region is sufficiently broad.
In Figure 9.3 we show the p_{T} distributions for the fixed-order NNLO calculation, generated

with PYTHIA and MC@NLO. We observe that the perturbative NNLO result breaks down at small p_{T} (note that the scale of the cross section in the p_{T} distribution in Figure 9.3 starts at (-1)). The p_{T} spectrum of PYTHIA is peaked at lower p_{T} than MC@NLO. To avoid problems associated with the low-p_{T} region in fixed order perturbative calculations, we then choose the first p_{T} bin, $[p_T^0 = 0, p_T^1]$, to be sufficiently broad by taking $p_T^1 = 25$ GeV. Therefore, for $p_T < 25\,\mathrm{GeV}$, we reweight all events with a uniform factor, maintaining the shape of the p_{T} distribution provided by the parton shower generator G, where the generators G in this study are PYTHIA and MC@NLO. Above 25 GeV, we trust the shape of the perturbative result and reweight in bins of 5 GeV

$$p_T^0 = 0, \quad p_T^1 = 25\,\mathrm{GeV}, \quad p_T^i = (25 + (i-1)5)\,\mathrm{GeV},$$

and

$$Y^j = 0.5(j-1)\,,\; j = 1 \ldots 9.$$

Note that this reweighting procedure leads to a discontinuity at $p_{\mathrm{T}} = p_T^1$ in the reweighted p_{T} spectrum computed with the generator G. Such a large first bin size corresponds to a constant K-factor, applied to the region were resummation takes place in the parton shower Monte Carlo. Thus the resummed shape of the Monte Carlos is kept. In what follows we take the first bin in p_{T} to be $[0 - 25$ GeV], unless explicitly stated otherwise.

The dependence of the reweighting factors K^G on the p_{T} and rapidity is shown in Figure 9.3 for PYTHIA and MC@NLO. $K^G(p_T, Y)$ can vary significantly in different rapidity and p_{T}-bins. The reweighting factors for the p_{T} distribution, after integration over the rapidity, as well as the reweighting factors as a function of Y, after integrating over p_{T} are shown. For PYTHIA, we find K-factors ranging from 1.8 to 3.5, while for MC@NLO the K-factors can vary from 0.7 to 1.6 in bins with a significant number of events. The shape of the K-factors in the two variables is not uniform, confirming that a naive multiplication with a uniform K-factor from the total cross-section may not be adequate. More information about this study can be found in [119].

9.3.1 The Reweighting at NLO and NNLO

To see how big the dependence of the rapidity is after all cuts are applied, we validate first the reweighting approach to fixed order NNLO distributions. Thus we apply the reweighting procedure to PYTHIA and MC@NLO to study pp → H+X. First we check how the reweighting works at NLO by imposing a jet veto. This tests whether neglecting the additional hadronic radiation in our reweighting ansatz is problematic. We compare the acceptance in PYTHIA, MC@NLO, PYTHIA reweighted to NLO and pure NLO, when a jet veto at 30 GeV is applied. A very large disagreement, of order 30%, between the acceptances obtained using the generators and the fixed order NLO result is observed. What is occurring here is that this observable is very sensitive to the properties of the QCD radiation. Multiple partonic emissions are required to generate the correct jet p_{T} spectrum, and the NLO result contains only a single partonic emission. The p_{T} spectrum of this additional parton is generated for the first time at NLO, and is therefore not accurately predicted at this order in the perturbative expansion. We note that reweighting PYTHIA to the NLO result spoils the agreement

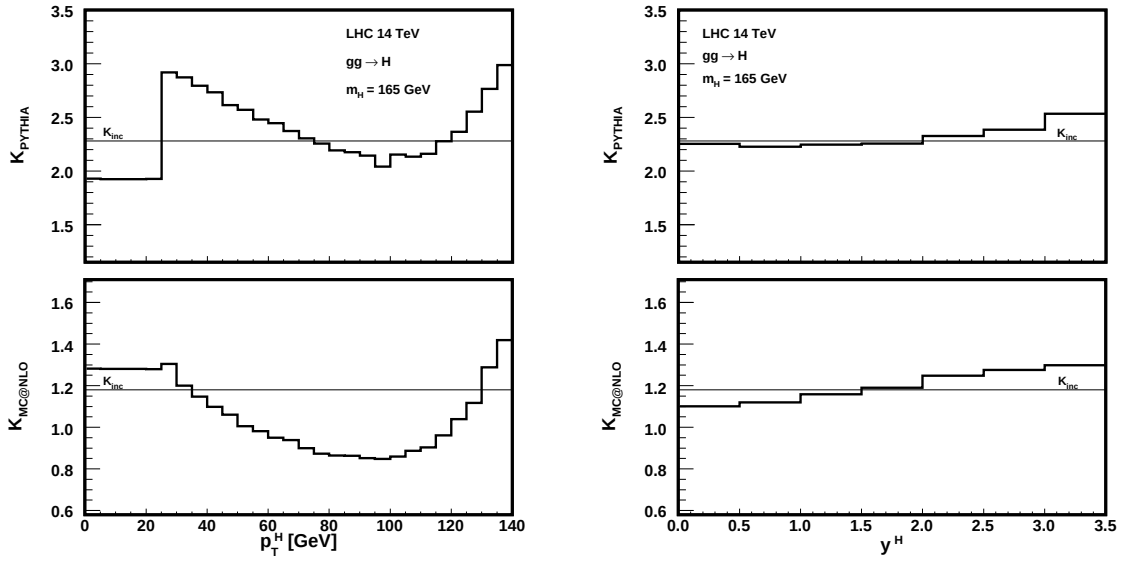

Figure 9.5: The reweighting factors integrated over rapidity for PYTHIA and MC@NLO as functions of the Higgs p_{T} (left). The reweighting factors, integrated over p_{T} , as functions of rapidity (right). The inclusive K-factor for the total cross-section is also shown on both plots as a horizontal line.

between its acceptance and that computed with MC@NLO. It was shown in [119] that multiple emissions are required also for the high p_{T} region. When doing the same at NNLO, we observe a much better agreement with the NNLO reweighting. The reweighted PYTHIA spectrum R(PYTHIA), the reweighted MC@NLO spectrum R(MC@NLO) and the fixed order NNLO result all agree with the PYTHIA and MC@NLO acceptances within 6%. The NNLO result contains two partons in the final state, which gives a more realistic accounting of the QCD radiation. It also contains the first radiative correction to the single parton p_{T} spectrum. The p_{T} spectrum obtained at NNLO is in better agreement with MC@NLO, as shown in Figure 9.3.
A comparison of the p_{T} spectrum from the reweighted generators with the resummed p_{T} distribution calculated with the program HqT [68] showed good agreement between
$\mathrm{R}^{\mathrm{NNLO}}$(MC@NLO), which is reweighted to the fixed NNLO predictions calculated with FEHIP, and the resummed calculation.
$\mathrm{R}^{\mathrm{NNLO}}$(PYTHIA) agrees with the intermediate and large p_{T} part of the resummed distribution, while there is a slight discontinuity induced by the first bin reweighting in the low p_{T} region. We conclude that even in the presence of significant cuts on the jets in the final-state, the simple reweighting of the Higgs boson double differential distribution at NNLO describes the acceptances well. In addition, since the NNLO result produces the correct normalization and contains drastically reduced scale dependences, reweighting MC@NLO with the fully differential NNLO result of FEHIP provides a very accurate prediction for the Higgs boson signal at the LHC.

Motivated by the success of the NNLO reweighting procedure, we now proceed with the Higgs decay. As a check of the reweighting procedure, the decay channel pp → H → $\gamma\gamma$ was studied with all relevant experimental cuts included, as this channel is available in the NNLO MC program FEHIP and can thus be compared to the reweighting ansatz. It was found that both the reweighted PYTHIA and the reweighted MC@NLO match very well the accepted cross-section as predicted by FEHIP. The distributions that have been proposed to discriminate between the Higgs signal and the background were studied as well, and both R(PYTHIA) and R(MC@NLO) describe the kinematic distributions well. They match the NNLO fixed-order result away from kinematic features, and exhibit the resummation present in the event generators near the kinematic boundaries.

9.3.2 The Effect of Including the Rapidity Dependence in the H → WW→ $\ell\nu\ell\nu$ Channel

The full H → WW → $\ell\nu\ell\nu$ decay in FEHIP is not implemented yet and a comparison of the reweighted PYTHIA or MC@NLO distributions to the NNLO distributions is thus not yet possible. In addition, HERWIG, which is a basic component of MC@NLO, does not have an implementation of the same decay with full spin correlations. Therefore, no leptonic observables can be presented with R(MC@NLO). Nonetheless, using R(PYTHIA), we can obtain a description of the Higgs boson rapidity distribution after cuts are applied, and examine the effect of this rapidity dependence. We find that the (p_{T},Y) dependent effective K-factor is 10% lower than the fully inclusive K-factor, while the K-factor coming from only reweighting to the p_{T} distribution is 13% lower than the inclusive K-factor, comparable with the results obtained in section 9.2 and [76]. The effect of the rapidity dependence is therefore less than 3%.
Since the distributions studied do not probe the hadronic radiation, we expect them to be very well described by R(PYTHIA).
In Figure 9.6 we plot the minimum and maximum transverse momentum distributions of the detected leptons for PYTHIA and R(PYTHIA) events. These distributions are characteristic of the Higgs signal and can be used to discriminate against the background.
We observe that the reweighting does not change the shape of distributions significantly. Depending on the accuracy needed in the analysis, an application of a constant K-factor would lead to similar results. However, the appropriate constant K-factor to multiply the PYTHIA results with is the effective K-factor 2.10, which is 10% lower than the fully inclusive K-factor.

We have presented a phenomenological approach to include higher order QCD corrections in event generators such as PYTHIA or MC@NLO. Without an extension of the MC@NLO procedure to NNLO, this offers a way of combining parton showering and hadronization with NNLO calculations. In addition, as no spin correlation is included in MC@NLO yet, MC@NLO is presently not suited for the H → WW → $\ell\nu\ell\nu$ channel. We demonstrated that by reweighting the p_{T} spectrum obtained with a parton shower Monte Carlo to a NNLO (or NNLO+NNLL) p_{T} Higgs spectrum, the effective K-factor is about 10-15 % smaller than the inclusive one. Reweighting to both p_{T} Higgs and the rapidity does change the effective K-factoronly by 3%, which can be neglected, depending on other uncertainties in the study.

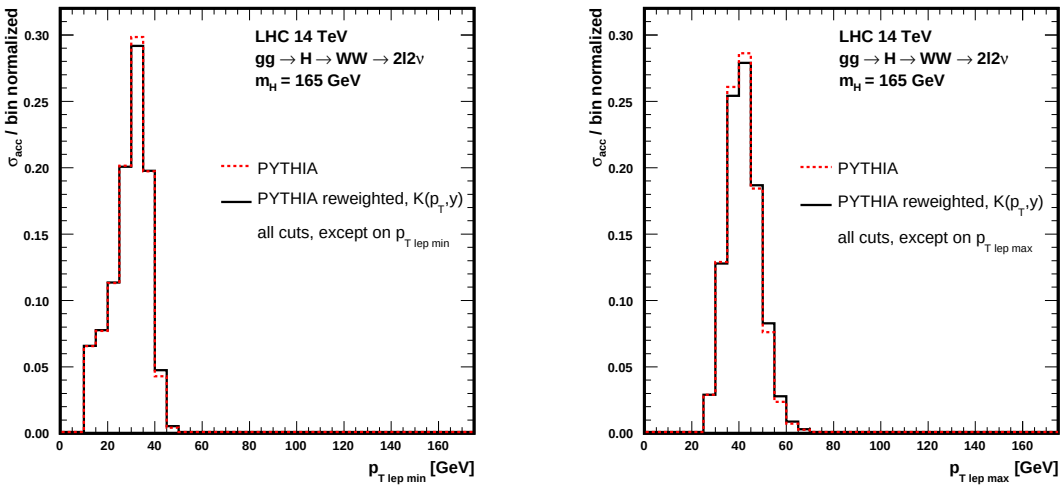

Figure 9.6: The minimum (left) and maximum (right) transverse momentum of the two leptons computed with PYTHIA and R(PYTHIA).

It is important to point out that reweighting to fixed NLO leads to a wrong result, as jet multiplicities cannot be described correctly in pure fixed order NLO. Reweighting of a parton shower Monte Carlo should thus be applied to the p_{T} (and, if available Y) distributions of a NNLO, or resummed NNLO+NNLL program.

Chapter 10

$t\bar{t}$ and Wtb Background

After having discussed how higher order QCD corrections can be included in the gg → H → WW → $\ell\nu\ell\nu$ process and the nonresonant WW background qq → WW → $\ell\nu\ell\nu$, we are now interested in the remaining main backgrounds of the gg → H → WW → $\ell\nu\ell\nu$ signal, which are the single top Wtb and $t\bar{t}$ production.
At leading order, the $t\bar{t}$ production process, pp → $t\bar{t}$ → WbWb → $\ell\nu\ell\nu$bb, where $\ell = e, \mu, \tau$ (an example is shown in Figure 10.1(left)), has a cross section times branching ratio of about 52 pb. Single top production pp → Wtb represents a contribution which is about ten times smaller. After applying a jet veto, the contribution from Wtb is increased with respect to $t\bar{t}$, as the second b-jet is produced at a much lower transverse momentum and the jet veto efficiency is thus lower.
In order to resum large logarithms of the form $\log[(m_t+m_W)/m_b]$, it is preferable to view the single top production process as one in which a b-quark is probed directly inside the proton. The leading order process is gb → Wt. An example is shown in Figure 10.1(right). Starting from this process, one can calculate NLO corrections, which partially include diagrams from $t\bar{t}$ production in the real radiation contribution. However, by applying a veto on the presence of an extra b-jet, the interference effect is greatly suppressed and the contribution from the $t\bar{t}$ diagrams can be unambiguously removed [121].
For the gg → H → WW → $\ell\nu\ell\nu$ channel, where a jet veto is used, the Wtb production rate can therefore be estimated also at NLO.

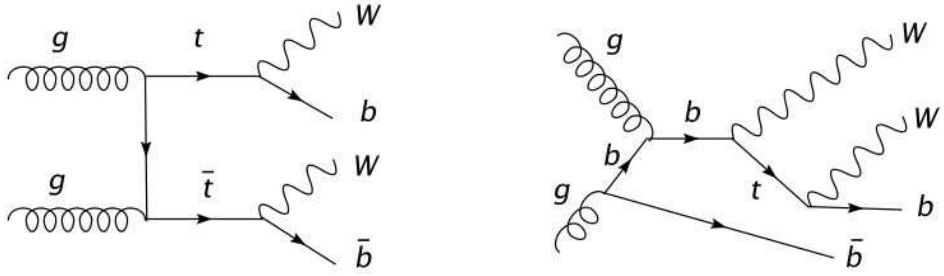

Figure 10.1: Examples of Feynman graphs for $t\bar{t}$ (left) and Wtb (right) production.

10.1 Generating Single Top Production Wtb

The NLO prediction for the rate depends on the region of phase space which is probed, and thus on the definition of the used jet veto.
The NLO cross section for Wtb production was calculated by J. Campbell and F. Tramontano using MCFM [122], a parton level Monte Carlo generator. The efficiencies obtained for the Higgs boson selection cuts were compared for MCFM at LO and NLO by John Campbell. Since MCFM is a parton level generator, the jet veto had to be applied directly on the b-parton, requiring no b partons with $p_{\mathrm{T}} > 40$ GeV. No requirement on the lepton isolation was added. After all selection cuts are applied, the accepted NLO cross section is about 0.7 times the LO cross section. The fact that the accepted cross section at NLO is lower than the one at LO is mostly because events with extra jets at NLO are cut away and thus the total efficiency is lower than in the LO case.
To account for the difference in the jet veto efficiency between NLO and LO, the K-factor that will be used to approximate NLO cross sections is determined in the signal region and is equal to 0.7. This also avoids double counting between $t\bar{t}$ and Wtb production since the two processes are separated in the signal region. After a jet veto requirement the double counting becomes negligible [121].
Experimentally, the jet veto is applied to reconstructed jets[1] and the jet energy does not correspond to an exact value of the parton p_{T}. At leading order, requiring no parton with $p_{\mathrm{T}} > 40$ GeV has a similar efficiency as requiring that no jet with $p_{\mathrm{T}} > 30$ GeV is reconstructed in the parton shower Monte Carlo. Thus a parton cut at 40 GeV will roughly correspond to a jet cut at 30 GeV. In Figure 10.2, Wtb is simulated with TopReX [**?**]. The Figure shows the selection efficiency, after requiring two leptons with $p_{\mathrm{T}} > 20$ GeV as a function of the b-quark p_{T}, when all jets with $p_{\mathrm{T}} > 30$ GeV are vetoed. In this case, 85% of the events have $\mathrm{p_T(b)} < 40$ GeV and 94% have $\mathrm{p_T(b)} < 60$ GeV. For the analysis, TopReX is used for the generation of such processes and a constant K-factor determined in the particular signal region. The theoretical error on the Wt cross section is estimated to be around 20% including PDF and scale variation [124].

10.2 NLO Simulation of the $t\bar{t}$ Background

Up until recently only Monte Carlo generators based on LO matrix elements were available for the simulation of $t\bar{t}$ processes and used for most CMS Monte Carlo samples. As the $t\bar{t}$ process already includes at least two high p_{T} jets in the final state, we assume that higher order QCD corrections should not change the shape of the observables significantly. We will investigate this in the following by comparing HERWIG to MC@NLO, to see how higher order corrections change the distributions of relevant observables for this study.
As the spin correlations are not yet included in MC@NLO, HERWIG 6.508 without spin correlation and MC@NLO 2.31 are compared. In this way, the uncertainty between the different Monte Carlos cannot come from the different treatment of the spin correlations. Moreover, as the same showering model is used (which is in both cases the one implemented in

[1] For this study, as before, the jets are reconstructed applying a cone algorithm using the generated stable particles.

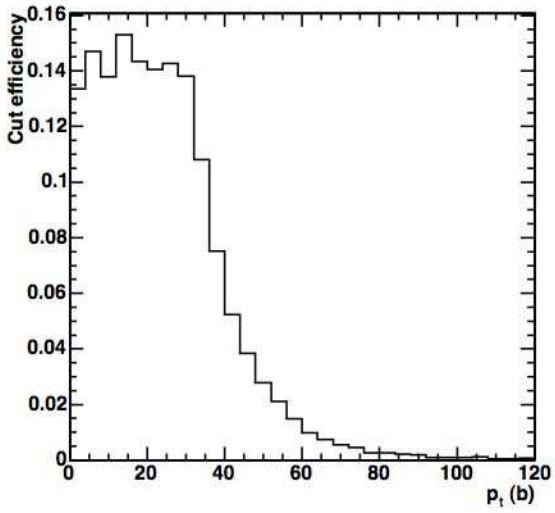

Figure 10.2: Efficiency as a function of the b transverse momentum, after requiring two isolated leptons with $p_T > 20$ GeV, $|\eta| < 2$ and no reconstructed cone jet with $p_T > 30$ GeV using TopReX.

HERWIG), the difference between the two simulations should be mostly due to the additional NLO matrix elements in MC@NLO.
One million pp $\rightarrow t\bar{t} \rightarrow WbW\bar{b} \rightarrow \ell\nu\ell\nu b\bar{b}$ events are generated and the events for this comparison are reconstructed starting with stable particles from the generator tree.
The selection used to search for the H $\rightarrow$ WW signal was then applied. First, a preselection requires two isolated[2] opposite charged leptons with E_T larger than 20 GeV and $|\eta|$ lower than 2 and rejecting all events including a jet with E_T larger than 30 GeV and $|\eta| < 2.5$ (jet veto). The second part of the selection requires:

- $E_T^{miss} > 40$ GeV (E_T^{miss} is formed using the vector sum of isolated lepton and jet transverse momenta)
- $\phi_{\ell\ell} < 45°$ (angle between the leptons in the transverse plane)
- 5 GeV $< m_{\ell\ell} <$ 40 GeV (the invariant mass of the two leptons)
- 30 GeV p_{Tmax}^{ℓ}<55 GeV (lepton with the largest p_T)
- $p_{Tmin}^{\ell} > 25$ GeV (lepton with the smallest p_T)

Figure 10.3 shows the transverse momentum of the leading jet for HERWIG and MC@NLO. The shapes look very similar, except in the high p_T region. MC@NLO produces harder jets

[2]The isolation variable was defined as the ratio of the energy sum of all stable particles inside a narrow cone around the lepton (ΔR=0.15) over the energy sum of all stable particles inside a larger cone (ΔR=0.5). The isolation variable has then to be larger than 0.9. The p_T of an isolated lepton should be larger than 10 GeV.

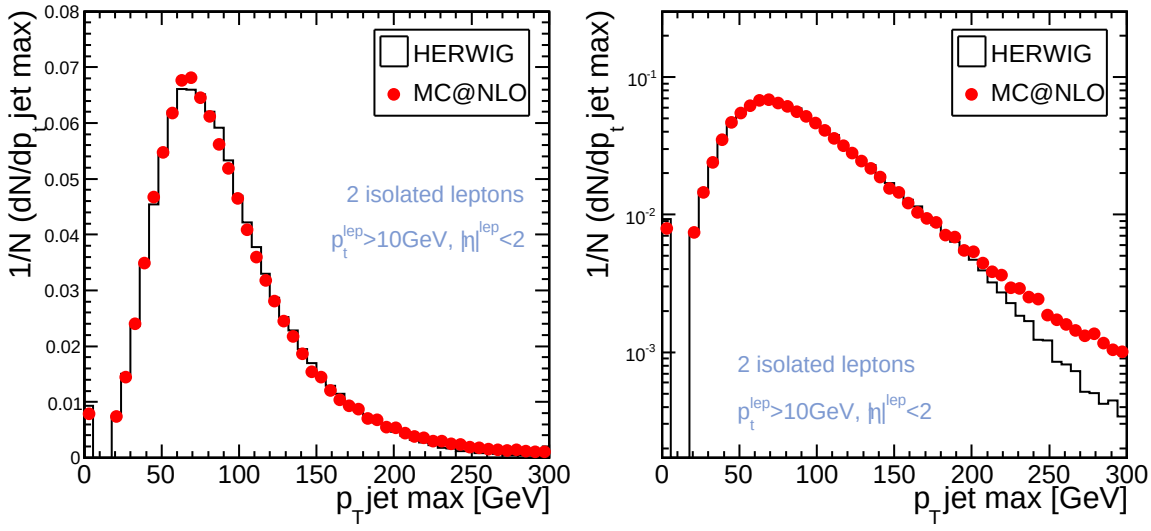

Figure 10.3: The p_{T} distribution of the leading jet in HERWIG and MC@NLO in linear and logarithmic scale.

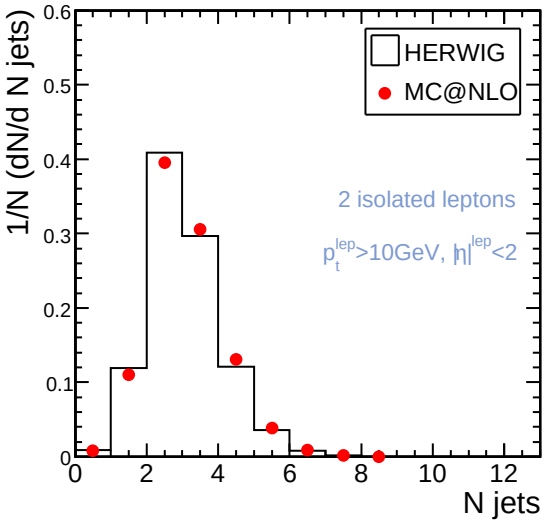

Figure 10.4: The number of jets in HERWIG and MC@NLO.

than HERWIG. This is not surprising since HERWIG, as a LO parton shower Monte Carlo generator, produces jets rather correctly in the soft and collinear region, but is inaccurate in the high p_{T} region, as discussed in Chapter 5. As a jet veto is applied in the selection cuts, the two Monte Carlo generators are very similar in our region of interest. Figure 10.4 shows that about the same number of jets are generated in HERWIG and MC@NLO. The

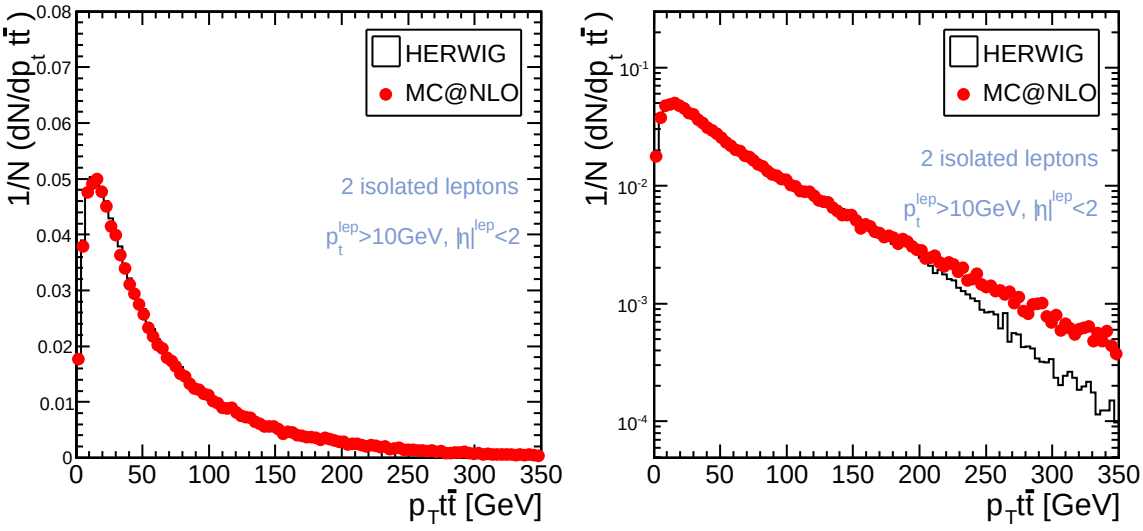

Figure 10.5: The p_T distribution of the $t\bar{t}$ system in HERWIG and MC@NLO in linear and logarithmic scale.

transverse momentum of the $t\bar{t}$ system is plotted in Figure 10.5 for HERWIG and MC@NLO. The $p_T^{Jet\ max}$ and $p_T^{t\bar{t}}$ variables are strongly correlated, as the $t\bar{t}$ system is balanced by jets. The transverse momentum spectrum is harder in MC@NLO, but HERWIG and MC@NLO agree very well at low p_T.

Table 10.1 shows the number of events and the relative selection efficiencies[3] for HERWIG and MC@NLO. In order to investigate the NLO contribution, one has to compare the first four columns, corresponding to MC@NLO and HERWIG without spin correlations. One would expect differences mostly in the jet veto efficiency and the isolation: these differences are actually very small. The relative efficiency of the jet veto in MC@NLO is 0.029 while in HERWIG its 0.032. As there are already two b-jets in the $t\bar{t}$ final state, the jet veto will tend to be less sensitive to additional jet activity. In addition, the shapes of all the other cut variables are very similar in MC@NLO and HERWIG without spin correlation.

This comparison shows that the NLO contribution has a small effect on the shapes of the variables considered and the selection efficiencies for the phase space relevant for the H $\rightarrow$ WW search. The region where NLO makes a difference is only at very high p_T whereas the bulk of the selected events is in the low p_T region. It should therefore be safe to use an inclusive K-factor.

[3]Relative efficiency means here the ratio between the number of events after and before the cut is applied.

	MC@NLO 2.31 without spin corr.		HERWIG 6.508 without spin corr.		HERWIG 6.508 with spin corr.	
	events	rel. eff.	events	rel. eff.	events	rel. eff.
2 isol. leptons	280656	0.2807±0.0004	284876	0.2849±0.0004	288015	0.2880±0.0004
$\lvert\eta^{\ell ep}\rvert < 2$	197614	0.7041±0.0009	193553	0.6795±0.0009	196034	0.6806±0.0009
jet veto	5764	0.0292±0.0004	6159	0.0318±0.0004	6046	0.0308±0.0004
$E_{\mathrm{T}}^{\mathrm{miss}} > 40$	4027	0.699±0.006	4414	0.717±0.006	4489	0.743±0.006
$\phi_{\ell\ell} < 45°$	608	0.151±0.006	632	0.143±0.005	724	0.161±0.006
5 GeV< $m_{\ell\ell} < 40$ GeV	354	0.58±0.02	379	0.60±0.02	416	0.57±0.02
30 GeV< $p^{\ell}_{\mathrm{Tmax}} < 55$ GeV	164	0.46±0.02	194	0.51± 0.03	191	0.46±0.02
p^{ℓ}_{Tmin} >25 GeV	71	0.43±0.04	76	0.39±0.04	77	0.40±0.04

Table 10.1: Number of events after selection cuts for MC@NLO and HERWIG with and without spin correlation. The relative efficiency is given after each specific cut is applied. One million events were generated with each Monte Carlo.

10.3 $t\bar{t}$ Production and the Effect of the Showering Model

The effects of different showering models on the variable shapes and selection efficiencies is studied by comparing PYTHIA 6.227 with HERWIG without spin correlations, as PYTHIA does not include spin correlations in this process yet.
Figure 10.6 shows the number of jets and Figure 10.7 the p_{T} spectrum of the hardest jet for PYTHIA and HERWIG. On average, PYTHIA produces fewer and softer jets than HERWIG. The shape of the transverse momentum of the $t\bar{t}$ system is slightly different in PYTHIA and HERWIG. Less events are predicted by HERWIG in the low p_{T} region whereas PYTHIA predicts more events in the high p_{T} region, as shown in Figure 10.8. The shapes of the other selection variables show no large differences. As an example, Figure 10.9 shows the maximum lepton transverse momentum before and after the selection cuts. The forth column in Table 10.1 and the second column in Table 10.2 show the relative efficiencies of PYTHIA and HERWIG without spin correlations. The isolation of the leptons is very similar in HERWIG and in PYTHIA, however the jet veto leads to a higher acceptance of the $t\bar{t}$ background in PYTHIA with respect to HERWIG, as the jets are softer and therefore fewer events are rejected. The relative efficiency ϵ in HERWIG is 0.032 while in PYTHIA it is 0.037. The difference is thus about 15 %.
This comparison shows that for the phase space relevant to the $H \rightarrow WW$ search, HERWIG and PYTHIA predict very similar lepton distributions and relative selection efficiencies, while jets from the $t\bar{t}$ system are somewhat different. PYTHIA produces fewer and softer jets than HERWIG. The difference due to the showering model can therefore be mostly observed in the jet veto efficiency and is around 15 %.

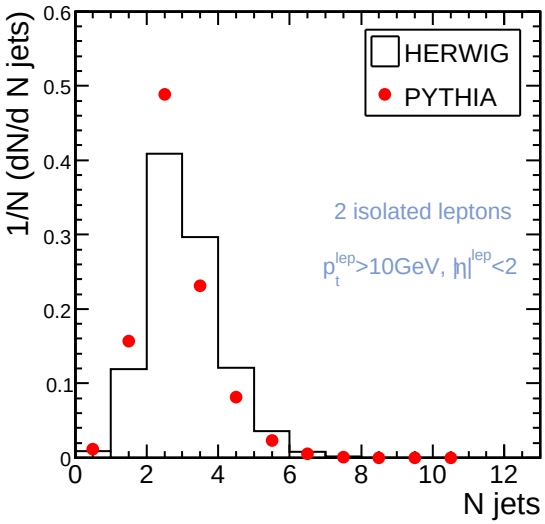

Figure 10.6: The number of jets in HERWIG and PYTHIA

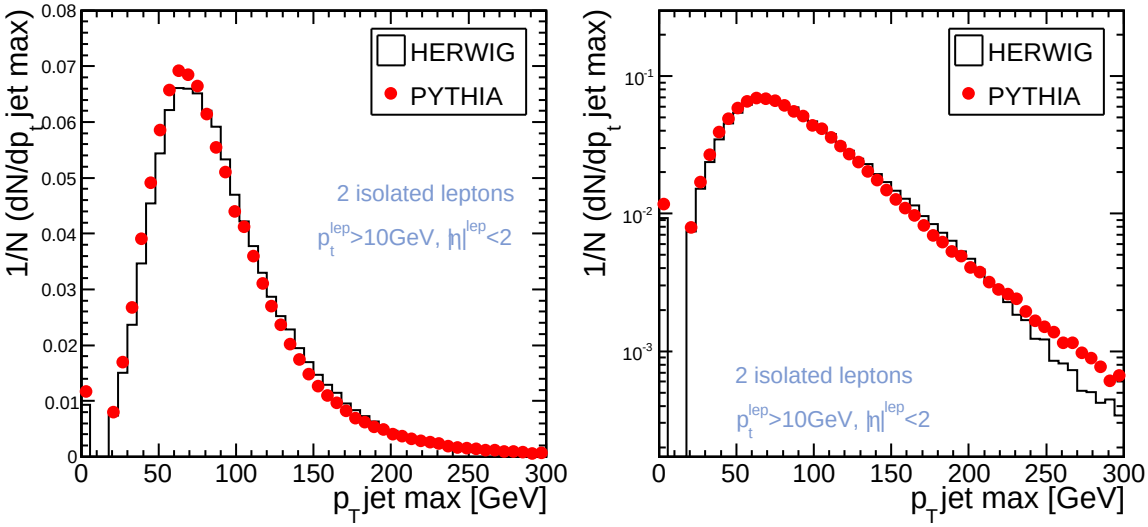

Figure 10.7: The p_{T} distribution of the leading jet in HERWIG and PYTHIA in linear (left) and logarithmic scale (right).

This shows that the uncertainty due to different showering models is rather large, mostly due to the different treatment of jets, observed in the p_{T} spectrum of the $t\bar{t}$ systems. In addition, we found in [125] that the new p_{T} ordered showering model of PYTHIA predicts the p_{T} spectrum of the jets and $t\bar{t}$ system similar to the HERWIG spectrum.

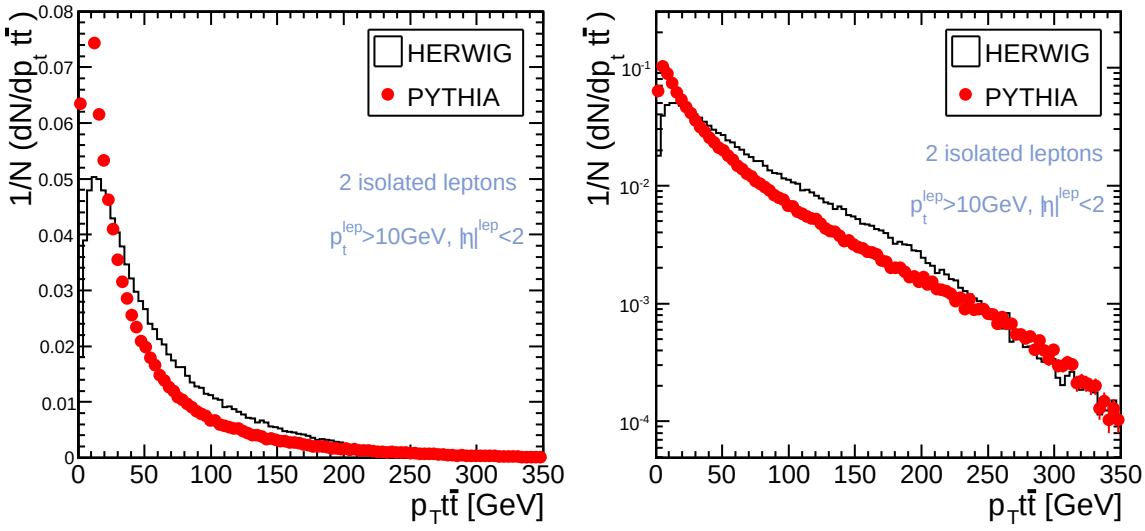

Figure 10.8: The p_{T} distribution of the $t\bar{t}$ system in HERWIG and PYTHIA in linear (left) and logarithmic scale (right).

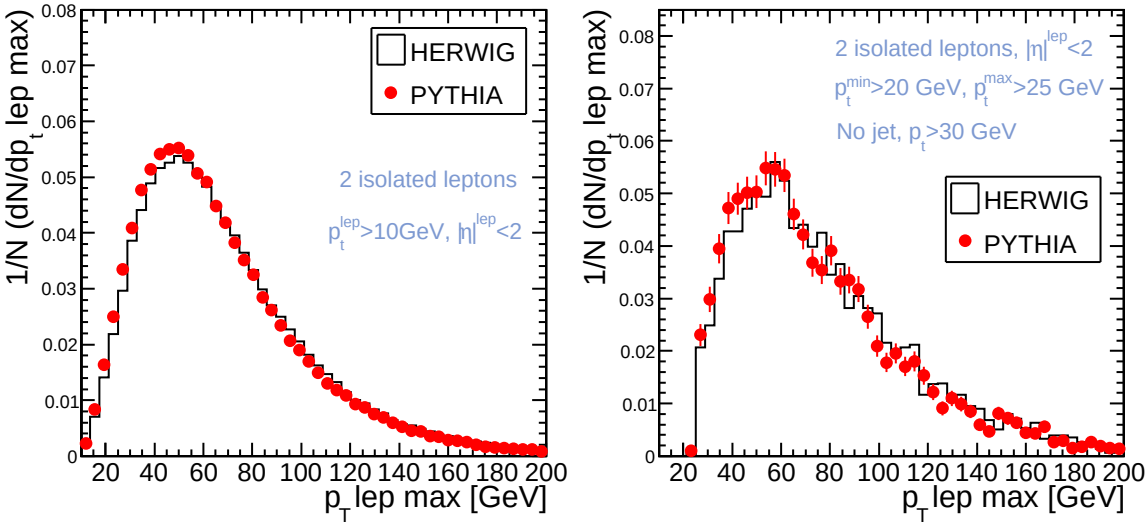

Figure 10.9: The p_{T} distribution of the lepton with the highest p_{T} in HERWIG and PYTHIA before (left) and after (right) the main cuts are applied.

10.4 Effect of the Spin Correlations

To study the effect of the spin correlations, the TopReX Monte Carlo is used. TopReX includes the full spin-correlation structure and an exact treatment of the top mass. The parton

	PYTHIA 6.227 without spin corr.		TopReX without spin corr.		TopReX with spin corr.	
	events	rel. eff.	events	rel. eff.	events	rel. eff.
2 isol. leptons	281624	0.2816±0.0004	293670	0.2937±0.0005	295707	0.2957±0.0005
$\|\eta^{\ell ep}\| < 2$	195343	0.6936±0.0009	203689	0.6936 ± 0.0009	205605	0.6953 ±0.0009
jet veto	7128	0.0365±0.0004	7804	0.0383±0.0004	7834	0.0381±0.0004
$E_{\mathrm{T}}^{\mathrm{miss}} > 40$	4976	0.698±0.005	5442	0.697±0.005	5586	0.713±0.005
$\phi_{\ell\ell} < 45^{\circ}$	731	0.147±0.005	801	0.147±0.005	962	0.172±0.005
5 GeV < $\mathrm{m}_{\ell\ell} < 40$ GeV	434	0.59±0.02	499	0.62±0.02	594	0.62±0.02
30 GeV< p^{ℓ}_{Tmax}< 55 GeV	214	0.49±0.02	258	0.52±0.02	296	0.50±0.02
p^{ℓ}_{Tmin} >25 GeV	85	0.40±0.03	113	0.44±0.03	125	0.42±0.03

Table 10.2: Number of events after selection cuts for PYTHIA and TopReX with and without spin correlations. The relative efficiency is given after each specific cut is applied. One million events were generated with each Monte Carlo.

shower simulation is provided by PYTHIA. TopReX with spin correlations is compared to PYTHIA and TopReX without spin correlations[4]. In a similar comparison, HERWIG with spin correlations is compared to HERWIG without spin correlations.
Differences originating from the inclusion of spin correlations are seen in the mass of the dilepton system and in the $\phi_{\ell\ell}$ distribution. Figure 10.10 shows the angle $\phi_{\ell\ell}$ between the leptons for the samples with and without spin correlations. In the left plots, the only requirement is to have two isolated leptons with $p_{\mathrm{T}} > 10$ GeV and $|\eta| < 2$. In the right plots, an additional jet veto is applied. A similar but smaller effect is observed in the $m_{\ell\ell}$ distribution. PYTHIA and TopReX without spin correlations (Figure 10.10) show the same $\phi_{\ell\ell}$ distribution. The difference in the distribution with and without spin correlations is slightly larger in the TopReX case than in the comparison with HERWIG. This is most probably due to the fact that TopReX does not the allow the top quarks to radiate gluons. In both comparisons one can see that the spin correlations make the $\phi_{\ell\ell}$ distribution flatter. After a jet veto is applied, the distributions with and without spin correlations look more similar.
The Higgs boson selection criteria were applied on both samples and Table 10.1 and 10.2 show the results. The relative efficiency after the $\phi_{\ell\ell}$ cut is 0.14 in HERWIG without spin correlations and 0.16 in HERWIG with spin correlations, while it's 0.15 in TopReX without spin correlations and 0.17 in TopReX with spin correlations. The relative efficiency in TopReX is slightly higher than in HERWIG. The difference of the relative efficiencies with and without spin correlations is about the same in both the TopReX and the HERWIG case. In conclusion, the difference due to the spin correlations is around 10%. Moreover the difference due to the use of diverse showering models is around 15% between HERWIG and

[4]The difference between PYTHIA and TopReX without spin correlation is mostly due to the fact that the top quarks are not allowed to radiate gluons in TopReX, and the different treatment of m_{top}.

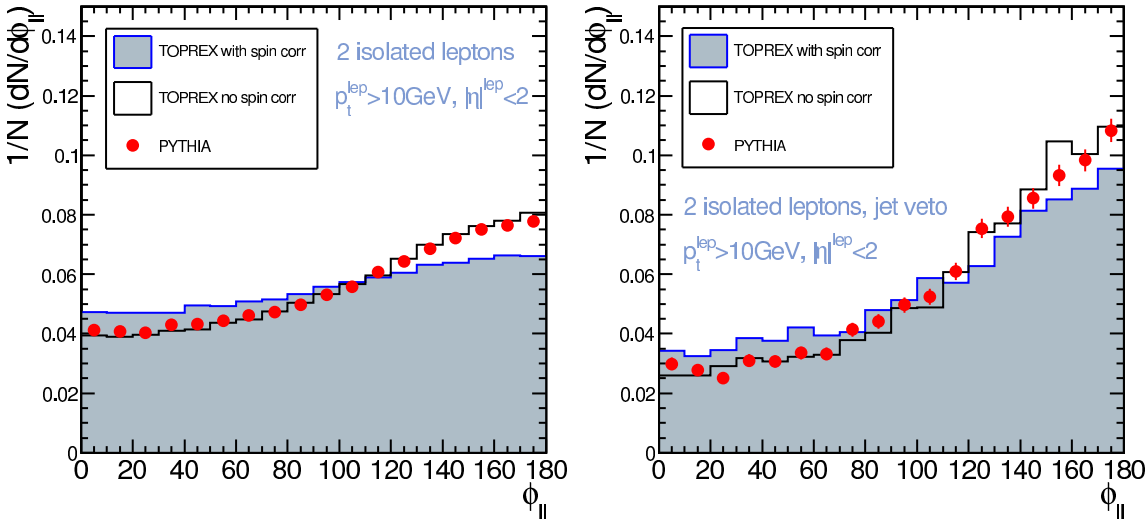

Figure 10.10: $\phi_{\ell\ell}$ distributions of the angle between the leptons in the plane transverse to the beam. TopReX with and without spin correlations is shown, as well as PYTHIA. On the left, only very basic cuts are applied, whereas on the right a jet veto is applied in addition. The Higgs-signal selection requires $\phi_{\ell\ell} < 45°$.

PYTHIA and 20% between TopReX and HERWIG.
These uncertainties are relatively large and it is therefore important to find a method how the $t\bar{t}$ background can be constraint using data. A method to do this will be presented in Chapter 11.

Chapter 11

H → WW → $\ell\nu\ell\nu$: Full Detector Simulation

It was shown in the last chapters how higher order QCD corrections can be included in the gg → H → WW → $\ell\nu\ell\nu$ analysis for the signal as well as for the nonresonant WW background qq → WW, and the top background processes $t\bar{t}$ and Wtb. In order to establish a full gg → H → WW → $\ell\nu\ell\nu$ analysis, a full detector simulation is needed together with a determination of the potential background systematics. To determine the discovery potential, the statistical and systematic uncertainties have to be included as precisely as possible.

11.1 Statistics and Systematics

The significance (or "number of standard deviation") of a signal above background is in the simplest form (without systematic uncertainties) given by

$$\text{Significance } \sigma_N = \frac{N_S}{\sqrt{N_B}}. \tag{11.1}$$

For a large number of events, the statistical fluctuations are approximately Gaussian. For a small number of events, the Poisson distribution is used. The statistical error for a large number of events N is approximately given by $\sqrt{N}$.
For example, one can consider a process with 5000 signal events and 10^6 background events remaining after cuts are applied. The signal over background ratio is then 0.005 and the signal significance could be claimed to be 5 standard deviations, withouth taking into account systematic errors ($\sigma_N = N_S/\sqrt{N_B} = 5000/\sqrt{10^6} = 5$). If more events would be simulated, the significance increases with $\sqrt{\mathcal{L}}$ (and therefore, as the cross section remains invariant, with $\sqrt{N}$). Obviously, the signal over background ratio would remain constant. If the background of 10^6 events would be increased by a factor 4 while the signal events remain the same, the significance of the process would still correspond to about 2.5 σ_N standard deviations, as the background enters the significance in the form $1/\sqrt{N_B}$, and thus in this example the significance is only reduced by a factor 1/2.
However, the significance changes drastically once background systematics are considered. In the considered example, e.g. a 1% background uncertainty, corresponding to 10000 events,

would prevent any signal detection. The $S/\Delta B$ ratio must thus be larger than 5 to obtain a 5σ signal significance. Therefore it is important to know the background as accurately as possible. In order to get a realistic estimate of the significance of a signal, one has to include systematic and statistical uncertainites.
In the following a full detector analysis is presented including most recent theoretical inputs and data driven background systematics.

11.2 The CMS Reconstruction Chain

In order to study the response of the detector and get as realistic events as possible in the simulation, events are generated with a parton shower Monte Carlos (normally PYTHIA or TopReX is used in CMS) and fed into the full detector simulation chain. The kinematics of the physics process is thus given by the Monte Carlo generator. Out of the particles produced in the interaction, only stable particles can be detected. Stable in this sense means that they travel a long enough distance through the detector before they would decay. Thus electrons, photons, muons, $K^{\pm}$, $\pi^{\pm}$, K^0_L, protons and neutrons can be detected. The interactions of these stable particles with the different sub-detectors are then simulated.
The program chain used to simulate the CMS detector is shown in the following, illustrated in Figure 11.1. The CMKIN program simulates the kinematics of the physics process, using an event generator like PYTHIA [126]. The output of CMKIN is a file containing a list of the generated particles and their corresponding 4-vectors. The interactions with the different subdetectors is then simulated with the GEANT program. The CMS specific version of GEANT [127], which uses the detector geometry and materials as well as the magnetic field configuration, is called OSCAR, for the C++ version, and CMSIM for the older Fortran version. The output of GEANT is a collection of so-called hits, which are defined every time a particle crosses a sensitive element of the detector and contains information about the position and time of the hit, the energy or charge deposit. At this step, pile-up and minimum bias events can be added. The hits are then transformed to signals (by simulating the electronic output), and so-called digis are obtained. The final step is performed with the so-called ORCA (Object Oriented Reconstruction for CMS Analysis) software [128]. ORCA reconstructs then the so-called RecHits, which translate the electronic signal into quantities like e.g. the energy deposited. As an example, ORCA translates a group of ADC counts in the ECAL in the amount of energy deposited in a crystal.

The subdetector responses are then combined within ORCA to reconstruct the different elements of the physics process signature, like electrons, photons, jets etc. The output are so-called RecObjects.
For the analysis described in the following, digis were processed running ORCA to reconstruct the different elements (clusters, tracks etc) of a given process. Finally, a program called PAX [129] was used to create the output file for analyses (in the form of root-files [130]). PAX is a set of C++ classes, based on 4-vectors, providing a convenient tool to analyze the reconstructed event.
During 2006 the CMS collaboration has decided to replace this software framework (ORCA and OSCAR were reconstruction and simulation frameworks) by a single new framework – the CMSSW [131], which will be ready in 2007.

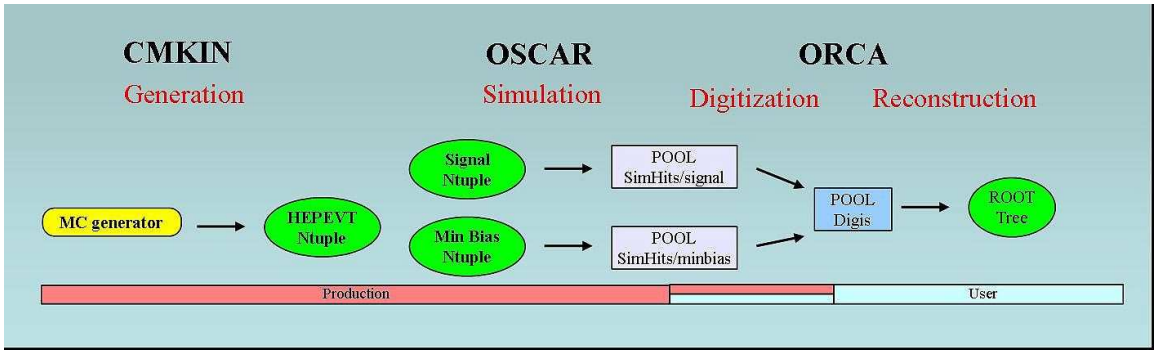

Figure 11.1: The CMS reconstructions chain, including CMKIN, OSCAR and ORCA.

11.3 Event Reconstruction

Now we will discuss how leptons, jets and the missing transverse energy $E_{\mathrm{T}}^{\mathrm{miss}}$ are reconstructed in the event analysis. The generated events including low luminosity pile-up are passed through a GEANT simulation of CMS. The events are then reconstructed using the CMS software ORCA.

11.3.1 Trigger selection

In the following we will treat the Monte Carlo events as if they were data. Thus they are first passed through the global Level 1 (L1) trigger. The remaining events have to pass at least one of the following High Level Trigger (HLT) paths: single-electron, double-electron, single-muon or double-muon trigger. The dotted curve in Figure 11.2(a) shows the combined L1+HLT trigger efficiencies as a function of the Higgs boson mass. The trigger efficiency is reduced since the W boson decays into τ are simulated but no specific τ trigger is used. The dashed curve shows the L1+HLT trigger efficiency for the events where the W bosons decay into electron and muons.
To estimate the number of 'useful events' rejected by this trigger requirement it is interesting to look at the trigger efficiency on events having exactly two leptons which fulfill the lepton selection cuts defined in section 11.3.2. In Figure 11.2(a) the solid curve shows the trigger efficiency for such events. In this case, the trigger efficiency is higher than 95% on the full mass range. Figure 11.2(b) shows this trigger efficiency for events with muon-muon, electron-muon and electron-electron final states. The trigger efficiency for muons is close to 100% whereas for electrons it is around 96%. In the future it would be interesting to study methods to recover this 4% loss (e.g. by a better Bremsstrahlung recovery or by using asymmetric di-electron triggers).

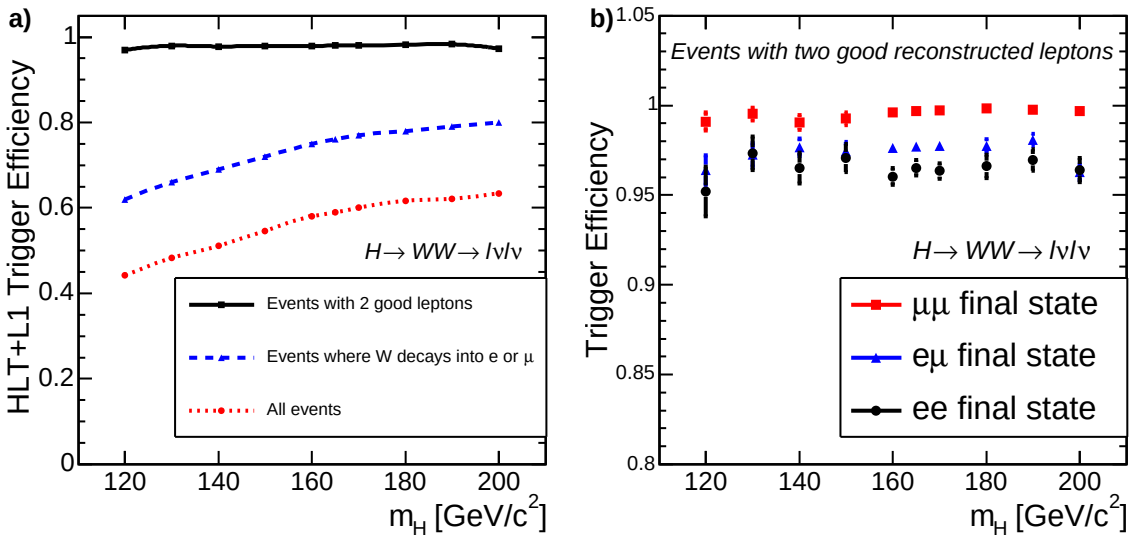

Figure 11.2: Trigger efficiencies as a function of the Higgs mass. (a) L1+HLT trigger efficiency for all generated events (W $\rightarrow e, \mu, \tau, \nu$)(dotted line), events where the W bosons are forced to decay in electrons and muons (dashed line) and for events where exactly two leptons pass the lepton selection cuts (solid line). (b) The trigger efficiency for events with two leptons passing the lepton selection cuts for muon-muon (squares), electron-muon (triangles) and electron-electron (circles) final states.

11.3.2 Lepton Selection and Reconstruction

Events are required to have exactly two opposite-charge leptons, electrons or muons, with $p_{\mathrm{T}} > 20$ GeV and $|\eta| < 2$, since the leptons from signal events are mainly central.
The efficiency to reconstruct a muon candidate with $p_{\mathrm{T}} > 20$ GeV and $|\eta| < 2$, corresponding to a generated muon with $p_{\mathrm{T}} > 20$ GeV and $|\eta| < 2$ ($\Delta R < 0.15$) is 97%, when looking at events accepted by the HLT. Additional isolation requirements are imposed. The energy in the calorimeters around the muon candidate, within a $\Delta\mathrm{R} = 0.3$ cone, must be lower than 5 GeV and the sum of the p_{T} of the tracks within a $\Delta\mathrm{R} = 0.25$ cone around the muon candidate must be lower than 2 GeV. This muon selection has an efficiency of 94% for muons in events which pass the HLT trigger. The separate efficiencies of the selection cuts are listed in Table 11.1(a).
Electrons are reconstructed starting with Super Clusters in the ECAL matched with a track. A track is associated to a Super Cluster if it points to a Super Cluster requiring $\Delta R_{track-SC}$ <0.15. Super Clusters are retained only if $E_T(SC) > 20$ GeV and $|\eta(SC)| < 2$. The efficiency to find such a Super Cluster within $\Delta R = 0.2$ of a generated electron with $p_{\mathrm{T}} > 20$ GeV and $|\eta| < 2$ is 92% for events that pass the HLT. The efficiency to find such a Super Cluster is around 80% if they are not required to pass the HLT. The HLT already applies preselection cuts such as a minimal p_{T}, a rough matching between the track and the cluster, a basic isolation, and cuts on the E_{hcal}/E_{ecal} ratio (called "H/E"). An electron candidate must then fulfill the following identification requirements:

- It deposits little energy in the HCAL: $E_{hcal}/E_{ecal} < 0.05$
- A precise matching of the electron track and cluster is required:
  in direction: $|\eta_{track} - \eta_{SC\,corr}| < 0.005$ and $|\phi_{track\,prop} - \phi_{SC}| < 0.02$[1]
  in magnitude: $E/p > 0.8$ and $|1/E - 1/p| < 0.02$

Finally, the electron candidate must be isolated by requiring $\sum_{tracks} p_T(track)/E_T(SC) < 0.05$ where the sum runs over all tracks with:

- $\Delta R_{SC-track} < 0.2$
- $p_T^{track} > 0.9$ GeV
- $|z_{track} - z_{electron}| < 0.2$ cm, where z is the position of the track along the beam line

This electron selection, applied on Super Clusters with an associated track, a transverse energy higher than 20 GeV and a pseudorapidity smaller than 2, has an efficiency of 87%. The efficiencies of each cut are listed in Table 11.1(b). Finally, a cut on the impact parameter

(a)

Muon selection	
Cut applied	Selection efficiency
Calorimeter isolation	96%
Tracker isolation	94% (98%)

(b)

Electron selection	
Cut applied	Selection efficiency
Isolation criteria	95%
$E_{hcal}/E_{ecal} < 0.05$	94% (99%)
$\|\eta_{track} - \eta_{SC\,corr}\| < 0.005$	92% (98%)
$\|\phi_{track\,prop} - \phi_{SC}\| < 0.02$	91% (99%)
$E/p > 0.8$	91% (100%)
$\|1/E - 1/p\| < 0.02$	87% (96%)

Table 11.1: The absolute and, in parentheses, relative efficiency (with respect to the previous cut) for (a) the muon selection-cuts and (b) the electron selection-cuts. The cuts are applied on leptons in events that are required to pass the HLT, which accepts mainly good leptons.

significance σ_{IP}, is applied in order to reduce the $b\bar{b}$ background. Each lepton is required to have $\sigma_{IP} < 3$. The two leptons are also required to come from the same vertex by demanding $|z_{lep1} - z_{lep2}| < 0.2$ cm.
The contribution of reducible background processes, like W+jet where one jet is misidentified as a lepton, is expected to be small [133].

[1]Where $\eta_{SC\,corr}$ is the Super Cluster pseudorapidity corrected for the vertex position and $\phi_{track\,prop}$ is the track angle propagated in the magnetic field up to the ECAL cluster position.

11.3.3 Jet Reconstruction

The inclusive cross section for $t\bar{t}$ background is at least 40 times larger than the signal cross section. This background can be strongly reduced by applying a jet veto. The reconstruction of jets is thus fundamental to ensure an efficient background rejection. At the LHC with the expected large number of pile-up events, it is important to differentiate between 'real' and 'fake' jets. Fake jets are expected to come from the underlying event, pile-up and noise. Their presence tends to reduce signal and background in a similar (but perhaps badly simulated) way.

The jets are reconstructed using a cone algorithm of $\Delta R = 0.5$ on calorimeter towers with $|\eta| < 4.5$ and $E_T^{tow} > 0.5$ GeV and $E^{tow} > 0.8$ GeV[2]. With the reconstruction software used for this study, the calibration constants were not available at the time for a jet transverse energy below 25 GeV. However the absolute value of the jet energy is not needed for our analysis, since we only apply a jet veto. Thus the raw energy of the jets is used for this study. For the jet energies relevant for our study, a generated jet transverse energy $E_T(jet)$ corresponds to 1.5-2 times the reconstructed jet transverse energy $E_T(raw)$ (where raw means that no calibration was applied).

In contrast to the signal, the kinematics of the $t\bar{t}$ process favors events with at least one central jet, as shown in Figure 11.3. Therefore we apply only a veto on events with central jets. This avoids also potential problems with fake jets in the forward region, as shown in the following. To estimate the contamination due to fake jets, it is useful to look at the

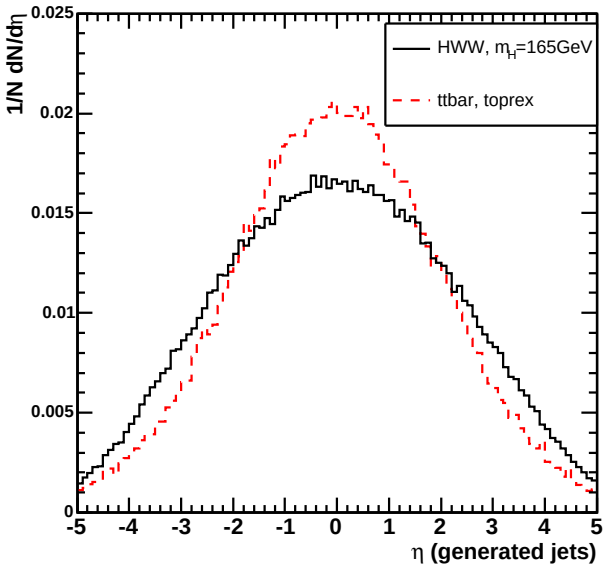

Figure 11.3: The pseudorapidity distribution for the generated jets in the signal sample for $m_H = 165$ GeV (solid line) and the $t\bar{t}$ sample (dashed line) without cuts.

[2]An additional cut on the tower energy is applied in order to reduce the fake jets coming from calorimeter tower noise and which are reconstructed mainly around $|\eta| \approx 0$ if only a cut on the tower transverse energy is applied.

generated jets. Here 'generated jets' means jets from the generator tree without detector simulation but using the same algorithms as the reconstructed jets. A jet is then considered 'real' if it can be matched to a generated jet, having $\Delta R_{gen-recjet} < 0.3$.
Figure 11.4 shows the fraction of matched jets over the total number of jets as a function of the raw transverse energy of the jet. The dots show the ratio of matched jets over the total number of jets without restricting the jet pseudorapidity and the dots shows the ratio of matched jet over all jets for jets with $|\eta_{jet}| < 2.5$.
A large number of fake jets decreases when applying an upper cut on η. For a raw jet energy above 20 GeV, the number of fake jets is negligible. In order to increase the background

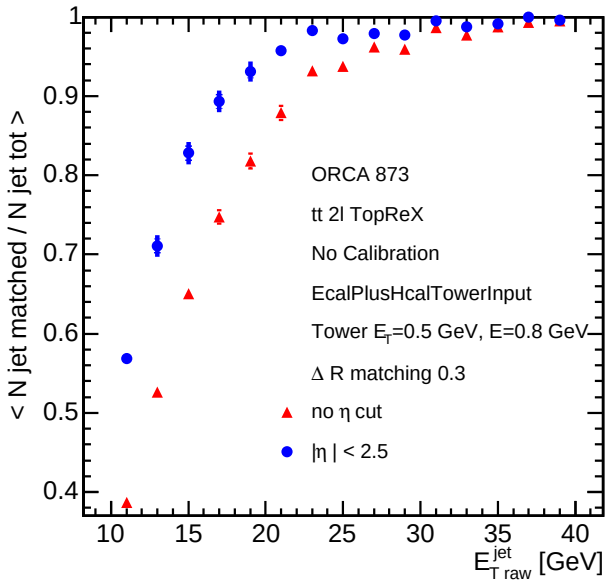

Figure 11.4: Ratio of reconstructed jets matched to a generated jet over all reconstructed jets as a function of the jet E_T^{raw}. The dots show all jets, while the triangles show all the jets with $|\eta_{jet}| < 2.5$. For a E_T^{raw} of 15 GeV for example, this means that around 35% of the reconstructed jets are fake jets, before a cut on $|\eta_{jet}|$ is applied, and around 18% after the cut is applied.

rejection, jets with a raw transverse energy smaller than 20 GeV could perhaps also be vetoed. However, as Figure 11.4 shows, the number of jets without an associated generated jet, so-called 'fake' jets, is quite high when the raw energies are below 20 GeV. In order to reduce these fake jets, it is useful to consider the track content of the jets, defining a so-called alpha parameter α [3]. Alpha is defined to be the ratio of the sum of p_{T} of all tracks inside the jet divided by the transverse jet energy in the calorimeter:

$$\alpha \equiv \frac{\sum p_T(tracks)}{E_T(jet)} \tag{11.2}$$

[3]This method is based on an idea proposed first by N. Ilina, V. Gavrilov and A. Krokhotin.

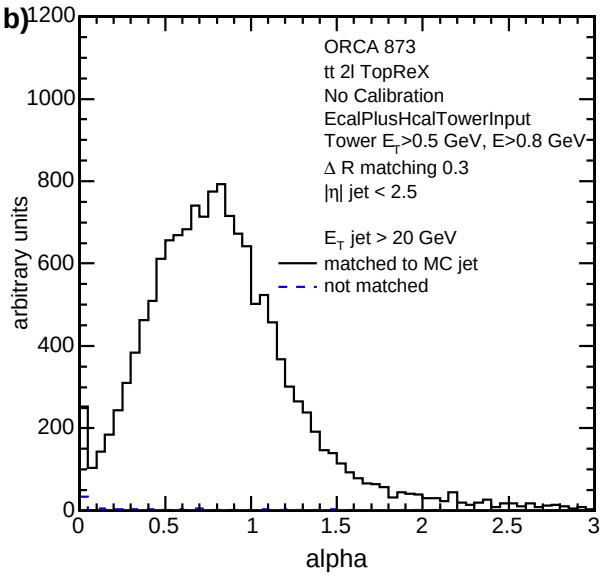

Figure 11.5: Alpha distribution for a jet transverse raw energy above 20 GeV.

For a perfect detector, the alpha parameter of a jet would be on average 0.66, because two thirds of a jet are charged particles. Fluctuations occur due to the jet multiplicities. The ratio is reduced by the detector energy resolution and the fact that particles need a minimal energy in order to be detected. In a fake jet, the alpha parameter looks different, as underlying events contain a lot of low p_T particles, where the neutral particles leave energy in the ECAL but the charged tracks are curled up in the magnetic field, and thus no associated track to a jet in the calorimeter is found. This magnetic field effect leads to an alpha parameter around zero.
To calculate the alpha of a jet, the following tracks are selected: First they have to be 'inside' the jet, i.e. $\Delta R_{track-jet} < 0.5$. Then they have to come from the event vertex [4], fulfilling $|z_{trk} - z_{vtx}| < 0.4$ cm. Finally, these tracks should have more than 5 hits and $p_{\mathrm{T}} > 2$ GeV.
For a jet transverse energy above 20 GeV, almost all jets are matched to the generated jets, as shown in Figure 11.5 and Figure 11.4. Below 20 GeV however, the unmatched jets tend to have an alpha parameter around 0. Therefore, fake jets can be reduced by requiring alpha > 0.2. Figure 11.6 shows the fraction of matched jets over the total number of jets as a function of E_T^{raw} for jets with $|\eta| < 2.5$. The dots show this fraction for jets with alpha > 0.2, whereas the triangles show jets without a cut on alpha. The matching efficiency increases by about 10% for jets between 15 and 20 GeV when the cut on alpha is applied. Adding a cut on alpha for jets with a raw transverse energy between 15 and 20 GeV allows to efficiently veto jets, keeping the fake rate low and a reasonable efficiency for the signal. This jet veto corresponds roughly to requiring that no quark or gluon with energy 40 GeV or above is produced. Summarizing, jets are reconstructed in this analysis using a cone algorithm with a cone size 0.5, using calorimeter towers with raw energy of $E_T^{tow} > 0.5$ GeV

[4]The event vertex is defined as the mean z position of the two leptons.

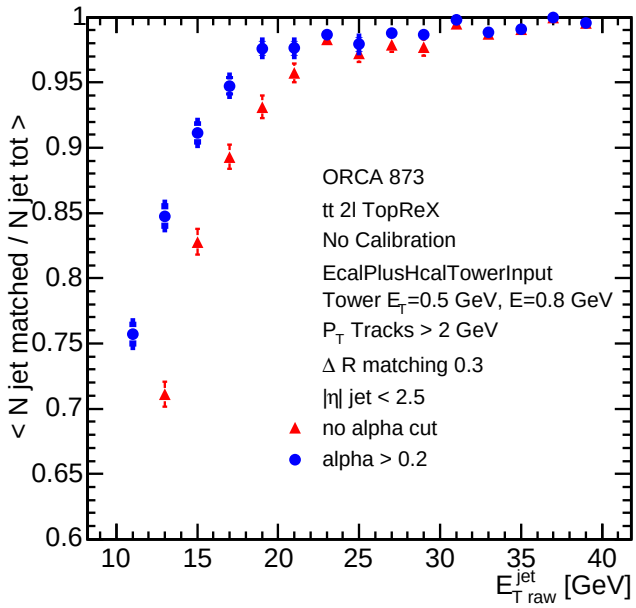

Figure 11.6: Fraction of matched jets to a generated jet over all reconstructed jets as a function of $E_{T\,raw}^{jet}$ for jets built with a constant tower energy cut and requiring $|\eta_{jet}| < 2.5$. The dots are the ones where a cut on alpha is applied, whereas triangles correspond to the sample where no alpha cut is applied.

and $E^{tow} > 0.8$ GeV. No calibration is applied on the jet energy. In order to reduce fake jets, we require that jets have $|\eta| < 2.5$. and for jets with E_T^{raw} between 15 and 20 GeV, it is further required that the sum of transverse momenta of all tracks associated to the jet represents a substantial fraction of the transverse jet energy (alpha > 0.2). For the signal selection, events containing such jets will be vetoed.
The missing energy is reconstructed by summing up the raw energy of all ECAL and HCAL towers, and correcting for muons. Since a jet veto is applied in the signal selection, further corrections to the missing energy did not lead to a significant improvement.

11.4 Simulation of Signal and Background

Having discussed the reconstruction of the leptons and jets, we now describe a full CMS detector simulation using ORCA 8.7.1. Details about this study can also be found in [132]. Table 11.2 lists the number of background events used in this study. The $H \rightarrow WW \rightarrow \ell\nu\ell\nu$ signal is simulated with PYTHIA 6.215, and between 20000 and 50000 events were generated, depending on the Higgs mass.
For simplification, the selection cuts are chosen to be mass independent, and are optimized

Channel	Generator version	Number of events
$WW \rightarrow \ell\ell$	PYTHIA 6.215	164000
$gg \rightarrow WW \rightarrow \ell\ell$	'ggWW' + PYTHIA 6.227	47000
$t\bar{t} \rightarrow \ell\nu\ell\nu bb$	TopReX 4.06	379271
$Wtb \rightarrow \ell\nu\ell\nu bb$	TopReX 4.06	191000
$WZ \rightarrow \ell\ell\ell\nu$	PYTHIA 6.215	92000
$ZZ \rightarrow \ell\ell/\nu\nu$	PYTHIA 6.215	56000

Table 11.2: The number of simulated background events used in this study together with version of the Monte Carlo generator.

for a Higgs with a mass between 160 and 170 GeV. Since the optimal values for these cuts, especially for the cuts on the lepton p_T depend on the Higgs mass, some more sophisticated tuning might be performed for other Higgs masses. However, to simplify the analysis of the background systematics, we choose to use fixed selection criteria which provide an acceptable signal to background ratio for Higgs masses between 150 GeV and 180 GeV.
The most important backgrounds are [5]:

- $qq \rightarrow WW \rightarrow \ell\nu\ell\nu$
- $gg \rightarrow WW \rightarrow \ell\nu\ell\nu$
- $qq \rightarrow t\bar{t} \rightarrow WbWb \rightarrow \ell\nu\ell\nu bb$
- $qq \rightarrow Wtb \rightarrow WbWb \rightarrow \ell\nu\ell\nu bb$

[5] For simplicity, no difference is made between the q and $\bar{q}$ production.

- $qq \rightarrow \mathrm{ZW} \rightarrow \ell\ell\ell\nu$
- $qq \rightarrow \mathrm{ZZ} \rightarrow \ell\ell\ell\ell, \ell\ell\nu\nu$

where three final states are reconstructed: ee, $\mu\mu$ and eμ. For the first time the gg $\rightarrow$ WW $\rightarrow \ell\nu\ell\nu$ background could be included in a full detector simulation. This background was calculated in LO in 2005 by two groups [80,81]. We then added parton showering to the parton level program provided by [81], and let it run through the full detector simulation of CMS. As was shown in [48], events from Drell-Yan (pp $\rightarrow \gamma$,Z) are negligible after the cuts on $E_{\mathrm{T}}^{\mathrm{miss}}$, m_{ll} and $\phi(ll)$ are applied. Similar, the W+jets background, where a jet is misidentified as a lepton, is not considered, as studies have shown that this background is very small and can be neglected [133].
The signal samples were generated using the PYTHIA Monte Carlo generator. The two major Higgs boson production modes relevant for the mass range under investigation were generated: gluon fusion and vector-boson fusion. Table 11.3 lists the cross section times H $\rightarrow$ WW branching ratio and the sum of branching ratios for W decaying into e, μ and τ[6] for different Higgs boson masses. The W boson decay into τ's (W $\rightarrow \tau\nu$) was also simulated but no specific τ reconstruction was applied: τ's are selected through their decays into e and μ. The cross sections are shown at leading order (LO), using the PYTHIA predictions,

	$\sigma^{LO} \times BR$ [pb] (PYTHIA)		$\sigma^{NLO} \times BR$ [pb]		
	Gluon fusion	VBF	Gluon fusion	VBF	Total
150 GeV	0.89	0.25	1.73	0.25	1.98
160 GeV	1.00	0.31	2.03	0.31	2.34
165 GeV	1.00	0.31	2.04	0.32	2.36
170 GeV	0.97	0.30	1.95	0.31	2.26
180 GeV	0.84	0.27	1.71	0.28	1.99

Table 11.3: The cross sections times branching ratio (H $\rightarrow$ WW, W $\rightarrow$ e, μ, τ) for Higgs boson production through gluon fusion and vector-boson fusion (VBF). The first two columns show the LO results from PYTHIA and the last three show the NLO results [134] used in this study.

and at next-to-leading order (NLO), using a calculation by M. Spira [134]. In order to get a consistent NLO estimate for the Higgs boson production through gluon fusion, the PYTHIA p_{T} spectrum was reweighted to the MC@NLO prediction, defining p_{T}-dependent K-factors as proposed in Ref. [76]. The CMS collaboration decided to use NLO cross sections where available. As this analysis was published as a CMS Note, we thus reweighted the PYTHIA events to the p_{T} spectrum of MC@NLO, instead of NNLO+NNLL. Including NNLO+NNLL corrections will have the effect that even less luminosity for a signal detection is required. Therefore, the results presented in this study represent a conservative estimate. The total cross section was then scaled to the NLO cross sections listed in Table 11.3.
For the backgrounds, continuum vector-boson production (WW, ZZ, WZ) was generated using PYTHIA. The $p_T(WW)$ spectrum was reweighted to the MC@NLO $p_T(WW)$ spectrum.

[6] No particular decay of τ is assumed.

A NLO cross section ($\sigma\times$ BR) of respectively 1.52 pb and 1.63 pb was assumed for ZZ and WZ production. WW production via gluon fusion was generated using a Monte Carlo provided by N. Kauer [81], using the parton shower simulation of PYTHIA. Top production

Process	$\sigma^{\mathrm{LO}} \times$ BR [pb]	$\sigma^{\mathrm{NLO}} \times$ BR [pb]
$qq \rightarrow \mathrm{WW} \rightarrow \ell\nu\ell\nu$	7.4	11.7
$\mathrm{gg} \rightarrow \mathrm{WW} \rightarrow \ell\nu\ell\nu$	0.48	-
$qq \rightarrow \mathrm{t\bar{t}} \rightarrow \mathrm{WbWb} \rightarrow \ell\nu\ell\nu\mathrm{bb}$	52.4	86.2
$qq \rightarrow \mathrm{Wtb} \rightarrow \mathrm{WbWb} \rightarrow \ell\nu\ell\nu\mathrm{bb}$	4.9	3.4
$qq \rightarrow \mathrm{ZW} \rightarrow \ell\ell\ell\nu$	0.88	1.63
$qq \rightarrow \mathrm{ZZ} \rightarrow \ell\ell\ell\ell, \ell\ell\nu\nu, \nu\nu\nu\nu$	1.06	1.52

Table 11.4: The cross sections times branching ratio BR(e, μ, τ) at LO given by PYTHIA (except for ggWW and Wtb) and at NLO for the different background processes [135]. The ggWW cross section is given in reference [81] and is generated using a matrix-element program linked to PYTHIA for the showering. This process is only known at LO. The Wtb cross section is calculated in Ref. [121], and details about the Wtb and $\mathrm{t\bar{t}}$production at NLO are described in 10.

($\mathrm{t\bar{t}}$ and Wtb) was generated using the TopReX Monte Carlo program. TopReX includes the full spin-correlation structure and an exact treatment of the top mass. The parton shower simulation is performed in PYTHIA. NLO cross sections of respectively 86.2 pb and 3.4 pb were used for $\mathrm{t\bar{t}}$ and Wtb [121]. Table 11.4 lists the cross sections times branching ratios for the different background processes and compares them with the LO cross section.

11.5 Kinematic Selection

The cuts used are similar to the ones described in Chapter 9. It was found that a better signal over background ratio could be obtained when some cuts were adjusted, which are the following:
The cut on $E_{\mathrm{T}}^{\mathrm{miss}}$ is stricter now ($E_{\mathrm{T}}^{\mathrm{miss}} > 50$ GeV), to better reduce the WW contribution, which shows a peak at 30 GeV, compared to 65 GeV for a signal at 165 GeV. This cut also reduces significantly the Drell-Yan background, which has a peak at 15 GeV. In addition, the upper cut on m_{ll} was lowered to 40 GeV instead of 45 GeV in the pure PYTHIA simulation. This cut reduces Drell-Yan events but also WW and $\mathrm{t\bar{t}}$ events which have a longer $m_{\ell\ell}$ tail than the signal (Figure 11.7(b)). A lower cut $m_{\ell\ell} < 12$ GeV was introduced to remove potential background from $\mathrm{b\bar{b}}$-resonances. It has a 97% efficiency on a 165 GeV Higgs boson signal.
The jet veto, which is mostly efficient against the $\mathrm{t\bar{t}}$ background, is now applied on the jet raw transverse energy at 15 GeV, which corresponds roughly to a veto on the corrected transverse energy of 25-30 GeV. In addition, the cuts on p_{Tmax}^{ℓ} are shifted by 5 GeV to 30 GeV and 55 GeV.
To give an uncertainty for the fact that the ggWW background is the only one which is not

known at NLO, the efficiency, after the jet veto is applied, is set to 1 [136] [7].
The cuts applied in this full detector analysis are summarized in the following. Starting with two oppositely-charged leptons fulfilling the cuts described above, these additional selection cuts were applied:

- E_T^{miss} >50 GeV (missing transverse energy)
- $\phi_{\ell\ell} < 45^\circ$ (angle between the leptons in the transverse plane)
- 12 GeV $< m_{\ell\ell} <$ 40 GeV (invariant mass of the two leptons)
- No jet with $E_T^{raw} > 15$ GeV and $|\eta|$ <2.5 (jet veto)
- 30 GeV $< p_T^{\ell\, max} <$ 55 GeV (lepton with the maximal p_T)
- $p_T^{\ell\, min} > 25$ GeV (lepton with the minimal p_T)

H $\rightarrow$ WW	$m_H = 150 GeV$	$m_H = 160 GeV$	$m_H = 165 GeV$	$m_H = 170 GeV$	$m_H = 180$ GeV
$\sigma \times$ BR(e, μ, τ) [fb]	1970	2330	2360	2250	1980
L1+HLT	1077 (55%)	1353 (58%)	1390 (59%)	1350 (60%)	1220 (62%)
2 lep, $\lvert\eta\rvert < 2$, $p_T > 20$GeV $\sigma_{IP} > 3$, $\lvert\Delta z_{lep}\rvert < 0.2$ cm	264 (25%)	359 (27%)	393 (28%)	376 (28%)	346 (28%)
$E_{\mathrm{T}}^{\mathrm{miss}} > 50$ GeV	150 (57%)	240 (67%)	274 (70%)	263 (70%)	239 (69%)
$\phi_{\ell\ell} < 45$	76 (51%)	139 (58%)	158 (58%)	139 (53%)	110 (46%)
12 GeV $< m_{\ell\ell} <$ 40 GeV	56 (73%)	107 (77%)	119 (75%)	100 (72%)	71 (64%)
Jet veto	29 (52%)	56 (52%)	63 (53%)	51 (51%)	35 (50%)
30 GeV< p_{Tmax}^{ℓ} <55 GeV	23 (80%)	49 (89%)	53 (85%)	41 (82%)	24 (68%)
$p_{\mathrm{Tmin}}^{\ell} > 25$ GeV	17 (75%)	42 (85%)	46 (86%)	33 (80%)	18 (76%)
$\varepsilon_{\mathrm{tot}}$	(0.86 ± 0.07)%	(1.80 ± 0.06)%	(1.95 ± 0.06)%	(1.47 ± 0.05)%	(0.91 ± 0.07)%

Table 11.5: The expected number of events for an integrated luminosity of 1 fb^{-1} for the signal with Higgs masses between 150 and 180 GeV. The relative efficiency with respect to the previous cut is given in parentheses. The last line shows the total selection efficiency together with the uncertainty from the limited Monte Carlo statistics.

These cuts were optimized to discover a Higgs boson with a mass between 160 and 170 GeV [8]. Tables 11.5 and 11.6 summarize, for the Higgs boson signal at different masses and the backgrounds, the number of expected events after each selection cut for 1 fb^{-1} integrated luminosity. The relative efficiencies are given in parentheses. The last line shows the total selection efficiency together with the error coming from the limited Monte Carlo statistics.
Figure 11.7(c) shows the $\phi_{\ell\ell}$ distribution for the signal and the different backgrounds after all other cuts are applied. A large broad signal above background is seen.
Figure 11.8 shows the $p_T^{\ell\, min}$ and $p_T^{\ell\, max}$ distributions for the sum of all backgrounds and the

[7] Another possibility for further investigation would be to use the same K-factors as for the signal, since it is also produced with two gluons in the initial state.

[8] For a specific study of a Higgs with a lower or higher mass in this channel a better efficiency could be obtained by defining mass dependent cuts. This will be done in an upcoming CMS study.

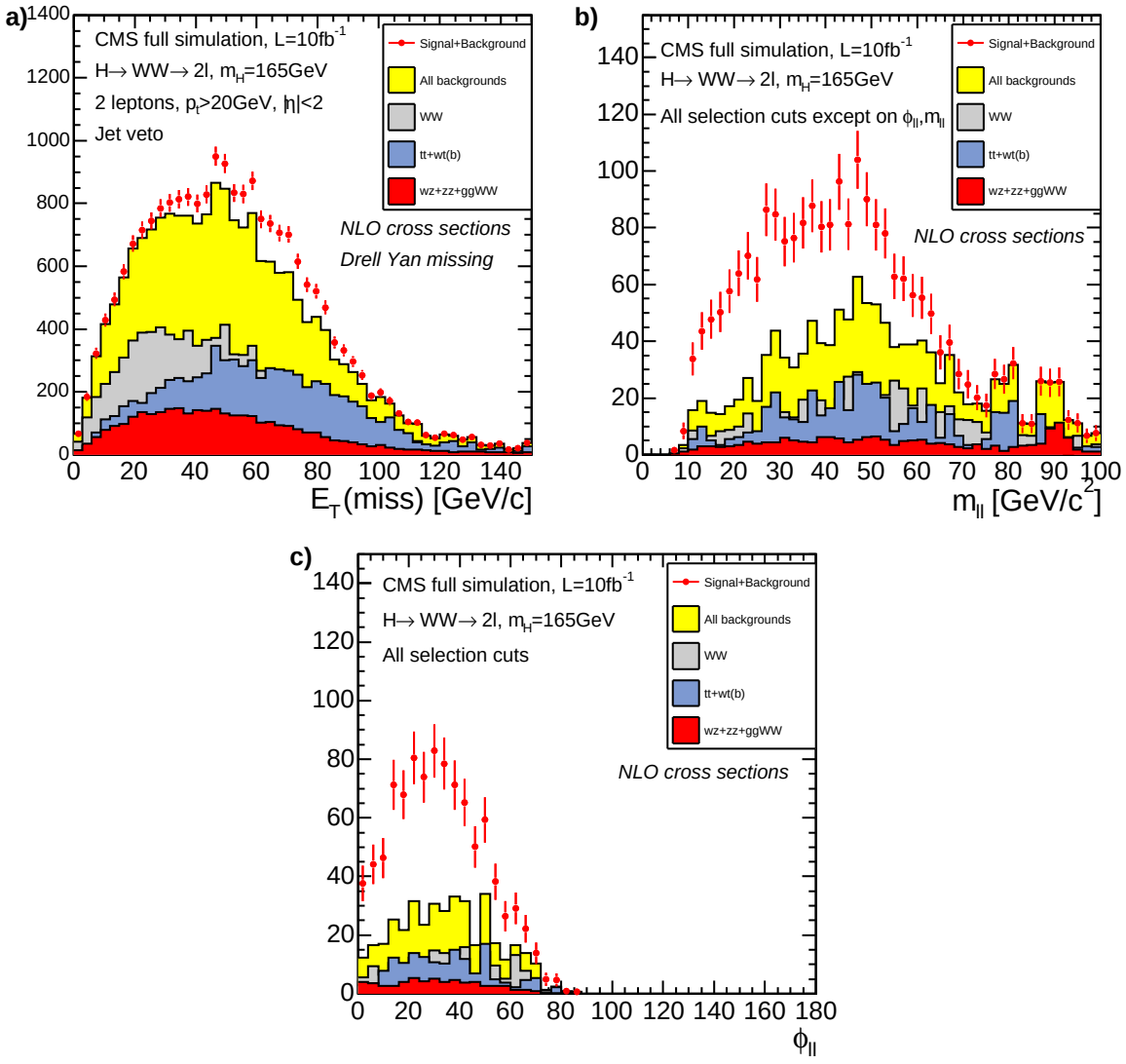

Figure 11.7: Distributions of selection variables for signal and the different backgrounds and an integrated luminosity of 10 fb^{-1}. The statistical uncertainties of the simulated data sample is shown. (a) The missing energy distribution after requiring two good leptons and applying the jet veto. (b) The invariant mass of the two leptons after all selection cuts are applied except the ones on $m_{\ell\ell}$ and $\phi_{\ell\ell}$. (c) The angle between the leptons in the transverse plane after all signal cuts excluding the one on $\phi_{\ell\ell}$.

	$qq\rightarrow$ WW	gg $\rightarrow$ WW	$t\bar{t}$	Wtb	WZ	ZZ
$\sigma \times$ BR(e, μ, τ) [fb]	11700	480	86200	3400	1630	1520
L1+HLT	6040 (52%)	286 (60%)	57380 (67%)	2320 (68%)	1062 (65%)	485 (32%)
2 lep, $\lvert\eta\rvert < 2$, $p_T > 20$GeV $\sigma_{IP} > 3$, $\lvert\Delta z_{lep}\rvert < 0.2$ cm	1398 (23%)	73 (26%)	15700 (27%)	676 (29%)	247 (23%)	163 (34%)
$E_T^{miss} > 50$ GeV	646 (46%)	43 (59%)	9332 (59%)	391 (58%)	103 (42%)	70 (43%)
$\phi_{\ell\ell} < 45$	59 (9.2%)	11 (26%)	1649 (18%)	65 (17%)	14 (13%)	10 (15%)
12 GeV $< m_{\ell\ell} <$ 40 GeV	29 (49%)	6.5 (57%)	661 (40%)	28 (43%)	1.8 (13%)	1.3 (12%)
Jet veto	23 (80%)	6.5[1]	24 (3.6%)	3.6 (13%)	1.2 (70%)	0.98 (75%)
30 GeV p^{ℓ}_{Tmax} <55 GeV	17 (74%)	5.1 (78%)	13 (54%)	2.3 (63%)	0.85 (70%)	0.46 (47%)
p^{ℓ}_{Tmin} >25 GeV	12 (69%)	3.7 (73%)	9.8 (74%)	1.4 (62%)	0.50 (58%)	0.35 (76%)
$\varepsilon_{\mathrm{tot}}$	(0.103± 0.008)%	(0.77± 0.04)%	(0.011± 0.002)%	(0.041± 0.005)%	(0.031± 0.006)%	(0.023± 0.006)%

Table 11.6: The expected number of events for an integrated luminosity of 1 fb^{-1} for the background processes. The relative efficiency with respect to the previous cut is given in parentheses. The last line shows the total selection efficiency together with the uncertainty from the limited Monte Carlo statistics.

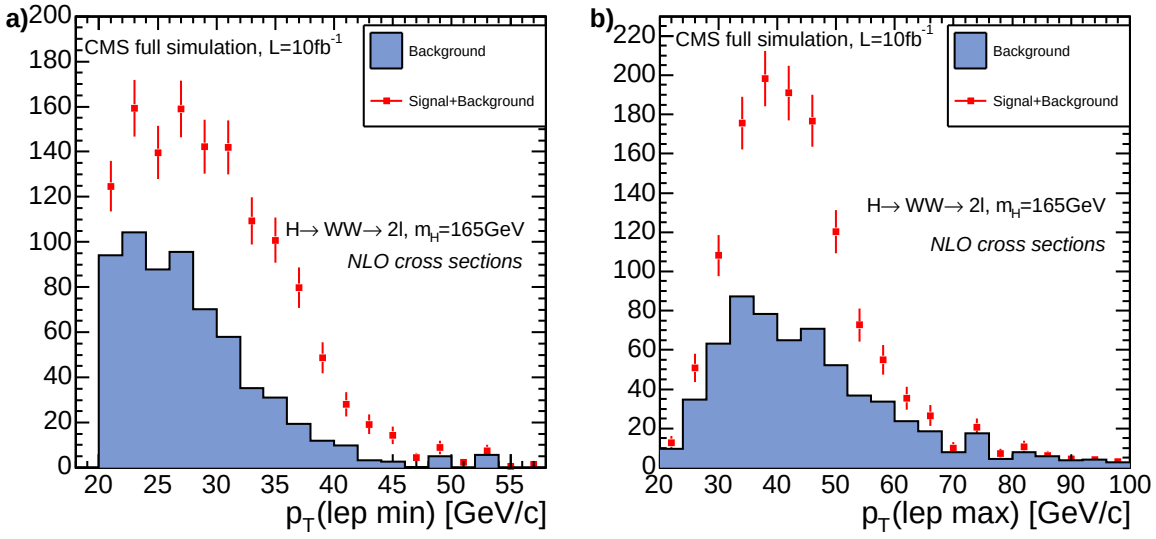

Figure 11.8: Distributions for a 165 GeV Higgs boson and the sum of all backgrounds after all other selection cuts are applied for the a) minimal and b) maximal lepton transverse-momentum. The statistical uncertainty of the simulated sample is shown.

signal for a 165 GeV Higgs boson. A cut on the higher part of the $p_T^{\ell max}$ spectrum provides an additional background reduction.
For Higgs boson masses between 160 GeV and 170 GeV the signal to background ratio is larger than one. The most important background component is continuum WW production. The inclusion of WW produced through gluon fusion increases this background by about 30%.
The $t\bar{t}$ production is the dominant contribution from top, while Wtb represents less than 15% of the $t\bar{t}$ contribution.
This study confirms that the background contribution from WZ and ZZ is small, respectively 1.8% and 1.2% of the total background.
The Drell-Yan background was considered using a 2.5 fb^{-1} sample of $pp \to \gamma, Z \to \mu\mu X$ (where the tau decays into muons were also simulated) that this background should represent less than 2% of the total background.
Table 11.7 compares the selection cut efficiencies for H $\to$ WW decays into two electrons, two muons and one electron and one muon. The W decays into τ were not taken into account here [9]. The trigger efficiency for the two-muon final state, 83%, is higher than for the two electron final state, 73%. Globally, the electron selection efficiency is lower due to the lower reconstruction efficiency coming from the fact that energy is deposited already in the tracker material. The efficiency of the $E_{\mathrm{T}}^{\mathrm{miss}}$ cut is also higher for the two muon final state, 74%, than for the two electron final state, 69%. This is probably due to the increased activity in the calorimeters when there are two electrons in the final state. These differences in the selection efficiencies between electron and muon final states are also observed for the different background samples.

$m_H = 165$ GeV	WW $\to$ ee	WW $\to \mu\mu$	WW $\to$ eμ
$\sigma \times$ BR(e, μ) [fb]	262	262	524
L1+HLT	190 (73%)	217 (83%)	394 (75%)
2 lep, $\lvert\eta\rvert < 2$, $p_T > 20$GeV $\sigma_{IP} > 3$, $\lvert\Delta z_{lep}\rvert < 0.2$ cm	77 (41%)	106 (49%)	176 (45%)
$E_T^{miss} > 50$ GeV	53 (68%)	79 (75%)	124 (71%)
$\phi_{\ell\ell} < 45$	30 (57%)	46 (58%)	71 (57%)
12 GeV $< m_{\ell\ell} <$ 40 GeV	22 (74%)	35 (76%)	53 (75%)
Jet veto	12 (52%)	19 (54%)	28 (53%)
30 GeV$< p_T^{\ell max} <$55 GeV	10 (87%)	16 (85%)	24 (86%)
$p_T^{\ell min} >$25 GeV	9.0 (90%)	14 (85%)	21 (87%)
$\varepsilon_{\mathrm{tot}}$	(3.4 ± 0.2)%	(5.3 ± 0.3)%	(4.0 ± 0.2)%

Table 11.7: The expected number of events for an integrated luminosity of 1 fb^{-1} for a 165 GeV Higgs boson for the two-electron, two-muon and electron-muon final states. The relative efficiency with respect to the previous cut is given in parentheses. The W decay into τ are not taken into account. The last line shows the total selection efficiency together with the uncertainty from the limited Monte Carlo statistics.

[9] For a 165 GeV Higgs the WW decays including τ represent only 4% of the total signal.

11.6 Background Normalization and Systematics

In Chapter 6 and 10 we have seen that different Monte Carlo models lead to a rather large uncertainty in the observed variables. In addition, the backgrounds are not under such good theoretical control as the signal. This is relevant for the present study, where the signal over background ratio is relatively small and no narrow mass peak can be observed. It is therefore desirable for the background to be as independent as possible from Monte Carlo models. Thus, a data driven approach to determine the size of the background is presented now.
In the case where backgrounds can be estimated using a normalization region in the data, the expected number of events for a background in the signal region, $N_{bkg}^{\text{signal region}}$, can be calculated using the following formula:

$$N_{\text{signal\_reg}} = \frac{N_{\text{signal\_reg}}^{\text{MonteCarlo}}}{N_{\text{control\_reg}}^{\text{MonteCarlo}}} N_{\text{control\_reg}} = \frac{\sigma_{\text{signal\_reg}} \cdot \epsilon_{\text{signal\_reg}}}{\sigma_{\text{control\_reg}} \cdot \epsilon_{\text{control\_reg}}} N_{\text{control\_reg}} \tag{11.3}$$

where $N_{\text{signal\_reg}}^{\text{MonteCarlo}}$ and $N_{\text{control\_reg}}^{\text{MonteCarlo}}$ are the number of events predicted by the Monte Carlo simulation in the signal and control region. Each of these two numbers can be expressed as a product of the theoretical cross section in the specific phase space area, $\sigma_{\text{signal\_reg}}$ and $\sigma_{\text{control\_reg}}$, and the experimental efficiency of reconstructing events in the same region, ϵ_{signal} and $\epsilon_{\text{control\_reg}}$[10]. This allows to better point out the different sources of systematic uncertainties. In particular, the theoretical predictions enter the procedure only via the ratio $\sigma_{\text{signal\_reg}}/\sigma_{\text{control\_reg}}$, leading to reduced scale dependency and thus to reduced theoretical uncertainties.
The control region should have the following characteristics, in order to keep the systematic uncertainties as low as possible:

- Theoretical calculations should be reliable in the chosen phase space area
- The contamination from other processes should be small
- The selections for the signal and control phase space regions should be as similar as possible

The contribution from other processes into the control regions, including the signal itself, will be treated as an additional systematic uncertainty, if it represents a sizable fraction of the expected number of events.
Such a procedure can be used to determine the $t\bar{t}$, WW and WZ background. The other background components, ggWW and Wtb, represent a small fraction of the total background. Currently, no method has been proposed which allow to isolate them, and their systematic uncertainties is determined using the Monte Carlo calculations.

[10]The experimental uncertainties could modify the boundaries defining the phase space where the cross section is calculated theoretically. This is the case in particular when the selections involve jets. The efficiencies in relation (11.3) are assumed to account also for this effect.

11.6.1 $t\bar{t}$ Background Normalization

Two procedures were studied to normalize the $t\bar{t}$ background (more details about this study can be found in Ref. [137]). The first one is based on a double b-tagging and the other one requires two hard E_T jets in the final state.
A first normalization region is defined by replacing the jet veto in the selection cuts by the requirement of two b-tagged jets in the final state. The other selection cuts are kept unchanged. For the b-tagging, one requires first two jets with $E_T > 20$ GeV and $|\eta| < 2.5$. A jet is b-tagged if it has at least two tracks with an impact parameter significance higher than 2. The contribution from other backgrounds, after the double jet veto is applied, is expected to be less than 1% of the $t\bar{t}$ contribution.
A second possibility is to replace the b-tagging by simply requiring two additional hard jets with respectively $E_T^{jet\,1} > 50$ GeV and $E_T^{jet\,2} > 35$ GeV. In this case, only eμ final states are considered, in order to avoid a contamination from Drell-Yan background.
The systematic uncertainties are summarized in the following:

11.6.2 Systematics uncertainties

Our proposed procedures to estimate the number of $t\bar{t}$ events in the signal phase space region exploits relation (11.3). In order to compute the systematic uncertainties on the final result we consider separately each term of the formula.

- **Theoretical uncertainty.**

  Taking the ratio of the $t\bar{t}$ cross sections in the signal and control region avoids much of the theoretical systematic uncertainties. The theoretical uncertainty on the ratio $\sigma_{\text{signal\_reg}}/\sigma_{\text{control\_reg}}$ has been studied at parton level with LO precision in Ref. [138] by varying the renormalization and factorization scale. The error has been estimated to range between 3% and 10%, mostly due to the choice of the PDF.

  Chapter 10 has shown that the shapes of the distributions involved in the normalization procedure, i.e. the E_T spectra of the jets and the jet multiplicity are not affected by higher orders contributions. It is expected that the Monte Carlo predictions concerning $t\bar{t}$ topologies and kinematics will be intensively compared and tuned directly with the copious data at the LHC. In the following we will assume the theoretical uncertainty on the normalization procedure to be 10% as suggested in Ref. [138], even though this could be an optimistic estimation.

- **Jet Energy Scale uncertainty.**

  The Jet Energy Scale (JES) uncertainty is particularly important since it affects in opposite ways the signal region, defined by vetoing the jets, and the control region where the presence of two jets is required. To take into account the anticorrelation of $\epsilon_{\text{signal\_reg}}$ and $\epsilon_{\text{control\_reg}}$, we estimate the effect of the JES uncertainty directly on their ratio by rescaling the measured jet four momentum by a fractional uncertainty: $P'_{jet} = (1 + \lambda)P_{jet}$.

Figure 11.9 shows the relative variation of $\frac{\epsilon_{\text{signal\_reg}}}{\epsilon_{\text{control\_reg}}}$ for various values of λ[11]. The triangles represent the control region defined by requiring two jets with E_T higher than 50 and 30 GeV respectively, whereas the squares stand for the control region defined by requiring two jets with $\sigma_{IP} > 2$. In the latter case, the ratio $\epsilon_{\text{signal\_reg}}/\epsilon_{\text{control\_reg}}$ is less sensitive to the JES uncertainty as the E_T threshold for the b-jets candidates is 20 GeV and the few $t\bar{t}$ events have b-tagged jets with E_T close to that threshold.

The JES uncertainty for the first 1 fb^{-1} of data is foreseen to be 10% for jets with $E_T \sim 20$ GeV and 5% for jets with $E_T > 50$ GeV, using a calibration based on $t\bar{t}$ events. These uncertainties are expected to be reduced by half with 10 fb^{-1} of integrated luminosity. For this integrated luminosity, the corresponding relative variation of $\epsilon_{\text{signal\_reg}}/\epsilon_{\text{control\_reg}}$ is $\sim 8\%$ for the control region defined by b-tagging and $\sim 10\%$ for the control region defined by high-E_T jets.

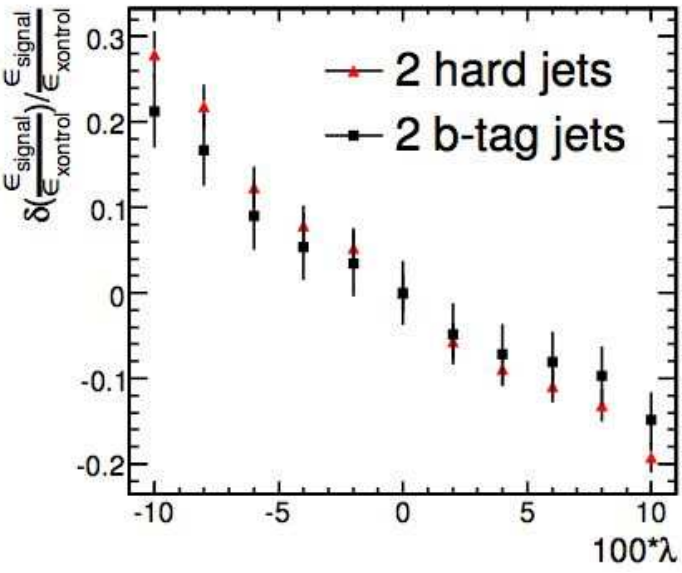

Figure 11.9: Relative variation of $\frac{\epsilon_{\text{signal\_reg}}}{\epsilon_{\text{control\_reg}}}$ as a function the jet momentum rescaling factor (λ). The triangles represent the control region defined by two hard jets whereas the squares correspond to the two b-tagged jets phase space area.

- **α criterion uncertainty.**

  To prevent the contamination from fakes when vetoing jets down to a raw transverse energy of 15 GeV, it is useful to cut on the track content of the jets. For jets with E_T ranging from 15 to 20 GeV, as explained in section 11.3.3, the α criterion is then exploited.

[11] The dependency of the JES uncertainty from the jet E_T is taken into account by dividing λ by 2 for jets above 50 GeV.

To estimate the systematic uncertainty due to this criterion, the cut on α has been varied from 0.15 to 0.25. Moreover different values of the minimum p_T for a track to be included in the sum have been tried, from 2 to 3 GeV. These changes imply a variation of $\epsilon_{\text{signal\_reg}}$ of about 4%.

- **b-tagging uncertainty.**

  The precision at which the b-tagging efficiency will be known is expected to be ± 11% for 1 fb^{-1} integrated luminosity and it is foreseen to improve to ± 7% with 10 fb^{-1} [139]. These values are used for the uncertainty on $\epsilon_{\text{control\_reg}}$ if the control region is defined by requiring two b-tagged jets.

- **Uncertainties on $\mathbf{N_{control\_reg}}$.**

  The selection criteria used to identify the control region identify almost entirely $t\bar{t}$ events. In the worst case, i.e. when the control region is defined by two high E_T jets, the fraction of events coming form other processes is smaller than 4%. Provided that this fraction is small, it is safe to simply neglect this source of systematic error.

The experimental systematics involved in the $t\bar{t}$ normalization procedure are summarized in Table 11.8. For an integrated luminosity of 10 fb^{-1} these uncertainties are about 11% for both control regions. Including the assumed 10% theoretical uncertainty this uncertainty becomes 15%.

In both procedures, systematic uncertainties are larger than statistical uncertainties. This

Uncertainty	"b-tagging" control region	"hard jets" control region
JES	8%	10%
b-tagging	7%	-
α criterion	4%	4%
$N_{\text{control\_reg}}$	negligible	negligible
Total	11.4%	10.8%

Table 11.8: Summary of the different experimental systematics involved in the $t\bar{t}$ normalization procedure. The total uncertainties are calculated by adding quadratically each single contribution. Results are shown for an integrated luminosity of 10 fb^{-1}.

list of systematics might not be exhaustive once real data will be available, but gives a guideline on how the normalization might be performed. The statistical uncertainties from the number of events in the normalization region are negligible here. Summing these uncertainties in quadrature, a global uncertainty of 16% is expected for an integrated luminosity of 5 fb^{-1}. Note that the b-tagging method might be hard to apply on early data as the systematics of b-tagging might need more understanding. Thus, the method where two high energetic jets are required might be more adapted at the startup phase of LHC.

11.6.3 WW Background Normalization

A normalization region for WW can be defined by requiring $\phi_{\ell\ell} < 140$ and $m_{\ell\ell} > 60$ GeV, keeping all other signal selection cuts unchanged. This mass cut eliminates essentially all

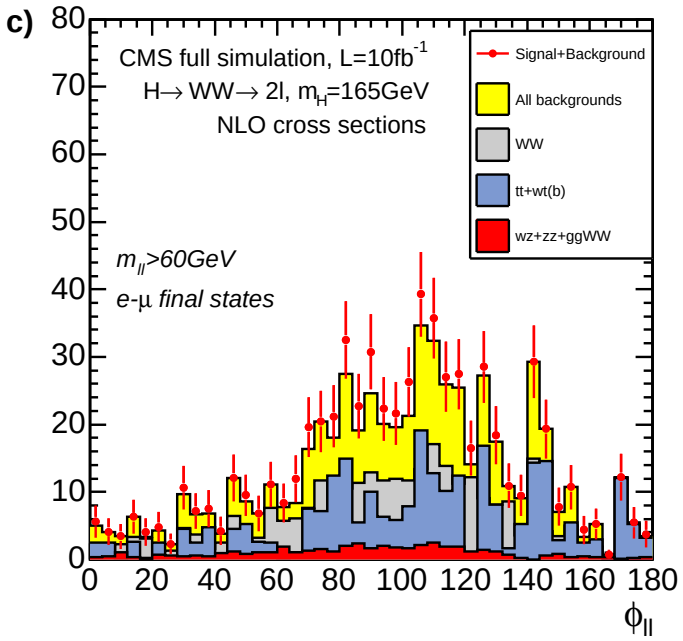

Figure 11.10: Distribution of the angle between the leptons in the transverse plane for the signal and the different backgrounds, for an integrated luminosity of 10 fb^{-1}. The WW normalization region is considered, with all signal cuts applied but $m_{\ell\ell} > 60$ GeV. Only electron-muon events are kept.

events with a small $\phi_{\ell\ell}$. In this case and for an integrated luminosity of 5 fb^{-1}, the error on the theoretical prediction of the ratio between the number of WW events in the signal and in the normalization region is expected to be small compared to the other sources of uncertainty [140]. Only the eμ final state is considered in order to reduce the contribution of Drell-Yan and WZ.

Figure 11.10 shows the $\phi_{\ell\ell}$ distributions for the different processes in this normalization region. For an integrated luminosity of 5 fb^{-1}, about 124 WW events are expected in this signal-depleted region, 88 from $t\bar{t}$, and 30 events from the other backgrounds (12 from Wtb, 12 from ggWW and 6 from WZ). This leads to a total of 242 background events. An additional 28 signal events for a Higgs boson mass of 165 GeV are expected, compared to 230 events in the signal region.

Systematic uncertainties of 16%, 20%, 22% and 30% can be expected on the $t\bar{t}$, WZ, Wtb and ggWW backgrounds respectively, as discussed in the previous and following sections. The systematic uncertainty on WW events is given by adding the statistical and systematic error in quadrature:

$$\sqrt{242 + (88 \cdot 0.16)^2 + (12 \cdot 0.2)^2 + (12 \cdot 0.3)^2 + (6 \cdot 0.2)^2} = 21.5$$

This represents a relative systematic error of $21.5/124 = 17\%$ on the WW background. With data, the WW background should be normalized assuming that no signal is present. Therefore, in presence of a signal, the WW background will be overestimated in a first step by about 10%. This estimation can be then refined in an iterative procedure. The statistical uncertainty is the dominant uncertainty on the WW background. With 60 fb^{-1}, this error should be reduced by a factor of 2.

In a further study, the uncertainty on WW could be reduced by combining more normalization regions. Moreover with a suitable Drell-Yan simulation, the inclusion of ee and $\mu\mu$ final states in the normalization region could increase the statistics, thus reducing the statistical

uncertainty.

11.6.4 WZ Background Normalization

The WZ background can be normalized by keeping the same selection cuts as in the signal region but requiring an additional lepton in the final state. To gain statistics, the cuts on $\phi_{\ell\ell}$ and $m_{\ell\ell}$ are removed. For an integrated luminosity of 5 fb^{-1}, about 36 WZ events and 14 $t\bar{t}$ events are expected. Assuming a 16% accuracy on the $t\bar{t}$ background and an additional 3% for the selection of the additional lepton, an accuracy of about 20% is expected on WZ with 5 fb^{-1}.
The ZZ background was not considered in the systematics study since it is expected to make a contribution of only 1.2% to the background in the signal region.

11.6.5 ggWW and Wtb Normalization

So far no clear normalization region has been found for the ggWW and Wtb backgrounds. However, as they represent only a small fraction of the background events, the Monte Carlo models can be used to predict them. The systematic uncertainty is then given by the following formula:

$$\Delta N_{bkg} = \Delta_{stat} \oplus \Delta_{2\,lep} \oplus \Delta_{jet\ veto} \oplus \Delta_{missing\ energy} \oplus \Delta_{theory} \tag{11.4}$$

The error on the jet veto and the missing energy was determined by the variation in the

Systematic source	Wtb	ggWW
Lepton identification	4.2%	4.2%
Missing energy	<1%	3%
Calorimeter energy scale	9%	1.5%
Theoretical error	20%	30%
Total	22%	30%

Table 11.9: Systematic sources of uncertainty on the single resonant top production and continuum WW production via gluon fusion.

global selection efficiency after varying respectively the jet energy by ±2% and the missing energy value by ±2%. The theoretical uncertainty dominates and is about 30% for ggWW and about 20% for Wtb [124]. Table 11.9 summarizes the different sources of systematic errors on these two backgrounds. The theoretical uncertainty are dominant.
The systematic uncertainties on the different backgrounds are summarized in Table 11.10.

11.7 Results including Background Systematics

The possible signal significance is a combination of statistical and systematic uncertainties. The background uncertainty, ΔN_B, is taken into account by applying a Gaussian smearing of $\sigma = \Delta N_B$ on the number of expected background events [141]. For a large number of

Process	Systematic uncertainty
$t\bar{t}$	16%
qqWW	17%
WZ	20%
Wtb	22%
ggWW	30%
Total	10%

Table 11.10: Systematic uncertainties of the different backgrounds for an integrated luminosity of 5 fb^{-1}. Note that the total systematic uncertainty is obtained by quadratically summing up the systematic errors of each process.

events, the significance, taking into account the background uncertainties, can be expressed with the following formula:

$$\text{Significance} = \frac{N_S}{\sqrt{N_B + \Delta N_B^2}} \tag{11.5}$$

Taking into account the sum of the different backgrounds, an overall uncertainty of 10% is found on the total background if only the background systematics are considered. Adding the contribution from limited Monte Carlo statistics, this uncertainty increases to 13%. However, it can be expected that at the LHC startup enough Monte Carlo events will be generated. These results are calculated for an integrated luminosity of 5 fb^{-1}. For integrated luminosities of 1, 2 and 10 fb^{-1}, the total systematic uncertainties scale to 19%, 16% and 11%, respectively. Figure 11.12 and Table 11.11 show the signal significance after the systematic uncertainties are taken into account.

For a Higgs boson mass of 165 GeV, the inclusion of background systematics increases the luminosity needed for a 5σ discovery by a factor of 1.8, going from 0.5 fb^{-1} to 0.9 fb^{-1}. Due to the high signal-to-background ratio of 1.7, the signal is less sensitive to background fluctuations, leading to this restricted change in the required luminosity for a discovery. Figures 11.11 and 11.12 and Table 11.11 show the signal to background ratio, the signal significance with 5 fb^{-1} and the luminosity needed for a 5σ discovery for different Higgs masses. The signal significance is defined as the probability that the observed background, N_B, fluctuates above the sum of the signal and background, $N_S + N_B$, following a Poisson distribution with mean $\mu = N_B$. For a Higgs boson mass higher than 180 GeV and lower than 150 GeV, the inclusion of background systematics prevents a 5σ discovery. The reason is that the signal to background ratio is lower than 0.5 in these regions. In this study we concentrated on the mass region around $m_H = 165$ GeV. The selection cuts were optimized for this region. In principle the sensitivity of this channel could be increased by specifically tuning the cuts on the p_{T} of the leptons [117]. Moreover, one might also expect that, with more luminosity, the background systematics can be further reduced.

m_H [GeV]	S/B	Significance for 5 fb^{-1}		$\mathcal{L}_{\text{disc}}$ [fb^{-1}]		
		no bkg syst	with bkg syst and MC stat	no bkg syst	with bkg syst	with bkg syst and MC stat
150	0.61	6.6	4.0	3.0	7.1	8.2
160	1.51	14	7.7	0.58	1.0	1.1
165	1.66	15	8.3	0.50	0.81	0.90
170	1.19	11	6.3	0.88	1.5	1.7
180	0.65	6.7	3.7	2.7	5.7	7.3

Table 11.11: The signal to background ratio for the different Higgs boson masses together with the integrated luminosity needed for a 5σ discovery, with and without the inclusion of background uncertainties.

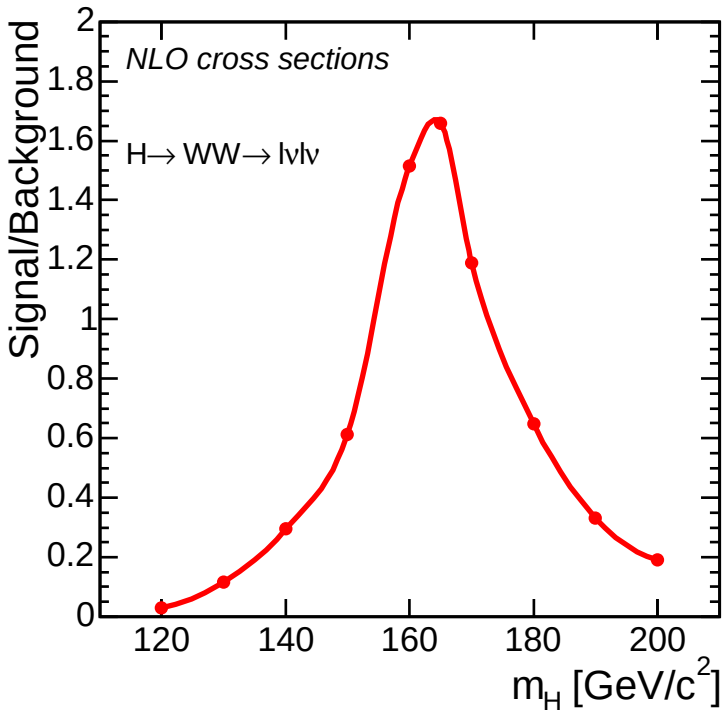

Figure 11.11: Signal to background ratio as a function of different Higgs boson masses for the H $\rightarrow$ WW channel.

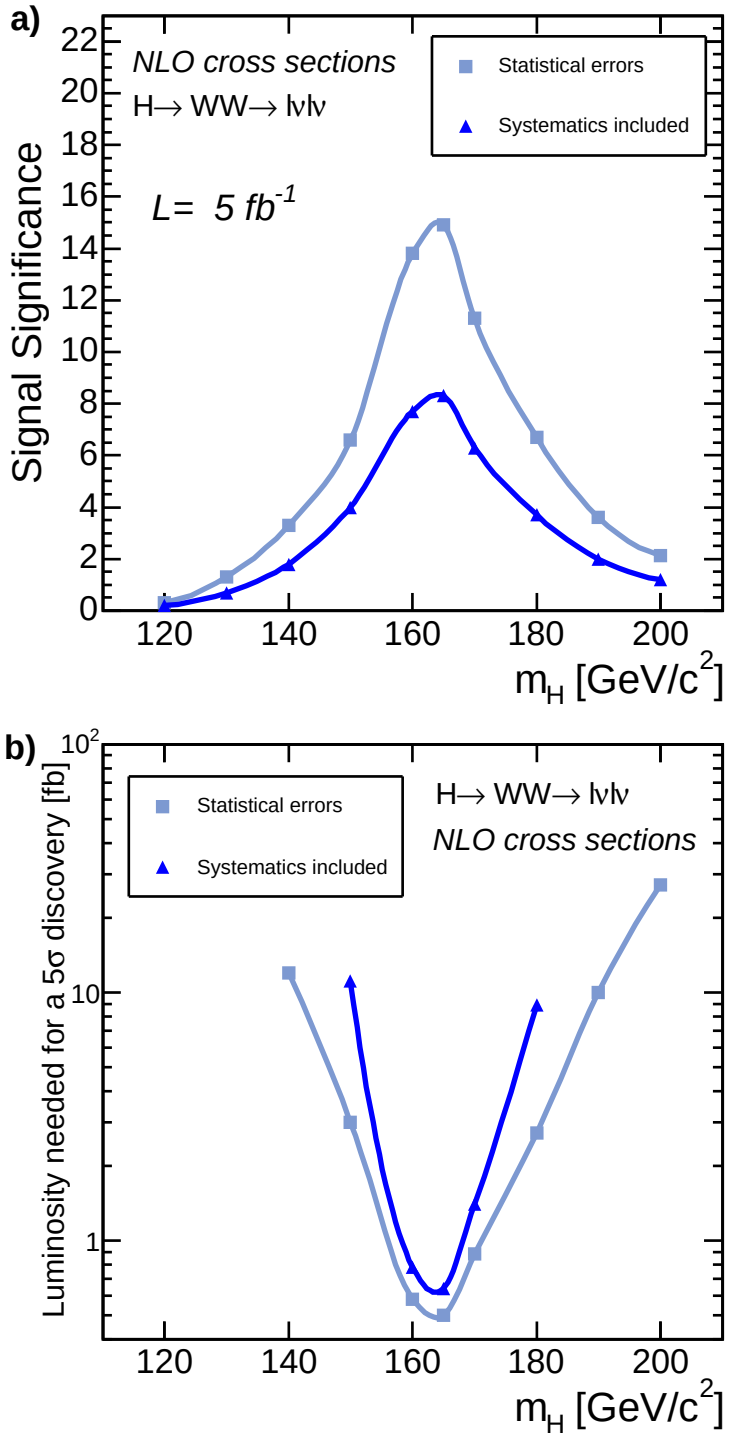

Figure 11.12: a) Signal significance for an integrated luminosity of 5 fb^{-1} and b) the integrated luminosity needed for a 5σ discovery as a function of different Higgs boson masses for the H $\rightarrow$ WW channel. The grey curve (squares) is with statistical errors only while the solid curve (triangles) also contains systematic uncertainties from background control and limited Monte Carlo statistics.

Using a full CMS detector simulation and including background uncertainties, it was confirmed that the Standard Model Higgs boson can be discovered in the $H \rightarrow WW \rightarrow \ell\nu\ell\nu$ channel with less than 1 fb^{-1} if its mass is around 165 GeV. If it has a mass of around 150 and 180 GeV, a 5σ signal can be seen with a luminosity of about 10 fb^{-1}.

Chapter 12

Higgs Mass Determination

The Higgs discovery potential including background systematics and the most-up-to-date theoretical predictions were presented in the previous chapters. Once a signal is found in the channel $H \rightarrow WW \rightarrow \ell\nu\ell\nu$, the next questions are: *is it consistent with a SM Higgs boson*, *what is its mass*, and *what properties does it have*?
As we have seen in the introduction, it is not easy to find a Higgs boson in the mass region between 150 and 180 GeV in another decay channel than $H \rightarrow WW \rightarrow \ell\nu\ell\nu$ with an integrated luminosity below 100 fb^{-1}. As the cuts to reduce the enormous $qq \rightarrow$WW background in the $H \rightarrow WW \rightarrow \ell\nu\ell\nu$ channel are based on the spin-zero character of the Higgs boson, a signal found with low statistics and in this mass region will presumably be a spin-zero boson. To measure the CP properties of the Higgs and the structure of the HVV and $Ht\bar{t}$ coupling, the vector boson fusion channels $qq \rightarrow qqH$ can be used.
We present now how the mass can be determined in the $H \rightarrow WW \rightarrow \ell\nu\ell\nu$ channel, assuming that it is a SM Higgs. In contrast to the $H \rightarrow \gamma\gamma$ and the $H \rightarrow ZZ \rightarrow 4\ell$ process, the two undetectable neutrinos in $H \rightarrow WW \rightarrow \ell\nu\ell\nu$ do not allow the direct reconstruction of a mass peak and some model dependent Monte Carlo techniques have to be used. Such procedures are not new and have previously been used successfully for the mass determination of the W boson and the top quark at hadron colliders (for example in Ref. [142]). Among other observables the so called transverse mass distribution has been suggested in the past to constrain the mass of hypothetical particles decaying into one or more neutrino-like particles (Ref. [114]). This transverse mass determination involves directly the measurement of the missing transverse momentum with the related experimental uncertainty and depends to some extend also on the various required selection cuts and the details of p_T^H. For the proposed selection of $gg \rightarrow H \rightarrow WW \rightarrow \ell\nu\ell\nu$ a qualitative determination of the Higgs mass using the directly available charged lepton p_T spectra has been suggested in Ref. [118].
The signal selection criteria from Chapter 9, which are based on the criteria proposed in Refs. [117], [118] and [76], are used. PYTHIA is reweighted to the NNLO + NNLL p_T Higgs spectrum obtained with the HqT program. As we have seen in Chapter 8, the effect of reweighting to the rapidity spectrum of the Higgs is small. Thus we use the reweighting technique to the resummed p_T spectrum, as this is supposed to be currently the most reliable p_T Higgs spectrum.

For the purpose of this analysis, the Higgs mass determination, we choose to use fixed

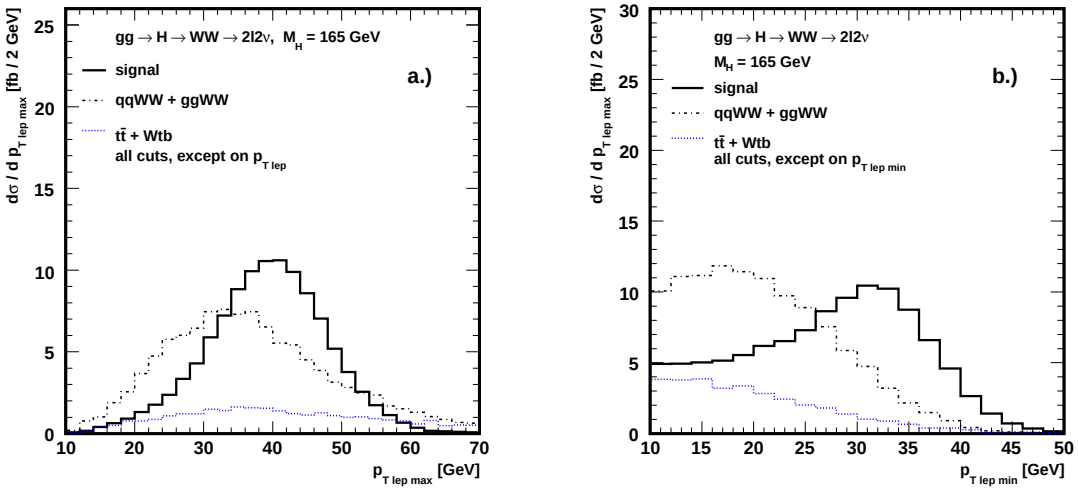

Figure 12.1: Cross section of the Higgs signal (M_H = 165 GeV) as well as the main backgrounds, that is qqWW, ggWW, $t\bar{t}$ and Wtb, as a function of the p^{ℓ}_{Tmax}(a) and p^{ℓ}_{Tmin} (b). All cuts are applied except the ones on the p_T of the leptons. The events are generated with PYTHIA and TopReX [123] and reweighted to NNLO and NLO respectively. WW production via gluon fusion was generated using a Monte Carlo provided by N. Kauer [81], with parton shower simulation in PYTHIA.

selection criteria which provide an acceptable signal to background ratio for Higgs masses between 150 GeV and 180 GeV. Since the optimal values for these cuts, especially for the cuts on the lepton p_T depend on the Higgs mass, some more sophisticated tuning might be performed for other Higgs masses. The most relevant backgrounds are included, which are the continuum WW production ($qq\rightarrow$ WW $\rightarrow \ell\nu$, gg $\rightarrow$ WW $\rightarrow \ell\nu\ell\nu$) and events related to the production of top quarks ($qq\rightarrow$ tt $\rightarrow$ WbWb $\rightarrow \ell\nu$b$\ell\nu$b, $qq\rightarrow$ tWb $\rightarrow$ WbWb $\rightarrow \ell\nu$b$\ell\nu$b). The corresponding lepton p_T spectra for different backgrounds and for a signal of m_H = 165 GeV are shown in Figure 12.1a and 12.1b and in Figure 12.2a and 12.2b for the sum of all backgrounds with and without the signal.
Figure 12.3 shows the transverse momentum spectra of the two charged leptons from the Higgs signal (m_H = 155 GeV, 165 GeV and 175 GeV), requiring only a minimal lepton transverse momentum of 10 GeV and isolation. Figure 12.4 shows the signal distributions of the lepton transverse momenta after all cuts except the final lepton p_T cuts are applied. The Higgs mass dependence, as shown in Figure 12.3 (before) and Figure 12.4 (after cuts), of the lepton p_T spectra remains after the selection cuts are applied.
It should be clear that a convincing real data analysis needs to study in detail the number of accepted events for the different cuts and for signal enhanced and signal depleted phase space areas. Such an study has been performed in a recent detailed full detector simulation study in CMS, [132], described in Chapter 11. This study has demonstrated that such a model

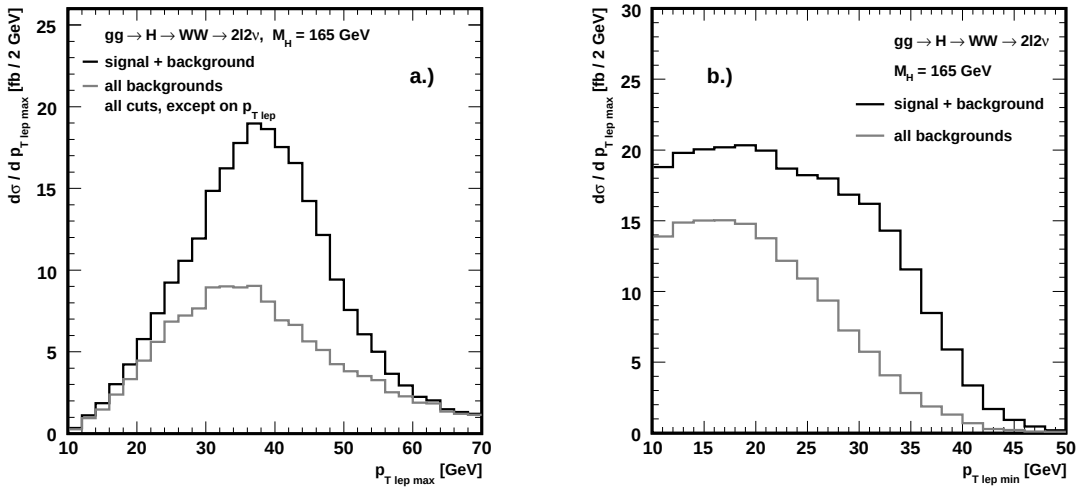

Figure 12.2: Cross section of the Higgs signal (M_H = 165 GeV) and the sum of the main backgrounds, that is qqWW, ggWW, $t\bar{t}$ and Wtb, and the background alone, as a function of the p_T of p^{ℓ}_{Tmax}(a) and p^{ℓ}_{Tmin} (b). All cuts are applied except the ones on the p_T of the leptons. The events are generated with PYTHIA and TopReX and reweighted to NNLO and NLO respectively. WW production via gluon fusion was generated using a Monte Carlo provided by N. Kauer [81], with parton shower simulation in PYTHIA.

independent data driven analysis allows to constrain the $t\bar{t}$ background with an accuracy of about 16%. In a similar approach the background from WW continuum events have been estimated. A combination of these background uncertainties, weighting the relative errors and adding them quadratically resulted in a total systematic background error of 10%. In the following we use this result from Chapter 11 to investigate how well a potential Higgs signal cross section can be determined.

12.1 Accepted Signal Cross Section and the Higgs Mass

The number of signal events is the product of the theoretical signal cross section, the luminosity and the detection efficiency. Table 12.1 summarizes the Standard Model Higgs signal cross section, the efficiency after all cuts are applied, and the number of expected events for an integrated luminosity of 10 fb^{-1}. One can see that the expected number of events depend strongly on the Higgs mass.
In order to use this information, the uncertainties from background, from the detection efficiency, the luminosity and the theoretical signal cross-sections have to be estimated. It is obviously impossible to know exactly how well such measurements can be performed using recorded data at LHC. Nevertheless, assuming that the detectors can be operated as well as previous high energy hadron collider experiments, the achievable systematic uncertainties

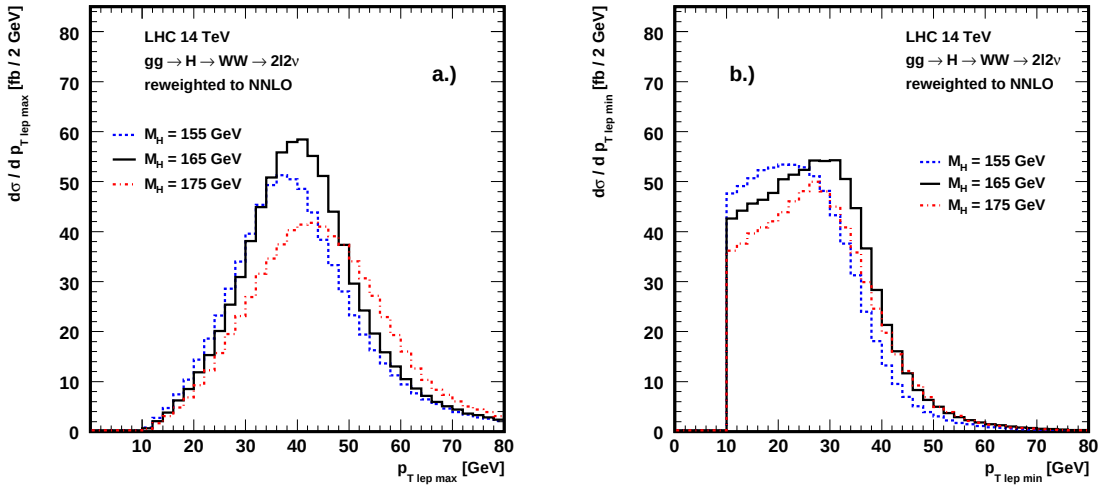

Figure 12.3: Cross section of gg → H → WW → $\ell\nu\ell\nu$ process for a Higgs mass of 155, 165 and 175 GeV as a function of the lepton p_{T} of p^{ℓ}_{Tmax}(a) and p^{ℓ}_{Tmin} (b). Only the lepton isolation cut and the minimal p_{T} of 10 GeV are applied.

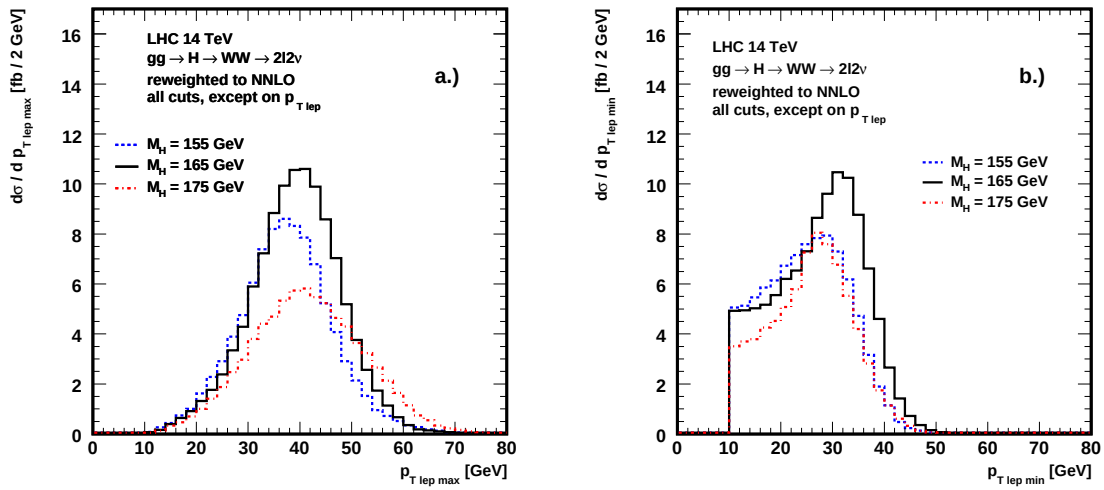

Figure 12.4: Cross section of the Higgs signal decaying into WW → $\ell\nu\ell\nu$ for a Higgs mass of 155, 165 and 175 GeV as a function of p^{ℓ}_{Tmax}(a) and p^{ℓ}_{Tmin} (b). All cuts, except the final ones on the p_{T} of the leptons, are applied.

signal H $\rightarrow$ WW $\rightarrow \ell\nu\ell\nu$			
m_H [GeV]	σ [pb]	ϵ [%]	accepted events per 10 fb^{-1}
150	1.93	1.07	206 $\pm$9.9%(stat.)$\pm$10.2%(syst.)
155	2.08	1.45	302 $\pm$7.5%(stat.)$\pm$7.0%(syst.)
160	2.23	2.07	464 $\pm$5.6%(stat.)$\pm$4.5%(syst.)
165	2.23	2.18	486 $\pm$5.4%(stat.)$\pm$4.3%(syst.)
170	2.12	1.69	358 $\pm$6.7%(stat.)$\pm$5.9%(syst.)
175	1.96	1.28	250 $\pm$8.6%(stat.)$\pm$8.4%(syst.)
180	1.82	0.859	179 $\pm$11.0%(stat.)$\pm$11.8%(syst.)
background process			
$qq \rightarrow t\bar{t} \rightarrow$ WbWb $\rightarrow 2\ell\ 2\nu$bb	86	0.004	30.3$\pm$16%
$qq \rightarrow$ tWb $\rightarrow$ WbWb $\rightarrow 2\ell\ 2\nu$bb	3.4	0.026	8.7$\pm$20%
$qq \rightarrow$ WW $\rightarrow 2\ell\ 2\nu$	9.09	0.113	103 $\pm$13%
gg $\rightarrow$ WW $\rightarrow 2\ell\ 2\nu$	0.48	1.473	70 $\pm$30%
Combined background	99.3		211 $\pm$ 10%

Table 12.1: The expected cross section for a SM Higgs at NNLO with different masses and for the dominant backgrounds at NLO (except ggWW which is only known at LO) are given. The efficiencies and the number of accepted events for a luminosity of 10 fb^{-1} are also shown. Both, the theoretical uncertainty for the cross section, $\Delta\sigma/\sigma$, and the signal efficiency uncertainty, $\Delta\epsilon/\epsilon$, are currently estimated to be about 5%. The uncertainties from background subtraction systematics depend on the signal to background ratio and are is summarized in the last row.

can be estimated. The experimental uncertainties are listed first:

1. For the background uncertainty we use the results from the "data" driven CMS analysis, described in Chapter 11, where an accuracy of 10% has been found [132].

2. For the signal efficiency it can be assumed that the efficiency for isolated high p_{T} leptons can be controlled from the data, using the inclusive Z $\rightarrow$ ee and Z $\rightarrow \mu\mu$ samples. Such a procedure should allow to control the charged lepton detection efficiency uncertainty with uncertainties of perhaps $\pm$ 1% but certainly smaller than 5%.

3. Other efficiency uncertainties come from the Monte Carlo modeling of the assumed Higgs p_{T} spectrum, from the rapidity dependence and from the jet activity in signal events. We assume that these efficiencies can be measured to some extend also from data using various control samples like leptonic decays of inclusive W and Z events. Especially the Z events, with and without jets, allow to study in detail the underlying event with high precision, as those events have almost no background. Furthermore, the Z p_{T} spectrum can be measured from the leptons alone and with very good accuracy. A detailed analysis of the jet activity in the Z+X events, especially with a p_{T} jet close to the cut value used for the jet veto, allows to "calibrate" the jet veto efficiency from

the data with accuracies well below 5%.
The proposed signature requires only the identification of two isolated charged leptons and a veto against jets with a p_{T} above 30 GeV. As this signature is much simpler than the signal selection for $\mathrm{t\bar{t}}$ events, we can use a recent detailed CMS analysis of the $\mathrm{t\bar{t}}$ cross section measurement [143] to estimate an upper limit for the Higgs signal efficiency uncertainty. The signal for $\mathrm{t\bar{t}}$ events requires at least one isolated lepton, some jets with a large invariant mass and with a possible additional requirement that one jet is tagged as a b-flavoured jet. The CMS analysis concluded that the $\mathrm{t\bar{t}}$ signal efficency can be determined with a total systematic uncertainty of 9%, dominated by the b-tagging efficiency uncertainty of 7%. The remaining uncertainties from other sources were estimated with an uncertainty of roughly 5-6% . One can thus conclude that the much simpler Higgs signal signature, with two isolated high p_{T} leptons only, can be selected with an accuracy of $\pm 5\%$ or better.

Combining these mostly experimental errors, one finds that the backgound uncertainties of 10% ($\Delta B/B$), varying with the particular signal to background ratio, and the efficiency uncertainty of 5% match roughly the expected statistical errors already for a luminosity of 10 fb^{-1}.
In order to make an interpretation of the accepted Higgs signal cross section, theoretical predictions and the luminosity uncertainties have to be estimated as well. The main contributions are the following:

1. Today, the signal cross section is known with NNLO accuracy from perturbation theory. The uncertainty from unknown higher order calculations was estimated in Ref. [94], where it was shown that the calculations are converging rapidly and that the difference between the Higgs cross section at $\mathrm{N^3LO}$ and NNLO is about 5%. [1].

2. The absolute luminosity uncertainty is in general believed to be known with an accuracy of about 5%. A much more accurate relative luminosity and cross section measurement, as proposed in [144] should allow a smaller normalization uncertainty, reaching eventually 1%. This approach has been used in Ref. [145], where it was pointed out that the uncertainties from parton distribution functions (PDFs), from α_s and other related systematics are very similar for the LHC cross sections of the SM Higgs and for the W and that the relative rates are already understood with an accuracy of 2-3% [2].

Thus, one finds that the theoretical cross section interpretation of a hypothetical signal is currently dominated by the 5% uncertainties from future higher order calculations, if relative cross section measurements for the Higgs signal and for the inclusive W and Z production are used.

[1] The residual uncertainties due to uncalculated contributions of yet higher orders is often estimated by varying μ_f and μ_R. Instead of the 5% from the $\mathrm{N^3LO}$ calculations, one might take the scale uncertainty from NNLO, which is $\approx$ 8-9%, into account, in order to consider the fact that the $\mathrm{N^3LO}$ cross section was calculated in the soft approximation.

[2] Other sources, e.g. an analysis presented by W. Tung [146, 147], claimed that todays PDF uncertainties for the W and Z cross section and for the ratio between the Higgs and the W/Z cross section might be somewhat larger. We assume however, that the PDF constraints using a few fb^{-1} LHC data on W, Z, γ-Jet and Z-Jet data will reduce the PDF uncertainties dramatically, following the scheme from Ref. [144].

We now use the expected number of signal events, as given in Table 12.1, to discuss how these hypothetical signals can be used for a signal cross section measurement and its interpretation with respect to the Higgs mass.
The statistical error of a cross section measurement is defined as $\Delta S/S = 1/\sqrt{S+B}$. As can be seen from Table 12.1, the analysis will reach statistical uncertainties between 5-11% for an integrated luminosity of about 10 fb^{-1}. It is straightforward to use the results from Table I to estimate the statistical uncertainties for any other integrated luminosity.
To summarize, the systematic uncertainties from backgrounds ($\Delta B/B$), currently estimated to be about 10% for an integrated luminosity of 10 fb^{-1}, seem to be the dominant contribution to the systematic uncertainty of the number of events. For a signal to background ratio of 1:1 this would correspond to a 10% signal uncertainty. For a better signal to background ratio of 2:1 the overall uncertainty would drop to 5%.
Larger data sets, combined with a well understood detector and more accurate MC generators might result in some reduction of this background uncertainty. However, such future improvements can easily be included into the strategy and the results obtained with the current assumptions. The uncertainty from the detection efficiency, as discussed before, can be expected to be about 5%. In addition, one must take the uncertainty from the theoretical prediction into account. It is currently assumed that, using relative measurement and optimal cross section ratios, an accuracy of 5% has been reached already. Thus, combining all these errors an entire systematic uncertainty of 10-15% for the cross section measurement seems to be realistic. The systematic uncertainty starts to be the dominant error once a luminosity of about 10-20 fb^{-1} is reached. Figure 12.5 shows the number of hypothetical signal events within the Standard Model and for an integrated luminosity of 10 fb^{-1}.
In order to demonstrate how such a "result" can be interpreted in terms of the Higgs mass, the theoretical expectation for accepted Higgs signal events was determined for different Higgs masses such that an analytic function could be used to approximate the prediction for all Higgs mass values. The accepted events were obtained with PYTHIA reweighted to the HqT program. A fit with two Gaussian functions was used to obtain the curve. The experimental and theoretical uncertainties will be split in the following way. The band indicates the $\pm$ 5% theoretical cross section uncertainty. As can be seen from Figure 12.5, a broad maximum of signal events is predicted for a mass between 160 and 168 GeV. For lower and higher masses, the expected rate of signal events decreases steeply. On the left side of the Figure, the estimated number of accepted events for three different Higgs masses, as listed in Table 12.1, are shown. The corresponding number of events are 206 $\pm$ 29 for a Higgs mass of 150 GeV, 302 $\pm$ 35 events for a Higgs mass of 155 GeV and 486 $\pm$ 34 for 165 GeV. The statistical and the estimated experimental systematic errors have been added in quadrature. Taking first the expected number of 302 $\pm$ 35 events the graphical interpretation leads directly to a possible SM Higgs mass of either the correct mass of 155 $\pm$ 2 GeV or to a second solution of 173 $\pm$ 2 GeV. A similar accuracy and twofold ambiguity would be obtained for other hypothetical number of events outside the peak region.
For signal numbers between 460 to 480 events, the uncertainty being about $\pm$ 35 events, one would interpret this result with a SM Higgs somewhere between 160 and 168 GeV with nearly equal probability.
Assuming a nearly flat probability distribution for all masses within this interval, one could

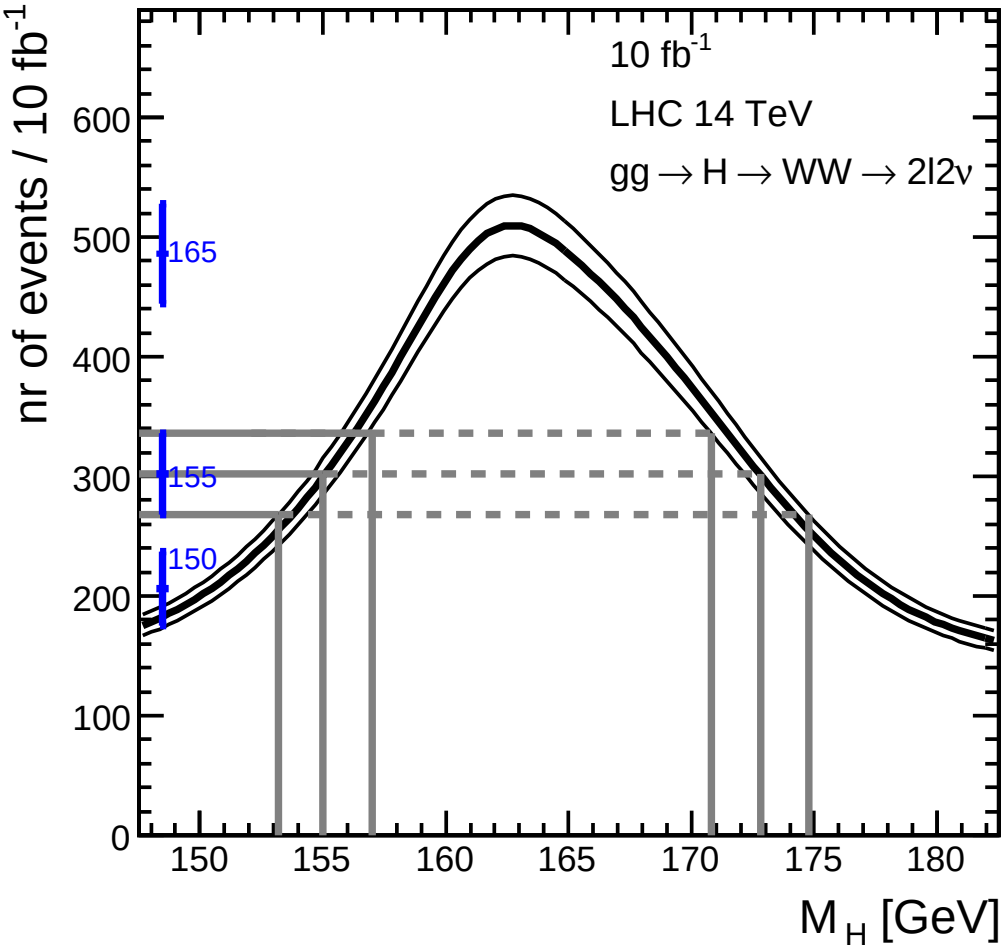

Figure 12.5: Number of SM Higgs events events for 10 fb^{-1} with all cuts applied and approximated with a fit of two Gaussian distributions for Higgs masses between 150-180 GeV and assuming a theoretical cross section uncertainty of $\pm$ 5%. Three hypothetical experimental numbers of signal events, including statistical and systematic error, are also shown. For the case of a hypothetical result corresponding to a Higgs mass of 155 GeV, the possible graphical interpretation in terms of the SM Higgs mass is also indicated.

estimate that the most likely mass value would be 164 GeV with the corresponding root-mean-square (RMS) error of 2.3 GeV, as defined from a box-like distribution with a width of 8 GeV (RMS = width/$\sqrt{12}$).

12.2 Higgs Mass and Lepton p_T Spectra

In the previous section we have shown how a potential Higgs signal cross section measurement in the mass range between 150-180 GeV can be used for a first estimate of the Higgs mass. If one finds another observable which is suited to distinguish between the now ambigious mass predictions in the tails of the mass curve, an accuracy of about ± 2 to 2.5 GeV can be found, assuming that the Higgs has Standard-Model-like properties.
In order to find such an observable, we study the correlation between the Higgs mass and the lepton p_T spectra. It has been shown in Figures 12.3 and 12.4, that the p_T spectrum of both leptons, before and after the selection cuts, depends on the Higgs mass. In the following we investigate the average transverse momenta of both leptons, selected according to ptlmax and ptlmin and their scalar difference of the lepton transverse momenta. In the future, other correlations and their systematics might be investigated in detail.
Figure 12.6a shows the Higgs cross section as a function of the Higgs p_T for different Monte

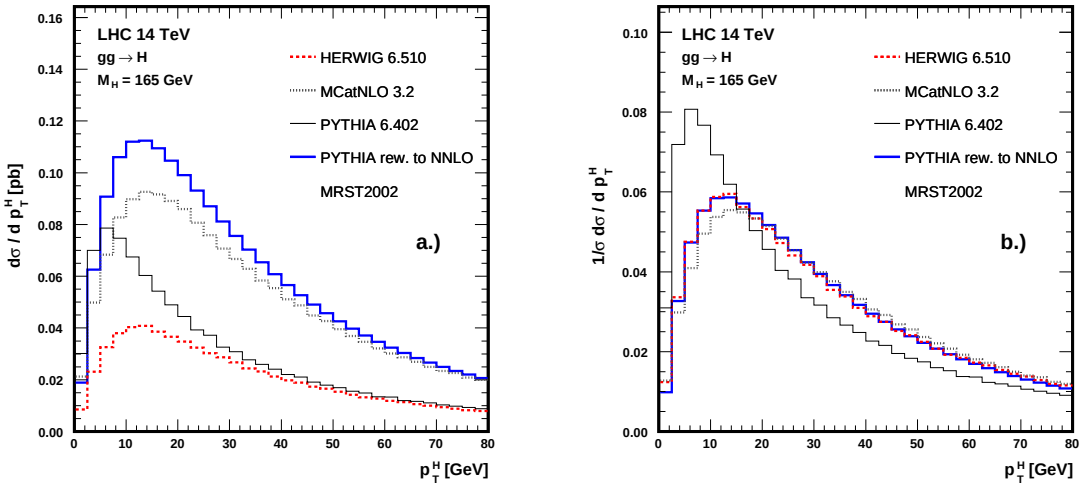

Figure 12.6: The p_T Higgs spectrum for a Higgs mass of 165 GeV and four different Monte Carlo programs: HERWIG, MC@NLO, PYTHIA and PYTHIA reweighted to NNLO. Absolute (a) and normalized (b) scale. No cuts are applied. For PYTHIA, the q-ordered showering is used. More p_T Higgs spectra, including the predictions from k_T-ordered shower in PYTHIA and results with CASCADE [86], can be found in [89] p.246-250 and [82] p.127-131.

Carlo predictions (m_H = 165 GeV). Compared are PYTHIA, HERWIG, MC@NLO, and HqT. Figure 12.6b shows the normalized cross section to compare the shapes of the different

calculations.
For Higgs transverse momenta smaller than 10-15 GeV, large unknowns prevent currently an accurate calculation of the Higgs p_{T} spectrum.
The used search strategy requires various selection criteria, especially the jet veto, which essentially remove all events where the Higgs has a transverse momentum larger than the value for the jet veto cut ($p_{\mathrm{T}}^{\mathrm{Jet}}$), which is chosen to be at 30 GeV. Figure 12.6 and the discussion in Chapter 6 demonstrate that the Higgs p_{T} spectrum can currently not be calculated precisely. In addition, the Higgs p_{T} spectrum can not be measured directly in this channel. One should therefore try to find an observable which is rather independent from the specific Higgs p_{T} spectrum. We will investigate in the following if the Higgs mass sensitivity of the lepton p_{T} spectra is large enough compared to the potential correlations with the not well known Higgs p_{T} spectrum.
The studied experimental observables are the lepton p_{T} spectra (p_{Tmax}^{ℓ} and p_{Tmin}^{ℓ}) and Δp_{T}, defined on an event by event basis (p_{Tmax}^{ℓ}- p_{Tmin}^{ℓ}).
Figure 12.7 shows the mean value of Δp_{T} without (12.7a) and with (12.7b) cuts as a function of the Higgs p_{T} and for a Higgs mass of 155 GeV, 165 GeV and 175 GeV.
It is interesting to see that this observable, before and after cuts, is essentially independent

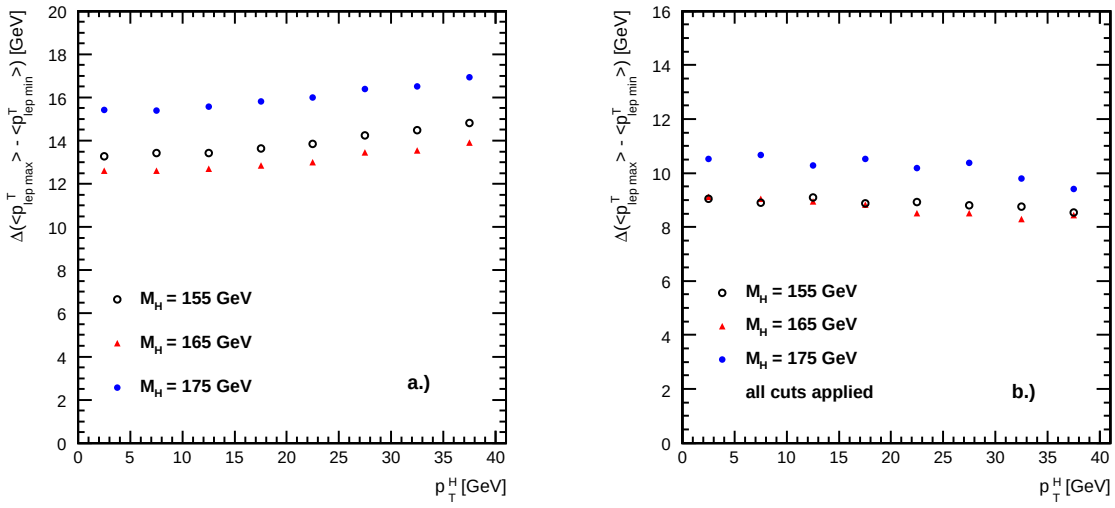

Figure 12.7: Average Δ p_{T} between the leptons as a function of p_{T} Higgs. (a) No cuts are applied except two isolated leptons required (b) all cuts are applied.

from the Higgs p_{T} spectrum. Consequently, the unknown details of the Higgs p_{T} spectrum are not relevant for the interpretation of this observable. We will investigate now how well the predictions for a Higgs mass of 155 GeV and 175 GeV can be distinguished. With all cuts applied (Figure 12.7b) the p_{T} difference of the two charged leptons is on average about 10 GeV for a Higgs mass of 175 GeV compared to about 9 GeV for a mass of 165 GeV and lower. This difference of about 1 GeV should be compared to the error for the mean value, expected to be roughly RMS/$\sqrt{N}$, or about 5.3 GeV/$\sqrt{302}$ = 0.3 GeV for an integrated luminosity of

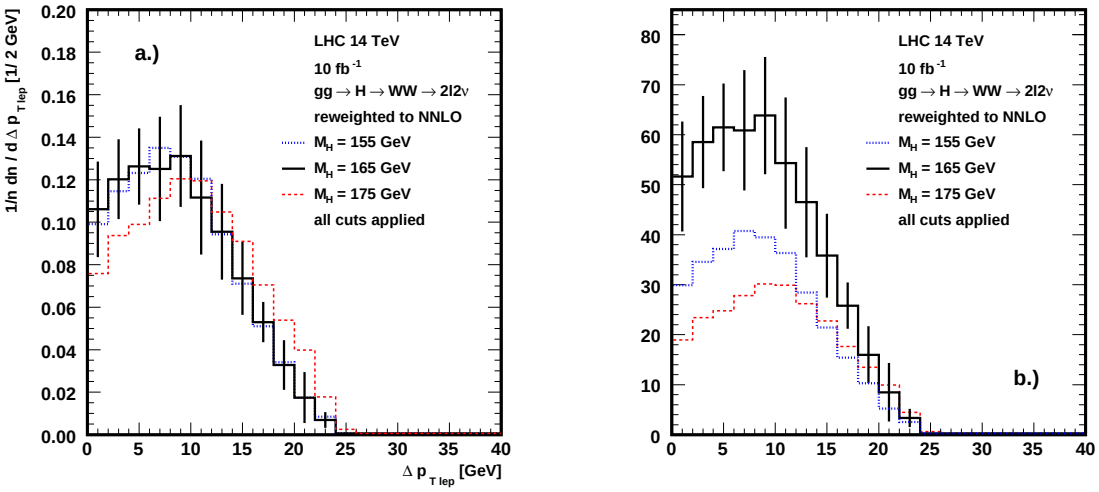

Figure 12.8: Difference between the p_T distributions of the leptons for different Higgs masses. The error for m_H 165 GeV is given for a luminosity of 10 fb^{-1}. (a) Normalized and (b) absolute number of events for 10 fb^{-1}. All cuts are applied.

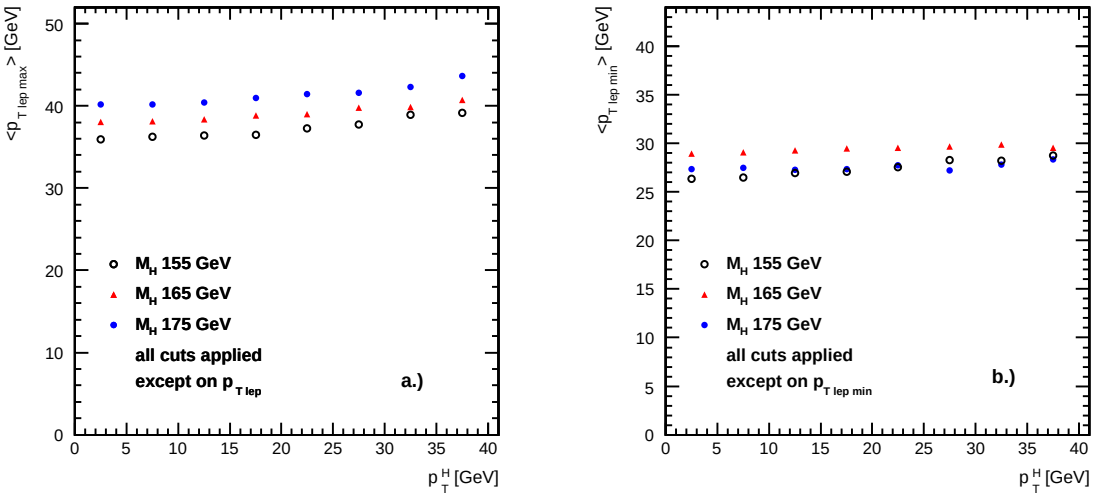

Figure 12.9: Average transverse momenta of the leptons as a function of p_T Higgs, all cuts applied, except the ones on p_T of the leptons (a) and except the one on p^{ℓ}_{Tmin} (b).

10 fb^{-1} and a mass of 155 GeV. Consequently, the distribution allows to distinguish a mass of 155 GeV and 175 GeV with at least 3 sigma.
Next, the shape of the entire Δp_{T} distribution, shown in Figure 12.8a (normalized) show the predicted shape and Figure 12.8b in addition the differential distribution expected from the Standard Model using the NNLO prediction (with reweighting) from the HqT program for 10 fb^{-1} and with all cuts applied.
Using only the shapes, shown in 12.8a, the statistics from a measurement with a luminosity of 10 fb^{-1} should be sufficient to distinguish a Higgs mass of 155 GeV from one at 175 GeV independent from any cross section assumptions. In a more detailed analysis and once a signal has been observed, a detailed shape analysis would accurately count the number of signal events per Δp_{T} bin. For example one could measure the fraction of signal events with Δp_{T} larger than 15 GeV in Figure 12.8a, resulting in a difference of about 2 sigma between 175 GeV and the two lower mass hypotheses 165 GeV and 155 GeV. Such an analysis would certainly also benefit from much larger luminosities. Similar and if in addition the SM cross section prediction is assumed, as shown in Figure 12.8b, even a mass between 165 GeV and 155 GeV can be separated easily.
Finally, one can study how the lepton p^{ℓ}_{Tmax} and p^{ℓ}_{Tmin} distributions are correlated with the Higgs mass and the Higgs p_{T} spectrum. Figure 12.9 shows (1) that the average values for p^{ℓ}_{Tmax} and p^{ℓ}_{Tmin} are essentially independent from details of the Higgs p_{T} spectrum and (2) that some correlation with the Higgs mass exists. Figure 12.10a and 12.10b show the shape of the p^{ℓ}_{Tmax} and p^{ℓ}_{Tmin} distributions for accepted events with all cuts except the final lepton p_{T} cuts in the p^{ℓ}_{Tmax} distribution and all cuts except the cuts on p^{ℓ}_{Tmin} in the p^{ℓ}_{Tmin} distribution applied. The corresponding distributions with the absolute cross section are shown in Figure 12.11a and 12.11b. These distribution demonstrate clearly that a more detailed analysis of the p_{T} spectrum, especially when much larger luminosities become available, can increase the potential mass range for this signature perhaps to Higgs masses well below 150 GeV and should improve the Higgs mass measurement considerably. For example, as one can see in Figure 12.11a, about 21% of the excess events and a Higgs mass of 175 have a p^{ℓ}_{Tmax} larger than 50 GeV. This should be compared with about 11% for a mass of 165 GeV and 6% for a mass of 155 GeV. Once an excess of Higgs-signal-like events has been demonstrated one would then analyze the distributions of p^{ℓ}_{Tmax} and p^{ℓ}_{Tmin} in much more detail. For example, one could measure the excess of signal events for p^{ℓ}_{Tmax} larger than 50 GeV and/or p^{ℓ}_{Tmin} between 10 GeV and 20 GeV and compare this to the mass dependence in the most accurate Monte Carlo simulations.
Figures 12.7 and 12.9 demonstrate that the Higgs mass and the average lepton transverse momenta are correlated, while essentially no correlation between the transverse Higgs momentum and the average lepton p_{T} can be seen.
This on the first view surprising result can be qualitatively understood as follows. The transverse momentum spectra of the leptons depend essentially only on the mass of the intermediate W, their p_{T}, and the spin correlations between the two W's.
For a Higgs mass slightly above 160 GeV, essentially both W bosons are on shell. For lower Higgs masses one finds that it is more likely that the available decay energy will rather go into the W mass than into its momentum. For larger Higgs masses, the energy of the W boson and thus its average transverse momentum will increase rapidly. For example, in the

rest frame of the Higgs with a mass of 180 GeV, decaying into two on shell W's, one expects already an average W momentum of about 40 GeV.
Depending on the spin orientation, the charged leptons will either be emitted in the direction of the W momentum or against it in the rest frame of the Higgs. In case the lepton is emitted in the direction of the W, its momentum will also be increased. In contrast, if its emitted opposite the W momentum, as forced by the spin correlations in the W rest frame, its momentum in the lab frame will be reduced. As long as the mass of the W is much larger than its p_T, the two resulting leptons will have a small opening angle in the lab frame.
For very large Higgs masses, this condition is not fulfilled any more, and the small opening

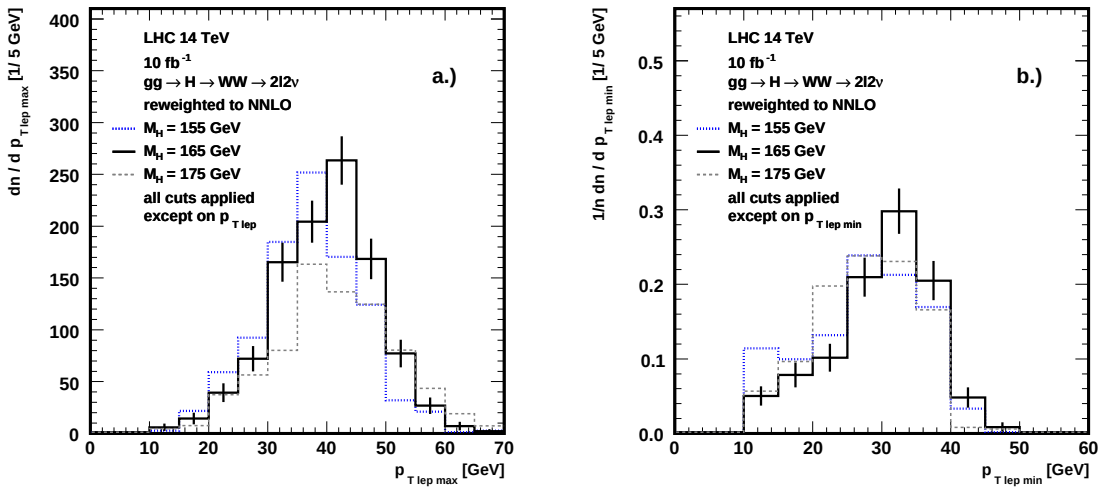

Figure 12.10: Normalized p_T distribution of the leptons for different Higgs masses and for a luminosity of 10 fb^{-1}. (a) All cuts are applied except the ones on p_T of the leptons (b) all cuts are applied except the one on p^{ℓ}_{Tmin} .

angle between the two charged leptons, which is the signal signature, will disappear.
What happens now when the Higgs boson, with a mass close to 2 m_W, itself has a small (compared to m_W) transverse momentum? On average and very qualitatively, this will add some transverse momentum to the W emitted in the direction of the momentum of the Higgs boson and reduce the transverse momentum of the other W boson. Consequently, one charged lepton gets a slightly larger p_T and the other one a slightly smaller p_T. As a result one would expect that the width of the lepton p_T spectrum gets broader while their mean values and especially their difference remain essentially unchanged as long as the selection criteria do not cut too strongly in the low momentum tail.

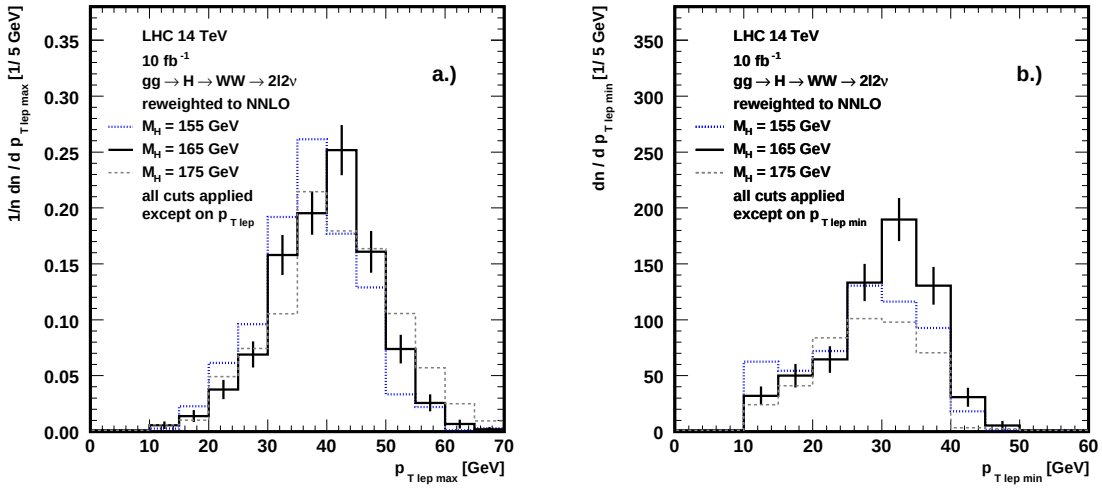

Figure 12.11: p_{T} distribution of the leptons for different Higgs masses and for a luminosity of 10 fb^{-1}. (a) All cuts are applied except the ones on p_{T} of the leptons (b) all cuts are applied except the one on p^{ℓ}_{Tmin} .

12.3 Combined Higgs Mass Measurement

In section 12.1 the correlation between the number of expected signal events with the Higgs mass has been used to estimate the Higgs mass. As a result a mass measurement with an error between 2.0 GeV and 2.5 GeV has been obtained assuming the validity of the Standard Model cross section calculation with a theoretical accuracy of 5%. However, the cross section interpretation for masses below 160 GeV or above 168 GeV leads to two possible Higgs masses. In section 12.2 correlations between the lepton transverse momenta and the Higgs mass have been studied. In particular we have demonstrated that the lepton p_{T} spectra and their difference originating from a Higgs with a mass of 155 GeV and 175 GeV differ, in a rather model independent way, by more than 3 standard deviations. Thus, once the number of signal events is not consistent with the mass intervall between 160-168 GeV, the cross section ambiguities for the mass interpretation can be resolved by a detailed analysis of the lepton p_{T} spectra. A combination of the accepted number of events (or accepted cross section) with the analysis of the lepton p_{T} spectra will allow to identify which of the mass hypotheses is valid. For example, if about 300 signal events would be selected for a luminosity of 10 fb^{-1}, either a mass of 155 $\pm$ 2 GeV or 173 $\pm$ 2 GeV would be possible. The analysis of the lepton p_{T} spectra indentifies the correct solution. In a similar approach and once a signal has been identified, one would test if the mass interpretation from the Standard Model cross section predicts also a good agreement with the observed lepton p_{T} spectrum. If this is not the case, and with larger statistics, the lepton p_{T} spectra can be used to demonstrate that the observed signal deviates from the SM.

Chapter 13

Summary

In this thesis, the channel gg $\rightarrow$ H $\rightarrow$ WW $\rightarrow \ell\nu\ell\nu$ has been studied in unprecedent detail. In comparison with the original study by Dittmar and Dreiner, who established H $\rightarrow$ WW $\rightarrow \ell\nu\ell\nu$ as the discovery channel in the mass region between 150 and 180 GeV, the following approvements could be made:
The signal selection was described at NNLO, and most backgrounds could be included at NLO. In addition, the gg$\rightarrow$WW background was included for the first time. Observables like the $p_{\mathrm{T}}^{\mathrm{H}}$ and p_{Tmax}^{ℓ} spectrum were compared in different Monte Carlo predictions and uncertainties of up to 20-30% due to the use of different Monte Carlos were found. A full detector simulation was performed and a data driven approach to determine the background was presented. And finally, a quantitative method to determine the mass of a SM Higgs in this channel was performed, following some ideas outlined in the paper by Dittmar and Dreiner. We will summarize these achievements in the following.
The kinematics of Higgs boson production at LHC is basically described by its transverse momentum p_{T} and rapidity η. If one assumes $K(\eta)$, which is the K-factor as a function of the rapidity, to be constant in the region important for our signal selection, only the p_{T} spectrum dependence can be taken into account in a first approximation. Higher order QCD corrections can thus be included in the signal analysis by reweighting the p_{T} spectrum of the Higgs obtained with a parton shower Monte Carlo like PYTHIA to the most up-to-date p_{T} spectra at higher order, which is currently the resummed NNLO+ NNLL spectrum for the p_{T} spectrum of the Higgs; the NNLO+NNLL spectrum is obtained with the program HqT, written by Grazzini et al. We found that the effective K-factor (2.1 for a scale $\mu_R = \mu_f = m_H$) is only about 10 to 15% smaller than the inclusive one (2.3 for a scale $\mu_R = \mu_f = m_H$). Including the higher order correction by this reweighting procedure multiplies the LO cross section by a factor of about 2, depending on the scale chosen for μ_R and μ_f (Chapter 8, 9). The dependence on the rapidity was investigated by reweighting PYTHIA and MC@NLO to the differential NNLO transverse momentum and rapidity spectra of the Higgs, calculated with the fixed order NNLO program FEHIP. It was found that the effect of the rapidity is smaller than 3%, and thus indeed very small. Without an extension of the MC@NLO procedure to NNLO, the reweighting procedure currently offers the best way of combining parton showering and hadronization with NNLO calculations. In addition, as no full spin correlation is included in MC@NLO in this channel yet, MC@NLO cannot be used to per-

form a full analysis in $H \rightarrow WW \rightarrow \ell\nu\ell\nu$ (Chapter 9).
It is important to point out that reweighting to fixed order NLO leads to a wrong result due to the inaccurate multiplicities at fixed order NLO. Reweighting of a parton shower Monte Carlo should thus be applied to the p_T (and, if available, rapidity) distributions provided by a resummed NNLO+NNLL, parton shower NLO, or a NNLO program.
Higher order QCD corrections to the nonresonant WW channel $qq\rightarrow$ WW were included by reweighting the PYTHIA p_T^{WW} spectrum to the NLO+NLL spectrum, predicted by HqT, and an effective K-factor of about 1.4 was found, which is about 15 - 20% smaller than the inclusive K-factor (Chapter 9).
The inclusion of higher order QCD corrections was also studied in the $t\bar{t}$ background. Large improvements were made in the theoretical understanding of the top background in the last years. For a long time it was not clear how to consider the processes Wtb and $t\bar{t}$ in an independent way at higher order, as $t\bar{t}$ is a higher order diagram of the Wtb background. It was found that if a jet veto is applied, the single and double resonant top backgrounds can be separated and thus higher order corrections be included disjoined in both channels (Chapter 10).
We then studied if applying an inclusive K-factor is sufficient for the $t\bar{t}$ background, or if we need to include effective K-factors. For this, the shapes of the different observables in a LO and NLO program were compared. It was shown that, as the leading order process has already two high energetic jets, higher order QCD corrections do not change the shapes of the observables significantly and an inclusive K-factor can be used. The K-factor for $t\bar{t}$ production is 1.6. For Wtb it was found to be 0.7 (Chapter 10).
The gg→WW background was included for the first time in a full parton shower Monte Carlo study. This reaction was calculated at leading order two years ago by two different groups. We added parton showering to the events which were generated at partonic level and analysed it using the full CMS detector simulation. It was found that the gg→WW process contributes about 30% to the total WW background (Chapter 11).
The uncertainty in the predictions of the Higgs p_T spectrum obtained with different Monte Carlo generators was studied and found to be rather large (10-15%, Chapter 6). However, this uncertainty can be reduced when reweighting the p_T spectra to the most up-to-date p_T spectra predicted at NNLL+NNLO. The uncertainty on the jet veto efficiency was found to be about 10%. This uncertainty can be reduced in a data driven approach to determine the background. Once data is g, the change in the slope of the jet transvere momentum distribution can be determined in respect to a change in the transverse energy scale. This can be used to tune the Monte Carlo generators (Chapter 11).
Different observables were also compared in the $t\bar{t}$ background and the uncertainty due to the use of different Monte Carlo programs found to be large: the difference when spin correlations are included in a program or not is around 10%. Moreover, the difference due to the use of diverse showering models is around 15% between HERWIG and PYTHIA and 20% between TopREX and HERWIG (Chapter 10). As these uncertainties are rather big, it is important to find a way to determine the backgrounds as independently as possible from Monte Carlo predictions. A data driven approach to determine background systematics was therefore used in Chapter 11 and 12.
A full CMS detector analysis study based on GEANT and performed at NLO confirms previ-

ous results obtained without full detector simulation, with a similar signal over background ratio and slightly reduced efficiency.
A background determination tuned on data was presented. Taking into account the sum of the different backgrounds, an overall uncertainty of 10% is found on the total background if only the background systematics are considered. Adding the contribution from limited Monte Carlo statistics, this uncertainty increases to 13%. These results are calculated for an integrated luminosity of 5 fb^{-1}. For integrated luminosities of 1, 2 and 10 fb^{-1}, the total systematic uncertainty scales to 19%, 16% and 11%, respectively. For a Higgs boson mass of 165 GeV, the inclusion of background systematics increases the luminosity needed for a 5σ discovery by a factor of 1.8, going from 0.5 fb^{-1} to 0.9 fb^{-1}, thus confirming the results from the first rough simulation in 1997 [48]. Due to the relatively high signal over background ratio of 1.7, the signal is less sensitive to background fluctuations, leading to the relatively small change in the required luminosity for a discovery.
Using a full CMS detector simulation and including background uncertainties, it was demonstrated that the Standard Model Higgs boson can be discovered in the H $\rightarrow$ WW$\rightarrow \ell\nu\ell\nu$ channel with an integrated luminosity of less than 1 fb^{-1} if its mass is around 165 GeV. If it has a mass between 150 and 180 GeV, a 5σ signal can be seen with a luminosity of less than 10 fb^{-1} (Chapter 11).
Assuming that the LHC experiments will discover a Higgs-like signal in the channel gg $\rightarrow$ H$\rightarrow$ WW $\rightarrow \ell\nu\ell\nu$, different experimental observables have been analysed in order to establish how and how well the Higgs mass can be measured in this channel. Using the now well established selection procedure, the observed event rate can be used to determine the Higgs mass, assuming Standard Model couplings. In addition it is shown that the observable lepton p_{T} spectra are also sensitive to the Higgs mass, while details of the QCD modelling of the Higgs p_{T} spectrum are not important for the Higgs mass measurement.
Combining the hypothetical cross section measurement with the lepton p_{T} spectra and the estimated systematic uncertainties of about 10-15%, associated with this signature, we find that the mass of a Standard-Model-Higgs-like signal in the mass range from 150-180 GeV can be measured with an accuracy of 2 to 2.5 GeV. In case that no further improvements in the systematics for this channel can be achieved, our analysis shows also that such a mass measurement will be dominated by systematic uncertainties once integrated luminosities between 10 to 20 fb^{-1} can be analysed (Chapter 12).

Acknowledgements

It was very enriching to be part of the Instiute for Particle Physics of ETH and of the community at CERN.
I want to thank Prof. Felicitas Pauss for giving me the possibility to perform my PhD thesis in such an inspiring surrounding, her enthusiasm and the good working conditions I came across.
A special thank goes to Prof. Zoltan Kunszt for being my coreferee, and for the useful comments concerning the theoretical background of electroweak symmetry breaking.
I wish to express my sincere thank to Michael Dittmar for his excellent supervision. He was always there when a question occured and supported my work throughout all parts of this thesis. His expertise and enthusiasm were very enriching.
My special thank goes to Anne-Sylvie for being such a good collaborator during all those years and the help with PAX and ORCA.
I am thankful that I met Babis Anastasiou, who was not only an inspiring collaborator, but also there in many other issues. In this context I also want to thank Kiril Melnikov and Frank Petriello for the work on the common paper.
Sascha Nikitenko and the Higgs group for new inputs and ideas, and the whole $H \rightarrow WW$ group, especially Marco Zanetti, for the good collaboration.
Massimiliano Grazzini, Gennaro Corcella, Stefano Frixione and Hannes Jung for their advice on the different theoretical and Monte Carlo generator issues.
Torbjorn Sjostrand for having always an open ear for the various questions concerning the many tuning parameters in PYTHIA.
Fabio Maltoni and John Campbell for their work on the top background and Nikolas Kauer for providing us with his ggWW program.
Guenther Dissertori and Filip Moortgat for being there when a question came up.
André and Fabian for their competent support in computer questions and Gabriele for her help in administrative issues in all those years.
Many persons enriched my social life in and outside of CERN, in particular Rico, Jan, Pol, Anselmano, Cug, Anne-Sylvie, Fabian, André, Peter and Pedja.
And finally I want to express my gratitude to my family for providing me with viande des Grisons in the crucial moments and the support they gave me during my life.

Having performed these studies, I am very curious about what will happen in the next years at LHC and about what theory we can tell the next generations in 50 years from now (or they will tell us!). This thesis is therefore dedicated to Gian Andrin and Maurus Fabian, who was just born when I completed these last lines.

Appendix A

List of Abbreviations

ALICE	A Large Ion Collider Experiment
ATLAS	A Toroidal LHC ApparatuS
B	Background
BGO	Bismuth Germanate
BR	Branching Ratio
CERN	European Organization for Nuclear Research
CMS	Compact Muon Solenoid
CSC	Cathode Strip Chambers
DAQ	Data Acquisition
DESY	Deutsches Elektronen Synchrotron ("German Electron Synchrotron")
DGLAP	Dokshitzer-Gribov-Lipatov-Altarelli-Parisi, also called Altarelli-Parisi equation
DT	Drift Tubes
ECAL	Electromagnetic Calorimeter
GeV	Giga Electron Volt
GUT	Grand Unification Theory
HCAL	Hadron Calorimeter
HERA	Hadron Elektron Ringanlage ("Hadron Electron Ring Accelerator")
HLT	High Level Trigger
JES	Jet Energy Scale
ME	Matrix Element
L3	Experiment at LEP
LEP	Large Electron Positron Collider
LHC	Large Hadron Collider
LHCb	Large Hadron Collider beauty
LINAC	Linear Accelerator
LO	Leading Order
MC	Monte Carlo
MeV	Mega Electron Volt
MSSM	Minimal Supersymmetric Standard Model

N	Number of events
(N)NLL	(Next to) Next to Leading Logarithm
(N)NLO	(Next to) Next to Leading Order
$PBWO_4$	Lead Tungstate
PDF	Parton Distribution Function
QCD	Quantum Chromodynamics
QED	Quantum Electrodynamics
RPC	Resistive Plate Chambers
RF	Radio Frequency
RPC	Resistive Plate Chambers
S	Signal
SM	Standard Model
SUSY	Supersymmetry
SV(C)	Soft-Virtual (-Collinear) Approximation
TESLA	TeV Energy Superconducting Linear Accelerator
TeV	Tera Electron Volt
TEC	Tracker End Caps
TIB	Tracker Inner Barrel
TID	Tracker Inner Disks
TOB	Tracker Outer Barrel
UE	Underlying Event
VBF	Vector Boson Fusion
VEV	Vacuum Expectation Value

Appendix B

Overview of Monte Carlo Programs

LO programs

PYTHIA [74] is a LO parton shower event generator for the description of collisions at high energies between elementary particles such as e+, e-, p and $\bar{\text{p}}$. It contains theory and models for a number of physics aspects, including hard and soft interactions, parton distributions, initial and final state parton showers, multiple interactions, fragmentation and decay. PYTHIA is based on the DGLAP evolution equations and provides leading order calculations of the cross sections. The formation of hadrons is simulated using the LUND string model. From PYTHIA version 6.3 on, one can choose between the Q^2-ordered showering model and the p_{T}-ordered showering model.

HERWIG [75] is a general purpose LO parton shower event generator which including the simulation of hard lepton-lepton, lepton-hadron and hadron-hadron scattering and soft hadron-hadron collisions. HERWIG implements the cluster hadronization approach to describe the fragmentation of quarks into hadrons via non-perturbative gluon splitting. The coloured objects in the final state are combined to colour-singlet clusters which are subsequently fragmented into hadrons. HERWIG is based on the DGLAP evolution equations and provides leading order calculations of the cross sections. The cluster algorithm is used to form hadrons from clusters of quark-antiquark states in a colour-singlet configuration.

TopReX [123] is a LO event generator specialized in top production (single and pair production), H+jets, W+jets and Z+jets. TopReX is interfaced with PYTHIA for the parton showering. The spin polarizations of the top-quarks are taken into account in the subsequent decay of the top-quarks. All calculated subprocesses can be accessed from PYTHIA as external processes. In addition, TopReX can be used as stand alone event generator, providing partonic final states before showering.

The Monte Carlo generator CASCADE [86] is a full hadron level Monte Carlo generator for ep and pp scattering at small x according the CCFM evolution equation. In CASCADE the direct heavy quark production processes are implemented using off-shell matrix elements convoluted with unintegrated parton distributions in the proton. For the final state parton

showers PYTHIA is used, and thus the formation of hadrons simulated using the LUND string model. The unintegrated gluon density in the proton has been determined in fits to the inclusive structure function data.

NLO programs

MC@NLO [69] is a parton shower event generator with next-to-leading-order QCD matrix elements. The total cross section is given at NLO. MC@NLO is interfaced to HERWIG for parton showering.

MCFM [122] is a parton level Monte Carlo generator, specialized in processes like W+jets, Z+jets, H+jets. The program is designed to calculate cross-sections for various femtobarn-level processes at hadron-hadron colliders. For most processes, matrix elements are included at next-to-leading order and full spin correlations are incorporated.

NNLO programs

HqT [68] computes the transverse momentum distribution for Higgs production in pp collisions at NLL+LO and NNLL+NLO accuracy. At NLL+LO the normalization is fixed to the total NLO cross section, while at NNLL+NLO the normalization is fixed to the total NNLO cross section. At small p_{T} the logarithmically-enhanced terms are resummed to all orders up to next-to-next-to-leading logarithmic accuracy. The resummed component is consistently matched to the next-to-leading order calculation valid at large p_{T}.

FEHiP [65] computes the production cross section and fully differential distributions for Higgs boson production at hadron colliders through NNLO in perturbative QCD. Arbitary cuts can be imposed on partonic jets and on the decay products of the Higgs boson. The Higgs decay into two photons is currently implemented.

List of Figures

List of Tables

Bibliography

[1] S. L. Glashow, Nucl. Phys. **20** 579 (1961); A. Salam, in *Elementary Particle Theory*, N. Svartholm, Almqvist and Wiksells, Stockholm; S.Weinberg, Phys. Rev. Lett. **19** 1264 (1967).

[2] P.W. Higgs, Phys. Rev. Lett. 13 (1964) 508; Phys. Rev. 145 (1966) 1156; F. Englert and R. Brout, Phys. Rev. Lett. 13 (1964) 321; G.S. Guralnik, C.R. Hagen and T. Kibble, Phys. Rev. Lett. 13 (1965) 585; T. Kibble, Phys. Rev. 155 (1967) 1554.

[3] The LEP Collaboration (ALEPH, DELPHI, L3 and OPAL), Phys. Lett. B565 (2003) 61.

[4] B. A. Kniehl, Standard-model Higgs boson production at HERA, Prepared for Workshop on Future Physics at HERA (Preceded by meetings 25-26 Sep 1995 and 7-9 Feb 1996 at DESY), Hamburg, Germany, 30-31 May 1996.

[5] M. Krawczyk, arXiv:hep-ph/9609477.

[6] The CDF and DØ collaborations and the Tevatron Electroweak Working Group, hep-ex/0404010.

[7] M. Gell-Mann, Phys. Lett. 8 (1964) 214; G. Zweig, CERN-Report 8182/TH401 (1964); H. Fritzsch, M. Gell-Mann and H. Leutwyler, Phys. Lett. B47 (1973) 365; D. Gross and F. Wilczek, Phys. Rev. Lett. 30 (1973) 1343; H.D. Politzer, Phys. Rev. Lett. 30 (1973) 1346; G. t' Hooft, Marseille Conference on Yang–Mills fields (1972).

[8] G. t' Hooft, Nucl. Phys. B33 (1971) 173; Nucl. Phys. B35 (1971) 167; G. 't Hooft and M. Veltman, Nucl. Phys. B44 (1972) 189.

[9] Particle Data Group, K. Hagiwara *et al.*, Phys. Rev. D66 (2002) 010001; S. Eidelman *et al.*, Phys. Let. B592 (2004) 1.

[10] F.J. Hasert *et al.* (Gargamelle Collaboration), Phys. Lett. B46 (1973) 121; *ibid.* Phys. Lett. B46 (1973) 138; T. Eichten *et al.* (Gargamelle Collaboration), Phys. Lett. B46 (1973) 274.

[11] G. Arnison *et al.* (UA1 Collaboration), Phys. Lett. B122 (1983) 103; M. Banner *et al.* (UA2 Collaboration), Phys. Lett. B122 (1983) 476; G. Arnison *et al.* (UA1 Collaboration), Phys. Lett. B126 (1983) 398; P. Bagnaia *et al.* (UA2 Collaboration), Phys. Lett. B129 (1983) 130.

[12] Y. Nambu, Phys. Rev. Lett. 4 (1960) 380; Y. Nambu and G. Jona–Lasinio, Phys. Rev. 122 (1961) 345; *ibid.* Phys. Rev. 124 (1961) 246; J. Goldstone, Nuov. Cim. 19 (1961) 154; J. Goldstone, A. Salam and S. Weinberg, Phys. Rev. 127 (1962) 965.

[13] M. Gomez-Bock, M. Mondragon, M. Muhlleitner, R. Noriega-Papaqui, I. Pedraza, M. Spira and P. M. Zerwas, J. Phys. Conf. Ser. **18** (2005) 74 [arXiv:hep-ph/0509077].

[14] T. Cheng, E. Eichten and L. Li, Phys. Rev. D9 (1974) 2259; B. Pendleton and G. Ross, Phys. Lett. B98 (1981) 291; C. Hill, Phys. Rev. D24 (1981) 691; J. Bagger, S. Dimopoulos and E. Masso, Nucl. Phys. B253 (1985) 397; M. Beg, C. Panagiotakopoulos and A. Sirlin, Phys. Rev. Lett. 52 (1984) 883; M. Duncan, R. Philippe and M. Sher, Phys. Lett. B153 (1985) 165; K. Babu and E. Ma, Phys. Rev. Lett. 55 (1985) 3005.

[15] K.G. Wilson and J. Kogut, Phys. Rept. 12 (1974) 75.

[16] M. Lindner, M. Sher and H.W. Zaglauer, Phys. Lett. 228B (1989) 139; M. Sher, Phys. Lett. B317 (1993) 159; *ibid.* Phys. Lett. B331 (1994) 448; G. Altarelli and I. Isidori, Phys. Lett. B337 (1994) 141; J.A. Casas, J.R. Espinosa and M. Quiros, Phys. Lett. B342 (1995) 171; J. Espinosa and M. Quiros, Phys. Lett. B353 (1995) 257.

[17] M. Sher, Phys. Rept. 179 (1989) 273.

[18] G. Isidori, G. Ridolfi and A. Strumia, Nucl. Phys. B609 (2001) 387.

[19] J. Casas, J. Espinosa, M. Quiros, and A. Riotto, Nucl. Phys. B 436, 3 (1995); L. Maiani, G. Parisi, and R. Petronzio, Nucl. Phys. B 136, 115 (1978).

[20] K. Riesselmann, arXiv:hep-ph/9711456.

[21] D. N. Spergel *et al.*, arXiv:astro-ph/0603449.

[22] O. Lahav and A. R. Liddle, arXiv:astro-ph/0601168.

[23] G. Barenboim, O. Mena Requejo and C. Quigg, Phys. Rev. D **74**, 023006 (2006) [arXiv:astro-ph/0604215].

[24] S. P. Martin, arXiv:hep-ph/9709356.

[25] J. Lykken, "Introduction to Supersymmetry," hep-th/9612114.

[26] H. E. Haber and G. L. Kane, "The Search for Supersymmetry: Probing Physics Beyond the Standard Model, Appendix B," Phys. Rept. 117 (1985) 75.

[27] F.Moortgat, PhD thesis,"Discovery Potential of MSSM Higgs bosons using supersymmetric decay modes with the CMS detector", 2004.

[28] Thomas G. Rizzo, Phenomenology of Higgsless Electroweak Symmetry Breaking, http://www.citebase.org/abstract?id=oai:arXiv.org:hep-ph/0405094, 2004.

[29] TESLA Technical Design Report, DESY 2001-011; ECFA 2001-209; March 200.1

[30] Proposal to the Rutherford Appleton Laboratory, An International Muon Ionization Cooling Experiment, MICE-Note 21, http://www.mice.iit.edu/mnp/MICE0021.pdf.

[31] O.Bruning et al., LHC design report Vol.I : the LHC Main Ring, CERN-2004-003;2003.

[32] ATLAS Collaboration, *Detector and Physics Performance Technical Design Report*, Vols. 1 and 2, CERN–LHCC–99–14 and CERN–LHCC–99–15.

[33] CMS Technical Proposal, CERN/LHCC/94–38 and LHCC/P1.

[34] LHCB Technical Proposal, CERN/LHCC/98-4; February 1998.

[35] ALICE Technical Proposal, CERN/LHCC/95-71, December 1995.

[36] U. A. Wiedemann, AIP Conf. Proc. **842** (2006) 11.

[37] R. F. Avila, E. G. S. Luna and M. J. Menon, Braz. J. Phys. **31** (2001) 567 [arXiv:hep-ph/0105065].

[38] R. Bailey, Prepared for 11th Workshop on Electronics for LHC and Future Experiments (LECC 2005), Heidelberg, Germany, 12-16 September 2005.

[39] A. Zabi, CMS-CR-2006-067 Prepared for 12th International Conference on Calorimetry in High Energy Physics (CALOR 06), Chicago, Illinois, 5-9 Jun 2006.

[40] M. Spira, M. Dittmar, "Standard Model Higgs cross sections (NLO) and PYTHIA", CMS Note 1997/080

[41] R. V. Harlander, W. B. Kilgore,hep-ph/0211380

[42] Z. Kunszt, S. Moretti, W. J. Stirling, Z. Phys. C **74**, 479 (1997), [hep-ph/9611397]

[43] A. Djouadi, J. Kalinowski and M. Spira, Comput. Phys. Commun. **108** (1998) 56 [arXiv:hep-ph/9704448].

[44] D. Rainwater, M. Spira, D. Zeppenfeld, "Higgs boson production at hadron colliders", hep-ph/0203187

[45] A. Djouadi, Czech. J. Phys. **55** (2005) B23 [arXiv:hep-ph/0412238].

[46] A.S. Nicollerat, *Prospects of Measuring $qq \to qqH$ and $gg \to H$ Cross Sections at the LHS with CMS* or *The Higgs files*, Diploma thesis ETH Zürich, 2001

[47] D. Rainwater, M. Spira and D. Zeppenfeld in Report of the Higgs Working Group, Proceedings of the Les Houches Workshop on "Physics at TeV Colliders", 2003, hep-ph/0406152.

[48] M. Dittmar and H. Dreiner, Phys. Rev. D55 (1997) 167; M. Dittmar, hep-ex/9901009.

[49] D. Green *et al.*, J. Phys. G26 (2000) 1751; K. Jakobs and Th. Trefzger, ATLAS Note ATL–PHYS–2003–024.

[50] S. Zmushko *et al.*, ATLAS Internal Note PHYS-NO-008 (1992); S. Abdullin and N. Stepanov, CMS-TN/94-178 (1994).

[51] J.-C. Chollet *et al.*, ATLAS note PHYS-NO-17 (1992); L. Poggioli, ATLAS Note PHYS-NO-066 (1995); D. Denegri, R. Kinnunen and G. Roullet, CMS-TN/93-101 (1993); I. Iashvili R. Kinnunen, A. Nikitenko and D. Denegri, CMS TN/95-076; D. Bomestar *et al.*, Note CMS TN-1995/018; C. Charlot, A. Nikitenko and I. Puljak, CMS TN/95-101; G. Martinez, E. Gross, G. Mikenberg and L. Zivkovic, ATLAS Note ATL-PHYS-2003-001 (2003).

[52] For recent studies using the new software, see the talks of S. Hassani, T. Lagouri and M. Sani, at the Conference "Physics at LHC" in Proceedings of the Conference "Physics at LHC" in Vienna, 13–17 July 2004; see the web site: `wwwhephy.oeaw.ac.at/phlhc04/`.

[53] J. Gunion, G. Kane and J. Wudka, Nucl. Phys. B299 (1988) 231.

[54] J. Gunion, P. Kalyniak, M. Soldate and P. Galison, Phys. Rev. D34 (1986) 101.

[55] E. Eichten, I. Hinchliffe, K. Lane and C. Quigg, Rev. Mod. Phys. 56 (1984) 579.

[56] J. Stirling, R. Kleiss and S.D. Ellis, Phys. Lett. 163B (1985) 261; J. Gunion, Z. Kunst and M. Soldate, Phys. Lett. 163B (1985) 389; J. Gunion and M. Soldate, Phys. Rev. D34 (1986) 826; E. Glover, J. Ohnemus and S. Willenbrock, Phys. Rev. D37 (1988) 3193; V. Barger, G. Bhattachrya, T. Han and B. Kniehl, Phys. Rev. D43 (1991) 779.

[57] J. Smith, D. Thomas and W.L. van Neerven, Z. Phys. C44 (1989) 267; B. Mele, P. Nason and G. Ridolfi, Nucl. Phys. B357 (1991) 409; S. Frixione, P. Nason and G. Ridolfi, Nucl. Phys. B383 (1992) 3; J. Ohnemus and J.F. Owens, Phys. Rev. D43 (1991) 3626; J. Ohnemus, Phys. Rev. D44 (1991) 1403; Phys. Rev. D44 (1991) 3477; Phys. Rev. D47 (1992) 940; S. Frixione, Nucl. Phys. B410 (1993) 280; U. Baur, T. Han and J. Ohnemus, Phys. Rev. D48 (1993) 5140; Phys. Rev. D51 (1995) 3381; Phys. Rev. D48 (1996) 1098; Phys. Rev. D57 (1998) 2823; L.J. Dixon, Z. Kunszt and A. Signer, Phys. Rev. D60 (1999) 114037.

[58] E. Glover and J. van der Bij, Nucl. Phys. B321 (1989) 561 and Phys. Lett. B219 (1991) 488; E. Richter-Was, Z. Phys. C64 (1994) 227; C. Zecher, T. Matsuura and J.J. van der Bij, Z. Phys. C64 (1994) 219; D. Kominis and V. Koulovassilopoulos, Phys. Rev. D52 (1995) 2737; C. Balazs and C.-P. Yuan, Phys. Rev. D59 (1999) 114007; K.L. Adamson, D. de Florian and A. Signer, Phys. Rev. D65 (2002) 094041.

[59] R. Cahn and M. Chanowitz, Phys. Rev. Lett. 56 (1986) 1327.

[60] Ph. Mine, S. Moreau and I. Puljak, CMS Note 1999/071; I. Puljak, Ph.D Thesis, Ecole Polytechnique, 2000.

[61] S. Dawson, P. Nason and R.K. Ellis, Nucl. Phys. B303 (1988) 607; Nucl. Phys. B327 (1989) 49; W. Beennakker, H. Kuijf, W. van Neerven and J. Smith, Phys. Rev. D40 (1989) 54. For later developments, see the review of S. Frixione, M. Mangano, P. Nason

and G. Ridolfi, hep-ph/9702287. See also, N. Kauer and D. Zeppenfeld, Phys. Rev. D65 (2002) 014021.

[62] R.K. Ellis and S. Veseli, Phys. Rev. D60 (1999) 011501; Nucl. Phys. B511 (1998) 649; J.M. Campbell and R.K. Ellis, Phys. Rev. D62 (2000) 114012; Phys. Rev. D65 (2002) 113007.

[63] M. Dittmar, "LHC Luminosity Estimates to observe the Higgs and test its properties", talk given at FERMILAB workshop on "The future of Higgs Physics", FERMILAB, Illinois, USA, May 3, 2001.

[64] C. Anastasiou, K. Melnikov and F. Petriello, Phys. Rev. Lett. **93**, 262002 (2004) [arXiv:hep-ph/0409088].

[65] C. Anastasiou, K. Melnikov and F. Petriello, Nucl. Phys. B **724**, 197 (2005) [arXiv:hep-ph/0501130].

[66] C. Balazs and C. P. Yuan, Phys. Lett. B **478**, 192 (2000) [arXiv:hep-ph/0001103];

[67] S. Catani, D. de Florian, M. Grazzini and P. Nason, JHEP **0307**, 028 (2003) [arXiv:hep-ph/0306211].

[68] G. Bozzi, S. Catani, D. de Florian and M. Grazzini, Phys. Lett. B **564**, 65 (2003) [arXiv:hep-ph/0302104]; G. Bozzi, S. Catani, D. de Florian and M. Grazzini, Nucl. Phys. B **737**, 73 (2006) [arXiv:hep-ph/0508068]. D. de Florian, M. Grazzini and Z. Kunszt, Phys. Rev. Lett. **82** (1999) 5209. [arXiv:hep-ph/9902483].

[69] S. Frixione and B. R. Webber, arXiv:hep-ph/0601192.

[70] S. Frixione and B. R. Webber, JHEP **0206** (2002) 029 [arXiv:hep-ph/0204244]
S. Frixione, P. Nason and B. R. Webber, JHEP **0308** (2003) 007 [arXiv:hep-ph/0305252].

[71] P. Nason, JHEP **0411**, 040 (2004) [arXiv:hep-ph/0409146].

[72] Z. Nagy and D. E. Soper, arXiv:hep-ph/0503053.

[73] M. Kramer, S. Mrenna and D. E. Soper, arXiv:hep-ph/0509127.

[74] T. Sjostrand, L. Lonnblad, S. Mrenna and P. Skands, arXiv:hep-ph/0308153.

[75] G. Corcella *et al.*, JHEP **0101** (2001) 010.

[76] G. Davatz, G. Dissertori, M. Dittmar, M. Grazzini and F. Pauss, JHEP **0405**, 009 (2004) [arXiv:hep-ph/0402218].

[77] K. Cranmer, B. Mellado, W. Quayle and S. L. Wu, hep-ph/0307242.

[78] S. Catani, D. de Florian and M. Grazzini, JHEP **0201** (2002) 015.

[79] L. J. Dixon, Z. Kunszt and A. Signer, Phys. Rev. D **60** (1999) 114037.

[80] M. Duhrssen, K. Jakobs, J. J. van der Bij and P. Marquard, JHEP **0505** (2005) 064 [arXiv:hep-ph/0504006].

[81] T. Binoth, M. Ciccolini, N. Kauer and M. Kramer, JHEP **0503** (2005) 065, [arXiv:hep-ph/0503094].

[82] G.Davatz, A.-S. Giolo, M.Zanetti, Effect of parton showering on gluon induced WW production p.93-94; in C. Buttar *et al.*, "Les Houches physics at TeV colliders 2005, standard model, QCD, EW, and arXiv:hep-ph/0604120.

[83] J.Campbell, G.Davatz, A.-S. Giolo, F.Maltoni, S.Willenbrock, M.Zanetti, Single resonant top production as background to the H→WW search p.110-112; in C. Buttar *et al.*, "Les Houches physics at TeV colliders 2005, standard model, QCD, EW, and arXiv:hep-ph/0604120.

[84] G. Altarelli and G. Parisi, Nucl. Phys. B126 (1977) 298.

[85] V. Gribov and L. Lipatov, Sov. J. Nucl. Phys.15 (1972) 438; Y. Dokshitzer, Sov. Phys. JETP 46 (1977) 641.

[86] H. Jung, Comput. Phys. Commun. **143** (2002) 100 [arXiv:hep-ph/0109102].

[87] M. Ciafaloni, Nucl. Phys. B **296**, 49 (1988).

[88] S. Catani, F. Fiorani and G. Marchesini, Nucl. Phys. B **336**, 18 (1990).

[89] G.Davatz and A.Nikitenko, "Uncertainties on gg → H due to a jet veto", p. 246-251; in S. Alekhin *et al.*, "HERA and the LHC - A workshop on the implications of HERA for LHC physics: arXiv:hep-ph/0601012.

[90] G. Corcella and S. Moretti, Phys. Lett. B **590** (2004) 249 [arXiv:hep-ph/0402146].

[91] CMS Collaboration, CMS TDR 6.2, 2002, CERN-LHCC-2002-26, ch.15, p.317.

[92] I. Dawson, C. Buttar and A. Moraes, Czech. J. Phys. **54**, A221 (2004).

[93] R. Field [CDF Collaboration], AIP Conf. Proc. **828**, 163 (2006).

[94] S. Moch and A. Vogt, Phys. Lett. B **631** (2005) 48 [arXiv:hep-ph/0508265].

[95] A. Djouadi, M. Spira and P.M. Zerwas, Phys. Lett. **B264**, 440 (1991); D. Graudenz, M. Spira and P.M. Zerwas, Phys. Rev. Lett. **70**, 1372 (1993); M. Spira, A. Djouadi, D. Graudenz and P.M. Zerwas, Nucl. Phys. **B453**, 17 (1995).

[96] S. Dawson, Nucl. Phys. B359 (1991) 283.

[97] R. V. Harlander, Phys. Lett. B **492** (2000) 74 [arXiv:hep-ph/0007289].

[98] R. Hamberg, W.L. van Neerven and T. Matsuura, Nucl. Phys. B359 (1991) 343 and (E) B644 (2002) 403.

[99] R. V. Harlander and W. B. Kilgore, Phys. Rev. D **64** (2001) 013015 [arXiv:hep-ph/0102241].

[100] S. Catani, D. de Florian and M. Grazzini, JHEP **0105** (2001) 025 [arXiv:hep-ph/0102227].

[101] R. V. Harlander and W. B. Kilgore, Phys. Rev. Lett. **88** (2002) 201801 [arXiv:hep-ph/0201206].

[102] C. Anastasiou and K. Melnikov, Nucl. Phys. B **646** (2002) 220 [arXiv:hep-ph/0207004].

[103] M. Krämer, E. Laenen and M. Spira, Nucl. Phys. B511 (1998) 523.

[104] S. Catani, D. de Florian, M. Grazzini, *Higgs production at hadron colliders in (almost) NNLO QCD*, hep-ph/0106049, June 2001.

[105] R. Harlander and W. Kilgore, hep-ph/0211380.

[106] A. Djouadi and S. Ferrag, Phys. Lett. B **586** (2004) 345 [arXiv:hep-ph/0310209].

[107] A.D. Martin, R.G. Roberts, W.J. Stirling and R.S. Thorne, Phys. Lett. B531 (2002) 216.

[108] S.Catani, D. de Florian, M.Grazzini and P. Nason in arXiv:hep-ph/0204316.

[109] G. Davatz, "Effects of Higher Order QCD Corrections for Higgs Detection in the Channel H → W W → l nu l nu at the LHC", Diploma thesis, 2003.

[110] G. Miu and T. Sjöstrand, Phys. Lett. B **449** (1999) 313.

[111] M. Dobbs *et al.*, Proceedings of the Workshop on Physics at TeV Colliders, Les Houches, France, 2003, hep-ph/0403100.

[112] J. M. Campbell and R. K. Ellis, Phys. Rev. D **60** (1999) 113006.

[113] J. Ohnemus, Phys. Rev. D **44** (1991) 1403; S. Frixione, Nucl. Phys. B **410** (1993) 280.

[114] E. W. N. Glover, J. Ohnemus and S. S. D. Willenbrock, Phys. Rev. D **37** (1988) 3193.

[115] V. Barger, G. Bhattacharya, T. Han, B. A. Kniehl, Phys. Rev. D **43**, 779 (1991).

[116] M. Dittmar, H. Dreiner, hep-ph/9703401, March 1997.

[117] M. Dittmar and H. K. Dreiner, Phys. Rev. D **55**, 167 (1997) [arXiv:hep-ph/9608317].fin

[118] M. Dittmar and H. K. Dreiner, Contributed Paper to the 1997 EPS conference in Jerusalem and CMS Note 97/080.

[119] G. Davatz, F. Stockli, C. Anastasiou, G. Dissertori, M. Dittmar, K. Melnikov and F. Petriello, JHEP **0607** (2006) 037 [arXiv:hep-ph/0604077].

[120] Z. Sullivan and E. L. Berger, Phys. Rev. D **74** (2006) 033008 [arXiv:hep-ph/0606271].

[121] J. Campbell and F. Tramontano, Nucl. Phys. B **726**, 109 (2005) [arXiv:hep-ph/0506289]. and C. Buttar *et al.*, arXiv:hep-ph/0604120.

[122] J. Campbell and K. Ellis, "Monte Carlo for FeMtobarn processes", http://mcfm.fnal.gov/

[123] S.R. Slabospitsky, L. Sonnenschein, Comput. Phys. Commun. **148** (2002) 87, [arXiv:hep-ph/0201292].

[124] N. Kauer and J. Campbell, private communication.

[125] G.Davatz, A.-S. Giolo, M.Zanetti, Top background generation for the H-¿WW channel p.101-110; in C. Buttar *et al.*, "Les Houches physics at TeV colliders 2005, standard model, QCD, EW, and arXiv:hep-ph/0604120.

[126] Monte Carlo Generators for CMS: http://cmsdoc.cern.ch/cms/generators/ .

[127] More about GEANT: http://wwwasd.web.cern.ch/wwwasd/geant4/geant4.html .

[128] More about ORCA can be found on http:cmsdoc.cern.ch/orca/

[129] PAX homepage: http://www-ekp.phys.uni-karlsruhe.de/ẽrdmann/paxguide/ . See also M. Erdmann *et al.*, *In the Proceedings of 2003 Conference for Computing in High-Energy and Nuclear Physics (CHEP 03), La Jolla, California, 24-28 Mar 2003, pp THLT008* [arXiv:physics/0306085].

[130] More about ORCA can be found on http://root.cern.ch.

[131] More about CMSSW can be found on http://cmsdoc.cern.ch/cms/cpt/Software/html/General/.

[132] G.Davatz, A.-S. Giolo-Nicollerat, M.Dittmar, CMS-NOTE 2006/047.

[133] A.S. Giolo-Nicollerat, "Jets Faking Leptons, Estimation of the W+jets Background for the $H \to WW \to \ell\nu\ell\nu$ Channel", CMS-IN2005/028.

[134] M. Spira, Fortsch. Phys. **46** (1998) 203 [arXiv:hep-ph/9705337].

M. Spira, arXiv:hep-ph/9510347.

A. Djouadi, J. Kalinowski and M. Spira, Comput. Phys. Commun. **108** (1998) 56 [arXiv:hep-ph/9704448].

[135] The WW, WZ, ZZ, tWb cross sections are calculated by J. Campbell using MCFM (J. M. Campbell and R. K. Ellis, Phys. Rev. D **62**, 114012 (2000) [arXiv:hep-ph/0006304].). The ggWW cross section is from reference [81]. The $t\bar{t}$ cross section has been calculated in R. Bonciani, S. Catani, M. L. Mangano and P. Nason, "NLL resummation of the heavy-quark hadroproduction cross-section," Nucl. Phys. B **529** (1998) 424 [arXiv:hep-ph/9801375].

[136] C. Buttar *et al.*, arXiv:hep-ph/0604120.

[137] G. Davatz, A.-S. Giolo-Nicollerat, M. Zanetti, *Systematic uncertainties of the top background in the H→WW channel,* CMS NOTE-2006/048.

[138] N. Kauer, "Top background extrapolation for H → W W searches at the LHC," Phys. Rev. D **70** (2004) 014020 [arXiv:hep-ph/0404045].

[139] J. D'Hondt, J. Heyninck, S. Lowette and P. Vanlear, *Offline Calibration of b-Jet Identification Efficiency* CMS AN-2005/013.

[140] V. Drollinger et al., *Modeling the production of W pairs at the LHC,* CMS NOTE 2005/024.

[141] The significance is calculated using the "scp" program: Bityukov et al., Program for evalutation of the significance, confidence intervals and limits by direct calculation of prbabilities, PHYSTAT'05 proceedings, http://www.physics.ox.ac.uk/phystat05/proceedings/files/bityukov-talk2_final.pdf

[142] D. Genzinski, http : //ichep06.jinr.ru/reports/17_15p10_Glenzinski.ppt and further references therein.

[143] J. D'Hondt, J. Heyninck and S. Lowette, CERN-CMS-NOTE-2006-064.

[144] M. Dittmar, F. Pauss and D. Zurcher, Phys. Rev. D **56** (1997) 7284 [arXiv:hep-ex/9705004].

[145] A. D. Martin, R. G. Roberts, W. J. Stirling and R. S. Thorne, Eur. Phys. J. C **28** (2003) 455 [arXiv:hep-ph/0211080].

[146] J. Pumplin, A. Belyaev, J. Huston, D. Stump and W. K. Tung, JHEP **0602** (2006) 032 [arXiv:hep-ph/0512167].

[147] W. K. Tung, *Prepared for 12th International Workshop on Deep Inelastic Scattering (DIS 2004), Strbske Pleso, Slovakia, 14-18 Apr 2004* for an update see proceedings of DIS 2007, Munich, Germany.